Developing quantum field theoretical computational methods for quantum dynamics and statistical mechanics simulations in quantum chemistry

by

Songhao Bao

A thesis
presented to the University of Waterloo
in fulfillment of the
thesis requirement for the degree of
Doctor of Philosophy
in
Chemistry

Waterloo, Ontario, Canada, 2024

© Songhao Bao 2024

Examining Committee Membership

The following served on the Examining Committee for this thesis. The decision of the Examining Committee is by majority vote.

External Examiner:	Gustavo Scuseria Professor, Dept. of Chemistry Rice University
Supervisor	Marcel Nooijen Professor, Dept. of Chemistry, University of Waterloo
Internal Member(s):	Pierre-Nicholas Roy Professor, Dept. of Chemistry, University of Waterloo
	Tao Zeng Associate Professor, Dept. of Chemistry, York University
Internal-External Member:	Roger Melko Professor, Dept. of Physics, University of Waterloo

Author's Declaration

This thesis consists of material all of which I authored or co-authored: see Statement of Contributions included in the thesis. This is a true copy of the thesis, including any required final revisions, as accepted by my examiners.

I understand that my thesis may be made electronically available to the public.

Statement of Contributions

The first part of chapter 3 has been published in: M. Nooijen and S. Bao, "Normal ordered exponential approach to thermal properties and time-correlation functions: general theory and simple examples", *Mol. Phys.* **119**, 21-22 (2021). The original theory is proposed by M. Nooijen and the article is mainly composed by M. Nooijen. Computer programs are implemented and tested on simple examples by me.

The chapter 5 has been published in: S. Bao, N. Raymond and M. Nooijen, "Time dependent vibrational electronic coupled cluster (VECC) theory for non-adiabatic nuclear dynamics", *J. Chem. Phys*, **160**, 094105 (2024). The original idea is proposed by M. Nooijen. The primary implementation and investigation are mainly performed by me. N. Raymond optimize the primary implementation, developed code and equation generators to facilitate the development of the program and contribute on benchmark the method against the multi-configuration time-dependent Hartree (MCTDH) simulations.

The chapter 6 has been published in: S. Bao, N. Raymond, T. Zeng and M. Nooijen, "Vibrational Electronic-Thermofield Coupled Cluster (VE-TFCC) Theory for Quantum Simulations of Vibronic Coupling Systems at Thermal Equilibrium", *J. Chem. Theory Comput.*, **20**, 14 (2024). The theory is proposed by M. Nooijen and me. The implementation of the method and benchmark on vibronic models against the sum-over-states (SOS) are mostly done by me. N. Raymond contribute the revision of the manuscript and the computer program developed by N. Raymond are applied to read-in vibronic model parameters to my main simulation program from the MCTDH standard `*.op` files. The calculation of the vibronic model for the CoF_4^- anion is performed by T. Zeng. T. Zeng also contributed on analysis of the results for both the electronic structure calculations and simulation data of the vibronic model for the CoF_4^- anion.

Abstract

This thesis presents the development of two approaches—thermal normal-ordered exponential (TNOE) and thermofield coupled cluster (TFCC)—for simulating quantum dynamics and statistical mechanics in quantum chemistry, grounded in quantum field theoretical formulations. The TNOE approach employs a normal-ordered exponential ansatz to parameterize the thermal density operator, allowing the calculation of thermal properties through cluster expansions and imaginary time integration of equations of motion (EOMs). The TFCC approach introduces a fictitious space and Bogoliubov transformation to express the thermal density operator as a "pure state," similarly enabling thermal property calculations through imaginary time integration. The two approaches are verified to be mathematically equivalent and they are applied to two specific problems: the electronic structure problem and the vibronic coupling problem. The application on the thermal electronic structure problems encounters challenges due to N-representability issues. Modifications to the TNOE approach lead to the vibrational electronic coupled cluster (VECC) method, effectively simulating the quantum dynamics of vibronic coupling systems with impressive efficiency and accuracy. The statistical mechanics formulation of the VECC method, vibrational electronic-thermofield coupled cluster (VE-TFCC), utilizes imaginary time integration to successfully calculate thermal properties of vibronic coupling systems with enhanced efficiency and accuracy compared to conventional methods. Overall, the VECC and VE-TFCC approaches, in combination with vibronic models, provides a robust framework for simulating quantum dynamics and thermal equilibrium properties of vibronic coupling systems.

Acknowledgements

"*Though I walk through the valley of the shadow of death, I will fear no evil: for thou art with me.*"

Time flies. My PhD journey eventually draws to an end. During all the five years, I experienced the darkest as well as the finest moments.

Covid 19 was a big hit. Not only did it change everyone's life, but also had deeply affect our society. The science and technology we once boasted about proved inadequate during the initial stages of this public health crisis. The universal values that we human beings have developed and practiced since the dawn of the civilization were challenged. Fortunately, the pandemic does not affect a lot on my research and my family in China remained healthy. Working from home made my life reminiscent of an ancient hermit's, providing me with the serenity to contemplate deep theories. As life gradually returns to normalcy after the chaos, the freedom we once took for granted is now cherished. Simple daily activities such as grocery shopping or gathering for dinner or parties became extremely dangerous during the pandemic.

My trip to Europe for the ICQC conference was an incredible experience. During the conference, I met many illustrious scientists in our field and had the opportunity for in-person discussions with several, including Professors Piotr Piecuch, Gustove Scuseria, Garnet Chan, Jianwen Liu, Artur Izmaylov, Dominika Zgid, etc., during my poster session and Q & A. My work was well-received. Additionally, I visited Dr. Ondřej Demel at his home institute in Prague and enjoyed an engaging chat with him for an entire afternoon. Ondřej showed me his poster on his recent work on local MRCC development and discussed the institute's famous alumni. I thoroughly enjoyed my stay in Prague, appreciating the city's classic architectural style and rich culture.

This thesis would not have been possible without the help of a few individuals, and I express my sincere gratitude to those who supported me throughout my PhD journey.

First of all, I want to express my gratitude to my supervisor Prof Marcel Nooijen who brought me to this excited PhD journey. Whether through course projects or my own research projects, Prof Nooijen gave me the freedom to explore and think deeply without pushing me through deadlines or trivial onerous tasks. I enjoyed many insightful discussions with him on the coupled cluster theory, Feynman diagrams and statistical mechanics. Through these discussions and free explorations, I was cultivated to have the ability for critical thinking and a good taste for research projects. I also appreciate Prof Nooijen's stringency in terms of the results and not allowing quick, low quality works to be published. This attitude towards science will have seminal impact on my academic career. In addition, I am also grateful to my collaborator and committee member, Prof. Toby Zeng, whose expertise in electronic structure theory and vibronic coupling systems was instrumental. Prof Zeng patiently gave me lectures on the fundamental concepts of the vibronic coupling systems and the diabatization protocol developed by his group to run calculations to construct vibronic models. I also give thanks to Prof Fabrizio Santoro and Prof Garnet Chan. Prof Santoro kindly shared the original data and explained in details for their paper on the MCTDH simulation of absorption spectra for hexahelicene. Prof Chan explained me in details on their

work on the time-dependent coupled cluster theory and shared me the original note by Dr Alex White. I was inspired a lot by their work to develop the TNOE and TFCC approach in this thesis.

I am sincerely thankful to all other internal and external members of my PhD committee, including Professors Pierre-Nicholas Roy, Scott Hopkins, Roger Melko, Michel Gingras, and Gustave Scuseria, for their feedback and advice.

I also want to express my gratitude to my group members: Neil Raymond, Haobo Liu, Benny Chen, Oz Mohammed, Wenxue Zhang, and Coco Song. Special thanks to Neil for dedicating time to teach me programming and reviewing manuscripts. Collaborating with Neil on various projects has been a pleasure. I am thankful to all other members of the theoretical chemistry group for their friendship and support.

Lastly, I want to thank my parents for supporting my career choice and taking care of me throughout my life. My early childhood was far from straight. I was the "trouble maker", the "outlier" and the "bad example" and I was never a standard "good student" for most of my teachers. I could not have achieved this without the unwavering support and understanding of my parents.

Table of Contents

List of Figures **xiii**

List of Tables **xvi**

List of Abbreviations **xvii**

List of Listings **xx**

1 Introduction **1**

1.1 Problem and scope of the thesis 1

1.2 Roadmap of the thesis 3

2 Background knowledge **5**

2.1 Quantum chemistry of many-electrons: electronic structure theory 5

2.1.1 Born-Oppenheimer approximation (BOA) 5

2.1.2 Hartree-Fock (HF) method 7

2.1.3 Second quantization 9

2.1.4 Coupled Cluster (CC) theory 12

2.1.5 Normal order and Wick's theorem 14

2.2 Quantum chemistry at finite temperature: statistical mechanics 15

2.2.1 Classification of the statistical ensembles 16

2.2.2 Quantum mechanical formulation of the statistical mechanics 17

2.3 Quantum chemistry beyond BOA: vibronic coupling problem 18

2.3.1 Origin of vibronic coupling interaction 18

2.3.2 Techniques to incorporate the vibronic coupling in quantum chemistry 19

2.3.3 Applications of the vibronic coupling effect 20

3 General Theory **23**

3.1 Thermal normal-ordered exponential (TNOE) approach . . . 23

3.1.1 TNOE ansatz and generalized (simple) Wick's theorem . . . 24

3.1.2 Derivation of the equations of motion (EOM) . . . 26

3.1.3 Calculate thermal properties using the TNOE approach . . . 28

3.1.4 Zero temperature limit for the TNOE approach . . . 30

3.2 Thermofield coupled cluster (TFCC) theory . . . 34

3.2.1 Definition of the thermostate . . . 34

3.2.2 Bogoliubov transformation and exponential ansatz . . . 36

3.2.3 Derivation of the coupled cluster equation of motion (CC-EOM) . . . 40

3.2.4 Calculate thermal properties using TFCC approach . . . 41

3.3 Connection between TNOE and TFCC . . . 43

3.3.1 Comparing number of independent parameters . . . 43

3.3.2 Mappings between cluster amplitudes . . . 44

3.3.3 The connection of the EOMs . . . 46

3.3.4 The connection of the reference states . . . 49

3.4 Summary of the chapter . . . 51

4 Application: thermal properties for pure electronic structure problems **52**

4.1 Theory and implementation . . . 53

4.1.1 Thermofield coupled cluster (TFCC) method for electronic structure problem . . . 53

4.1.2 Introduce the completed active space (CAS) . . . 60

4.1.3 Constraints and N-representability problem . . . 66

4.2 Result and discussion . . . 74

4.2.1 Test on model magnetic systems . . . 74

4.2.2 Test on small molecular systems . . . 81

4.3 Summary of this chapter . . . 105

5 Application: quantum dynamics simulations for the vibronic problems **107**

5.1 Abstract . . . 107

5.2 Introduction . . . 107

5.3 Theory . . . 111

5.3.1 General overview of VECC Theory . . . 111
5.3.2 Exploring four single-surface approaches . . . 112
5.3.3 Approach for full vibronic models . . . 119
5.3.4 Calculating time-dependent properties with VECC . . . 126
5.4 Result and discussion . . . 131
5.4.1 Summary of vibronic models . . . 132
5.4.2 two by two models . . . 133
5.4.3 Small molecules . . . 137
5.4.4 Large molecules . . . 140
5.5 Concluding remarks . . . 143
5.5.1 In Summary . . . 143
5.5.2 Final Remarks . . . 144

6 Application: statistical mechanics simulations for the vibronic problems 147
6.1 Abstract . . . 147
6.2 Introduction . . . 147
6.3 Theory . . . 149
6.3.1 Single-surface formulation: vibrational TFCC theory . . . 151
6.3.2 Vibronic multi-surface formulation: VE-TFCC theory . . . 162
6.4 Benchmarks and Application . . . 167
6.4.1 Benchmark on two by two vibronic models . . . 168
6.4.2 Benchmark on the vibronic model for CoF_4^- anion . . . 171
6.4.3 Analysis of thermochemistry calculations . . . 176
6.5 Concluding Remarks . . . 180

7 Concluding remarks and future orientations 183
7.1 Concluding remarks . . . 183
7.2 Future orientations . . . 184

Bibliography 187

APPENDICES 202

A Proof of the (anti)-commutation rule of the Bogoliubov transform operators 202

A.1 Proof of commutation rules of the Bogoliubov transformed Bosonic operators 202

A.2 Proof of anti-commutation rules of the Bogoliubov transformed Fermonic operators 204

B Proof of vacuum state condition of Bogoliubov transformed operator with the respect to $|\theta(\beta)\rangle$ state 207

B.1 Proof of the vacuum state condition for Bosonic operators 207

B.2 Proof of the vacuum state condition for Fermionic operators 209

C Proof of the EOMs translate between the TNOE and the TFCC approaches for Bosonic vibrational Hamiltonian 211

D Explicit expression of the Bogoliubov transformed two-electron integrals 217

E Subroutines that implement the TFCC residual equations for electronic structrue problem 219

F Discussion of spin and spin-adaptation 224

G Proof of the connectedness for the coupled cluster (CC) energy and amplitude equations 227

H Supporting information for chapter 5 228

H.1 Vibronic model parameters 228

H.1.1 two by two models 228

H.1.2 Water H_2O model 228

H.1.3 Ammonia NH_3 model 229

H.1.4 Pyrazine $C_4H_4N_2$ model 229

H.1.5 Hexahelicene $C_{26}H_{16}$) model 229

H.2 Spectra simulation for model A and model B 230

H.3 Explicit scheme to test convergence behaviour of Z operator excitation level . 231

H.3.1 Scheme to compute diabatic state population 232

H.3.2 Scheme to compute auto-correlation function (ACF) and spectra . . . 233

H.3.3 Make direct comparison to the original operator version of the VECC method 233

I Supporting information for chapter 6 **246**

I.1 Expression of Bogoliubov transformed Hamiltonian (up to quadratic) 246

I.2 The initial cluster amplitudes (at high T) 247

I.3 Motivation of the ansatz for the vibronic problem 248

I.4 Detailed scheme for calculating the variance of the position (q-variance) using VE-TFCC 250

I.5 Data for standard thermochemistry calculation 252

I.5.1 Details on calculations of the reaction energy at 0 K 252

I.5.2 Thermal internal energy corrections data 253

I.5.3 Entropies at 298 K 254

List of Figures

2.1 Illustration of the potential energy surface (PES)s in a molecular system. [35] 7

2.2 Illustration of the HF procedure 9

2.3 Illustration of the quantum dynamics process for vibronic coupling systems [55] 21

4.1 Illustration of complete active space (CAS) 61

4.2 A diagram illustrates the three parameters in the model magnetic Hamiltonian in Eq. (4.81) 75

4.3 Plot of the thermal properties for the weakly coupling model 77

4.4 Plot of the minimum matrix elements of P, Q, G cumulants as functions of temperature for the weakly coupling model 78

4.5 Plot of the thermal properties for the strongly coupling model 79

4.6 Plot of the occupation number and minimum matrix elements of P, Q, G cumulants as functions of temperature for the strongly coupling model . . . 80

4.7 Representation of (a) structure (b) coordinates for HF molecule. 81

4.8 Representation of (a) structure (b) coordinates for H_2O molecule. 82

4.9 Plot of thermal internal energy for HF (6-31g basis) 83

4.10 Plot of thermal internal energy for H_2O (6-31g basis) 84

4.11 Plots of occupation number as a function of temperature (a) with N-representability constraints (b) without N-representability constraints for HF molecule. . . . 86

4.12 Plots of occupation number as a function of temperature (a) with N-representability constraints (b) without N-representability constraints for H_2O molecule. . . 87

4.13 Plots of the minimum P,Q,G cumulants ($\alpha\beta$ component) (a) with N-representability constraints (b) without N-representability constraints for HF molecule. . . . 89

4.14 Plots of the minimum P,Q,G cumulants ($\alpha\beta$ component) (a) with N-representability constraints (b) without N-representability constraints for H_2O molecule. . . 90

4.15 Representation of (a) structure (b) coordinates for N_2 molecule. 91

4.16 Representation of (a) structure (b) coordinates for O_2 molecule. 92

4.17 Illustration of (a) occupation scheme (b) active orbitals for N_2 molecule. . . 93
4.18 Illustration of (a) occupation scheme (b) active orbitals for O_2 molecule. . . 94
4.19 Plot of thermal internal energy for N_2 (ccpvdz basis) 95
4.20 Plot of thermal internal energy for O_2 (ccpvdz basis) 96
4.21 Plots of occupation number as a function of temperature (a) with N-representability constraints (b) without N-representability constraints for N_2 molecule. . . . 98
4.22 Plots of occupation number as a function of temperature (a) with N-representability constraints (b) without N-representability constraints for O_2 molecule. . . . 99
4.23 Plots of the minimum P,Q,G cumulants ($\alpha\beta$ component) (a) with N-representability constraints (b) without N-representability constraints for N_2 molecule. . . . 101
4.24 Plots of the minimum P,Q,G cumulants ($\alpha\beta$ component)(a) with N-representability constraints (b) without N-representability constraints for O_2 molecule. . . . 102
4.25 Illustration of (a) configuration (b)coordinate for ArO_2 molecule. 103
4.26 Illustration of (a) configuration (b)coordinate for ArON molecule. 104
4.27 Plot of thermal internal energy for ArO_2 (ccpvdz basis) 104
4.28 Plot of thermal internal energy for ArON (ccpvdz basis) 105

5.1 Diagram illustrates how excited state wave-function evolves over time. . . . 109
5.2 Comparison of the different absorption spectra produced by the single-surface approaches. Spectra are benchmarked using exact diagonalisation (ED). . . 119
5.3 By introducing $e^{\hat{T}^\dagger}$, we shift the center of the initial wave-function, or reference state, to align it with the current wave-function at time τ. 122
5.4 Simulated spectra of model-C using VECC and ED. The convergence of VECC is compared against ED for various excitation levels of the $\hat{Z}$ operator. . . . 135
5.5 Simulated diabatic state population of model-C using VECC and ED. The convergence of VECC is compared against ED for various excitation levels of the $\hat{Z}$ operator. 136
5.6 Simulated absorption spectra of water and ammonia molecular compounds using VECC and MCTDH. Both are generated through a Fourier transform of their time-autocorrelation functions using `autospec84`. 138
5.7 Simulated diabatic state population of water and ammonia models using VECC and MCTDH. The symmetry label of each state is listed in parentheses. 139
5.8 We simulate the absorption spectra of pyrazine (2 states, 24 modes) using the VECC and MCTDH methods. The model and Fourier transform parameters were obtained from the reference by Raab et al. [128] 141

5.9 Simulated and experimental absorption spectra of hexahelicene (14 states, 63 modes). Comparing the VECC method against the ML-MCTDH method used in Aranda et al, [56] after 300 fs propagation. 143

6.1 Compared to the sum over states method with a converged basis set, the thermal one-body reduced density matrix calculated using the expression from the TFCC method produces numerical exact result for the single-surface vibrational problem when truncated up to quadratic terms. 160

6.2 Simulated energy related thermal properties of model A, which has smaller linear displacements. 169

6.3 Simulated energy related thermal properties of model B, which has larger linear displacements. 170

6.4 Simulated q-variance ($\langle \Delta \hat{q}_i \rangle$) of model A, which has smaller linear displacements. 171

6.5 Simulated q-variance ($\langle \Delta \hat{q}_i \rangle$) of model B, which has larger linear displacements. 171

6.6 Active orbitals and occupation schemes for (a) the ^{5}E ground state of CoF_4^- in T_d symmetry and (b) the $^5A_1^{'}$ ground state of CoF_3. 172

6.7 Illustration of the 168.46 cm^{-1} e bending modes of the CoF_4^-anion. The dimensionless reduced normal mode coordinates are labeled as x and y, corresponding to the e_x and e_y component modes. 173

6.8 Plots of (a) adiabatic and (b) diabatic of E $\times$ e PESs of the CoF_4^- anion. . 173

6.9 Comparison of the thermal internal energies for CoF_4^- anion calculated using different approximations. 175

6.10 The ground state adiabatic PES of the E $\times$ e model in Eq. (6.111). 178

6.11 Plot of vibrational density of first excited A_1 state of dynamic Jahn-Teller (JT) and ground state of static JT. 180

7.1 Illustration of the future orientations 186

H.1 Simulated absorption spectra of two by two models using VECC and ED. Both are generated through a Fourier transform of their time-autocorrelation functions using `autospec84`. Parameters for both models are given in Table H.1 and Table H.2. 231

List of Tables

4.1 List of model parameters for the weakly coupling and strongly coupling models. . . . 75

4.2 Compare the ground state energies obtained from different approaches of HF and H_2O molecules (all energies are in unit Hartree) . . . 84

4.3 Compare the ground state energies obtained from different approaches of N_2 and O_2 molecules (all energies are in unit Hartree) . . . 97

4.4 Compare the ground state energies obtained from different approaches of ArO_2 and ArON molecules (all energies are in unit Hartree) . . . 105

6.1 two by two model parameters. . . . 168

6.2 Summary of the thermochemistry data (Reaction energies and free energies are all in units of kJ/mol and the entropy is in units of kJ/mol/K.) . . . 176

6.3 Comparison of electronic reaction energies at 0 K. . . . 177

H.1 two by two model parameters. . . . 228

H.2 in (eV). . . . 228

H.3 H_2O model parameters (eV). . . . 229

H.4 NH_3 model parameters (eV). . . . 229

I.1 Calculated thermal internal energy corrections (kJ/mol) at 298K for the three species in Eq. 6.105. . . . 253

I.2 Calculated entropies (in kJ/mol/K) of the species in Eq. (6.105) at 298K. . . . 254

List of Abbreviations

1-RDM one-body reduced density matrix. 68, 85

ACF auto-correlation function. xi, 21, 110, 112–115, 120, 127, 137, 140, 233

AI artificial intelligence. 185

AIMS ab initio multiple spawning. 108

AO atomic orbital. 8, 53, 63, 64

BCH Baker–Campbell–Hausdorff. 114, 128, 207, 209, 227

BE Bose-Einstein. 37

BHS both hand sides. 27, 41, 47, 58, 215

BOA Born-Oppenheimer approximation. viii, 5–7, 16, 18–20, 147, 148, 160, 184

CAS complete active space. xiii, xx, 52, 60–65, 81, 91, 94–97, 103, 105, 106

CC coupled cluster. xi, 9, 12–14, 28, 33, 39, 42, 52, 59, 66, 110, 111, 113–120, 122, 123, 125–131, 140–145, 153, 161, 164, 166, 167, 183, 184, 227

CC-EOM coupled cluster equation of motion. ix, 40

CI configurational interaction. 91, 115–124, 126, 144, 145, 164, 166, 167, 184

CSE contracted Schrödinger equation. 32

D.H.O. displaced harmonic oscillator. 112, 113

DFT density functional theory. 13

DoF degrees of freedom. 4, 43, 148, 149, 151, 163, 165, 167, 181, 248

ED exact diagonalisation. xiv, 105, 113–115, 117–120, 132–136

EOM equations of motion. ix, xi, 3, 23, 26, 27, 30–33, 40, 41, 43, 46–52, 58, 59, 66, 111, 114–119, 121, 123–126, 130, 150, 151, 155, 157, 158, 160, 164–166, 181, 183, 184, 211, 214, 216, 231, 232, 248, 249

EOMCC equation of motion coupled-cluster. 109

FC Frank–Condon. 21

FCI full configurational interaction. 60, 95–97, 105

FD Fermi-Dirac. xx, 25, 38, 50, 54, 55, 57, 58

GBOA group Born-Oppenheimer approximation. 148

GMC-QDPT general multi-configurational quasi-degenerate Perturbation theory. 172, 177, 178

GPU graphics processing unit. 185

H.O. harmonic oscillator. 6, 16, 110, 148, 150, 161, 166, 169, 170, 179, 232, 233

HF Hartree-Fock. viii, xiii, xx, 7, 9, 11, 13, 53–55, 62, 65, 82, 91, 92

JT Jahn-Teller. xv, 4, 22, 133, 137, 172, 174–177, 179, 180, 183, 252, 254

LVC linear vibronic-coupling constants. 133

MBPT many body perturbation theory. 2, 109

MC Multi-configuration. 61

MCTDH multi-configuration time-dependent Hartree. iv, vi, xiv, xv, 22, 107, 110, 114, 132, 133, 137–144, 148, 167, 172

MO molecular orbital. 1, 7, 8, 53, 60, 63, 64, 84, 91, 97

N.A.C non-adiabatic coupling. 20

NISQ noisy intermediate-scale quantum. 185

ODE ordinary differential equation. 2, 3, 114, 116, 132

PES potential energy surface. xiii, xv, 6, 7, 16, 18, 108, 112, 124, 148, 160, 173, 178, 179

PIMC Path Integral Monte Carlo. 148

R.R. rigid rotor. 6, 16, 148

SCF self-consistent field. xx, 7, 53, 61–63, 65

SD singles and doubles. 3, 27, 113, 115

SE Schrödinger equation. 1

SOS sum-over-states. iv, 41, 60, 76, 91, 95, 104, 148, 167, 170, 184

SR-CC single reference coupled cluster. 3, 14, 27, 31, 32, 49, 114, 158

TD-DFT time-dependent Density Functional Theory. 109, 133

TDCC time dependent coupled cluster. 2, 23

TDSE time-dependent Schrödinger equation. 2, 21, 26, 111, 113, 115, 116, 121, 126, 150

TF thermofield. 3, 34, 147, 149, 151, 152, 155, 158, 164, 168, 180, 181

TFCC thermofield coupled cluster. v, vii, ix, xi, xv, xx, 3, 4, 23, 36, 39–47, 49–54, 58–61, 65, 66, 69, 74–76, 80–82, 84, 91, 94–97, 103–106, 153, 155, 157–160, 162, 183, 184, 211, 213, 214, 216, 219–223

TISE time-independent Schrödinger equation. 1, 5–7, 13, 19

TNOE thermal normal-ordered exponential. v, vii, ix, xi, 3, 4, 18, 23, 24, 26–28, 30–33, 39, 43–47, 49–51, 110, 149–151, 155, 157, 159, 180, 181, 183, 211, 213, 214, 216

VCC vibrational coupled cluster. 111

VE-TFCC vibrational electronic-thermofield coupled cluster. v, 22, 147, 149, 163, 164, 167–171, 174–176, 180–182, 184, 250, 252, 254

VECC vibrational electronic coupled cluster. v, x, xi, xiv, xv, 22, 107, 110–113, 119, 125, 126, 128–146, 149, 166, 168, 181, 183, 184, 230–234

VG vertical gradient. 21

ZPE zero point energy. 174, 179, 252

List of Listings

4.1 Example Python script to run PySCF HF calculations 54
4.2 Example Python script to extract information from PySCF HF calculations . 55
4.3 Explicit Newtonian procedure to determine the Fermi-Dirac (FD) occupation number and the chemical potential at the reference temperature β 57
4.4 Example CAS-self-consistent field (SCF) calculations using PySCF 62
4.5 Python script to pick core and active orbitals based on the CAS-SCF calculation 63
4.6 Python script to construct effective one-electron integrals 64
4.7 Construct the Hamiltonian in model CAS based on effective one-electron integrals and two-electron integrals 65
4.8 Python script that implements constraint one 68
4.9 Python script that implements constraint two 69
4.10 Python script that implements constraint three 71
4.11 Python script that implements constraint four 73
E.1 Import necessary python libraries 219
E.2 Subroutines to calculate intermediate quantities for the TFCC singles residual 220
E.3 Subroutines to calculate intermediate quantities for the TFCC doubles residual 221
E.4 Subroutines to calculate TFCC singles and doubles residuals 222
E.5 Subroutine to calculate the TFCC constant residual 223
H.1 model A operator file 235
H.2 model B operator file 237
H.3 model C operator file 239
H.4 Water operator file 241
H.5 Ammonia operator file 243

Chapter 1

Introduction

1.1 Problem and scope of the thesis

Quantum chemistry is a subject that applies fundamental laws of quantum mechanics to understand properties of chemical systems. As been stated by Dr Paul Dirac decades ago "*the underlying physical laws necessary for the mathematical theory of ... the whole of chemistry are thus completely known, and the difficulty is only that the exact application of these laws leads to equations much too complicated to be soluble*" [1]. Solving the quantum mechanical equations associated with the chemical systems is the primary goal in quantum chemistry. Unfortunately, finding the exact solutions to the Schrödinger equation (SE) for chemical systems is an exponential hard computational task. For example, in a typical molecular electronic structure problem that have N molecular orbital (MO)s, its wavefunction can be expanded as a linear combination of the slater determinants with N one-electron basis functions.

$$|\Psi\rangle_{elec} = \sum_{n_1,n_2,...,n_N} C_{n_1,n_2,...,n_N} |n_1, n_2, ..., n_N\rangle \,, \ \forall \ n_i \in \{0, 1\} \tag{1.1}$$

Thus, the computational complicity to solve the time-independent Schrödinger equation (TISE) of the electronic structure problem:

$$\hat{H}_{elec} |\Psi\rangle_{elec} = E |\Psi\rangle_{elec} \,, \tag{1.2}$$

$$\hat{H}_{elec} = \sum_{ij} \langle i| \hat{h} |j\rangle \, \hat{i}^\dagger \hat{j} + \frac{1}{4} \sum_{ijkl} \langle ij \| kl \rangle \hat{i}^\dagger \hat{j}^\dagger \hat{l} \hat{k}, \tag{1.3}$$

is $O(2^N)$. Although it is not always feasible to find the exact solution to the SE, systematical approximations can be applied in quantum chemistry that provide accurate heuristic solutions. Thus, developing computational methods to (approximately) solve the electronic structure problem is one of the primary goals of quantum chemistry.

Over the decades, many efforts have been made to develop ab initio computational methods to solve the molecular electronic structure problem as described in Eq. (1.1) and Eq. (1.2). These methods make a balance between efficiency and accuracy to approximate the ground

state and excited states energies as well as the corresponding electronic wavefunctions from the molecular electronic Hamiltonian. The molecular electronic structure problem plays an important role to understand the chemical properties of molecular system and mechanisms of chemical reactions. However, the solution of energy eigenvalues and eigenstates of molecular electronic Hamiltonian is not always sufficient to obtain properties that are of real interest. There is a gap between these solutions and quantities that can be directly observed through experiments such as spectroscopy, state populations and thermochemistry properties. To fill this gap, computational methods that can simulate the statistical mechanics and quantum-dynamics of chemical systems are required. This is the motivation of this thesis.

Before looking at the detailed problems (as will be elaborated in the later chapters), let me firstly define the problem in a general context. For a general quantum many-body system, the statistical average of an arbitrary physical observable $\hat{O}$ in a thermal ensemble is defined as:

$$\left\langle \hat{O}(\beta) \right\rangle \equiv \frac{\mathrm{Tr}\left(\hat{O}\hat{D}(\beta)\right)}{\mathrm{Tr}\left(\hat{D}(\beta)\right)} \; ; \; \hat{D}(\beta) \equiv e^{-\beta\hat{H}}, \tag{1.4}$$

and its time-dependent properties is defined as:

$$\left\langle \hat{O}(\tau) \right\rangle \equiv \frac{\langle\Psi(\tau)|\,\hat{O}\,|\Psi(\tau)\rangle}{\langle\Psi(\tau)|\Psi(\tau)\rangle} \; ; \; |\Psi(\tau)\rangle \equiv e^{-i\hat{H}\tau}\,|\Psi(0)\rangle\,. \tag{1.5}$$

The two seemingly very different properties described in Eq. (1.4) and Eq. (1.5) are actually closely related if we reformulate them in a form of differential operator equations:

$$i\frac{\mathrm{d}}{\mathrm{d}\tau}\hat{U}(\tau) = \hat{H}\hat{U}(\tau) \; ; \; \hat{U}(\tau) \equiv e^{-i\hat{H}\tau}, \tag{1.6}$$

and

$$-\frac{\mathrm{d}}{\mathrm{d}\beta}\hat{D}(\beta) = \hat{H}\hat{D} \; ; \; \hat{D}(\beta) \equiv e^{-\beta\hat{H}}. \tag{1.7}$$

Both Eq. (1.6) and Eq. (1.7) are first order ordinary differential equation (ODE)s and the only difference is that the real time (τ) is replaced by the imaginary time (β) in the latter equation. Both equations can be regarded as the time-dependent Schrödinger equation (TDSE). However, with the same arguments as discussed in the electronic structure problem, solving the TDSE in Eq. (1.6) and Eq. (1.7) is computationally exponential hard when resolving them in a finite basis set for a general quantum many-body Hamiltonian.

Therefore, computational methods that can more efficiently (heuristically) solve the TDSE in Eq. (1.6) and Eq. (1.7) without the exponentially hard direct sum over states is required. The original idea of this thesis is based on the quantum field theoretical formulation of the statistical mechanics, in which standard interaction picture and perturbation theory are adopted. The first attempt to obtain thermal properties from this idea in quantum chemistry can be dated back to 1990s when Mukherjee and his co-workers developed the thermal cumulant approach. [2, 3, 4, 5] In recent years, there is a resurgence of this topic. The approaches can be mainly classified into three types: the time dependent coupled cluster (TDCC) approaches [6, 7, 8, 9], many body perturbation theory (MBPT) approaches [10,

11, 12, 13, 14] and self-consistent Green's function approaches [15, 16, 17, 18, 19].

However, most of these formulations are closely tied to single-reference perturbation theory, which poses challenges for studying the thermal properties of systems. To effectively investigate these properties, a system must exhibit a significant thermal population of excited electronic states at finite temperatures. This often requires multiple low-lying electronic states, with the ground state exhibiting a multi-reference nature. Therefore, we take a different approach, avoiding conventional perturbation theory and the interaction picture.

In this thesis, we develop the thermal normal-ordered exponential (TNOE) approach to directly calculate the thermal and quantum dynamics of chemical systems without explicitly relying on perturbation theory. The TNOE approach employs a normal-ordered exponential ansatz to parameterize the thermal density operator, enabling the expansion of thermal properties via generalized Wick's theorem and unique contraction rules. This allows for the extraction of thermal (dynamics) properties through numerical integration of ODEs involving low-ranking (e.g., singles and doubles (SD)) cluster operators, yielding computational efficiency due to its low-order polynomial scaling with respect to the degrees of freedom in the quantum many-body system.

Additionally, we utilize thermofield (TF) dynamics [20, 21, 22] to simplify our formulation. In TF dynamics, the thermal density operator of a statistical ensemble can be propagated as a "pure state" by introducing the physical-ancillary dual space and applying the Bogoliubov transformation [23, 24]. As a result, the orginal TNOE ansatz reduces to the simple exponential ansatz as in the conventional single reference coupled cluster (SR-CC) approach without explicitly introducing normal-ordering and the equations of motion (EOM)s are significantly simplified.

1.2 Roadmap of the thesis

This thesis is organized as follow.

In chapter 2, we give an introduction of quantum chemistry in three aspects: the electronic structure theory, the statistical mechanics and the vibronic coupling problem. This chapter serves as the theoretical basis of this thesis. In the later chapters, the knowledge covered in this chapter is applied for the specific problems.

In chapter 3, we introduce theoretical framework to directly calculate thermal and time-dependent properties. The discussion is in a general context which does not specify the quantum many-body system and this family of approaches can be in principle applied to a general form of Hamiltonian (either Fermionic or Bosonic). The chapter starts by introducing the TNOE approach that is based on the work by Nooijen and Bao. [25] A detailed first principle derivation is given. Then we introduce an alternative formulation which is known as the thermofield coupled cluster (TFCC) theory. It is firstly introduced to quantum chemistry by Harsha et al. [26, 27, 28, 29, 30] We provided an independent derivation of the TFCC equations. Our derivation is slightly different from the original formulation, in which we do not rely on the response theory and Λ-equations to calculate thermal properties. Instead,

the thermal properties are mapped directly through the cumulant expression of the thermal density matrix which follows the track in the TNOE approach. Finally, the connection between the TNOE and TFCC is discussed.

In chapter 4, we discuss about the application of the general theory on the thermal electronic structure problem. Explicit formulation and implementation are elaborated. The approach does not produce expected results due to the N-representability problem. We discuss in details about this problem and attempt to resolve it by systematically applying the constraints to the thermal reduced density matrices. Theoretical insights are obtained through the benchmark studies on model magnetic systems and small molecular compounds.

In chapter 5, we discuss about another specific application of the general theory: simulation of spectroscopy and quantum-dynamics properties of the non-adiabatic vibronic models. This chapter is based on the work by Bao, Raymond and Nooijen. [31] We introduced a compact representation of the time-dependent wavefunction ($|\Psi(\tau)\rangle = e^{-i\hat{H}\tau}\,|\Psi(\tau=0)\rangle$) by applying the TNOE ansatz (in its reduced form and modified) and resulting a favourable computational cost. Though this computational method is fully quantum mechanical, it is an operator based approach which is basis set free and has a classical (polynomial) scaling over the degrees of freedom (DoF)s of the non-adiabatic vibronic models.

In chapter 6, we discuss about the application of the general theory on calculating thermal properties for vibronic coupling systems (typically Jahn-Teller (JT) systems). This chapter is based on the work by Bao, Raymond, Zeng and Nooijen. [32] The computational method developed in this chapter can be regarded as a statistic-mechanical formulation of the method discussed in the chapter 5. The major difference is that the real time propagation is replaced by the imaginary time propagation to calculate properties at the thermal equilibrium. We showed that this method in conjunction with vibronic models can be applied as a effective protocol to calculate thermochemistry properties that incorporate the dynamical JT effect.

In chapter 7, we draw conclusions and give final remarks of this thesis.

Chapter 2

Background knowledge

In this chapter, we will provide essential background information that forms the theoretical foundation of this thesis. Our aim is to keep the discussion brief and focused. For further details on the topics addressed, please refer to the cited references.

2.1 Quantum chemistry of many-electrons: electronic structure theory

We begin our discussion with electronic structure theory, which aims to understand the interaction between many-electron systems and nuclear potentials in polyatomic molecules. The electronic structure of a molecule determines how chemical bonds are formed, ultimately leading to the stability of the molecular system. Therefore, it is crucial for understanding the fundamental mechanisms of chemical reactions.

2.1.1 Born-Oppenheimer approximation (BOA)

In this section, we introduce one of the most important approximations in quantum chemistry: the BOA. Our starting point is to solve the TISE of the quantum molecular Hamiltonian ($\hat{H}$):

$$\hat{H}\Psi(\vec{R},\vec{r}) = E\Psi(\vec{R},\vec{r}). \tag{2.1}$$

In this TISE, the full quantum molecular Hamiltonian ($\hat{H}$) can be written as

$$\begin{aligned}\hat{H} &= -\frac{1}{2}\sum_{\alpha}\frac{1}{M_\alpha}\nabla_\alpha^2 - \frac{1}{2}\sum_i \nabla_i^2 + \sum_{i<j}\frac{1}{r_{ij}} + \sum_{i,\alpha} -\frac{z_\alpha}{r_{i\alpha}} + \sum_{\alpha,\beta}\frac{z_\alpha z_\beta}{R_{\alpha,\beta}} \\ &= \hat{T}_N + \hat{T}_e + \hat{V}_{ee} + \hat{V}_{Ne} + \hat{V}_{NN},\end{aligned} \tag{2.2}$$

which consists five terms: the nuclear kinetic operator ($\hat{T}_N$), electronic kinetic operator ($\hat{T}_e$), electron-electron interaction operator ($\hat{V}_{ee}$), nuclear-electron interaction operator ($\hat{V}_{Ne}$)

and nuclear-nuclear interaction operator ($\hat{V}_{NN}$). We can separate electronic Hamiltonian operator at a particular nuclear configuration $\vec{R}$ from the full molecular Hamiltonian:

$$\hat{H}_{el}(\vec{R}) \equiv \hat{T}_e + \hat{V}_{ee} + \hat{V}_{Ne} + \hat{V}_{NN}, \tag{2.3}$$

in which we exclude the nuclear kinetic operator ($\hat{T}_N$) term in Eq. (2.2).

To solve the TISE in Eq. (2.1), we can expand the full molecular wavefunction $\Psi(\vec{R}, \vec{r})$ into a completed basis:

$$\Psi(\vec{R}, \vec{r}) = \sum_{\lambda} \phi_{\lambda}(\vec{r}; \vec{R}) X_{\lambda}(\vec{R}), \tag{2.4}$$

where the basis function in the expansion consist of a product of the electronic wavefunction $\phi_{\lambda}(\vec{r}; \vec{R})$ and the nuclear wavefunction $X_{\lambda}(\vec{R})$. The electronic wavefunction $\phi_{\lambda}(\vec{r}; \vec{R})$ is a function of the coordinates of electrons $\vec{r}$ and parametrically depends on the nuclear coordinates $\vec{R}$. At a fixed nuclei, the electronic wavefunction is defined as the eigenfunction of the electronic Hamiltonian $\hat{H}_{el}$ [1]:

$$\hat{H}_{el}(\vec{R})\phi_{\lambda}(\vec{r}; \vec{R}) = E^{el}_{\lambda}(\vec{R})\phi_{\lambda}(\vec{r}; \vec{R}), \tag{2.5}$$

where the energy eigenvalues $E^{el}_{\lambda}(\vec{R})$ are functions of the nuclear coordinates and it is known as the potential energy surface (PES) and the eigenstates are known as the adiabatic or the Born-Oppenheimer states. While, the nuclear wavefunction $X_{\lambda}(\vec{R})$ is a function of the nuclear coordinates $\vec{R}$. The expansion in Eq. (2.4) is known as the Born-Huang expansion [33] and under infinite basis limit, the expansion leads to exact solution to the TISE in Eq. (2.1).

In the Born-Huang expansion in Eq. (2.4), if we drop the summation and use one of the basis functions to approximate the full molecular wavefunction, we obtain the BOA [34]:

$$\Psi(\vec{R}, \vec{r}) \approx \phi(\vec{r}; \vec{R}) X(\vec{R}). \tag{2.6}$$

Substituting Eq. (2.6) and Eq. (2.5) into the original TISE, we get:

$$\left(\hat{T}_N + E^{el}_{\lambda}(\vec{R})\right) X_{\lambda,n}(\vec{R}) = E_n X_{\lambda,n}(\vec{R}). \tag{2.7}$$

In this way, the TISE for the nuclear wavefunction can be solved separately from the electronic structure problem.

As shown in Fig. 2.1, under BOA, the PESs can be defined as functions of nuclear coordinates. The TISE of the full molecular Hamiltonian in Eq. (2.1) can be decomposed by separately solving equations of electronic and nuclear problems. This allows us to tackle the complete quantum molecular problem in two steps. Firstly, we determine the minimum of the ground state PES by solving the electronic structure problem outlined in Eq. (2.5) at the optimized nuclear configuration. Secondly, we apply the harmonic oscillator (H.O.) and rigid rotor (R.R.) approximations to the vibrational and rotational problems centered at the minimum of the ground state PES to solve the nuclear TISE.

[1] Sometimes, this is known as the clamped nuclei.

This approach to solving the TISE for full molecular problems is generally applicable to most systems, though it does have some limitations. The BOA relies on the assumption that the nuclear wavefunction is decoupled from the electronic wavefunction in a quantum molecular system. This assumption holds because the energy separation between different electronic eigenstates is typically much greater than that of the nuclear eigenstates. Consequently, the influence of nuclei manifests as fine structures in molecular spectroscopy.

However, the assumption that the large energy separation between electronic eigenstates is not universally applicable. The BOA fails at molecular systems with close-lying electronic states. In section 2.3, we will discuss these scenarios and explore quantum chemistry that extends beyond the BOA.

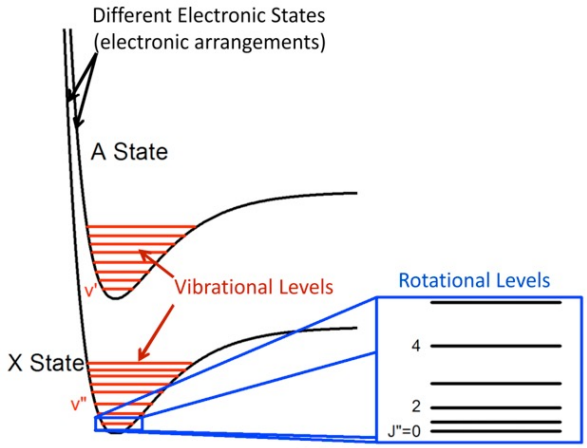


Figure 2.1: Illustration of the PESs in a molecular system. [35]

2.1.2 Hartree-Fock (HF) method

Under the BOA, the electronic structure problem involves solving the TISE as defined in Eq. (2.5) for a specific nuclear configuration. However, finding an exact solution to the TISE for this problem is computationally exponential hard. Fortunately, heuristic approximate solutions that balance efficiency and accuracy are feasible.

One of the most fundamental approximation methods is the HF method. [36, 37, 38, 39, 40] The HF method employs a single Slater determinant ansatz ($|\Phi\rangle$) to approximate the ground state electronic wavefunction, such that $|\Psi\rangle_{elec} \approx |\Phi\rangle$. Through the self-consistent field (SCF) procedure, the HF method optimizes the single-particle functions, or canonical MOs, within the framework of this single Slater determinant.

The HF method is summarized in the flowchart in Fig. 2.2. We define the related quantities as follows:

The Slater determinant:

$$|\Phi\rangle = \frac{1}{\sqrt{N!}} \begin{vmatrix} \varphi_i(r_1) & \varphi_i(r_2) & ... & \varphi_i(r_N) \\ \varphi_j(r_1) & \varphi_j(r_2) & ... & \varphi_j(r_N) \\ & ... & & \\ \varphi_l(r_1) & \varphi_l(r_2) & ... & \varphi_l(r_N) \end{vmatrix} \equiv |\varphi_i \varphi_j ... \varphi_l\rangle \tag{2.8}$$

where $\varphi_i, ..., \varphi_l$ single-particle function and they form orthonormal canonical MO basis $\{|\varphi_i\rangle\}$:

$$\langle \varphi_i | \varphi_j \rangle = \delta_{ij}. \tag{2.9}$$

The canonical MOs can be constructed by linear combinations of atomic orbital (AO)s:

$$|\varphi_i\rangle = \sum_\lambda |\chi_\lambda\rangle \, C_{\lambda i}. \tag{2.10}$$

The one electron integrals:

$$h_{\mu\nu} = \int \chi^*_\mu(\vec{r}) \hat{h} \chi_\nu(\vec{r}) d^3\boldsymbol{r}, \tag{2.11}$$

where

$$\hat{h} \equiv \hat{T}_e + \hat{V}_{Ne}. \tag{2.12}$$

The two electron integrals:

$$\langle \mu\nu | \sigma\delta \rangle = \int \chi^*_\mu(\vec{r}_1) \chi^*_\nu(\vec{r}_2) \frac{1}{r_{12}} \chi_\sigma(\vec{r}_1) \chi_\tau(\vec{r}_2) d^3\boldsymbol{r}_1 d^3\boldsymbol{r}_2 \tag{2.13}$$

The overlap matrix:

$$S_{\mu\nu} = \int \chi^*_\mu(\vec{r}) \chi_\nu(\vec{r}) d^3\boldsymbol{r} \tag{2.14}$$

The one-electron reduced density matrix:

$$D_{\mu\nu} = \sum_{i \in \text{occ}} C^*_{\mu i} C_{\nu i} \tag{2.15}$$

Fock matrix (for closed shell systems):

$$F_{\mu\nu} = h_{\mu\nu} + \sum_{\sigma\tau} (2 \langle \mu\nu | \sigma\delta \rangle - \langle \mu\nu | \delta\sigma \rangle) D_{\sigma\tau} \tag{2.16}$$

Notice that both the Fock matrix and the two-electronic integrals are currently defined in the AO basis. Both of them can be transformed to the canonical MO basis based on the MO coefficient defined in Eq. (2.10):

$$F_{\mu\nu}(\text{AO basis}) \to F_{pq}((MObasis)) \tag{2.17}$$

$$\langle \mu\nu | \sigma\tau \rangle \, (\text{AO basis}) \to \langle pq | rs \rangle \, (\text{MO basis}) \tag{2.18}$$

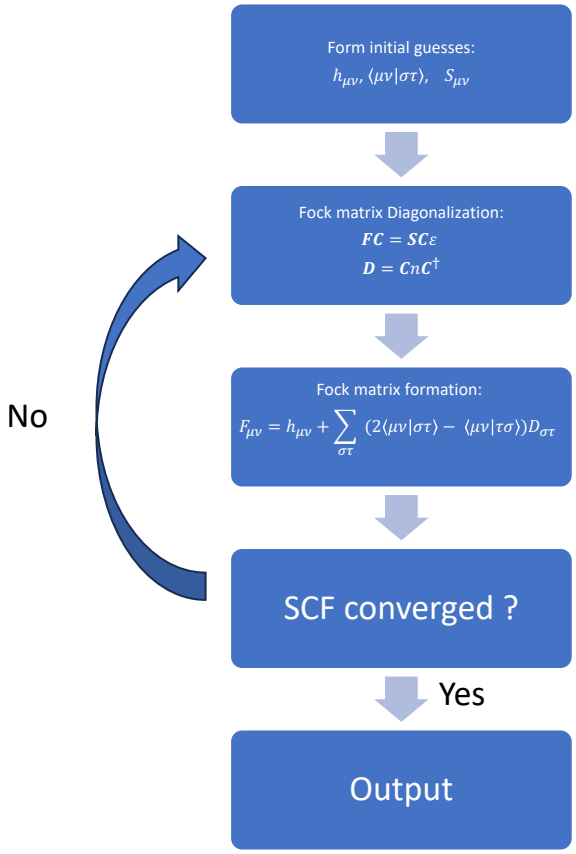


Figure 2.2: Illustration of the HF procedure

The HF method is significant for two reasons. First, it can achieve approximately 99% accuracy in predicting the ground state energy for most molecules at their optimized geometries.[2] Second, the HF method serves as a foundational step for more advanced wavefunction-based methods, such as the coupled cluster (CC) method, which will be discussed in section 2.1.4.

2.1.3 Second quantization

In the HF method, all quantities are defined within the framework of first quantization. However, for more advanced electronic structure methods, it is often more convenient to use second quantization, which provides a more intuitive representation of excitations in molecular electronic structure. In this section, we will introduce the second quantization technique.

We recall the definition of the normalized Slater determinant in Eq. (2.8) ($|\Phi\rangle = |\varphi_i\varphi_j...\varphi_l\rangle$). To introduce the second quantization, we can introduce another representation of the Slater

[2]However, the accuracy of the HF method is often insufficient for many chemistry applications, as its errors typically exceed the threshold of chemical accuracy (1 kcal/mol).

determinant. For an arbitrary Slater determinant it can be represented with M basis functions as:

$$|\Phi\rangle \equiv |n_1, n_2, .., n_M\rangle \,, \tag{2.19}$$

where n_p is defined as the occupation number for the spin orbital p.

$$\forall p \in 1, ..., M : n_p = \begin{cases} 1, \text{if spin orbital } p \text{ is occupied} \\ 0, \text{if spin orbital } p \text{ is unoccupied} \end{cases} \tag{2.20}$$

For convenience, in the rest of this section, we denote labels i,j,k,l to be occupied orbitals and labels a,b,c,d to be unoccupied (virtual) orbitals. Based on this new representation of the Slater determinant and the second quantized construction operators can be defined as follow: For arbitrary spin orbital p:

1. Creation operator $\hat{a}_p^\dagger$ is defined as

$$\hat{a}_p^\dagger \, |n_1, n_2, ..., n_p, ..., n_M\rangle = (1 - n_p)(-1)^{\eta_p} \, |n_1, n_2, ..., n_p, ..., n_M\rangle \,. \tag{2.21}$$

2. annihilation operator $\hat{a}_p$ is defined as:

$$\hat{a}_p \, |n_1, n_2, ..., n_p, ..., n_M\rangle = n_p(-1)^{\eta_p} \, |n_1, n_2, ..., n_p, ..., n_M\rangle \,. \tag{2.22}$$

In these definition the prefactor $(-1)^{\eta_p}$ takes account of the permutation of spin orbitals and η_p denotes the number of occupied orbitals in front of the spin orbital p.

According to the Pauli exclusion principle, it is not allowed on add one electron from an occupied orbital:

$$\hat{a}_i^\dagger \, |\Phi\rangle = 0. \tag{2.23}$$

It is not allowed to remove one electron from an unoccupied orbital neither:

$$\hat{a}_a \, |\Phi\rangle = 0. \tag{2.24}$$

The definition of second quantized construction operators in Eq. (2.21) and Eq. (2.22) naturally adapt with the conditions in Eq. (2.23) and Eq. (2.24). [3]

From the definition of the second quantized construction operators, the Slater determinant in Eq. (2.8) can be defined as:

$$|\Phi\rangle \equiv |\varphi_i \varphi_j ... \varphi_l\rangle = \hat{a}_i^\dagger \hat{a}_j^\dagger ... \hat{a}_l^\dagger \, |0_1, 0_2, ..., 0_M\rangle \,, \tag{2.25}$$

where $|0_1, 0_2, ..., 0_M\rangle$ is defined as the vacuum state in the Fock space. For simplicity we denote: $|0\rangle \equiv |0_1, 0_2, ..., 0_M\rangle$ in the rest part of this thesis.

In addition, the second quantized operators obey the canonical anti-commutation relation

[3] For occupied orbitals $n_p = 1$ and for unoccupied orbitals $n_p = 0$.

for arbitrary spin orbitals p and q:

$$\{\hat{a}_p^\dagger, \hat{a}_q^\dagger\} = \hat{a}_p^\dagger \hat{a}_q^\dagger + \hat{a}_p^\dagger \hat{a}_q^\dagger = 0, \tag{2.26}$$

$$\{\hat{a}_p, \hat{a}_q\} = \hat{a}_p \hat{a}_q + \hat{a}_p \hat{a}_q = 0, \tag{2.27}$$

$$\{\hat{a}_p, \hat{a}_q^\dagger\} = \hat{a}_p \hat{a}_q^\dagger + \hat{a}_p^\dagger \hat{a}_q = \delta_{pq}, \tag{2.28}$$

to adapt with the anti-symmetry of the many-electron wavefunction:

$$|\Psi_{elec}(\vec{r}_1, .., \vec{r}_i, ...\vec{r}_j, ...)\rangle = -|\Psi_{elec}(\vec{r}_1, .., \vec{r}_j, ...\vec{r}_i, ...)\rangle . \tag{2.29}$$

For the convenience of algebraic derivation, we can redefine the creation and annihilation operator based upon the a reference Slater determinant $|\Phi_0\rangle$. This approach is referred to as the quasiparticle formalism. We designate a single Slater determinant as the "Fermi vacuum".[4] $|vac\rangle \equiv |\Phi\rangle$ In this framework, the creation and annihilation operators are redefined relative to the "Fermi vacuum" rather than the physical vacuum $|0\rangle$. These new operators are termed q-creation and q-annihilation operators. For hole states (occupied orbitals) i,j,k,l, the q-creation and q-annihilation operators are defined as:

$$\hat{b}_i = \hat{a}_i^\dagger, \tag{2.30}$$

$$\hat{b}_i^\dagger = \hat{a}_i. \tag{2.31}$$

For particle states (unoccupied orbitals) a,b,c,d, the q-creation and q-annihilation operators are defined as:

$$\hat{b}_a = \hat{a}_a, \tag{2.32}$$

$$\hat{b}_a^\dagger = \hat{a}_a^\dagger. \tag{2.33}$$

From the definitions of the quasiparticle operators, single Slater determinant $|vac\rangle$ serves as the “vacuum state”:

$$\langle vac|\, \hat{b}^\dagger = \hat{b}\, |vac\rangle = 0. \tag{2.34}$$

The canonical anti-commutation relation of the original construction operators (in Eq. (2.26), Eq. (2.27) and Eq. (2.28)) still holds for the quasi-particle construction operators.

Based on the second quantization formalism, a general linear operator can be defined as:

$$\hat{A} = \sum_{X,Y} A_{XY} \hat{X}^\dagger \hat{Y}, \tag{2.35}$$

where $\hat{X}$ and $\hat{Y}$ are ordered products of annihilation operators:

$$\hat{X}, \hat{Y} = \hat{a}_q \hat{a}_p ..., p < q < ... \tag{2.36}$$

From this definition of the general linear operator in Eq. (2.35), the electronic Hamiltonian

[4]This Slater determinant can be obtained from the mean-field approximation, such as the HF method, for the ground electronic state.

operator in Eq. (2.3) can be defined as:

$$\hat{H}_{el} = \hat{h} + \hat{V}, \tag{2.37}$$

where

$$\hat{h} \equiv \sum_{ij} h_{ij} \hat{a}_i^\dagger \hat{a}_j (\hat{X} = \hat{a}_i, \hat{Y} = \hat{a}_j) \tag{2.38}$$

and

$$\hat{V} \equiv \frac{1}{4} \sum_{ijkl} \langle ij \| kl \rangle \hat{a}_i^\dagger \hat{a}_j^\dagger \hat{a}_l \hat{a}_k (\hat{X} = \hat{a}_j \hat{a}_i, \hat{Y} = \hat{a}_l \hat{a}_k). \tag{2.39}$$

The second quantization representation offers several advantages compared to other representations. (1) It transfers the anti-symmetry property of the wavefunction from the Slater determinant in the first quantization framework to operators, utilizing the anti-commutation relations of Fermionic creation and annihilation operators. [41] (2) It inherently preserves the symmetry of spin and particle number because of the anti-commutation relations of the second quantized operators. Specifically, $[\hat{S}^2, \hat{H}_{el}] = 0$ and $[\hat{N}, \hat{H}_{el}] = 0$. This is in contrast to the qubit representation of the electronic Hamiltonian that is developed recently, in which a basis of Pauli words is applied ($\hat{H} = \sum_I C_I \hat{P}_I$), can lead to the breaking of particle conservation and spin symmetry without additional constraints [42] (3) The second quantization framework allows for effective wavefunction parameterizations, such as those used in the CC method, which will be discussed in section 2.1.4.

2.1.4 Coupled Cluster (CC) theory

In this section, we introduce the CC theory for the electronic structure problem. CC is a quantum many-body wavefunction-based method that employs the second-quantized exponential ansatz to parameterize the many-electron wavefunction, effectively incorporating electron correlation in electronic structure calculations. The CC method was first introduced by Čížek and Paldus in 1966 [43, 44] and has since become one of the most widely used electronic structure methods in quantum chemistry. We will provide a brief overview of CC theory in this section.

As been discuss in section 2.1.3, the electronic Hamiltonian can be represented in second quantization as:

$$\hat{H}_{el} = \sum_{ij} h_{ij} \hat{a}_i^\dagger \hat{a}_j + \frac{1}{4} \sum_{ijkl} \langle ij \| kl \rangle \hat{a}_i^\dagger \hat{a}_j^\dagger \hat{a}_l \hat{a}_k, \tag{2.40}$$

The electronic wavefunction can be expanded by an exponential ansatz for the many-electron wavefunction that is based upon a reference state $|\Phi_0\rangle$:

$$|\Psi_{elec}\rangle \equiv e^{\hat{T}} |\Phi_0\rangle , \tag{2.41}$$

where the reference state $|\Phi_0\rangle$ can be defined as a single Slater determinant that can be

obtained from the HF calculations and the cluster operator $\hat{T}$ is defined as:

$$\hat{T} = \sum_{\mu} \hat{T}_{\mu} \tag{2.42}$$

In Eq. (2.42), $\hat{T}_{\mu}$ are excitation operators: [5]

$$\hat{T}_1 = \sum_{ia} t_i^a \hat{a}_a^\dagger \hat{a}_i; \tag{2.43}$$

$$\hat{T}_2 = \frac{1}{4} \sum_{ijab} t_{ij}^{ab} \hat{a}_a^\dagger \hat{a}_b^\dagger \hat{a}_j \hat{a}_i; \tag{2.44}$$

$$... \tag{2.45}$$

Applying the exponential ansatz defined in Eq. (2.41), we can derive CC equations now. Firstly, we substitute the exponential ansatz into the TISE:

$$\hat{H}_{el} e^{\hat{T}} |\Phi_0\rangle = E_{cc} e^{\hat{T}} |\Phi_0\rangle . \tag{2.46}$$

Secondly, we project against the manifolds $\langle\Phi_0| e^{-\hat{T}}$ and $\langle\Phi_0| \hat{\Omega}_\mu^\dagger e^{-\hat{T}} (\hat{\Omega}_\mu \equiv \{\hat{a}_a^\dagger \hat{a}_i, \hat{a}_a^\dagger \hat{a}_b^\dagger \hat{a}_j \hat{a}_i\}, ..)$. Then we can derive the CC energy equation: [6]

$$E_{cc} = \langle\Phi_0| \left(\hat{H}_{el} e^{\hat{T}}\right)_{conn.} |\Phi_0\rangle , \tag{2.47}$$

and CC amplitude equations:

$$0 = \langle\Phi_\mu| \left(\hat{H}_{el} e^{\hat{T}}\right)_{conn.} |\Phi_0\rangle , \tag{2.48}$$

where

$$\langle\Phi_\mu| \equiv \langle\Phi_0| \hat{\Omega}_\mu^\dagger; \mu = 1, 2, ... \tag{2.49}$$

and the subscript *conn.* means that the equations are connected:

$$\left(\hat{H}_{el} e^{\hat{T}}\right)_{conn.} = e^{-\hat{T}} \hat{H}_{el} e^{\hat{T}} . \tag{2.50}$$

The proof of Eq. (2.50) is shown in appendix G. [7]

The CC method has many good features. It is non-perturbative and size-consistent, and unlike other electronic structure methods, such as density functional theory (DFT), that require additional empirical parameters, the CC approach is grounded purely in first

[5] These operators are called excitation operators since they can be regarded as the excitation of electrons from the occupied orbitals of the HF ground state to the virtual orbitals. In other words, they contain q-creation operators only with the respect of the single Slater determinant reference state $|\Phi_0\rangle$.

[6] The correlation energy (E_{corr}) is defined as the energy difference of the ground state energy obtained from the CC approach and that of the HF method ($E_{corr} \equiv E_{cc} - E_{HF}$).

[7] In proof of the connectedness of the similarity transform Hamiltonian, we make use of the Wick's theorem which will be discussed in section 2.1.5.

principles. It also establishes a hierarchy, with its infinite cluster expansion limit representing the exact solution to the Schrödinger equation.

However, the CC method has some limitations. First, it exhibits high-order polynomial scaling with respect to the number of electrons and spin orbitals, making it computationally expensive and limiting its application to small and medium-sized molecular systems. Second, the SR-CC approach, which uses a single Slater determinant as the reference state, struggles with strongly correlated electronic systems. In such cases, multiple close-lying or degenerate electronic states mean that the ground state cannot be adequately described by a single dominant Slater determinant. Over the years, many efforts have been made to enhance both the efficiency and accuracy of the canonical CC method.

2.1.5 Normal order and Wick's theorem

As been mentioned in the previous section, to proof the connectedness of the CC equations, the normal order and Wick's theorem are required. We give a detailed description of them in this section. In the single-reference quasi-particle formalism, the normal order of an arbitrary string of construction operator $\hat{A}$ is defined as a certain order that all q-creation operators are to the left of all annihilation operators are to the right:

$$\{A\} \equiv (-1)^{\sigma(\hat{P})}\hat{b}_i^\dagger \hat{b}_a^\dagger ... \hat{b}_j \hat{b}_c \tag{2.51}$$

where the curly bracket "{}" denotes the normal order and the prefactor $(-1)^{\sigma(\hat{P})}$ takes account the permutation of the construction operator based on their canonical anti-commutation relations defined in Eq. (2.26), Eq. (2.27) and Eq. (2.28).

Based on the definition of the normal order in Eq. (2.51), the Wick's theorem states that "The product of two normal ordered strings is equal to their normal product plus the sum of all possible normal products with contractions": [45]

$$\{\hat{A}\}\{\hat{B}\} = \{\hat{A}\hat{B}\} + \sum\{\overline{\hat{A}\hat{B}}\} + \sum\{\overline{\overline{\hat{A}\hat{B}}}\} + ..., \tag{2.52}$$

where each overline denotes the possible contraction that can be obtained by taking one construction operator from $\hat{A}$ and one from $\hat{B}$ and in Wick's theorem, we sum over all the possibilities. The contraction of two fermionic construction operators ($\hat{x}$ and $\hat{y}$) is defined as:

$$\overset{\sqcap}{\hat{x}\hat{y}} \equiv \hat{x}\hat{y} - \{\hat{x}\hat{y}\}. \tag{2.53}$$

If they are not in normal order, the contraction will be the anti-commutator and if they are in normal order, the contraction will be zero.

To illustrate the Wick's theorem described in Eq. (2.52), we give a simple example as

follow. In Eq. (2.52), if we set $\hat{A} \equiv \hat{b}_p \hat{b}_q$ and $\hat{B} \equiv \hat{b}_r^\dagger \hat{b}_s^\dagger$, we have:

$$\begin{aligned}\{\hat{A}\}\{\hat{B}\} &= \{\hat{b}_p \hat{b}_q \hat{b}_r^\dagger \hat{b}_s^\dagger\} + \{\hat{b}_p \hat{b}_q \hat{b}_r^\dagger \hat{b}_s^\dagger\} + \{\hat{b}_p \hat{b}_q \hat{b}_r^\dagger \hat{b}_s^\dagger\} + \{\hat{b}_p \hat{b}_q \hat{b}_r^\dagger \hat{b}_s^\dagger\} + \{\hat{b}_p \hat{b}_q \hat{b}_r^\dagger \hat{b}_s^\dagger\} \\ &+ \{\hat{b}_p \hat{b}_q \hat{b}_r^\dagger \hat{b}_s^\dagger\} + \{\hat{b}_p \hat{b}_q \hat{b}_r^\dagger \hat{b}_s^\dagger\} \\ &= \hat{b}_r^\dagger \hat{b}_s^\dagger \hat{b}_p \hat{b}_q + \delta_{pr} \hat{b}_s^\dagger \hat{b}_q - \delta_{qr} \hat{b}_s^\dagger \hat{b}_p + \delta_{qs} \hat{b}_r^\dagger \hat{b}_p - \delta_{ps} \hat{b}_r^\dagger \hat{b}_q \\ &+ \delta_{ps}\delta_{qr} - \delta_{pr}\delta_{qs}\end{aligned} \tag{2.54}$$

The definition of normal order, as presented in Eq. (2.51), is based on a single Slater determinant reference state. However, it can be extended to an arbitrary reference state which can be a linear combination of a few Slater determinants in general:

$$|ref\rangle \equiv C_1 |\Phi\rangle + C_2 |\Phi'\rangle + C_3 |\Phi''\rangle + ... \tag{2.55}$$

In this context, the normal ordering can be generalized to define the order of the string of the creation and annihilation operators such that the expectation value over the reference state is zero:

$$\langle ref| \{\hat{A}\} |ref\rangle = 0. \tag{2.56}$$

The Wick's theorem in Eq. (2.52) remains valid with this generalized definition of normal order in Eq. (2.56). The generalized definition of normal ordering was first proposed by Kutzelnigg and Mukerjee [46], and the generalized Wick's theorem was later rigorously proved by Kong et al [47].

In chapter 3.1, we will demonstrate that these generalized definition of the normal order and Wick's theorem can be applied to the statistical ensembles at thermal equilibrium. In this case, the expectation value over the reference state is replaced by the trace over a zeroth-order density matrix, leading to the formulation of Wick's theorem in an analogous manner:

$$\langle ref| \hat{O} |ref\rangle \to \mathrm{Tr}\Big(\hat{O}\hat{D}_0(\beta)\Big). \tag{2.57}$$

This approach to normal ordering and Wick's theorem for statistical ensembles at thermal equilibrium has also been considered by Qin and Hirata. [14, 48] Before going in the details of this advanced approach, we will firstly introduce the basics of statistical mechanics in section 2.2.

2.2 Quantum chemistry at finite temperature: statistical mechanics

Finite temperature effect plays an important role in quantum chemistry, as most chemical reactions are thermodynamically driven. Experimental thermochemical quantities, such as reaction energy, free energy, and entropy, depend on temperature. To incorporate these finite temperature effects into quantum chemistry calculations, we must introduce concepts from statistical mechanics.

Recall the PESs illustrated in Fig. 2.1, under BOA, the electronic structure problem and nuclear vibrational / rotational problem can be treated separately. In standard quantum chemistry methods, only the ground electronic state is considered. Using the ground state PES, H.O. and R.R. approximations are applied at the minimum to solve the vibrational and rotational problems. Thermochemical properties can then be calculated by obtaining analytical expressions for the H.O. and R.R. partition functions of the vibrational and rotational degrees of freedom separately. [8]

However, these methods are valid only when the energy gap between the ground state PES and the excited state PESs is large, making the thermal population of excited electronic states negligible. This is not always the case; some molecular systems can exhibit multiple low-lying electronic states, making the thermal contributions from excited states significant. Therefore, it becomes essential to incorporate finite temperature effects into the electronic structure problem to accurately calculate thermochemistry properties in these systems. Motivated by this need, we developed a computational method aimed at efficiently calculating the statistically averaged thermal properties of the electronic structure problem, as will be discussed in chapter 4.

In this section, we will cover some basics of statistical mechanics. Statistical mechanics is a branch of physics that studies the equilibrium and evolution of collections of microscopic particles, known as ensembles. It connects multiple microscopic quantum states to their net or average behavior on a macroscopic scale. The fundamental postulate of statistical mechanics states that "if an isolated system is in equilibrium, it can be found with equal probability in each one of its accessible states" which is also known as "equal a priori probabilities". [49]

2.2.1 Classification of the statistical ensembles

There are mainly two classes of statistical ensembles that are used in quantum chemistry: the grand canonical ensemble and the canonical ensemble.

In a grand canonical ensemble, the system reaches thermal equilibrium with its environment such that the ensemble average of the total number of particles is kept invariant. The fluctuation or exchange of particles between subsystems within the ensemble is allowed. The partition function of a grand canonical ensemble can be written as:

$$Q(\beta, \mu) = \sum_{i,n} \Omega_i e^{-\beta(E_{i,n} - \mu n)}, \tag{2.58}$$

where Ω_i is the degeneracy of the quantum state i, n is the total number of particles in a certain quantum state, $E_{i,n}$ is the energy eigenvalue of the corresponding quantum state and μ is an addition parameter (known as the chemical potential) to keep the ensemble average

[8] While more accurate results can be achieved by going beyond the H.O./R.R. approximations, the single electronic state assumption of the BOA is still maintained.

of the number of particle to be a constant:

$$\left\langle \hat{N} \right\rangle = n_{el}. \tag{2.59}$$

Canonical ensemble has more restrictions. The system also reaches thermal equilibrium with its environment but no particle exchange is allowed which means that all quantum states in a canonical ensemble have the same total number of particles. The partition function of a canonical ensemble can be written as:

$$Z(\beta, \mu, \nu) = \sum_{i,n} \Omega_i e^{-\beta(E_{i,n} - \mu n - \nu n^2)}. \tag{2.60}$$

Comparing to the partition function of a grand canonical ensemble in Eq. (2.58), we introduce the additional parameter ν such that the variance of the total number of particle is kept to be zero as well. Thus, the canonical ensemble satisfies the following constraints: [9]

$$\left\langle \hat{N} \right\rangle = n_{el} \tag{2.61}$$

$$\left\langle (\hat{N} - n_{el})^2 \right\rangle = 0. \tag{2.62}$$

2.2.2 Quantum mechanical formulation of the statistical mechanics

There is a more graceful and concise quantum mechanical formulation of the statistical mechanics that is based on the density operator. In general a N-particle density operator is defined as:

$$^N\hat{D} \equiv \sum_{\alpha} W_\alpha \left|\Psi_\alpha\right\rangle \left\langle\Psi_\alpha\right| \tag{2.63}$$

where W_α is defined as the probability to find the ensemble at the quantum state $|\Psi_\alpha\rangle$ and it satisfies:

$$0 \leq W_\alpha \leq 1. \tag{2.64}$$

In special cases, at thermal equilibrium, the corresponding density operator for grand canonical ensemble is define as:

$$\hat{D}(\beta, \mu) \equiv e^{-\beta(\hat{H} - \mu\hat{N})}, \tag{2.65}$$

and the density operator for canonical ensemble is defined as:

$$\hat{D}(\beta, \mu, \nu) \equiv e^{-\beta(\hat{H} - \mu\hat{N} - \nu\hat{N}^2)}. \tag{2.66}$$

[9] In most textbooks, the parameters μ and ν are not introduced in the canonical ensemble, as they typically sum over all states with the same total number of particles. However, this approach is not practical, as summing over states is computationally infeasible for quantum many-body systems. Instead, we adopt an alternative formulation that introduces additional constraints to preserve the average number of particles in the ensemble while ensuring that the variance of the particle number remains zero.

By introducing these definitions of the thermal density operators, we can have a unified concise expression of the partition function Ξ as the trace over the thermal density operator:

$$\Xi = \mathrm{Tr}\Big(\hat{D}\Big). \tag{2.67}$$

The corresponding ensemble average of an arbitrary observable $\hat{O}$ is can be expressed as:

$$\Big\langle \hat{O} \Big\rangle = \frac{\mathrm{Tr}\Big(\hat{O}\hat{D}\Big)}{\mathrm{Tr}\Big(\hat{D}\Big)}. \tag{2.68}$$

In practice, directly calculating thermal properties by taking the trace or summing over states, as suggested in Eq. (2.68), can be computationally expensive. As a result, this approach may not always be feasible for investigating the chemical systems of interest. Fortunately, the quantum mechanical operator formulation of statistical mechanics allows us to manipulate the thermal density operator using many-body quantum field theoretical methods. This enables us to heuristically calculate thermal properties without needing to take the trace over the entire Hilbert space.

There are two well-established formulations based on this concept. One is the Matsubara Green's function formulation, where the partition function is evaluated in parallel with the calculation of the S-matrix in quantum field theory [15]. The other is thermofield dynamics, in which the thermal density operator is treated as a pure state in a physical-ancillary dual space, utilizing the Bogoliubov representation [20, 21, 22]. In this framework, thermal properties can be directly evaluated as expectation values of this pure state.

In this thesis, we introduce a new approach known as the TNOE approach. [25] In this approach, we apply the generalized Wick's theorem based on the definition of normal order for statistical ensembles. By using unique contraction rules for reduced density matrices and the normal-ordered exponential ansatz, we can form a compact representation of the thermal density operator. The thermal properties can then be obtained through imaginary time integration over the cluster operators. This approach will be elaborated in chapter 3.1.

2.3 Quantum chemistry beyond BOA: vibronic coupling problem

In addition to the finite temperature effect, another important effect in quantum chemistry is known as the vibronic coupling effect which extend beyond the BOA. We will elaborate this effect in this section.

2.3.1 Origin of vibronic coupling interaction

We begin the discussion by introducing the origin of the vibronic coupling interactions. Recall that in section 2.1.1, we introduced the BOA to define the adiabatic PESs for a molecular

system. However, the BOA relies on the assumption that the energy separation between electronic states is much greater than that of vibrational and rotational levels. This assumption is not always valid. For molecular systems with closely lying or degenerate electronic states, the BOA breaks down. In such cases, the coupling between the nuclear wavefunction and the electronic wavefunction becomes strong and non-negligible. This interaction is referred to as the vibronic coupling effect or non-Born-Oppenheimer effect [50, 51].

2.3.2 Techniques to incorporate the vibronic coupling in quantum chemistry

Having discussed the origin of vibronic coupling interactions, we will now briefly introduce common numerical techniques for incorporating the vibronic coupling effect in quantum chemistry. Recall that we introduced the full molecular Hamiltonian in Eq. (2.2). By substituting the Hamiltonian in Eq. (2.2) and the Born-Huang expansion of the full molecular wavefunction in Eq. (2.4) into the TISE and then project against the electronic wavefunction $\phi^*_\mu(\vec{r};\vec{R})$, we can derive:

$$\begin{aligned}
&(\mathbf{A})\ \sum_\lambda \left(\int \phi^*_\mu(\vec{r};\vec{R}) \sum_\alpha -\frac{1}{2M_\alpha}\nabla^2_\alpha \phi_\lambda(\vec{r};\vec{R}) d\boldsymbol{r} \right) \chi_\lambda(\vec{R}) + \\
&(\mathbf{B})\ \delta_{\lambda\mu} \left(\sum_\alpha -\frac{1}{2M_\alpha}\nabla^2_\alpha \right) \chi_\lambda(\vec{R}) + \\
&(\mathbf{C})\ \sum_\alpha \left(\int \phi^*_\mu(\vec{r};\vec{R}) \nabla_\alpha \phi_\lambda(\vec{r};\vec{R}) d\boldsymbol{r} \right) (-\frac{1}{M_\alpha}) \nabla_\alpha \chi_\lambda(\vec{R}) + \\
&(\mathbf{D})\ \delta_{\lambda\mu} E^{elec}_\lambda(\vec{R}) \chi_\lambda(\vec{R}) \\
&= E \sum_\lambda \delta_{\mu\lambda} \chi_\lambda(\vec{R}).
\end{aligned} \tag{2.69}$$

In Eq. (2.69):

(1). Term **A** and term **C** take account of the vibronic coupling effect. If we neglect them, we obtain the usual BOA:

$$\left(\hat{T}_N + E_\lambda(\vec{R}) \right) \chi_{\lambda,n}(\vec{R}) = E_n \chi_{\lambda,n}(\vec{R}), \tag{2.70}$$

in which the electronic wavefunction is decoupled from the nuclear wavefunction.

(2). The diagonal elements of term **A** can be served as a small correction to the potential term under the BOA:

$$\left(\hat{T}_N + E_\lambda(\vec{R} + A_\lambda(\vec{R})) \right) \chi_{\lambda,n}(\vec{R}) = E_n \chi_{\lambda,n}, \tag{2.71}$$

where

$$A_\lambda \equiv \int \phi_\lambda^*(\vec{r};\vec{R}) \sum_\alpha -\frac{1}{2m_\alpha}\nabla_\alpha^2 \phi_\lambda(\vec{r};\vec{R}) d\boldsymbol{r}. \tag{2.72}$$

It serves as the additional diagonal correction to the potential in BOA. The off-diagonal contribution are negligible:

$$\left(\int \phi_\mu^*(\vec{r};\vec{R}) \sum_\alpha -\frac{1}{2m_\alpha}\nabla_\alpha^2 \phi_\lambda(\vec{r};\vec{R}) d\boldsymbol{r} \right) \approx 0 (\forall \mu \neq \lambda) \tag{2.73}$$

In general, the contribution the term **A** is small and will not be consider in remaining part of this thesis.

(3). If we choose the real function as the basis the electronic wavefunction $\phi_\lambda(\vec{r};\vec{R})$, the the diagonal elements of term **C** are always zero.

(4). The off-diagonal elements of term **C** are known as the non-adiabatic coupling (N.A.C)s. The strength of the N.A.Cs are proportional to the reciprocal of the energy difference between the two adiabtic electronic states:

$$C_{\mu\lambda}(\mu \neq \lambda) \propto \frac{1}{E_\mu^{elec} - E_\lambda^{elec}}. \tag{2.74}$$

Thus, when the energy separation between the two electronic states is large, the N.A.C is small and negligible. However, the N.A.C tends to diverge when the two electronic states are close-lying or degenerate. This is problematic. In practice to incorporate the N.A.C effect for close-lying electronic states in quantum chemistry, the numerical technique known as diabatization is introduced.

$$\begin{bmatrix} \hat{T}_1 & N.A.C. \\ N.A.C. & \hat{T}_2 \end{bmatrix} + \begin{bmatrix} E_1(\vec{R}) & 0 \\ 0 & E_2(\vec{R}) \end{bmatrix} \xrightarrow[ization]{Diabat-} \begin{bmatrix} \hat{T}_1 & 0 \\ 0 & \hat{T}_2 \end{bmatrix} + \begin{bmatrix} V_{11}(\vec{R}) & V_{12}(\vec{R}) \\ V_{21}(\vec{R}) & V_{22}(\vec{R}) \end{bmatrix} \tag{2.75}$$

As shown in Eq. (2.75), the diabatization procedure involves unitarily transforming the original Hamiltonian from the adiabatic representation to the diabatic representation ($\left|\psi^{diab}\right\rangle = \hat{U}\left|\psi^{adiab}\right\rangle$). The goal of this unitary transformation is to eliminate N.A.C and form a matrix potential where the matrix elements are smooth functions of nuclear coordinates. As a result, the diabatic electronic wavefunction changes slowly with respect to nuclear coordinates, maintaining its character. This approach effectively avoids the divergence issues associated with N.A.C for closely lying electronic states while preserving the eigenvalues and eigenvectors by representing the Hamiltonian in the diabatic basis. Diabatization has become a well-established technique for incorporating vibronic coupling effects in quantum chemistry, with many standard diabatization protocols now available [52, 53, 54, 55, 56, 57, 58].

2.3.3 Applications of the vibronic coupling effect

With the diabatic vibronic Hamiltonian obtained from the ab initio electronic structure calculations and diabatization procedures, we can apply it to study many important phenomenon

in physics and chemistry.

The first application of the vibronic coupling effect is in studying the quantum dynamics of vibronic coupling systems. Fig. 2.3 illustrates the quantum dynamics process of such systems. Vibronic couplings facilitate population transfer between electronic states in molecular systems. Quantitatively analyzing the quantum dynamics of these systems enhances our understanding of the optical properties of materials. This has broad applications in the development of novel materials, including photo-catalysts and photo-electronic devices.

In addition, we can generate the electronic spectra from the quantum dynamics simulation of the vibronic coupling systems. The auto-correlation function (ACF) can be calculated from the quantum dynamics simulations. By definition, the ACF is the overlap between the time-dependent wavefunction of at $t = 0$ and $t = \tau$:

$$C(\tau) = \langle \Psi(t=0) | \Psi(t=\tau) \rangle \,, \tag{2.76}$$

where $|\Psi(t=\tau)\rangle$ can be determined by solving the TDSE of the vibronic coupling systems:

$$-i\hbar \frac{\mathrm{d}}{\mathrm{d}t} |\Psi(t)\rangle = \hat{H}_{vibr} |\Psi(t)\rangle \,. \tag{2.77}$$

The corresponding spectra can be generated from the Fourier transform of the ACF:

$$I(\omega) = \int_{-\infty}^{+\infty} e^{-i2\pi\omega t} C(\tau) d\tau. \tag{2.78}$$

The vibronic coupling effect is crucial for accurately simulating absorption spectra. It alters both the peak intensities and positions compared to the conventional vertical gradient (VG)-Frank–Condon (FC) approach. Quantum dynamics simulations of the diabatic vibronic Hamiltonian offer a viable method for obtaining spectra that incorporate the vibronic coupling effect.

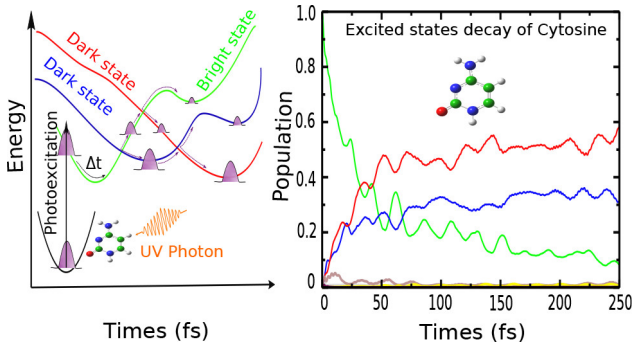


Figure 2.3: Illustration of the quantum dynamics process for vibronic coupling systems [55]

Another application of vibronic coupling is in studying the statistical mechanics of these systems. As previously mentioned, many chemical reactions are thermodynamically driven. Vibronic coupling plays a significant role in accurately calculating thermochemical data for

various molecular systems, such as JT systems. This can have applications on understanding many bio-chemical processes and facilitate the drug discovery.

Conventionally, multi-configuration time-dependent Hartree (MCTDH) approaches [59, 60, 61, 62, 63] and their imaginary-time evolution versions [64, 65] have been used to simulate both quantum dynamics and statistical mechanics of vibronic coupling systems. However, these methods often require large basis sets for accurate convergence [10] and the multi-layer settings can be challenging to use. As a result, the application of MCTDH approaches is typically limited to small and medium-sized vibronic models.

To simulate the quantum dynamics and statistical mechanics of larger vibronic coupling systems, more efficient computational methods are necessary. Motivated by this need, we develop novel computational methods (namely the vibrational electronic coupled cluster (VECC) approach and the vibrational electronic-thermofield coupled cluster (VE-TFCC) approach) for quantum dynamics and statistical mechanics simulations of vibronic coupling systems. We will elaborate on these methods in chapter 5 and chapter 6.

[10] In the worst-case scenario, the computational cost scales exponentially with the number of vibrational modes in a vibronic coupling system.

Chapter 3

General Theory

In this chapter, we will give a general discussion about the quantum field theoretical approaches to calculate thermal properties in quantum chemistry. We will discuss two different formulations, namely, the TNOE approach and the TFCC approach. The former approach is developed by Nooijen and Bao [25] and closely related to the TDCC formulation that is developed by White and Chan. [6, 7, 8] The latter approach is initial proposed by Mukherjee and his coworkers [2] and recently re-introduced by Scuseria group. [26, 27, 28, 29, 30]

The main purpose of the this chapter is as follow: Firstly, we give an independent first principle derivation of the EOMs for both TNOE and TFCC approaches. Secondly, we derive the expression of the thermal reduced density matrices in both approaches. Unlike other approaches from literatures [6, 7, 8, 26, 27, 28, 29, 30] that apply energy derivatives or response theory to calculate thermal properties, we heuristically map the reduced density matrices from the cluster amplitudes on-the-fly along the imaginary time propagation. As a result, the thermal properties derived from our approaches are different from the result of the original formulations. Thirdly, we build the connection between the TNOE and the TFCC approaches. We prove that both the expression of the thermal reduced density matrices and the EOMs translate from one to another for the two approaches. Thus, the two approaches are mathematically identical.

We keep the discussion in this chapter in an abstract fashion aiming at building the general theoretical framework for direct calculation of thermal properties in quantum chemistry. Only simple examples are given to illustrate the basic soundness of the theories. We will cover the specific applications of these general theoretical frameworks for real quantum chemistry simulations in the later chapters.

3.1 Thermal normal-ordered exponential (TNOE) approach

In this section, we introduce the TNOE approach. It is a summary of the paper by Nooijen and Bao [25] with more details. The goal of the TNOE approach is to efficiently calculate the thermal statistical average of a physical observable (defined in Eq. (1.4)) and avoid directly summing over states which scales exponentially as the number of particles in the

quantum many-body system. In the TNOE approach, a normal-ordered exponential ansatz is applied to parameterize the thermal density operator ($\hat{D} \equiv e^{-\beta \hat{H}}$). By defining the suitable contraction rules, thermal properties can be expanded out through the cumulant expression of cluster operators applying the generalized (simple) Wick's theorem. In this way, the thermal properties can be efficiently (approximately) computed through the truncation of first few low rank cluster operators in the cumulant expression.

3.1.1 TNOE ansatz and generalized (simple) Wick's theorem

In the TNOE approach, the thermal density operator is parametrized as

$$\hat{D}(\beta) \equiv \{e^{\hat{S}(\beta)}\}\hat{D}_0, \tag{3.1}$$

where the brace denotes the normal ordering with the respect to the "reference density operator" $\hat{D}_0$ that is assumed to be obtained from some external sources. The cluster operator $\hat{S}(\beta)$ is expanded in terms of the normal-ordered substitution operators and a constant term.

$$\hat{S}(\beta) = s_0(\beta) + \sum_{\lambda} s_\lambda(\beta)\{\hat{\Omega}_\lambda\} \tag{3.2}$$

In analog to the simple Wick's theorem (in Eq. (2.52)), in the TNOE approach, we define the product of two normal operators as their normal product with all possible contractions:

$$\{\hat{A}\}\{\hat{B}\} = \{\hat{A}\hat{B}\} + \sum\{\overline{\hat{A}\hat{B}}\} + \sum\{\overline{\overline{\hat{A}\hat{B}}}\} + ..., \tag{3.3}$$

Comparing to the original simple Wick's theorem, the normal order is re-defined with the respect to the reference density operator $\hat{D}_0$ to satisfy

$$\mathrm{Tr}\Big(\{\hat{C}\}\hat{D}_0\Big) \equiv \Big\langle\{\hat{C}\}\Big\rangle = 0. \tag{3.4}$$

Note that for a normal-ordered string of operators the expectation value is zero, except when the string contains no operators. Then the result is 1 for a normalized $\hat{D}_0$.

As a result, the contraction rules are also re-defined to satisfy the "vacuum state" condition define in Eq. (3.4):

$$\begin{aligned}
&\overbrace{\hat{p}^\dagger \hat{q}} \equiv \mathrm{Tr}\Big(\hat{p}^\dagger \hat{q}\hat{D}_0\Big) \equiv f_p\delta_{pq}, \\
&\overbrace{\hat{p}\hat{q}^\dagger} \equiv \mathrm{Tr}\Big(\hat{p}\hat{q}^\dagger \hat{D}_0\Big) \equiv \bar{f}_q\delta_{pq} \equiv (1 \pm f_q)\delta_{pq} (+ \text{ for } \text{ Bosons; } - \text{ for } \text{ Fermions}),
\end{aligned} \tag{3.5}$$

where f_p is an arbitrary constant and $\hat{p}^\dagger$ and $\hat{q}$ are second quantized operators which can be either Fermonic or Bosonic.

In the case of the electronic structure problem, p and q can be regarded as labels of spin orbitals. As an example to show how to determine the f and $\bar{f}$ that is associated with the

new contraction rules defined in Eq. (3.5) we choose the reference density operator to be: [1]

$$\hat{D}_0 \equiv \hat{D}(\beta = 0) = \alpha\hat{1}. \tag{3.6}$$

In this case, the constant f can be determined based on the fact that the total number of electrons are conserved in the electronic structure problem. To determine the constant f, firstly, we define the number operator as:

$$\hat{N} = \sum_{pq} \hat{p}^\dagger \hat{q}. \tag{3.7}$$

On one hand, according to the contraction rule defined in Eq. (3.6), we have

$$\left\langle \hat{N} \right\rangle = Mf \tag{3.8}$$

where M is the total number of the spin orbitals. On the other hand, the number operator can be expressed as a constant (total number or electrons) plus its normal-ordered term:

$$\hat{N} = n_{el} + \{\hat{N}\}. \tag{3.9}$$

Applying the condition defined in Eq. (3.4), we have

$$\left\langle \hat{N} \right\rangle = n_{el}. \tag{3.10}$$

In this way, from Eq. (3.9) and Eq. (3.10), the constant f and $\bar{f}$ can be determined:

$$f = \frac{n_{el}}{M} \tag{3.11}$$

and

$$\bar{f} = 1 - f = \frac{M - n_{el}}{M}. \tag{3.12}$$

Note that in Eq. (3.11) and Eq. (3.12), the spin orbital labels of f and $\bar{f}$ are dropped since they are the same for all spin orbitals which a special case of the general definition of f and $\bar{f}$ and only true when we choose $\hat{D}_0$ to be at $\beta = 0$. This is due to the fact that we choose the reference density operator $\hat{D}_0$ to be at $\beta = 0$ which is diagonal and uniform. We will show later that in the more general scenario, f and $\bar{f}$ can be associated with the Fermi-Dirac (FD) occupation number of the orbital energies for $\beta \neq 0$:

$$f_p = n_p = \frac{1}{1 + e^{\beta\epsilon_p}}, \tag{3.13}$$

and

$$\bar{f}_p = 1 - n_p = \frac{e^{\beta\epsilon_p}}{1 + e^{\beta\epsilon_p}}, \tag{3.14}$$

[1] The choice of the reference density operator is not unique, it can be the density operator at an arbitrary β: $\hat{D}_0(\beta)$.

where ϵ_p denotes the orbital energy.

3.1.2 Derivation of the EOM

With the unique contraction rule defined in Eq. (3.5) and the TNOE ansatz of the density operator in Eq. (3.1), we can derive the EOM of the thermal density operator. Substituting the TNOE ansatz into the TDSE defined in Eq. (1.7), we have:

$$-\frac{\mathrm{d}}{\mathrm{d}\beta}\{e^{\hat{S}(\beta)}\}\hat{D}_0 = \hat{H}\{e^{\hat{S}(\beta)}\}\hat{D}_0. \tag{3.15}$$

In the right hand side of Eq. (3.15), we can prove the following expression applying the generalized Wick's theorem:

$$\hat{H}\{e^{\hat{S}(\beta)}\} = \{(\hat{H}\{e^{\hat{S}(\beta)}\})_{conn.})e^{\hat{S}(\beta)}\}, \tag{3.16}$$

where the subscript "*conn.*" denotes connected which means that there is at least one contraction between the Hamiltonian operator $\hat{H}$ and the cluster operator $\hat{S}(\beta)$ within the parenthesis.

To prove Eq. (3.16), we firstly Taylor expand the TNOE operator in the left hand side of the equation:

$$\hat{H}\{e^{\hat{S}(\beta)}\} = \sum_n^{\infty} \frac{1}{n!}\hat{H}\{\hat{S}(\beta)^n\}. \tag{3.17}$$

Applying Wick's Theorem, we can distinguish $\hat{S}$ amplitudes that are contracted to the Hamiltonian and those that are not. If in a particular term of power n, k amplitudes $\hat{S}$ are contracted to $\hat{H}$, indicated by an overbar, while n-k are not contracted to $\hat{H}$, there are $\binom{n}{k}$ unique contractions terms. Thus, Eq. (3.17) can be rewritten as:

$$\sum_n^{\infty} \frac{1}{n!}\hat{H}\{\hat{S}(\beta)^n\} = \sum_n^{\infty} \frac{1}{n!}\sum_{k=0}^{n}\binom{n}{k}\{(\overline{\hat{H}\{\hat{S}(\beta)^k\}})\hat{S}(\beta)^{n-k}\}, \tag{3.18}$$

where

$$\binom{n}{k} \equiv \frac{n!}{k!(n-k)!}. \tag{3.19}$$

Substituting Eq. (3.19) into Eq. (3.18), we get the desired result:

$$\begin{aligned}\hat{H}\{e^{\hat{S}(\beta)}\} &= \{\sum_k \frac{1}{k!}(\overline{\hat{H}\{\hat{S}(\beta)^k\}})\sum_m \frac{1}{m!}\hat{S}(\beta)^m\} \\ &= \{(\hat{H}\{e^{\hat{S}(\beta)}\})_{conn.})e^{\hat{S}(\beta)}\}.\end{aligned} \tag{3.20}$$

Thus, the proof of Eq. (3.16) is completed. The expression of Eq. (3.16) can be generalized

to an arbitrary physical operator $\hat{O}$:

$$\hat{O}\{e^{\hat{S}(\beta)}\} = \{(\hat{O}\{e^{\hat{S}(\beta)}\})_{conn.})e^{\hat{S}(\beta)}\}, \tag{3.21}$$

Applying Eq. (3.16), the original EOM in Eq. (3.15) can be rewritten as:

$$-\{\frac{\mathrm{d}\hat{S}(\beta)}{\mathrm{d}\beta}e^{\hat{S}(\beta)}\}\hat{D}_0 = \{(\hat{H}\{e^{\hat{S}(\beta)}\})_{conn.}e^{\hat{S}(\beta)}\}\hat{D}_0. \tag{3.22}$$

For non-singular exponential operator ($e^{\hat{S}(\beta)} \neq 0$), in Eq. (3.22), the operators that multiply the exponential operator within the normal product should equal to each other on both hand sides (BHS) of the equation. This implies that the TNOE EOM should be connected:

$$-\{\frac{\mathrm{d}\hat{S}(\beta)}{\mathrm{d}\beta}\}\hat{D}_0 = \{(\hat{H}\{e^{\hat{S}(\beta)}\})_{conn.}\}\hat{D}_0. \tag{3.23}$$

We can project the operator EOM in Eq. (3.23) against a completed set of normal-ordered substitution operators $\hat{\Omega}_\mu \equiv \{\hat{1}, \hat{i}^\dagger\hat{j}, \hat{i}^\dagger\hat{j}^\dagger\hat{k}\hat{l}, ...\}$ applying the contraction rules defined in Eq. (3.5) and we have:

$$-\left\langle \{\hat{\Omega}_\mu^\dagger\}\{\frac{\mathrm{d}\hat{S}(\beta)}{\mathrm{d}\beta}\}\right\rangle = \left\langle \{\Omega_\mu^\dagger\}\{(\hat{H}\{e^{\hat{S}(\beta)}\})_{conn.}\}\right\rangle. \tag{3.24}$$

Eq. (3.24) defines the projected EOM for the TNOE approach. The resulting equation resembles the canonical SR-CC theory but with the difference that index of $\hat{S}$ amplitudes span all spin orbitals with no distinction of occupied and virtual orbitals as in SR-CC case in the electronic structure theory.

As an example for electronic structure application with cluster operator that truncate at SD, the $\hat{S}(\beta)$ operator can be expressed as follow:

$$\begin{aligned}\hat{S}(\beta) &= \sum_\mu s_\mu(\beta)\{\hat{\Omega}_\mu\} \\ &= s_0(\beta)\hat{1} + \hat{S}_1(\beta) + \hat{S}_2(\beta) + ...\end{aligned} \tag{3.25}$$

$$\begin{aligned}\hat{S}_1(\beta) &= \sum_{p,q}^{M,M} s_q^p(\beta)\{\hat{p}^\dagger\hat{q}\} \\ \hat{S}_2(\beta) &= \frac{1}{4}\sum_{p,q,s,r}^{M,M,M,M} s_{sr}^{pq}(\beta)\{\hat{p}^\dagger\hat{q}^\dagger\hat{r}\hat{s}\}.\end{aligned} \tag{3.26}$$

In principle the EOM in Eq. (3.24) can be applied to the general form of the Hamiltonian (both Bosons and Fermions) by defining different commutation relations and contraction rules of the construction operators.

With the EOM derived in Eq. (3.24), we can propagate the cluster amplitudes through the

imaginary time integration. Since the cluster amplitude essentially parameterize the thermal density operator ($e^{-\beta\hat{H}}$), thermal properties can be mapped from the cluster amplitudes. In the section 3.1.3, we will elaborate how to map the thermal properties from the cluster amplitudes.

3.1.3 Calculate thermal properties using the TNOE approach

Unlike conventional canonical CC theory that applies response theory and Λ-equation to calculate properties[45], thermal properties can be directly calculated from the expansion of cluster amplitudes in the TNOE approach. Since in the latter theory, the contractions are defined based upon the trace over density operator (as shown in Eq. (3.5)), and thus, all thermal averages can naturally be evaluated through contractions and the Wick's theorem. We will explicitly explain this idea in the remaining part of this section.

Firstly, the partition function can be evaluated as follow:

$$\begin{aligned} Q(\beta) &\equiv \mathrm{Tr}\Big(\hat{D}(\beta)\Big) \\ &= \mathrm{Tr}\Big(\{e^{\hat{S}(\beta)}\}\hat{D}_0\Big) \\ &= \Big\langle\{e^{\hat{S}(\beta)}\}\Big\rangle \\ &= e^{s_0(\beta)} \end{aligned} \tag{3.27}$$

In the last equality in Eq. (3.27), we use the Wick's theorem as usual and the only surviving term of the TNOE operator in the expectation value are the constant terms according to Eq. (3.4).

Then, we evaluate the thermal statistical average of an arbitrary operator $\hat{O}$. The thermal average of $\hat{O}$ is defined as follow:

$$\Big\langle\hat{O}(\beta)\Big\rangle \equiv \frac{\mathrm{Tr}\Big(\hat{O}\hat{D}(\beta)\Big)}{\mathrm{Tr}\Big(\hat{D}(\beta)\Big)}. \tag{3.28}$$

In Eq. (3.28), the denominator is the partition function whose expression is given in Eq. (3.27). To evaluate Eq. (3.28), we need to determine the numerator.

To evaluate the numerator, we first partition the physical operator $\hat{O}$ into a constant term and a normal-ordered term with the respect to the reference density operator $\hat{D}_0$:

$$\hat{O} = o_0 + \{\hat{O}\}. \tag{3.29}$$

Then, we expand out the numerator in Eq. (3.28):

$$\begin{aligned}
\mathrm{Tr}\Big(\hat{O}\hat{D}(\beta)\Big) &= \mathrm{Tr}\Big((o_0 + \{\hat{O}\})\{e^{\hat{S}(\beta)}\}\hat{D}_0\Big) \\
&= \Big\langle (o_0 + \{\hat{O}\})\{e^{\hat{S}(\beta)}\}\Big\rangle \\
&= \Big\langle o_0\{e^{\hat{S}(\beta)}\}\Big\rangle + \Big\langle \{\hat{O}\}\{e^{\hat{S}(\beta)}\}\Big\rangle \\
&= e^{s_0(\beta)}o_0 + \Big\langle \{(\{\hat{O}\}\{e^{\hat{S}(\beta)}\})_{conn.}e^{\hat{S}(\beta)}\}\Big\rangle \\
&= e^{s_0(\beta)}\left(o_0 + \Big\langle (\{\hat{O}\}\{e^{\hat{S}(\beta)}\})_{f.c.}\Big\rangle\right),
\end{aligned} \tag{3.30}$$

where the subscript $f.c.$ denotes the equation is fully contracted. Again, we use the generalized Wick's theorem and contraction rules. Eq. (3.21) is applied to derive the connectedness in Eq. (3.30).

Finally, we substitute numerator in Eq. (3.30) and denominator in Eq. (3.27) into the definition of the thermal average of the physical operator $\hat{O}$ (in Eq. (3.28)), we have:

$$\Big\langle \hat{O}(\beta)\Big\rangle = o_0 + \Big\langle (\{\hat{O}\}\{e^{\hat{S}(\beta)}\})_{f.c.}\Big\rangle. \tag{3.31}$$

Eq. (3.31) gives the general cumulant expression of the thermal average of an arbitrary physical operator $\hat{O}$.

In a special case, if we choose the physical operator to be the substitution operators ($\hat{O} \equiv \hat{\Omega}_\mu$), then the cluster expansion of the reduced thermal density matrix is given:

$$d_\mu(\beta) \equiv \frac{\mathrm{Tr}\Big(\Omega_\mu\hat{D}(\beta)\Big)}{\mathrm{Tr}\Big(\hat{D}(\beta)\Big)} = \Big\langle \hat{\Omega}_\mu\Big\rangle + \Big\langle \Big(\{\hat{\Omega}_\mu\}\{e^{\hat{S}(\beta)}\}\Big)_{f.c.}\Big\rangle, \tag{3.32}$$

where the first term $\Big\langle \hat{\Omega}_\mu\Big\rangle$ denote a constant term as o_0 in the general expression of thermal properties in Eq. (3.31).

As examples of Eq. (3.32), we can derive the expression of one-body and two-body thermal density matrices in the electronic structure case as follow:

$$D^p_q(\beta) = \Big\langle \hat{p}^\dagger\hat{q}(\hat{1} + \hat{S}_1(\beta))\Big\rangle = f_p\delta_{pq} + f_p\bar{f}_q s^q_p(\beta), \tag{3.33}$$

and

$$\begin{aligned}
D^{pq}_{rs}(\beta) &= \Big\langle \hat{p}^\dagger\hat{q}^\dagger\hat{s}\hat{r}(\hat{1} + \hat{S}_1(\beta) + \frac{1}{2}\{\hat{S}_1(\beta)^2\} + \hat{S}_2(\beta))\Big\rangle = ... \\
&= D^r_p(\beta)D^s_q(\beta) - D^s_p(\beta)D^r_q(\beta) + f_pf_q\bar{f}_r\bar{f}_s s^{rs}_{pq}(\beta)
\end{aligned} \tag{3.34}$$

One can think of the normal-ordered exponential ansatz as a reduced density cumulant ansatz, and this is the perspective of Mukherjee and coworkers. [2, 3] In the section 3.1.4,

we will discuss about the zero temperature limit of the TNOE approach. It is natural to build connection between cluster amplitudes in the TNOE approach with the reduced density matrix since the thermal density operator can be regarded as the ensemble average of eigenstates of the Hamiltonian and it reduces to a single (ground) pure state at zero temperature limit:

$$\lim_{\beta\to\infty}\hat{D}(\beta)=\frac{1}{N}lim_{\beta\to\infty}\sum_{\lambda=0}^{\infty}e^{-\beta E_\lambda}\left|\Psi_\lambda\right\rangle\left\langle\Psi_\lambda\right|=\left|\Psi_0\right\rangle\left\langle\Psi_0\right|, \tag{3.35}$$

where N is a normalization constant. In this way, the density operator ansatz reduces to a wavefunction ansatz at zero temperature.

3.1.4 Zero temperature limit for the TNOE approach

The zero temperature limit (or $\beta\to\infty$) of the TNOE approach can be obtained by taking $\frac{\mathrm{d}\hat{S}(\beta)}{\mathrm{d}\beta}=0$, since the $\hat{S}$ amplitudes are monotonous functions of β that reach their extremes at $\beta\to\infty$. From the EOM derived in Eq. (3.24), we get the residual equations at the zero temperature:

$$\left\langle\Omega_\mu^\dagger\{(\hat{H}\{e^{\hat{S}(\beta)}\})_{conn.}\right\rangle=0;\forall\ \hat{\Omega}_\mu. \tag{3.36}$$

The ground state corresponds to the lowest energy solution of Eq. (3.36). The thermal differential equations automatically converge to the ground state. The excited state solutions for the zero-temperature equations are additional solutions associated with the non-linearity of the equations.

Unlike the formulation by Chan et al [6, 7, 8, 9] as well as the previous work by Sanyal et al [2], we do not introduce the interaction picture in the TNOE formulation. In the remaining part of this section, we will use the non-interacting Fermionic Hamiltonian as an example to illustrate the zero temperature solution of the TNOE approach and relate to the other approach by Chan et al.

Consider a non-interacting Fermionic Hamiltonian that consists of a constant part and a normal-ordered one-body part:

$$\hat{H}=h_0+\sum_{pq}h_q^p\{\hat{p}^\dagger\hat{q}\}. \tag{3.37}$$

The corresponding cluster operator is defined as:

$$\hat{s}(\beta)=s_0(\beta)+\sum_{pq}s_q^p(\beta)\{\hat{p}^\dagger\hat{q}\}. \tag{3.38}$$

Apply the generalized Wick's theorem and Fermionic contraction rule (in Eq. (3.5)) to

Eq. (3.24), the explicit working equation of TNOE EOM can be derived as:

$$
\begin{aligned}
-f_q\bar{f}_p\frac{\mathrm{d}s_q^p(\beta)}{\mathrm{d}\beta} &= f_q\bar{f}_p\left(h_q^p+\sum_r h_r^p\bar{f}_r s_q^r(\beta)-\sum_r h_q^r f_r s_r^p(\beta)-\sum_{rs}h_s^r f_r s_r^p(\beta)\bar{f}_s s_q^s(\beta)\right),\\
-\frac{\mathrm{d}s_0(\beta)}{\mathrm{d}\beta} &= h_0+\sum_{pq}h_q^p f_p\bar{f}_q s_p^q(\beta).
\end{aligned}
\tag{3.39}
$$

Eq. (3.39) can be further simplified if we define the new cluster amplitude:

$$
t_q^p \equiv \bar{f}_p f_q s_q^p. \tag{3.40}
$$

Then, Eq. (3.39) can be simplified as:

$$
\begin{aligned}
-\frac{\mathrm{d}t_q^p(\beta)}{\mathrm{d}\beta} &= f_q\bar{f}_p h_q^p+\bar{f}_p\sum_r h_r^p t_q^r(\beta)-f_q\sum_r h_q^r t_r^p(\beta)-\sum_{rs}h_s^r t_r^p(\beta)t_q^s(\beta),\\
-\frac{\mathrm{d}s_0(\beta)}{\mathrm{d}\beta} &= h_0+\sum_{pq}h_q^p t_p^q(\beta).
\end{aligned}
\tag{3.41}
$$

In Eq. (3.41), only terms that have external contractions on the Hamiltonian operators have the additional factor f or $\bar{f}$. These equations resemble the EOM obtained by White and Chan [6] with the difference that we do not introduce interaction picture in our formulation and thus there is no exponential factor associated with our cluster amplitude.[2] As a result, the zero temperature limit of TNOE approach does not converge to the SR-CC ground state solution as in the White and Chan's formulation. [6]

Now, we will show that Eq. (3.41) has no dependence of f or $\bar{f}$ by substituting the cumulant expression of one-particle density matrices that is defined in Eq. (3.32). Substituting Eq. (3.40) into Eq. (3.33), the one-particle density matrix can be re-written as:

$$
d_q^p(\beta) = f_p\delta_{pq}+t_q^p(\beta), \tag{3.42}
$$

and we define:

$$
\bar{d}_q^p(\beta) \equiv \delta_{pq}-d_q^p(\beta) = \bar{f}_p\delta_{pq}-t_q^p(\beta). \tag{3.43}
$$

[2] In the original paper by White and Chan[6], they used different external labels: a and i to distinguish different types of external contractions. This follows the conventional notation of particles and holes in the SR-CC theory but unlike the SR-CC, both i and a labels span the full orbital space without the distinction of occupied and unoccupied orbitals.

Substitute Eq. (3.42) and Eq. (3.43) into Eq. (3.41), the EOM can be re-written as:

$$\begin{aligned} -\frac{\mathrm{d}}{\mathrm{d}\beta} d_q^p(\beta) &= \sum_{rs} \bar{d}_r^p(\beta) h_s^r d_q^s(\beta), \\ -\frac{\mathrm{d}s_0(\beta)}{\mathrm{d}\beta} &= \sum_{pq} h_q^p d_q^p(\beta). \end{aligned} \tag{3.44}$$

By substituting the expression of d_q^p and $\bar{d}_q^p$ into the original TNOE EOMs, all the terms have no dependence of f and $\bar{f}$ and the equations depend on the reduced density matrices only. In this way, from Eq. (3.44), we verify that the EOM of the TNOE approach does not depend on the choice of f and $\bar{f}$. This conclusion can be generalized to a generic many-body Hamiltonian for both Bosons and Fermions. Thus, unlike the formulation of White and Chan [6], the zero temperature limit of the TNOE approach has no direct relation with the SR-CC solution but converge to the solution of the contracted Schrödinger equation (CSE) that is developed Mazziotti, Valdemoro and Nooijen et al[66, 67, 68, 69, 70]. The CSE equation in its connected form are exactly the same as the zero temperature limit of the TNOE approach.

Now, we build connection to the White and Chan formulation. To make the Eq. (3.41) reduces to the SR-CC equations at zero temperature, we need to associate the reference density matrix $\hat{D}_0$ with a specific reference state (i.e. Hartree-Fock reference state):

$$\hat{D}_0 \equiv |HF\rangle \langle HF| . \tag{3.45}$$

Then, by definition, the contractions and normal order are all associated with the single reference state $|HF\rangle$ as in the conventional case. Then the f and $\bar{f}$ are defined as:

$$f_i = 1 \ ; \ \bar{f}_i = 0, \tag{3.46}$$

and

$$f_a = 0 \ : \ \bar{f}_a = 1, \tag{3.47}$$

where a and i are particle and hole spin orbital labels based on the single reference state $|HF\rangle$, such that:

$$\hat{a} |HF\rangle = \hat{i}^\dagger |HF\rangle = 0. \tag{3.48}$$

Substituting the f and $\bar{f}$ defined in Eq. (3.46) and Eq. (3.47) in the original EOM, it reduces to the form that is identical to the White and Chan formulation [6]:

$$\begin{aligned} -\frac{\mathrm{d}t_i^a(\beta)}{\mathrm{d}\beta} &= h_i^a + \sum_r h_r^a t_i^r(\beta) - \sum_r h_i^r t_r^a(\beta) - \sum_{rs} h_s^r t_r^a(\beta) t_i^s(\beta), \\ -\frac{\mathrm{d}s_0(\beta)}{\mathrm{d}\beta} &= h_0 + \sum_{pq} h_q^p t_p^q(\beta). \end{aligned} \tag{3.49}$$

In Eq. (3.49), if we set the β derivatives to zero, it yields the SR-CC equations, at zero

temperature.[3]

The result can be generalized to two-body electronic Hamiltonian. However, in general, the TNOE approach does not depend on the choice of the reference density operator $\hat{D}_0$. Eq. (3.49) can be regarded as a special case of the general TNOE approach when we associate the reference density operator $\hat{D}_0(\beta)$ to a single reference state $|HF\rangle$.

In this way, we complete the formulation of the TNOE approach. The EOM for one-body Bosonic problem can be derived in a same fashion. Interestingly, for both one-body Bosonic and Fermonic problems, the TNOE approach yields numerical exact results for thermal properties since the projected EOMs are closed in both cases. We can prove that for any projected EOMs that are outside the given projection manifold always satisfy:

$$-\left\langle \hat{\Omega}_\mu \frac{\mathrm{d}\hat{S}(\beta)}{\mathrm{d}\beta} \right\rangle = 0;\ \forall\ \hat{\Omega}_\mu \notin \{\hat{1}, \{\hat{p}^\dagger \hat{q}\}\}. \tag{3.50}$$

Thus, the cluster operator that is beyond the given truncation in one-body Bosons and Fermons cases does not contribute the thermal density operator.

The numerical exactness for simple Bosonic problem (potential truncate up to quadratics) of the TNOE approach is an appealing feature. We will show later that this feature can be applied to design efficient algorithms for quantum dynamics simulations which will be discussed in chapter 5 and chapter 6.

However, the TNOE approach does not work well for the general electronic structure problem with an electronic Hamiltonian that contains both one-body and two-body terms:

$$\hat{H}_{el} = \sum_{ij} h_{ij} \hat{a}_i^\dagger \hat{a}_j + \frac{1}{4} \sum_{ijkl} \langle ij \| kl \rangle \hat{a}_i^\dagger \hat{a}_j^\dagger \hat{a}_l \hat{a}_k. \tag{3.51}$$

This is due to the N-representability problem. We will revisit this problem and elaborate it in chapter 4.

[3] we use a,i labels in energy expression that follows the convention of canonical CC theory

3.2 Thermofield coupled cluster (TFCC) theory

An alternative idea to effciently calculate thermal properties based on a quantum field theoretical formulation is known as the TF dynamics. [20, 21, 22] The key idea of the TF dynamics is that we can prepare a pure state ($|\Psi(\beta)\rangle\rangle$)(known as the thermostate) in which expectation value of an arbitrary physical operator over the state is equivalent to the statistical average of it ($\frac{\langle\Psi(\beta)|\hat{O}|\Psi(\beta)\rangle}{\langle\Psi(\beta)|\Psi(\beta)\rangle} = \frac{\mathrm{Tr}\left(\hat{O}\hat{D}\right)}{\mathrm{Tr}\left(\hat{D}\right)}$). To construct the thermostate, we need to introduce the fictitious, ancillary space which is a counterpart of the original physical Hilbert space. In the rest part of this section, we will elaborate the idea of the TF dynamics and discuss about how this idea can lead to a feasible computational scheme that can efficiently calculate thermal properties for quantum chemistry applications.

3.2.1 Definition of the thermostate

Recall that the general definition of the statistical average of an arbitrary physical operator in given in Eq. (1.4). The goal is to find a state whose expectation value is equivalent to the statistical average of the physical operator defined in Eq. (1.4). However, it can be rigorously proved that, the state does not exist in the physical space. [20] To define the thermostate that satisfies our goal, we need to introduce the additional fictitious, ancillary space ($\{|\tilde{n}\rangle\}$) and the thermal state spans the compound space of the physical and ancillary space ($\{|m,\tilde{n}\rangle\}$).

The thermal state in this compound space is defined as:

$$|\Psi(\beta)\rangle \equiv e^{-\beta\hat{H}/2}\,|U\rangle\,, \tag{3.52}$$

where the uniform state ($|U\rangle$) is defined as:

$$|U\rangle \equiv \sum_{m} |m,\tilde{m}\rangle\,, \tag{3.53}$$

in which $|m\rangle$ and $|\tilde{m}\rangle$ states have one-to-one correspondance.

With the only requirement that both the basis of the physical space ($|m\rangle$) and that of the fictitious, ancillary space ($|\tilde{m}\rangle$) are orthonormal:

$$\langle m|n\rangle = \delta_{mn}, \tag{3.54}$$

$$\langle \tilde{m}|\tilde{n}\rangle = \delta_{mn}, \tag{3.55}$$

It can be proved that the expectation value of a physical operator over the thermostate is

equivalent to its statistical average. The proof is as follow:

$$\begin{aligned}
\langle\Psi(\beta)|\,\hat{O}\,|\Psi(\beta)\rangle &= \sum_{m,n}\langle m,\tilde{m}|\,e^{-\beta\hat{H}/2}\hat{O}e^{-\beta\hat{H}/2}\,|n,\tilde{n}\rangle \\
&= \sum_{m,n}\langle m|\,e^{-\beta\hat{H}/2}\hat{O}e^{-\beta\hat{H}/2}\,|n\rangle\,\delta_{mn} \\
&= \mathrm{Tr}\Big(e^{-\beta\hat{H}/2}\hat{O}e^{-\beta\hat{H}/2}\Big) \\
&= \mathrm{Tr}\Big(\hat{O}e^{-\beta\hat{H}}\Big) \\
&= \mathrm{Tr}\Big(\hat{O}\hat{D}\Big).
\end{aligned} \tag{3.56}$$

In this proof, we applied the cyclic property of the trace.

To simplify the expression of the uniform state defined in Eq. (3.53),we introduce second quantized operators: $\hat{i}$, $\hat{i}^\dagger$ in physical space and $\tilde{i}$, $\tilde{i}^\dagger$ in fictitious, ancillary space. The operators obey normal (anti)-commutation rules to adapt the (anti)symmetry of (Fermions)Bosons.

For Bosons, the operators obeys (all other commutations are zero i.e. $[\hat{i},\hat{j}]=0$):

$$[\hat{i},\hat{j}^\dagger] = \hat{i}\hat{j}^\dagger - \hat{j}^\dagger\hat{i} = \delta_{ij}, \tag{3.57}$$

$$[\tilde{i},\tilde{j}^\dagger] = \tilde{i}\tilde{j}^\dagger - \tilde{j}^\dagger\tilde{i} = \delta_{ij}, \tag{3.58}$$

and

$$[\hat{i},\tilde{j}^\dagger] = [\tilde{i},\hat{j}^\dagger] = 0. \tag{3.59}$$

For Fermions, the operators obeys (all other anti-commutations are zero i.e. $\{\hat{i},\hat{j}\}=0$):

$$\{\hat{i},\hat{j}^\dagger\} = \hat{i}\hat{j}^\dagger + \hat{j}^\dagger\hat{i} = \delta_{ij}, \tag{3.60}$$

$$\{\tilde{i},\tilde{j}^\dagger\} = \tilde{i}\tilde{j}^\dagger + \tilde{j}^\dagger\tilde{i} = \delta_{ij}, \tag{3.61}$$

and

$$\{\hat{i},\tilde{j}^\dagger\} = \{\tilde{i},\hat{j}^\dagger\} = 0. \tag{3.62}$$

Making use of these second quantized operators, Eq. (3.53) can be expressed in a form of an exponential operator act on a vacuum state in the compound space ($\big|0,\tilde{0}\big\rangle$). For Fermions, we have:

$$|U\rangle = \prod_{p=1}^{M}(\mathbb{1}+\hat{p}^\dagger\tilde{p}^\dagger)\,\big|0,\tilde{0}\big\rangle = e^{\hat{u}}\,\big|0,\tilde{0}\big\rangle\,, \tag{3.63}$$

where M is total number of spin orbitals. For Bosons we have:

$$|U\rangle = \prod_{p=1}^{N}(\sum_{n=0}^{\infty}\frac{1}{\sqrt{n}}(\hat{p}^\dagger)^n\frac{1}{\sqrt{n}}(\tilde{p}^\dagger)^n)\,\big|0,\tilde{0}\big\rangle = e^{\hat{u}}\,\big|0,\tilde{0}\big\rangle\,, \tag{3.64}$$

where N is number of vibrational modes. In the Fermion case, p labels spin orbitals while

in the Boson case, p labels vibrational modes. In both cases:

$$\hat{u} \equiv \sum_{p} \hat{p}^{\dagger}\tilde{p}^{\dagger}. \tag{3.65}$$

3.2.2 Bogoliubov transformation and exponential ansatz

Bogoliubov transformation is originally introduced by Nikolay Bogolyubov and John George Valatin in 1958 to study the phonon-electron interaction for superconductivity applications. [23, 24] In this section, we will elaborate the definition of the Bogoliubov transformation and explain how it can be applied to simplify the formulation of the TFCC theory.

In general, the goal for Bogoliubov transformation is to find a set of transformation of the second quantized operators ($\{\hat{i}^{\dagger}, \hat{i}, \tilde{i}^{\dagger}, \tilde{i}\}$):

$$\{\hat{i}^{\dagger}, \hat{i}, \tilde{i}^{\dagger}, \tilde{i}\} \xrightarrow{\text{B.T.}} \{\hat{a}_i^{\dagger}, \hat{a}_i, \hat{b}_i^{\dagger}, \hat{b}_i\}, \tag{3.66}$$

such that the new transformed operators $\{\{\hat{a}_i^{\dagger}, \hat{a}_i, \hat{b}_i^{\dagger}, \hat{b}_i\}\}$ obey the original canonical (anti-)commutation relations. As a result, the we can re-define particles and holes based on an arbitrary model vacuum state through Bogoliubov transformation. For the purpose of the TFCC formulation, we choose the transformed particle and hole operators to be associated with the thermostate defined in Eq. (3.52) as the model vacuum state. In the rest of this section, we will elaborate on how this choice of the Bogoliubov transformation will lead to a dramatical simplification of the TFCC formulation.

First, let us consider the problem of the many free Bosons with the Hamiltonian given by:

$$\hat{H} = \sum_{i} \omega_i \hat{i}^{\dagger}\hat{i}, \tag{3.67}$$

in which the H.O. basis is its eigenbasis. According to the definition of the thermostate defined in Eq. (3.52), the thermostate for this specific problem is given by:

$$\begin{aligned} |\Psi(\beta)\rangle &= e^{-\beta/2\sum_i \omega_i \hat{i}^{\dagger}\hat{i}} \sum_{m} |m, \tilde{m}\rangle \\ &= e^{-\beta/2\sum_i \omega_i \hat{i}^{\dagger}\hat{i}} e^{\hat{u}} \left|0, \tilde{0}\right\rangle. \end{aligned} \tag{3.68}$$

The transformation can be defined as follow:

$$\begin{bmatrix} \hat{a}_i \\ \hat{b}_i^{\dagger} \end{bmatrix} = \begin{bmatrix} \cosh\theta_i(\beta) & -\sinh\theta_i(\beta) \\ -\sinh\theta_i(\beta) & \cosh\theta_i(\beta) \end{bmatrix} \begin{bmatrix} \hat{i} \\ \tilde{i}^{\dagger} \end{bmatrix}, \tag{3.69}$$

$$\begin{bmatrix} \hat{a}_i^{\dagger} \\ \hat{b}_i \end{bmatrix} = \begin{bmatrix} \cosh\theta_i(\beta) & -\sinh\theta_i(\beta) \\ -\sinh\theta_i(\beta) & \cosh\theta_i(\beta) \end{bmatrix} \begin{bmatrix} \hat{i}^{\dagger} \\ \tilde{i} \end{bmatrix}, \tag{3.70}$$

where

$$\cosh\theta_i(\beta) = \left(1 - e^{-\beta\hbar\omega_i}\right)^{-\frac{1}{2}}, \tag{3.71}$$

$$\sinh\theta_i(\beta) = e^{-\beta\hbar\omega_i/2}\left(1 - e^{-\beta\hbar\omega_i}\right)^{-\frac{1}{2}}, \tag{3.72}$$

and the hyperbolic functions satisfies:

$$\cosh^2\theta_i(\beta) - \sinh^2\theta_i(\beta) = 1. \tag{3.73}$$

Note that we specifically choose to relate the matrix elements of the Bogoliubov transformation in Eq. (3.69) and Eq. (3.70) to the Bose-Einstein (BE) occupation number. As a result, the thermostate serves as the model vacuum state with the respect to the Bogoliubov transformed Bosonic operators:

$$\hat{a}_i \left|\Psi(\beta)\right\rangle = \hat{b}_i \left|\Psi(\beta)\right\rangle = 0, \tag{3.74}$$

$$\left\langle\Psi(\beta)\right| \hat{a}_i^\dagger = \left\langle\Psi(\beta)\right| \hat{b}_i^\dagger = 0. \tag{3.75}$$

Eq. (3.69) and Eq. (3.70) define the Bogoliubov transformation for Bosons. The transformation is an isomorphism of the canonical commutation relation algebra of the original operators as in Eq. (3.57), Eq. (3.58) and Eq. (3.59) (All other commutations vanish i.e. $[\hat{a}_i, \hat{a}_j] = [\hat{b}_i, \hat{b}_j] = 0$):

$$[\hat{a}_i, \hat{a}_j^\dagger] = \hat{a}_i\hat{a}_j^\dagger - \hat{a}_j^\dagger\hat{a}_i = \delta_{ij}, \tag{3.76}$$

$$[\hat{b}_i, \hat{b}_j^\dagger] = \hat{b}_i\hat{b}_j^\dagger - \hat{b}_j^\dagger\hat{b}_j = \delta_{ij}, \tag{3.77}$$

$$[\hat{a}_i, \hat{b}_j^\dagger] = [\hat{b}_i, \hat{a}_j^\dagger] = 0. \tag{3.78}$$

Similarly, we can define Bogoliubov transformation for Fermions. Consider a N non-interacting Fermion system whose Hamiltonian is given as follow:

$$\hat{H} = \sum_i \epsilon_i \hat{i}^\dagger \hat{i}, \tag{3.79}$$

The Hamiltonian has a similar form as the many free-boson case in Eq. (3.67). The only difference is that the second-quantized Fermonic operators satisfy anti-commutation relation instead the commutation relation in the Bosonic case. As before, the thermal state is defined as:

$$\begin{aligned} \left|\Psi(\beta)\right\rangle &= e^{-\beta/2\sum_i \epsilon_i \hat{i}^\dagger \hat{i}} \sum_m \left|m, \tilde{m}\right\rangle \\ &= e^{-\beta/2\sum_i \epsilon_i \hat{i}^\dagger \hat{i}} e^{\hat{u}} \left|0, \tilde{0}\right\rangle \end{aligned} \tag{3.80}$$

The corresponding Bogoliubov transform is defined as:

$$\begin{bmatrix} \hat{a}_i \\ \hat{b}_i \end{bmatrix} = \begin{bmatrix} \cos\theta_i(\beta) & -\sin\theta_i(\beta) \\ \sin\theta_i(\beta) & \cos\theta_i(\beta) \end{bmatrix} \begin{bmatrix} \hat{i} \\ \tilde{i}^\dagger \end{bmatrix}, \tag{3.81}$$

$$\begin{bmatrix} \hat{a}_i^\dagger \\ \hat{b}_i^\dagger \end{bmatrix} = \begin{bmatrix} \cos\theta_i(\beta) & -\sin\theta_i(\beta) \\ \sin\theta_i(\beta) & \cos\theta_i(\beta) \end{bmatrix} \begin{bmatrix} \hat{i}^\dagger \\ \tilde{i} \end{bmatrix}, \tag{3.82}$$

where

$$\sin\theta_i(\beta) = \left(1 + e^{\beta\epsilon_i}\right)^{-\frac{1}{2}}, \tag{3.83}$$

$$\cos\theta_i(\beta) = e^{\beta\epsilon_i/2}\left(1 + e^{\beta\epsilon_i}\right)^{-\frac{1}{2}}, \tag{3.84}$$

and the trigonometric functions satisfy:

$$\sin^2\theta_i(\beta) + \cos^2\theta_i(\beta) = 1. \tag{3.85}$$

Note that, we specifically choose to relate the matrix elements of the Bogoliubov transformation in Eq. (3.81) and Eq. (3.82) to FD occupation number. As a result, the thermostate satisfies the quasi-particle vacuum state with the transformed Fermonic operators (All other anti-commutations are zero i.e. $\{\hat{a}_i, \hat{a}_j\} = \{\hat{b}_i, \hat{b}_j\} = 0$):

$$\hat{a}_i \left|\Psi(\beta)\right\rangle = \hat{b}_i^\dagger \left|\Psi(\beta)\right\rangle = 0, \tag{3.86}$$

$$\left\langle\Psi(\beta)\right| \hat{a}_i^\dagger = \left\langle\Psi(\beta)\right| \hat{b}_i = 0. \tag{3.87}$$

Notice that a, b labels can be regarded particle and hole labels as in the conventional electronic theory. However, the physical essence of these labels are very different since the Hilbert space is squared in the Bogoliubov represenation.

Eq. (3.81) and Eq. (3.82) define the Bogoliubov transformation for Fermions. The transformation is an isomorphism of the canonical anti-commutation relation algebra for the original operators in Eq. (3.60), Eq. (3.61) and Eq. (3.62):

$$\{\hat{a}_i, \hat{a}_j^\dagger\} = \hat{a}_i\hat{a}_j^\dagger + \hat{a}_j^\dagger\hat{a}_i = \delta_{ij}, \tag{3.88}$$

$$\{\hat{b}_i, \hat{b}_j^\dagger\} = \hat{b}_i\hat{b}_j^\dagger + \hat{b}_j^\dagger\hat{b}_j = \delta_{ij}, \tag{3.89}$$

$$\{\hat{a}_i, \hat{b}_j^\dagger\} = \{\hat{b}_i, \hat{a}_j^\dagger\} = 0. \tag{3.90}$$

In this way, we managed to define the Bogoliubov transformations for both Bosons and Fermions. The explicit proofs that the Bogoliubov transformed Bosonic(Fermonic) operator satisfies the canonical (anti-)commutation relation and the vacuum state condition are given in the appendix A and appendix B.

Now, we will introduce a numerical technique that can systematically approximate the thermal properties defined in Eq. (3.56) based on the definition of the Bogoliubov transformation and the thermostate. Consider a generic many body Hamiltonian (either Fermionic or Bosonic). It can always be partitioned into two components:

$$\hat{H} = \hat{h}_0 + \hat{V}. \tag{3.91}$$

The "mean-field" part of the Hamiltonian ($\hat{h}_0$) can always be defined as a diagonal one-particle term as in Eq. (3.67)(for Bosons) or Eq. (3.79) (for Fermions). Then, the perturbative

part can always be defined as:

$$\hat{V} = \hat{H} - \hat{h}_0. \tag{3.92}$$

In this way, we can define the state $|\theta(\beta)\rangle$ as the "mean-field" approximated thermostate in the same form as in Eq. (3.68) and Eq. (3.80):

$$|\theta(\beta)\rangle \equiv e^{-\beta\hat{h}_0/2} |U\rangle . \tag{3.93}$$

Making use of the cyclic property of the trace, we can expand the statistical average $(\mathrm{Tr}\left(\hat{O}\hat{D}\right))$ for an arbitrary physical operator $\hat{O}$ as:

$$\begin{aligned}
\mathrm{Tr}\left(\hat{O}\hat{D}(\tau)\right) &= \langle U| e^{-\tau\hat{H}/2}\hat{O}e^{-\tau\hat{H}/2} |U\rangle \\
&= \langle U| \hat{O}e^{-\tau\hat{H}} |U\rangle \\
&= \langle U| \hat{O}e^{-\tau\hat{H}}e^{\beta\hat{h}_0}e^{-\beta\hat{h}_0} |U\rangle \\
&= \langle U| e^{-\beta\hat{h}_0/2}\hat{O}e^{-\tau\hat{H}}e^{\beta\hat{h}_0}e^{-\beta\hat{h}_0/2} |U\rangle \\
&= \langle\theta(\beta)| \hat{O}e^{-\tau\hat{H}}e^{\beta\hat{h}_0} |\theta(\beta)\rangle .
\end{aligned} \tag{3.94}$$

From Eq. (3.94),we can introduce the exponential ansatz:

$$e^{-\tau\hat{H}}e^{\beta\hat{h}_0} |\theta(\beta)\rangle \approx e^{\hat{T}(\tau)} |\theta(\beta)\rangle \tag{3.95}$$

where

$$\hat{T} \approx t_0\mathbb{1} + \hat{t}_1 + \hat{t}_2 + ... \tag{3.96}$$

In this way, the thermal density operator can be approximated as a state in a same manner as the wavefunction ansatz for ground state electronic structure problem. As a result, the statisical average $(\mathrm{Tr}\left(\hat{O}\hat{D}(\tau)\right))$ can be evaluated through the cluster expansion:

$$\mathrm{Tr}\left(\hat{O}\hat{D}(\tau)\right) \approx \langle\theta(\beta)| \hat{O}e^{\hat{T}(\tau)} |\theta(\beta)\rangle . \tag{3.97}$$

In the definition of the exponential ansatz in Eq. (3.95), the cluster operator $\hat{T}$ can be either Fermionic or Bosonic and the reference state $|\theta(\beta)\rangle$ can be regarded as a "mean-field" approximated thermostate. The second quantized operators in the cluster amplitude $\hat{T}$ is defined in Bogoliubov representation. The key advantage to introduce the Bogoliubov transformation is that $\hat{T}$ contains excitation operators only since all de-excitation operators will vanish when acted on the reference state $|\theta(\beta)\rangle$ due to the quasi-particle vacuum state condition in Eq. (3.74), Eq. (3.75), Eq. (3.86) and Eq. (3.87). As a result, we can formulate a single-reference-like CC theory in the squared physical-ancillary dual space and the Bogoliubov representation. This will dramatically simplify the working equations comparing to the TNOE approach described in section 3.1. In section 3.2.3, we will elaborate on how explicitly the TFCC theory can be formulated based on the exponential ansatz defined in Eq. (3.95).

3.2.3 Derivation of the coupled cluster equation of motion (CC-EOM)

In this section, we will give a detailed derivation of the TFCC EOM. Making use of the cyclic rules, the statistical average of a physical property can be expressed as $\hat{O}$:

$$\begin{aligned} Tr(\hat{O}\hat{D}) &= \langle U|\, \hat{O}e^{-\tau\hat{H}}\, |U\rangle \\ &= \langle U|\, \hat{O}e^{-\tau\hat{H}}e^{\beta\hat{h}_0}e^{-\beta\hat{h}_0}\, |U\rangle \\ &= \langle U|\, e^{-\beta\hat{h}_0/2}\hat{O}e^{-\tau\hat{H}}e^{\beta\hat{h}_0}e^{-\beta\hat{h}_0/2}\, |U\rangle \\ &= \langle \theta(\beta)|\, \hat{O}e^{-\tau\hat{H}}e^{\beta\hat{h}_0}\, |\theta(\beta)\rangle \end{aligned} \tag{3.98}$$

From Eq. (3.98), we observe that if we define state $|\Phi(\tau)\rangle$ in the compound space as:

$$|\Phi(\tau)\rangle \equiv e^{-\tau\hat{H}}e^{\beta\hat{h}_0}\, |\theta(\beta)\rangle\,, \tag{3.99}$$

then the statistical average of $\hat{O}$ can be re-written as:

$$\mathrm{Tr}\Big(\hat{O}\hat{D}\Big) = \langle\theta(\beta)|\, \hat{O}\, |\Phi(\tau)\rangle\,. \tag{3.100}$$

Such a state $|\Phi(\tau)\rangle$ (if not orthogonal to $|\theta(\beta)\rangle$), can be represented as:

$$|\Phi(\tau)\rangle \equiv e^{\hat{T}(\tau)}\, |\theta(\beta)\rangle\,, \tag{3.101}$$

where

$$\hat{T}(\tau) = t_0(\tau)\mathbb{1} + \sum_{\lambda} t_\lambda(\tau)\hat{\Omega}_\lambda, \tag{3.102}$$

where $\hat{\Omega}_\lambda$ are excitation operators in the Bogoliubov representation.

Since $\hat{T}(\tau)$ is represented in Bogoliubov representation, we should represent $\hat{H}$ also in Bogoliubov representation when deriving the EOM:

$$|\Phi(\tau)\rangle \equiv e^{-\tau\tilde{H}}e^{\beta\hat{h}_0}\, |\theta(\beta)\rangle\,. \tag{3.103}$$

Eq. (3.101) can make analogy to the exponential ansatz of ground state wavefunction in the conventional coupled cluster theory. To derive the TFCC EOM, we take derivative over the imaginary τ on both hands sides of Eq. (3.101) and we have:

$$e^{\hat{T}(\tau)}\frac{\mathrm{d}\hat{T}(\tau)}{\mathrm{d}\tau}\, |\theta(\beta)\rangle = -\tilde{H}\, |\Phi(\tau)\rangle = -\tilde{H}e^{\hat{T}(\tau)}\, |\theta(\beta)\rangle\,. \tag{3.104}$$

In Eq. (3.104), we assume that $\frac{\mathrm{d}}{\mathrm{d}\tau}\, |\theta(\beta)\rangle = 0$.

In the final step, we project BHS of Eq. (3.104) against $\langle\theta(\beta)|\,\hat{\Omega}_\mu^\dagger e^{-\hat{T}(\tau)}$ to obtain:

$$-\langle\theta(\beta)|\,\hat{\Omega}_\mu^\dagger \frac{\mathrm{d}\hat{T}(\tau)}{\mathrm{d}\tau}\,|\theta(\beta)\rangle = \langle\theta(\beta)|\,\hat{\Omega}_\mu^\dagger(\tilde{H}e^{T(\tau)})_{conn.}\,|\theta(\beta)\rangle \tag{3.105}$$

where

$$e^{-\hat{T}(\tau)}\tilde{H}e^{\hat{T}(\tau)} = (\tilde{H}e^{\hat{T}(\tau)})_{conn.} \tag{3.106}$$

has been used. Thus, we manage to derive that TFCC EOM.[4]

Note that this equation is defined in a general context and the Hamiltonian operator can be either Bosonic or Fermionic. The explicit working equation can be derived using contraction rules and Wick's theorem as in the conventional coupled cluster theory. In this way, the cluster amplitude can be determined through the numerical imaginary integration over the EOM defined in Eq. (3.105). The thermal density operator is propagated as a "pure state" in this Bogoliubov representation.

In section 3.2.4, we will discuss how this TFCC formulation can lead to a powerful computational tool that can efficiently calculate thermal properties and avoid tracing over the full Hilbert space as in the conventional sum-over-states (SOS) approach.

3.2.4 Calculate thermal properties using TFCC approach

Eq. (3.97) provides a hint on how to evaluate a trace expression $(\mathrm{Tr}\left(\hat{O}\hat{D}\right))$in general. In this section, we will elaborate on how to calculate a statistical average of an arbitrary physical observable $\hat{O}$ in the TFCC approach using Eq. (3.97) as a starting point.

Our goal is to derive an expression of the statistical average in Eq. (1.4)$(\left\langle\hat{O}\right\rangle = \frac{\mathrm{Tr}\left(\hat{O}\hat{D}\right)}{\mathrm{Tr}\left(\hat{D}\right)})$ In general an arbitrary physical operator $\hat{O}$ can be decomposed into a formal:

$$\hat{O} = \sum_\lambda o_\lambda \hat{\Omega}_\lambda, \tag{3.107}$$

where $\hat{\Omega}_\lambda$ is a string of second quantized operators and o_λ the coefficient associated with it. Substituting Eq. (3.107) into the expression of the statistical average, we have:

$$\begin{aligned}\left\langle\hat{O}\right\rangle &= \frac{\sum_\lambda o_\lambda \,\mathrm{Tr}\left(\hat{\Omega}_\lambda\hat{D}(\tau)\right)}{\mathrm{Tr}\left(\hat{D}(\tau)\right)} \\ &= \sum_\lambda o_\lambda d_\lambda(\tau)),\end{aligned} \tag{3.108}$$

[4]In reference [26], the authors proposed two feasible formulations of the thermofield dynamics: the fixed reference formulation and the covariance formulation. The formulation we adopted is similar to the former.

where the reduced thermal density matrix ($d_\lambda(\tau)$)is defined as:

$$d_\lambda(\tau) \equiv \frac{\mathrm{Tr}\Big(\hat{\Omega}_\lambda \hat{D}(\tau)\Big)}{\mathrm{Tr}\Big(\hat{D}(\tau)\Big)}. \tag{3.109}$$

Thus, we convert the problem of calculating thermal properties into calculating reduced thermal density matrices ($d_\lambda(\tau)$). Once the latter is determined, the thermal properties can be calculated through the cumulant expansion of the thermal reduced density matrices in Eq. (3.108).

To determine the thermal reduced density matrix in physical space, we firstly obtain the reduced density matrices in the Bogoliubov representation whose matrix elements can be directly evaluation using Eq. (3.97):

$$\begin{aligned}
\tilde{d}_\lambda(\tau) &= \frac{\mathrm{Tr}\Big(\tilde{\Omega}_\lambda \hat{D}(\tau)\Big)}{\mathrm{Tr}\Big(\hat{D}(\tau)\Big)} \\
&= \frac{\langle\theta(\beta)|\, \tilde{\Omega}_\lambda e^{\hat{T}(\tau)}\, |\theta(\beta)\rangle}{\langle\theta(\beta)|\, e^{\hat{T}(\tau)}\, |\theta(\beta)\rangle} \\
&= \frac{e^{t_0(\tau)}\, \langle\theta(\beta)|\, \Big(\tilde{\Omega}_\lambda e^{\hat{T}(\tau)}\Big)_{f.c.}\, |\theta(\beta)\rangle}{e^{t_0(\tau)}} \\
&= \langle\theta(\beta)|\, \Big(\tilde{\Omega}_\lambda e^{\hat{T}(\tau)}\Big)_{f.c.}\, |\theta(\beta)\rangle\,,
\end{aligned} \tag{3.110}$$

where the subscript $f.c.$ denotes that the equation is fully contracted.

From Eq. (3.110), we can directly calculate the thermal reduced density matrices in Bogoliubov representation from CC amplitudes $\hat{T}(\tau)$. Once we obtain these matrices, we can inversely Bogoliubov transform them to the physical space since there is one-to-one mapping between them:

$$\tilde{d}_\lambda(\tau) \xrightarrow{\text{Inverse B. T.}} d_\lambda(\tau). \tag{3.111}$$

The transformation is performed by inverse Bogoliubov transform the construction operators in $\tilde{\Omega}_\lambda$ to physical space: $\tilde{\Omega}_\lambda \xrightarrow{\text{Inverse B. T.}} \hat{\Omega}_\lambda$ (using Eq. (3.69) and Eq. (3.70) (for Bosons) or Eq. (3.81) and Eq. (3.82) (for Fermions)). By re-combination and re-grouping different terms, we can find the mappings between the physical density matrices and the density matrices in the Bogoliubov representation.

In this way, we complete the formulation on calculating thermal properties using the TFCC approach. The procedure can be briefly summerized as follow: (1). Calculate thermal reduced density matrices in Bogoliubov representation using Eq. (3.110). (2). Map the physical thermal reduced density matrices through the inverse Bogoliubov transformation (Eq. (3.111)). (3). Calculate thermal properties from the trace of the thermal reduced density matrices in Eq. (3.108).

This scheme to calculate thermal properties has a few appealing features. Firstly, it scales

classically (polynomially) as the number of the DoF in the quantum many-body system which dramatically reduces the computational cost comparing to the conventional sum over states method (that has an exponential scaling). Secondly, unlike the other formulation by Harsha et al [26, 27, 28, 29, 30], this scheme does not apply the response theory to calcuate thermal properties which is simplier and more efficient since it does not require to introduce additional parameters to solve the Λ-equations. In fact, the TFCC formulation discussed in this section has close relation with the TNOE approach in section 3.1. We will discuss the explicit connections between the two approaches in section 3.3.

3.3 Connection between TNOE and TFCC

In this section, we will build connections between the TNOE and TFCC approaches discussed in section 3.1 and section 3.2. Apparently, the formulation of two approaches are very different. However, they are closely related if we take a deeper look.

3.3.1 Comparing number of independent parameters

The most obvious difference is that in the TFCC formulation, the cluster operator ($\hat{T}$) of exponential ansatz contains excitation operators only while the cluster operator ($\hat{S}$) of the TNOE ansatz contains both excitation and de-excitation operators. However, the later is defined in the squared Hilbert space in the Bogoliubov representation while the former is defined in the original physical Hilbert space. We will show that the number of independent parameters in both approaches is identical. To illustrate this, we will give a simple example.

Consider a second order Bosonic model Hamiltonian expressed in the following form:

$$\hat{H} = h_0 + \sum_i^M h_i \hat{i} + \sum_i^M h^i \hat{i}\hat{i}^\dagger + \sum_{ij}^M h^i_j \{\hat{i}^\dagger \hat{j}\} + \sum_{ij}^M h^{ij} \hat{i}^\dagger \hat{j}^\dagger + \sum_{ij}^M h_{ij} \hat{i}\hat{j}, \tag{3.112}$$

where M is the number of vibrational mode in the system. Both TNOE and TFCC can produce numerical exact result for this model due to the closeness of the their EOMs. However, the cluster operators have different expressions in the two approaches.

In the TNOE approach the ansatz and the cluster operator can be written as:

$$\begin{aligned} \hat{D} &= \{e^{\hat{S}}\}\hat{D}_0 \\ \hat{S} &= s_0 \mathbb{1} + \sum_i^M s_i \hat{i} + \sum_i^M s^i \hat{i}\hat{i}^\dagger + \sum_{ij}^M s^i_j \{\hat{i}^\dagger \hat{j}\} + \sum_{ij}^M s^{ij} \hat{i}^\dagger \hat{j}^\dagger + \sum_{ij}^M s_{ij} \hat{i}\hat{j}. \end{aligned} \tag{3.113}$$

While in the TFCC approach the ansatz and the cluster operator can be written as:

$$
\begin{aligned}
|\Psi(\tau)\rangle &= e^{\hat{T}(\tau)}\,|\theta(\beta)\rangle \\
\hat{T}(\tau) &= t_0\mathbb{1} + \sum_{p}^{2M} t^p \hat{p}^\dagger + \sum_{pq}^{2M} t^{pq}\hat{p}^\dagger\hat{q}^\dagger.
\end{aligned}
\tag{3.114}
$$

It seems that the TNOE ansatz in Eq. (3.113) has more parameters than that of the exponential ansatz in the TFCC in Eq. (3.114). Nevertheless, if one inspect the summation labels, it can be found that they run from 1 to M in the TNOE case but from 1 to $2M$ in the TFCC case. This indicate that each tensor in the $\hat{T}$ operator is twice the size of the tensors in $\hat{S}$ operator though there are less number of them in the $\hat{T}$ operator.

We will show that the number of independent parameters in both cases is equivalent. (1). t^p is a one-dimensional tensor with size $2M$ while both s^i and s_i are one-dimensional tensors with size M. Thus, the number of parameters contains in the t^p tensor $(2M)$ is equivalent to the sum of number of parameters in the s_i and s^i tensors $(M+M=2M)$. (2). The t^{pq} tensor contains $2M*2M=4M^2$ number of parameters. While each of the s^{ij}, s_{ij} and s^i_j tensors contains M^2 number of parameter and in total $3M^2$ parameters. The t^{pq} tensor is seemingly contains more parameters than that of s^{ij}, s_{ij} and s^i_j tensors. However, due to the fact that a and b set of the Bogoliubov tranformed operators commute ($[\hat{a}^\dagger_i, \hat{b}^\dagger_j] = [\hat{a}_i, \hat{b}_j] = [\hat{a}^\dagger_i, \hat{b}_j] = 0$), there are two $M*M$ blocks of t^{pq} tensor are identical:

$$
t^{a_i b_j} = t^{b_i a_j}. \tag{3.115}
$$

As a result, the number of independent parameters in t^{pq} tensor is $3M^2$ rather than $4M^2$. From (1) and (2), we verify that the number of independent parameters in TNOE and TFCC approaches are identical. In both cases, the number of independent parameters is $1+2M+3M^2$, where 1 comes from the constant term. This conclusion derived from the simple example can be generalized to an arbitrary quantum-many body Hamiltonian for both Bosons and Fermions.

3.3.2 Mappings between cluster amplitudes

Let us gain further insights on the connection between the two approaches. In section 3.3.1, we verfied that the TNOE ansatz and the exponential ansatz in the TFCC approach have the same number of independent parameters. In this section, we will illustrate that there is a one-to-one mapping to between the cluster amplitudes in both approaches.

The key to map the cluster amplitudes in the two approaches is through the expression of the reduced thermal density matrices. In both approaches, we can map the density matrices directly from the cluster amplitudes.

Let us continue to use the simple model Hamiltonian given in Eq. (3.112) as an example. According to Eq. (3.32), the reduced thermal density matrices can be expanded as follow in

the TNOE approach:

$$
\begin{aligned}
d^0 &= \left\langle \mathbb{1}\{e^{\hat{S}}\} \right\rangle = e^{s_0}, \\
d^i &= \left\langle \left(\hat{i}^\dagger\{e^{\hat{S}}\}\right)_{f.c.} \right\rangle = f_i s_i, \\
d_i &= \left\langle \left(\hat{i}\{e^{\hat{S}}\}\right)_{f.c.} \right\rangle = \bar{f}_i s^i, \\
d^i_j &= \left\langle \left(\hat{i}^\dagger \hat{j}\{e^{\hat{S}}\}\right)_{f.c.} \right\rangle = f_i \delta_{ij} + f_i \bar{f}_j s^i s_j + f_i \bar{f}_j s^j_i, \\
d^{ij} &= \left\langle \left(\hat{i}^\dagger \hat{j}^\dagger\{e^{\hat{S}}\}\right)_{f.c.} \right\rangle = f_i f_j s_i s_j + f_i f_j s_{ij}, \\
d_{ij} &= \left\langle \left(\hat{i}\hat{j}\{e^{\hat{S}}\}\right)_{f.c.} \right\rangle = \bar{f}_i \bar{f}_j s^i s^j + \bar{f}_i \bar{f}_j s^{ij}.
\end{aligned}
\tag{3.116}
$$

While according to Eq. (3.110) and Eq. (3.111), in the TFCC approach, the reduced thermal density matrices can be expressed as:

$$
\begin{aligned}
d^0 &= \langle\theta| e^{\hat{T}} |\theta\rangle = e^{t_0}, \\
d^i &= \langle\theta| \left((\cosh\theta_i \hat{a}^\dagger_i + \sinh\theta_i \hat{b}_i) e^{\hat{T}}\right)_{f.c.} |\theta\rangle = \sinh\theta_i t^{b_i}, \\
d_i &= \langle\theta| \left((\cosh\theta_i \hat{a}_i + \sinh\theta_i \hat{b}^\dagger_i) e^{\hat{T}}\right)_{f.c.} |\theta\rangle = \cosh\theta_i t^{a_i}, \\
d^i_j &= \langle\theta| \left((\cosh\theta_i \hat{a}^\dagger_i + \sinh\theta_i \hat{b}_i)(\cosh\theta_j \hat{a}_j + \sinh\theta_j \hat{b}^\dagger_j) e^{\hat{T}}\right)_{f.c.} |\theta\rangle \\
&= \sinh\theta_i \cosh\theta_j (t^{b_i a_j} + t^{b_i} t^{a_j}) + \sinh\theta_i \sinh\theta_j \delta_{ij}, \\
d^{ij} &= \langle\theta| \left((\cosh\theta_i \hat{a}^\dagger_i + \sinh\theta_i \hat{b}_i)(\cosh\theta_j \hat{a}^\dagger_j + \sinh\theta_j \hat{b}_j) e^{\hat{T}}\right)_{f.c.} |\theta\rangle \\
&= \sinh\theta_i \sinh\theta_j (t^{b_i b_j} + t^{b_i} t^{b_j}), \\
d_{ij} &= \langle\theta| \left((\cosh\theta_i \hat{a}_i + \sinh\theta_i \hat{b}^\dagger_i)(\cosh\theta_j \hat{a}_j + \sinh\theta_j \hat{b}^\dagger_j) e^{\hat{T}}\right)_{f.c.} |\theta\rangle \\
&= \cosh\theta_i \cosh\theta_j (t^{a_i a_j} + t^{a_i} t^{a_j}).
\end{aligned}
\tag{3.117}
$$

Comparing Eq. (3.116) and Eq. (3.117), we can find the mappings between $\hat{S}$ and $\hat{T}$

amplitudes:

$$\begin{aligned} s_0 &= t_0 \\ \sqrt{f}_i s^i &= t^{b_i} \\ \sqrt{\bar{f}_i} s_i &= t^{a_i} \\ \sqrt{f_i \bar{f}_j} s^i_j &= t^{b_i a_j} \\ \sqrt{f_i f_j} s^{ij} &= t^{b_i b_j} \\ \sqrt{\bar{f}_i \bar{f}_j} s_{ij} &= t^{a_i a_j}, \end{aligned} \tag{3.118}$$

where

$$\begin{aligned} \sqrt{f_i} &= \sinh(\theta_i), \\ \sqrt{\bar{f}_i} &= \cosh(\theta_i). \end{aligned} \tag{3.119}$$

Thus, we manage to build the one-to-one mappings between $\hat{S}$ and $\hat{T}$ amplitude in this simple example. This argument can be generalized to an arbitrary Hamiltonian and works for both Bosons and Fermions. The key is that in both approaches, there are one-to-one mappings between the cluster amplitude and the physical reduced thermal density matrices. In this way, we can built the mappings between the cluster operators from these density matrices:

$$\left\langle \left(\hat{\Omega}_\lambda \{ e^{\hat{S}} \} \right)_{conn.} \right\rangle \rightarrow d_\lambda \xleftarrow{\text{inverse B. T}} \langle \theta | \left(\tilde{\Omega}_\lambda e^{\hat{T}} \right)_{conn.} | \theta \rangle . \tag{3.120}$$

Thus, we manage to verify that at each temperature, the cluster amplitude can translate from TFCC to TNOE. In section 3.3.3, we will further illustrate that the EOMs of the two approaches can be translated from one to another. As a result, the two approaches produce identical result at all temperatures.

3.3.3 The connection of the EOMs

In this section, we use the non-interacting one-electronic Fermionic Hamiltonian (give in Eq. (3.37)) to prove that the EOMs between TNOE and TFCC can be translated from one to another.[5]

We start from the TNOE approach. The explicit EOMs are given in Eq. (3.39) and we reiterate them:

[5]For the proof of Bosonic vibrational Hamiltonian in Eq. (3.112), please see appendix C.

$$
\begin{aligned}
-\frac{\mathrm{d}s_0(\beta)}{\mathrm{d}\beta} &= h_0 + \sum_{pq} h_q^p f_p \bar{f}_q s_p^q(\beta), \\
-f_q\bar{f}_p\frac{\mathrm{d}s_q^p(\beta)}{\mathrm{d}\beta} &= f_q\bar{f}_p\left(h_q^p + \sum_r h_r^p \bar{f}_r s_q^r(\beta) - \sum_r h_q^r f_r s_r^p(\beta) - \sum_{rs} h_s^r f_r s_r^p(\beta)\bar{f}_s s_q^s(\beta)\right).
\end{aligned}
\tag{3.121}
$$

Similar to the mappings of cluster amplitude between TNOE and TFCC in Eq. (3.118) and Eq. (3.119) for Bosonic problem, the mappings for Fermionic problem reads:

$$
\begin{aligned}
s^0 &= t^0, \\
t_q^p &= \sqrt{\bar{f}_p}\sqrt{f}_q s_q^p,
\end{aligned}
\tag{3.122}
$$

where

$$
\begin{aligned}
\sin\theta_p &= \sqrt{f_p} \\
\cos\theta_p &= \sqrt{\bar{f}_p}.
\end{aligned}
\tag{3.123}
$$

We substitute these mapping in Eq. (3.122) and Eq. (3.123) into the original EOMs, we get:

$$
-\frac{\mathrm{d}t_0}{\mathrm{d}\beta} = h_0 + \sum_{pq} \sin\theta_p \cos\theta_q h_q^p t_p^q \tag{3.124}
$$

$$
-\frac{\mathrm{d}t_q^p}{\mathrm{d}\beta} = \cos\theta_p \sin\theta_q h_q^p + \sum_r \cos\theta_p \cos\theta_r h_r^p t_q^r - \sum_r \cos\theta_r \sin\theta_q h_q^r t_r^p - \sum_{rs} sin\theta_r \cos\theta_s h_s^r t_r^p t_q^s. \tag{3.125}
$$

Notice that in Eq. (3.125), we canceled out the common factor $\sqrt{\bar{f}_p}\sqrt{f_q}$ on BHS of the equation.

In this derivation a key step is as follow. When there is a contraction between the Hamiltonian and the cluster operator in the TNOE EOM, it will produce a f or $\bar{f}$ factor. Thus, we can re-write the factor into a product of its square root. We then place one of them in front of the Hamiltonian matrix element and the other in front of the TNOE amplitude. Lastly, the Hamiltonian matrix element can be converted to a contribution of the renormalized matrix element of the Bogoliubov transformed Hamiltonian and the TNOE amplitude can be mapped to the TFCC amplitude. For example, we can evaluate the term

$\sum_r \sqrt{f_q}\sqrt{\bar{f}_p} h_r^p \bar{f}_r s_q^r$ in Eq. (3.125) as follow:

$$\begin{aligned}\sum_r \sqrt{f_q}\sqrt{\bar{f}_p} h_r^p \bar{f}_r s_q^r &= \sum_r \sqrt{f_q}\sqrt{\bar{f}_p} h_r^p \sqrt{\bar{f}_r}\sqrt{\bar{f}_r} s_q^r \\ &= \sum_r \sqrt{\bar{f}_p}\sqrt{\bar{f}_r} h_r^p \sqrt{\bar{f}_r}\sqrt{f_q} s_q^r \\ &= \sum_r \cos\theta_p \cos\theta_r h_r^p t_q^r.\end{aligned} \tag{3.126}$$

Comparing these equations with the expression of the Bogoliubov transformed Hamiltonian:

$$\begin{aligned}\hat{h} &= h^0 + \sum_{pq} h_q^p (\cos\theta_p \hat{a}_p^\dagger + \sin\theta_p \hat{b}_p^\dagger)(\cos\theta_q \hat{a}_q + \sin\theta_q \hat{b}_q) \\ &= h_0 + \sum_{pq} \cos\theta_p \cos\theta_q h_q^p \hat{a}_p^\dagger \hat{a}_q + \sum_{pq} \cos\theta_p \sin\theta_q h_q^p \hat{a}_p^\dagger \hat{b}_q + \sum_{pq} \sin\theta_p \cos\theta_q h_q^p \hat{b}_p^\dagger \hat{a}_q + \sum_{pq} \sin\theta_p \sin\theta_q h_q^p \hat{b}_p^\dagger \hat{b}_q \\ &\equiv h_0 + \sum_{pq} \tilde{h}_{a_q}^{a_p} \hat{a}_p^\dagger \hat{a}_q + \sum_{pq} \tilde{h}_{b_q}^{a_p} \hat{a}_p^\dagger \hat{b}_q + \sum_{pq} \tilde{h}_{a_q}^{b_p} \hat{b}_p^\dagger \hat{a}_q + \sum_{pq} \tilde{h}_{b_q}^{b_p} \hat{b}_p^\dagger \hat{b}_q,\end{aligned} \tag{3.127}$$

where in the transformed Hamiltonian h_1^1 term can be divided into four blocks and each block has the same shape of the original Hamiltonian:

$$\begin{aligned}\tilde{h}_a^a &: \sum_{pq} \cos\theta_p \cos\theta_q h_q^p \hat{p}^\dagger \hat{q} \\ \tilde{h}_b^a &: \sum_{pq} \cos\theta_p \sin\theta_q h_q^p \hat{p}^\dagger \hat{q} \\ \tilde{h}_a^b &: \sum_{pq} \sin\theta_p \cos\theta_q h_q^p \hat{p}^\dagger \hat{q} \\ \tilde{h}_b^b &: \sum_{pq} \sin\theta_p \sin\theta_q h_q^p \hat{p}^\dagger \hat{q}.\end{aligned} \tag{3.128}$$

Substituting the renormalized matrix elements in the Bogoliubov transformed Hamiltonian in Eq. (3.127) and Eq. (3.128), the original EOMs in Eq. (3.124) and Eq. (3.125) can be re-written as:

$$-\frac{\mathrm{d}t_0}{\mathrm{d}\beta} = h_0 + \sum_{pq} \tilde{h}_{a_q}^{b_p} t_p^q \tag{3.129}$$

$$-\frac{\mathrm{d}t_q^p}{\mathrm{d}\beta} = \tilde{h}_{b_q}^{a_p} + \sum_r \tilde{h}_{a_r}^{a_p} t_q^r - \sum_r \tilde{h}_{b_q}^{a_r} t_r^p - \sum_{rs} \tilde{h}_{a_s}^{b_r} t_r^p t_q^s. \tag{3.130}$$

In Eq. (3.129) and Eq. (3.130), blocks of the Hamiltonian matrix elements that are

associated with a or b blocks can be regarded as particles or holes in the conventional SR-CC theory. However, unlike the latter, all summation label runs over the full orbital space without distinction of virtual and occupied orbitals. These equations are exactly the same as the TFCC EOMs. Since $\hat{T}$ operators in the TFCC approach contains excitation terms only due to the vacuum state condition in Eq. (3.86) and Eq. (3.87). Thus, the $\hat{T}$ operartor in the TFCC approach can be wrriten as:

$$\hat{T} = t_0 \mathbb{1} + \sum_{pq} t_{b_q}^{a_p} \hat{a}_p^\dagger \hat{b}_q. \tag{3.131}$$

From Eq. (3.131), Eq. (3.129) and Eq. (3.130), we verify that the TNOE EOMs can be translated to the TFCC EOMs:

$$-\frac{\mathrm{d}t^\mu}{\mathrm{d}\beta} = \left\langle \hat{\Omega}_\mu^\dagger \left(\tilde{H} e^{\hat{T}} \right)_{conn.} \right\rangle, \tag{3.132}$$

for non-interacting one-electron Hamiltonian. As a result, the two approaches produce identical results at all temperatures. This conclusion can be generalized to an arbitrary many-body Hamiltonian for either Fermions or Bosons.

Since the EOM of TNOE and TFCC can be translated from one to another, it is natural to build the connection between the reference density operator $\hat{D}_0(\beta)$ in the TNOE approach and the reference state $|\theta(\beta)\rangle$ in the TFCC approach. We will discuss about the in detail in section 3.3.4.

3.3.4 The connection of the reference states

In this section, we analyze the connection between the reference density operator ($\hat{D}_0(\beta)$) in the TNOE ansatz and the reference state $|\theta(\beta)\rangle$ in the TFCC approach. We will verify that the reference states are closely related and both approaches are independent of the choice of the reference state.

We firstly build the connection between $|\theta(\beta)\rangle$ and $\hat{D}_0(\beta)$. According the definition of the state $|\theta(\beta)\rangle$ in Eq. (3.93) and making use of the cyclic rule of the trace, we have:

$$\langle\theta(\beta)|\, \hat{i}^\dagger \hat{j}\, |\theta(\beta)\rangle = \langle U|\, e^{-\beta\hat{h}_0/2} \hat{i}^\dagger \hat{j} e^{-\beta\hat{h}_0/2}\, |U\rangle = \langle U|\, \hat{i}^\dagger \hat{j} e^{-\beta\hat{h}_0}\, |U\rangle = \mathrm{Tr}\left(\hat{i}^\dagger \hat{j} e^{-\beta\hat{h}_0} \right), \tag{3.133}$$

and

$$\langle\theta(\beta)|\, \hat{i}\hat{j}^\dagger\, |\theta(\beta)\rangle = \langle U|\, e^{-\beta\hat{h}_0/2} \hat{i}\hat{j}^\dagger e^{-\beta\hat{h}_0/2}\, |U\rangle = \langle U|\, \hat{i}\hat{j}^\dagger e^{-\beta\hat{h}_0}\, |U\rangle = \mathrm{Tr}\left(\hat{i}\hat{j}^\dagger e^{-\beta\hat{h}_0} \right). \tag{3.134}$$

Comparing to the definition of contraction in the TNOE theory in Eq. (3.5), we find that the expressions in Eq. (3.133) and Eq. (3.134) define the contractions in the TNOE theory if we set $\hat{D}_0(\beta) = e^{-\beta\hat{h}_0}$:

$$\langle\theta(\beta)|\, \hat{i}^\dagger \hat{j}\, |\theta(\beta)\rangle = \mathrm{Tr}\left(\hat{i}^\dagger \hat{j} \hat{D}_0 \right) = f_i \delta_{ij}, \tag{3.135}$$

$$\langle\theta(\beta)|\,\hat{i}\hat{j}^{\dagger}\,|\theta(\beta)\rangle = \mathrm{Tr}\Big(\hat{i}\hat{j}^{\dagger}\hat{D}_0\Big) = \bar{f}_i\delta_{ij}. \tag{3.136}$$

Eq. (3.135) and Eq. (3.136) build the connection between reference state $\hat{D}_0(\beta)$ in TNOE ansatz and the reference state $|\theta(\beta)\rangle$ in the exponential ansatz of TFCC approach.

We can further transform the physical operators in Eq. (3.135) and Eq. (3.136) to the Bogoliubov representation. For Bosons the contractions can be defined as:

$$\langle\theta(\beta)|\,(\cosh\theta_i\hat{a}_i^{\dagger} + \sinh\theta_i\hat{b}_i)(\cosh\theta_j\hat{a}_j + \sinh\theta_j\hat{b}_j^{\dagger})\,|\theta(\beta)\rangle = \sinh^2\theta_i\delta_{ij} = f_i\delta_{ij}, \tag{3.137}$$

and

$$\langle\theta(\beta)|\,(\cosh\theta_i\hat{a}_i + \sinh\theta_i\hat{b}_i^{\dagger})(\cosh\theta_j\hat{a}_j^{\dagger} + \sinh\theta_j\hat{b}_j)\,|\theta(\beta)\rangle = \cosh^2\theta_i\delta_{ij} = \bar{f}_i\delta_{ij}. \tag{3.138}$$

The result is consistent with what is obtained in section 3.3.2 (Eq. (3.119)). For Fermions, the contractions can be defined as:

$$\langle\theta(\beta)|\,(\cos\theta_i\hat{a}_i^{\dagger} + \sin\theta_i\hat{b}_i^{\dagger})(\cos\theta_j\hat{a}_j + \sin\theta_j\hat{b}_j)\,|\theta(\beta)\rangle = \sin^2\theta_i\delta_{ij} = f_i\delta_{ij}, \tag{3.139}$$

$$\langle\theta(\beta)|\,(\cos\theta_i\hat{a}_i + \sin\theta_i\hat{b}_i)(\cos\theta_j\hat{a}_j^{\dagger} + \sin\theta_j\hat{b}_j^{\dagger})\,|\theta(\beta)\rangle = \cos^2\theta_i\delta_{ij} = \bar{f}_i\delta_{ij}. \tag{3.140}$$

Comparing the definition of the $\sin\theta_i$ and $\cos\theta_i$ functions, Eq. (3.139) and Eq. (3.140) are consistent with the general definition of f and $\bar{f}$ in Eq. (3.13) and Eq. (3.14) in section 3.1 and they are naturally associated with the FD occupation numbers.

Both approaches are independent of the choice of the reference state. In the TNOE approach, as been discussed in section 3.1.4, the resulting EOMs can be expressed in terms of the reduced density matrices which is independent of the choice of f and $\bar{f}$. As a result, the TNOE approach does not depend on the choice of the reference density operator $\hat{D}_0$. Since all thermal properties can be expressed in a cumulant expansion reduced density matrices, they are independent of the choice of reference $\hat{D}_0$ as well.

Since we have proved in section 3.3.3 that EOMs translate from one another between the TNOE and the TFCC approach, the two approaches are supposed to produce identical result. Thus, we can deduce that the TFCC approach in our formulation is also independent of the choice of the reference state ($|\theta(\beta)\rangle$).

3.4 Summary of the chapter

In this chapter, we manage to formulate the theoretical framework and build connections of the TNOE and TFCC approaches. Both approaches are based upon the statistical mechanics formulations of the quantum field theory to form a compact representation of the thermal density operator ($\hat{D} \equiv e^{-\beta \hat{H}}$) and resulting efficient heuristic computational methods to simulate statistical mechanics (as well as real time quantum dynamics) for general quantum many-body systems through numerical integrations of the EOMs for the thermal density operator ($-\frac{\mathrm{d}}{\mathrm{d}\beta}\hat{D} = \hat{H}\hat{D}$). In both methods, we implicitly have well-defined reduced density matrices without the resort of energy derivatives or the response theory but directly defined as the expansion of cluster amplitudes. We think this is a simpler and more concise formulation comparing to the conventional approaches from literatures [6, 7, 8, 9, 26, 27, 28, 29, 30] and since we can directly calculate thermal properties on-the-fly without the need of solving additional response equations. The discussion in this chapter is limited in an abstract fashion. In the following chapters, we will discuss about the specific applications of the general theoretical framework introduced in this chapter. We will explain on how this general theoretical frameworks can be applied to simulate quantum dynamics and statistical mechanics properties for chemical systems that are of real interest.

Chapter 4

Application: thermal properties for pure electronic structure problems

In this chapter, we will introduce a specific application of the TFCC approach that is discussed in chapter 3.2 to the electronic structure problem. Unlike other finite temperature coupled cluster formulations for the same problem from literatures[6, 30], we do not introduce interaction picture in our formulation. As a result, our approach is independent of the choice of the reference state and the thermal properties can be calculated in an "on-the-fly" fashion through an one-shot imaginary time integration over the CC EOMs. The approach is implemented based upon subroutines of the open-source electronic structure program `PySCF`. [71] The code is available on `GitHub` repository `Thermal-Field`. [72]

This chapter is organized as follow:

In section 4.1, we discuss about the detailed theory and implementation of the TFCC approach for electronic structure problems. In section 4.1.1, we elaborate a primary implementation of the TFCC approach for electronic structure problem. In section 4.1.2, we introduced the complete active space (CAS). By restricting the application of the TFCC approach within the CAS, we can reduce the computational cost of compare the full orbital space TFCC approach and make direct comparison to the sum over states results which can be regarded as the numerically exact solution. In section 4.1.3, we discuss about the challenge of the TFCC approach: the N-representability problem and our attempts to resolve this problem: by systematically introducing constraints.

In section 4.2, we show some primary results of the TFCC approach for calculations of the thermal electronic properties. In section 4.2.1, we present the results of thermal properties for model magnetic systems. The approach works well for weakly coupling models. However, we show that the approach fails for strongly coupling models and the N-representability conditions are violated for those models. In section 4.2.2, we investigate more results on small molecular compounds and analyzed the results. Although the TFCC approach does not produce ideal results for those systems, we gain insights on the cause of the failure through these investigations. These data and analysis might provide valuable hints for readers on further improvements of the approach.

4.1 Theory and implementation

4.1.1 Thermofield coupled cluster (TFCC) method for electronic structure problem

In this section, we will elaborate the implementation details of the TFCC method that is described in the chapter 3.2 for electronic structure problems. The code is built on top of the `PySCF` electronic structure program. [71].

Recall that the essence of the TFCC approach is to apply the exponential ansatz to parameterize the thermal density operator in the Bogoliubov representation. In this way, we can propagate the thermal density operator as a pure state and calculate the thermal properties on-the-fly. The electronic Hamiltonian is defined as:

$$\hat{H}_{el} = \sum_{ij} h_{ij} \hat{a}_i^\dagger \hat{a}_j + \frac{1}{4} \sum_{ijkl} \langle ij \| kl \rangle \hat{a}_i^\dagger \hat{a}_j^\dagger \hat{a}_l \hat{a}_k. \tag{4.1}$$

The starting point of this approach is the HF calculation to construct the thermofield reference state $|\theta(\beta)\rangle \equiv e^{-\beta \hat{h}_0/2} |U\rangle$, where the mean-field Hamiltonian $\hat{h}_0$ is defined as the converged Fock matrix obtained from HF SCF procedure:

$$\hat{h}_0 = \sum_{pq} F_{pp} \hat{p}^\dagger \hat{p} \tag{4.2}$$

whose matrix elements (in AO basis) is defined as:

$$F_{\alpha\beta} = h_{\alpha\beta} + \sum_{\delta,\gamma} (2 \langle \alpha\delta | \beta\gamma \rangle - \langle \alpha\delta | \gamma\beta \rangle) D_{\delta\gamma} \tag{4.3}$$

where the density matrix $D_{\alpha\beta}$ is defined as:

$$D_{\alpha\beta} = \sum_{i \in \text{occ}} C_{\alpha i}^* C_{\beta i} \tag{4.4}$$

where $\boldsymbol{C}$ is defined as HF MO coefficients. The Fock matrix is then transformed to the canonical (MO) basis which is diagonal:

$$F_{\alpha\beta} \to F_{pq} \delta_{pq}. \tag{4.5}$$

Given the thermofield reference state, we can apply the exponential ansatz to parameterize the thermal density operator:

$$|\Phi(\tau)\rangle \equiv e^{-\tau \hat{H}} |U\rangle = e^{\hat{T}(\tau)} |\theta(\beta)\rangle , \tag{4.6}$$

where

$$\hat{T}(\tau) \approx t_0 \mathbb{1} + \sum_{pq}^{M} t_{b_q}^{a_p} \{\hat{a}_p^\dagger \hat{b}_q\} + \frac{1}{4} \sum_{pqrs}^{M} t_{b_r b_s}^{a_p a_q} \{\hat{a}_p^\dagger \hat{a}_q^\dagger \hat{b}_s \hat{b}_r\}, \tag{4.7}$$

and the construction operators $\hat{a}_p^\dagger, \hat{a}_q^\dagger, \hat{b}_r, \hat{b}_s$ are in the Bogoliubov representation and contains blocks for the q-creation operators only with the respect to $|\theta(\beta)\rangle$.

In a next step, we Bogoliubov transform the electronic Hamiltonian and rewrite them with the respect to the thermofield reference state $|\theta(\beta)\rangle$:

$$\hat{H}_{elec} \xrightarrow{\text{B.T.}} \tilde{H}_{elec}. \tag{4.8}$$

The matrix of the transformation is related to FD occupation number of the mean-field Hamiltonian $\hat{h}_0$:

$$\sin\theta_p = \sqrt{n_p} \tag{4.9}$$

$$\cos\theta_p = \sqrt{1 - n_p} \tag{4.10}$$

$$n_p = \frac{1}{1 + e^{\beta\epsilon_p}} \tag{4.11}$$

$$\epsilon_p = F_{pp} \tag{4.12}$$

In the last step, we perform imaginary time evolution of the TFCC amplitude and calculate thermal properties on-the-fly:

$$-\langle\theta(\beta)|\,\hat{\Omega}_\mu^\dagger \frac{\mathrm{d}\hat{T}(\tau)}{\mathrm{d}\tau}\,|\theta(\beta)\rangle = \langle\theta(\beta)|\,\hat{\Omega}_\mu^\dagger \left(\tilde{H}_{elec} e^{\hat{T}(\tau)}\right)_{conn.} |\theta(\beta)\rangle\,, \tag{4.13}$$

$$\langle O(\tau)\rangle = \langle\theta(\beta)|\,(\tilde{O} e^{\hat{T}(\tau)})_{f.c.}\,|\theta(\beta)\rangle\,. \tag{4.14}$$

We will give an explicit procedure of the implementation as follow.

Step 1: HF calculation from `PySCF`

Given the molecular structure and basis set as input, we can run `PySCF` HF calculations. An example Python script to run this calculation is shown in List 4.1.

```
# geometry of molecules (in Angstrom)

H2O = """
O 0 0       0
H 0 -2.757 2.587
H 0  2.757 2.587
"""

atom = H2O
molecule = "H2O"

# setup model input using gaussian-type-orbitals
molecular_HF = gto.M(
       atom=atom,  # in Angstrom
       basis="6-31g",
       symmetry=1,
)
```

```
18
19 # run HF calculation
20 mean_field = scf.HF(molecular_HF)
21 mean_field.kernel()
```

Listing 4.1: Example Python script to run PySCF HF calculations

We can extract one-electron integrals, two-electron integrals, orbital energies (diagonal element of the Fock matrix in the canonical basis), converged Fock matrix (at zero temperature), converged HF energy, nuclear repulsion energy and the total number of electrons from the HF calculation. The example Python script to achieve this is shown in List 4.2.

```
1  # 1-electron integral
2  h_core_AO = mol_HF.intor('int1e_kin_sph') + mol_HF.intor('int1e_nuc_sph')
3  print("1-electron integral (in AO basis):\n{:}".format(h_core_AO.shape))
4
5  # Fock matrix
6  fock_AO = mean_field.get_fock()
7  print("Fock matrix (in AO basis):\n{:}".format(fock_AO.shape))
8
9  # 2-electron integral
10 eri_AO = mol_HF.intor('int2e_sph', aosym=1)
11 print("2-electron integral (in AO basis):\n{:}".format(eri_AO.shape))
12
13 # transform matrix elements from AOs to MOs
14
15 # 1-electron integral
16 h_core_MO = np.einsum('pi,pq,qj->ij', mean_field.mo_coeff, h_core_AO, mean_field.mo_coeff)
17 print('1-electron integral (in MO basis):\n{:}'.format(h_core_MO))
18
19 # Fock matrix
20 fock_MO = np.einsum('pi,pq,qj->ij', mean_field.mo_coeff, fock_AO, mean_field.mo_coeff)
21 print("Fock matrix (in MO basis):\n{:}".format(fock_MO))
22
23 # 2-electron integral
24 eri_MO = ao2mo.incore.full(eri_AO, mean_field.mo_coeff)
25 print("2-electron integral (in MO basis):\n{:}".format(eri_MO))
26
27 # total number of electron
28 OccupationNumber = mean_field.mo_occ / 2
29 nof_electron = sum(OccupationNumber)
30 print("total number of electrons:{:}".format(nof_electron))
31
32 # get Nuclear Repusion Energy
33 NR_energy = mean_field.energy_nuc()
34 print("Nuclear repulsion energy:{:}".format(NR_energy))
```

Listing 4.2: Example Python script to extract information from PySCF HF calculations

Step 2: Construct Fock matrix at the reference temperature β

Based on the HF calculation in step 1, we can construct Fock matrix at the reference temperature β. To obtain the Fock matrix, we firstly calculate the orbital occupation number and chemical potential from the FD distribution at the reference temperature β:

$$n_p(\beta, \mu) = \frac{1}{1 + e^{\beta(\epsilon_p - \mu)}}, \tag{4.15}$$

where $n_p(\beta)$ is the occupation number,ϵ_p is the orbital energy at 0 K(obtained from the HF calculation) and μ is the chemical potential. To achieve this, we apply a Newtonian

procedure to iteratively solve the non-linear equation:

$$n_{el} = \sum_{p} n_p(\beta, \mu), \tag{4.16}$$

where n_{el} total number of electrons which is a constant. The explicit algorithm for the Newtonian procedure is shown in List 4.3.

```python
def Cal_mu_FD(n_el, E, beta):
    """
    calculate chemical potential that correct the total number of electrons using Newton's
    method
    n_el: total number of electrons
    E: orbital energies
    beta: reference temperature
    """
    # set initial guess to be zero
    mu = 0
    i = 0
    n_p = 1. / (1. + np.exp(beta * E - mu))
    while not isclose(sum(n_p), n_el):
        n_p = 1. / (1. + np.exp(beta * E - mu))
        n_mu = sum(n_p) - self.n_occ
        dn_mu = sum(n_p**2 * np.exp(beta * E - mu))
        mu -= n_mu / dn_mu
        i += 1
        print("NEWTON PROCEDURE STEP {:d}:".format(i))
        print("chemical potential mu:{:.3f}".format(mu))
        print("n(mu):{:.3f}".format(n_mu + self.n_occ))
        if i > 100:
            print("Warning: Newtonain procedure does not converge with in 100 iterations!")
            break
    return n_p, mu
```

Listing 4.3: Explicit Newtonian procedure to determine the FD occupation number and the chemical potential at the reference temperature β

With the occupation number $n_p(\beta, \mu)$, we can determine the Fock matrix (in canonical basis) at the reference temperature as follow:

$$F_q^p(\beta) = h_q^p + \sum_{rs} (2\langle pr|qs\rangle - \langle pr|sq\rangle) D_s^r(\beta, \mu), \tag{4.17}$$

where

$$D_s^r(\beta, \mu) \equiv n_r(\beta, \mu)\delta_{rs} \tag{4.18}$$

and h_q^p is the one-eletron integral that is obtained from the `PySCF` calculations.

Step 3: Bogoliubov transform the physical electronic Hamiltonian

Next, as been described in chapter 3.2, we Bogoliubov transform the electronic Hamiltonian: $\hat{H}_{elec} \xrightarrow{\text{B.T.}} \tilde{H}_{elec} = \tilde{F}(\beta) + \tilde{V}$. The Fock matrix consists of four blocks in the squared Bogoliubov representation:

$$\tilde{F}(\beta) = \sum_{pq} \tilde{F}_{a_q}^{a_p}(\beta)\hat{a}_p^\dagger \hat{a}_q + \sum_{pq} \tilde{F}_{b_q}^{a_p}(\beta)\hat{a}_p^\dagger \hat{b}_q + \sum_{pq} \tilde{F}_{a_q}^{b_p}(\beta)\hat{b}_p^\dagger \hat{a}_q + \sum_{pq} \tilde{F}_{b_q}^{b_p}(\beta)\hat{b}_p^\dagger \hat{b}_q, \tag{4.19}$$

where

$$\begin{aligned}
\tilde{F}_{a_q}^{a_p}(\beta) &\equiv \cos\theta_p \cos\theta_q F_q^p(\beta), \\
\tilde{F}_{b_q}^{a_p}(\beta) &\equiv \cos\theta_p \sin\theta_q F_q^p(\beta), \\
\tilde{F}_{a_q}^{b_p}(\beta) &\equiv \sin\theta_p \cos\theta_q F_q^p(\beta), \\
\tilde{F}_{b_q}^{b_p}(\beta) &\equiv \sin\theta_p \sin\theta_q F_q^p(\beta).
\end{aligned} \tag{4.20}$$

As mentioned before, the trigonometric functions are associated with the FD occupation number defined in Eq. (4.15):

$$\begin{aligned} \sin\theta_p &= \sqrt{n_p(\beta)}, \\ \cos\theta_p &= \sqrt{1-n_p(\beta)}. \end{aligned} \tag{4.21}$$

The two-electron integrals consist of sixteen blocks in the squared Bogoliubov representation. ($\hat{V} \xrightarrow{\text{B.T.}} \tilde{V}$) For all blocks associated with construction operators $\hat{a}_p^\dagger$ or $\hat{a}_p$, we assign a $\cos\theta_p$ factor, while for all blocks associated with construction operators $\hat{b}_p^\dagger$ or $\hat{b}_p$, we assign a $\sin\theta_p$ factor. The explicit expression of the Bogoliubov transformed two-electron integrals are shown in appendix D.

Step 4: Perform the TFCC propagation and calculate thermal properties on-the-fly

With the Bogoliubov transformed Hamiltonian obtained from the last step:

$$\tilde{H} = \tilde{F}(\beta) + \tilde{V}, \tag{4.22}$$

we can perform the TFCC imaginary time propagation on it. The explicit TFCC EOMs reads:

$$-\langle\theta(\beta)|\,\hat{\Omega}_\mu^\dagger \frac{d\hat{T}}{d\beta}\,|\theta(\beta)\rangle = \langle\theta(\beta)|\,\hat{\Omega}_\mu^\dagger \left((\tilde{H}-\mu\tilde{N})e^{\hat{T}}\right)_{conn.}\,|\theta(\beta)\rangle\,, \tag{4.23}$$

where

$$\hat{\Omega}_\mu \equiv \{\mathbb{1}, \hat{a}_p^\dagger\hat{b}_q, \hat{a}_p^\dagger\hat{a}_q^\dagger\hat{b}_r\hat{b}_s\}, \tag{4.24}$$

$$\hat{T} = t^0\mathbb{1} + \sum_{pq} t_q^p \hat{a}_p^\dagger\hat{b}_q + \frac{1}{4}\sum_{pqrs} t_{rs}^{pq}\hat{a}_p^\dagger\hat{a}_q\hat{b}_r\hat{b}_s. \tag{4.25}$$

In Eq. (4.23), we introduce the chemical potential μ and the number operator $\tilde{N}$ in Bogoliubov representation to fix the total number of electrons along the imaginary time propagation. This is achieved based on the fact that the trace of the one-particle density matrix is a constant:

$$\mathrm{Tr}\left(\hat{D}_1(\beta)\right) = n_{el}. \tag{4.26}$$

We take the derivative over β on BHS of the equation and we get:

$$\mathrm{Tr}\left(\frac{\mathrm{d}\hat{D}_1(\beta)}{\mathrm{d}\beta}\right) = 0. \tag{4.27}$$

where $\hat{D}_1$ is the one-particle density matrix whose elements can be mapped from the cluster amplitudes:

$$d_{pq} = \cos\theta_p \sin\theta_q t_{b_q}^{a_p} + \sin\theta_p \sin\theta_q \delta_{pq}. \tag{4.28}$$

Substituting Eq. (4.28) into Eq. (4.27) and we have:

$$\sum_p \cos\theta_p \sin\theta_p \frac{\mathrm{d}t_{b_p}^{a_p}}{\mathrm{d}\beta} = 0 \tag{4.29}$$

Substitute the TFCC EOM into Eq. (4.29), we obtain the expression of the chemical potential:

$$\mu = \frac{\sum_p \cos\theta_p \sin\theta_p R_1(\tilde{H})_{pp}}{\sum_p \cos\theta_p \sin\theta_p R_1(\tilde{N})_{pp}} \tag{4.30}$$

where R_1 represents a function that implements the TFCC singles residuals. Thus, we can implement the working equations of TFCC EOMs as follow:

$$-\frac{\mathrm{d}t^0}{\mathrm{d}\beta} = R_0(\tilde{H}) \tag{4.31}$$

$$-\frac{\mathrm{d}t^1}{\mathrm{d}\beta} = R_1(\tilde{H}) - \mu R_1(\tilde{N}) \tag{4.32}$$

$$-\frac{\mathrm{d}t^2}{\mathrm{d}\beta} = R_2(\tilde{H}) - \mu R_2(\tilde{N}) \tag{4.33}$$

where, as before, R_0, R_1 and R_2 are functions that implement TFCC constant, singles, doubles residuals respectively. In practice, we implemented the three functions by calling the modified `PySCF` subroutines which can be found in appendix E. The explicit residual equations are implemented in an optimized manner according to the reference [73]. Notice that explicit equations implemented in `PySCF` are conventional spin-adapted closed shell CC EOMs. The two-body operator that has been explicitly stored are the mixed spin ($\alpha\beta$) components and other components ($\alpha\alpha$ or $\beta\beta$) can be calculated using the spin symmetry:

$$X_{rs}^{pq} = X_{RS}^{PQ} = X_{rS}^{pQ} - X_{sR}^{pQ}, \tag{4.34}$$

where we use the lower case labels to denote α spin orbitals and upper case labels to denote β spin orbitals. In the rest of the chapter, we denote all the two-body operator to be the $\alpha\beta$ components by default. We give more detailed discussion on the spin-adaptation in appendix F.

To calculate the thermal properties, we call the subroutines of the constant residual:

$$\left\langle \hat{O} \right\rangle = R_0(\tilde{O}), \tag{4.35}$$

where $\hat{O}$ is an arbitrary physical operator and $\tilde{O}$ is the corresponding Bogoliubov transformed operator ($\hat{O} \xrightarrow{\text{B.T.}} \tilde{O}$).

For example, when $\hat{O} \equiv \hat{H}_{elec}$, we obtain the thermal internal energy:

$$E(\tau) = \left\langle \left(\tilde{H} e^{\hat{T}(\tau)} \right)_{f.c.} \right\rangle. \tag{4.36}$$

If we set $\hat{O} \equiv \mathbb{1}$, we obtain the grand canonical partition function:

$$Z(\tau) \equiv e^{t^0(\tau)}. \tag{4.37}$$

Once the partition function is obtained, we can calculate the Helmholtz free energy as follow:

$$A(\tau) = -\frac{1}{\tau} \ln(Z). \tag{4.38}$$

4.1.2 Introduce the completed active space (CAS)

In this section, we introduce the implementation of the CAS-TFCC approach. There are mainly two reasons to introduce the CAS.

Firstly, unlike the conventional coupled cluster theory for ground state electronic structure, all cluster amplitudes in the TFCC approach span the full orbital space. Thus, the canonical TFCC approach that we introduce in section 4.1.1 is expensive and only feasible for small molecules. To reduce the computational cost of the TFCC approach, we develop the CAS-TFCC approach in this section. As been illustrated in Fig. 4.1, in a typical scenario, the MOs in a molecular system can be classified into three types: the core orbitals, the active orbitals and the virtual orbitals. The thermal contribution of the excited states that is associated with the excitation from the core orbitals or to the virtual orbitals can be ignored since these states are usually high-lying and the corresponding Boltzmann factors are negligible. The general idea of the CAS-TFCC approach is that we treat the core electrons as a "screening effect" to the valence electrons and form an effective Hamiltonian that is restricted within the CAS. In this way, the TFCC approach can be applied on top the effective Hamiltonian and the cluster amplitudes can be restricted within the CAS that contains active orbitals only. Thus, the computational cost of the original TFCC approach can be dramatically reduced.

Secondly, it is feasible the obtain the numerical exact thermal properties through the exact diagonalization of the CAS-full configurational interaction (FCI) Hamiltonian within the CAS and directly SOS. In this way, it is easier for us the directly compare the result obtain from the TFCC results with the numerical exact result.

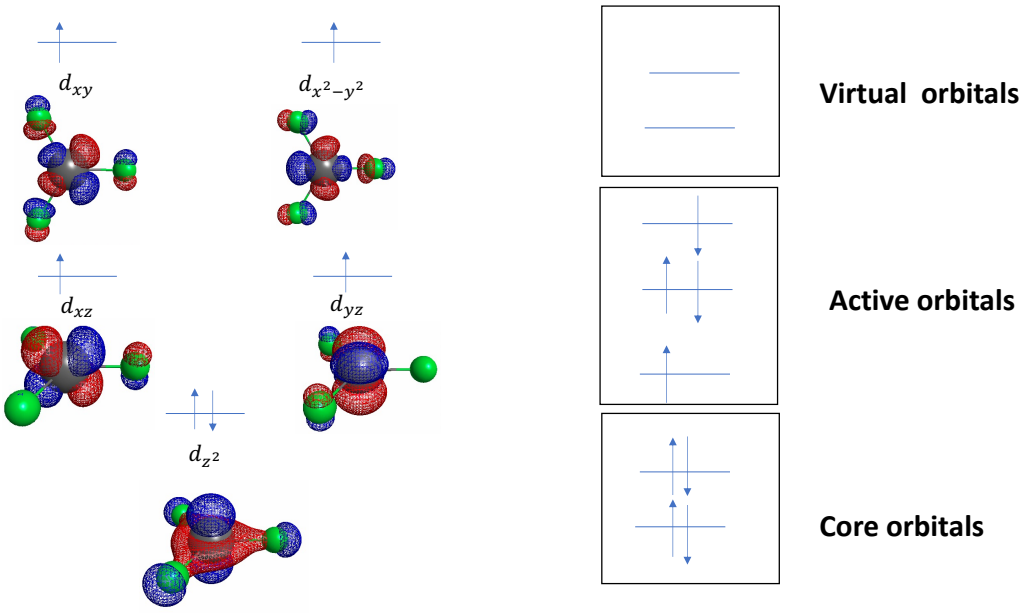


Figure 4.1: Illustration of CAS

Now, we will elaborate the explicit procedure of the CAS-TFCC approach.

Step 1: Perform CAS-SCF calculation

The starting point of the CAS-TFCC approach is the CAS-SCF calculations. We apply the Multi-configuration (MC)-SCF module in the `PySCF` to perform the calculation.

```
# geometry of molecules (in Angstrom)
N2 = 'N 0 0 0; N 0 0 2.0'

# active space of molecules (number of active spatial orbitals, number of active electrons)
CAS_N2 = (6, 6)

atom = N2
molecule = "N2"

# setup model input using gaussian-type-orbitals
molecular_HF = gto.M(
       atom=atom,  # in Angstrom
       basis='ccpvdz',
       symmetry=True,
       spin=0
)

# first run run HF calculation
mean_field = scf.RHF(molecular_HF).run()

# second run CAS-SCF on top of the HF calculation
# 6 orbital, 6 electrons
mycas = mean_field.CASSCF(CAS_HF[0], CAS_HF[1])
mycas.natorb = True
# Here mycas.mo_coeff are natural orbitals because .natorb is on.
# Note The active space orbitals have the same symmetry as the input HF
# canonical orbitals.  They are not fully sorted wrt the occpancies.
# The mcscf active orbitals are sorted only within each irreps.
mycas.kernel()
```

Listing 4.4: Example CAS-SCF calculations using `PySCF`

The example script to run CAS-SCF calculations is shown in List 4.4. We firstly input the molecular geometry and the basis set to run HF calculations. Then the CAS-SCF calculation is performed on top of the HF calculations. The additional input for the CAS-SCF calculation is the choice of active orbitals and active electrons. The `PySCF` program can automatically select the core orbitals based on the HF calculation and thus there is no need to manually specify the starting active orbital in the calculation.

Step 2: Construct the effective Hamiltonian in the model CAS

Firstly, based on the occupation number obtained from the CAS-SCF calculations, we can determine the core orbitals and the active orbitals. The orbitals that are fully occupied are core orbitals and the active orbitals are partially occupied. The explicit Python script to pick core and active orbitals are shown in List 4.5.

```python
# get occupation number for CASSCF
occupation_number = CAS_SCF.mo_occ / 2

# calculation number of orbitals
M = len(occupation_number)

# get core orbitals and active orbitals
core_orbitals = []
active_orbitals = []
for index, orbital in enumerate(occupation_number):
    if orbital == 1:
        core_orbitals.append(index)
    elif orbital > 0 and orbital < 1:
        active_orbitals.append(index)
    else:
        pass

print("core orbital labels:{:}".format(core_orbitals))
print("active orbital labels:{:}".format(active_orbitals))
```

Listing 4.5: Python script to pick core and active orbitals based on the CAS-SCF calculation

Secondly, we construct the effective one-electron integrals that take account of the contribution of the core electrons as a "mean-field" screening effect. To obtain the effective one-electron integrals, we firstly construct the core-electron density matrix:

$$D_{\alpha\beta} = \sum_{i \in core} C^*_{\alpha i} C_{\beta i}, \tag{4.39}$$

where α and β are AO labels and i is the core MO labels. Then, once the density matrix is determined, the effective one-electron integrals can be expressed as: [1]

$$h^{\alpha}_{\beta} = (h_{core})^{\alpha}_{\beta} + \sum_{\delta\gamma} (2 \langle \alpha\delta | \beta\gamma \rangle - \langle \alpha\delta | \gamma\beta \rangle) D^{\delta}_{\gamma}. \tag{4.40}$$

The explicit Python script to achieve this is shown in List 4.6.

[1] We assume that the core electrons are always in singlet states and the integrals are spin-adapted.

```python
def Cal_core_1_RDM(CI_coefficient, core_orbitals, M):
      """calculate core 1-RDM"""
      size_core = len(core_orbitals)
      RDM_1_core = np.zeros([M, M])
      for alpha, beta in it.product(range(M), repeat=2):
          for i in range(size_core):
              RDM_1_core[alpha, beta] += CI_coefficient[alpha, i] * CI_coefficient[beta, i]
      # print("core 1-RDM:\n{:}".format(RDM_1_core))

      return RDM_1_core

def Cal_one_electron_integral(h_core_AO, RDM_1_core, M, eri_AO):
    """calculate effective one electron integral in model CAS space"""
    h_core_AO_CAS = np.zeros([M, M])

    # add one-electron part
    h_core_AO_CAS += h_core_AO

    # add effective two electron part
    for a, b, c, d in it.product(range(M), repeat=4):
        h_core_AO_CAS[a, b] += RDM_1_core[c, d]*(2*eri_AO[a, b, c, d] - eri_AO[a, c, b, d])

    return h_core_AO_CAS
```

Listing 4.6: Python script to construct effective one-electron integrals

Lastly, we transform the effective one-electron integrals and two-electron integrals from AO basis to the MO basis and we pick the block that corresponds to the CAS. The explicit Python script for this is shown in List 4.7.

```
## Transform the one-electron integrals and two-electron integrals from AO basis to MO basis
nature_orbital = CAS_SCF.mo_coeff

## 1-electron integral
h_core_MO = np.einsum('pi,pq,qj->ij', nature_orbital, h_core_AO_CAS_full, nature_orbital)
print('1-electron integral (in MO basis):\n{:}'.format(h_core_MO.shape))

## 2-electron integral
eri_MO = ao2mo.incore.full(eri_AO, nature_orbital)
print("2-electron integral (in MO basis):\n{:}".format(eri_MO.shape))

# get CAS block from the full matrix

def Cal_one_electron_integral(h_core_AO, RDM_1_core, M, eri_AO):
    """calculate one electron integral in model CAS space"""
    h_core_AO_CAS = np.zeros([M, M])

    # add one-electron part
    h_core_AO_CAS += h_core_AO

    # add effective two electron part
    for a, b, c, d in it.product(range(M), repeat=4):
        h_core_AO_CAS[a, b] += RDM_1_core[c, d] * (2 * eri_AO[a, b, c, d] - eri_AO[a, c, b,
    d])

    return h_core_AO_CAS

def Cal_two_electron_integral(active_orbitals, eri_AO):
    """calculate two electron integral in model CAS space"""
    size_cas = len(active_orbitals)
    eri_AO_CAS = np.zeros([size_cas, size_cas, size_cas, size_cas])

    # calculate two electron integral is CAS model active_space
    for a, orbital_label_a in enumerate(active_orbitals):
        for b, orbital_label_b in enumerate(active_orbitals):
            for c, orbital_label_c in enumerate(active_orbitals):
                for d, orbital_label_d in enumerate(active_orbitals):
                    eri_AO_CAS[a, b, c, d] += \
                    eri_AO[orbital_label_a, orbital_label_b, \
                           orbital_label_c, orbital_label_d]

    return eri_AO_CAS

h_core_MO_CAS = Cal_Fock_ground_state(active_orbitals, h_core_MO)
eri_MO_CAS = Cal_two_electron_integral(active_orbitals, eri_MO)
```

Listing 4.7: Construct the Hamiltonian in model CAS based on effective one-electron integrals and two-electron integrals

Step 3: Perform TFCC propagation for the effective Hamiltonian in CAS

Once we construct the effective Hamiltonian in the model CAS:

$$\hat{H}_{cas} = \hat{h}_{cas} + \hat{V}_{cas}, \tag{4.41}$$

we can feed the effective one-electron integrals and two-electron integrals in the model space as input into the canonical TFCC code that is elaborated in section 4.1.1. [2]

[2]There is one tiny difference: we use CAS-SCF orbital energies rather than the HF orbital energies to define the occupation number and the Bogoliubov transformation in Eq. (4.15) and Eq. (4.21).

4.1.3 Constraints and N-representability problem

The TFCC approach for finite temperature electronic structure problem developed in this thesis is seemingly promising since it has a lot of good features including it is highly efficient (polynomial scaling), size consistent (inherited from the canonical CC theory), non-perturbative and independent of the choice of the reference state. However, it is problematic in practice. The major issue encountered is the N-representability problem which we will elaborate in this section.

By definition, the reduced density matrices (defined in Eq. (3.109)) are N-representable if they can be derived in the normalized N-particle density matrix that has all weights be positive ($\forall\lambda, w_\lambda \geq 0$). [70] The N-particle density matrix is defined as:

$$^N\hat{D} \equiv \sum_\lambda w_\lambda \left|\Psi_\lambda\right\rangle \left\langle\Psi_\lambda\right|, \tag{4.42}$$

where w_λ are weights for each eigenstate and the N-particle density matrices are normalized:

$$\sum_\lambda w_\lambda = 1. \tag{4.43}$$

The reduced density matrices are N-respresentable if:

$$\forall\lambda : w_\lambda \geq 0. \tag{4.44}$$

One of the N-representability conditions is known as the positivity condition. For an arbitrary one-particle quantum operator $\hat{o}_1$, we have:

$$\left|\Phi_\lambda\right\rangle \equiv \hat{o}_1 \left|\Psi_\lambda\right\rangle, \tag{4.45}$$

$$\left\langle\Phi_\lambda\right| \equiv \left\langle\Psi_\lambda\right| \hat{o}_1^\dagger, \tag{4.46}$$

$$\left\langle\Phi_\lambda|\Phi_\lambda\right\rangle = \left\langle\Psi_\lambda\right| \hat{o}_1^\dagger \hat{o}_1 \left|\Psi_\lambda\right\rangle \geq 0. \tag{4.47}$$

Thus, from Eq. (4.47) and Eq. (4.44), we can derive the general positivity condition as follow:

$$\mathrm{Tr}\left(\hat{o}_1^\dagger \hat{o}_1^N \hat{D}\right) = \sum_\lambda w_\lambda \left\langle\Psi_\lambda\right| \hat{o}_1^\dagger \hat{o}_1 \left|\Psi_\lambda\right\rangle = \sum_\lambda w_\lambda \left\langle\Phi_\lambda|\Phi_\lambda\right\rangle \geq 0 \tag{4.48}$$

Unfortunately, the positivity conditions are not automatically hold when we perform imaginary time propagation in the TFCC approach for electronic structure problems. In general, the reduced density matrices are not N-representable in the TFCC approach. To resolve the N-representability problem, we need to apply additional constraints to the TFCC EOMs. In the rest part of this section, we will elaborate our attempts to resolve the N-representability problems by systematically applying constraints.

Constraints one: symmetrize the thermal reduced density matrices

First of all, the most apparent constraint is that the physical thermal reduced density

matrices are supposed to be Hermitian:

$$\boldsymbol{D}_\mu = \boldsymbol{D}_\mu^\dagger. \tag{4.49}$$

We can enforce this condition by symmetrize the physical thermal reduced density matrices:

$$\boldsymbol{D}_\mu^{'} = \frac{1}{2}(\boldsymbol{D}_\mu + \boldsymbol{D}_\mu^\dagger). \tag{4.50}$$

We apply Eq. (4.50) to symmetrize the one-particle and two-particle thermal reduced density matrices and inversely map to the cluster amplitude. The explicit Python script to implement these constraints are shown in List 4.8.

```python
def _symmetrize_density_matrix(self, RDM_1, RDM_2):
    """symmetrize 1 and 2-RDM and mapping them to T amplitude"""
    def symmetrize_RDM_1(RDM_1):
        """symmetrize 1-RDM"""
        RDM_1_sym = np.zeros_like(RDM_1)
        RDM_1_sym += RDM_1
        RDM_1_sym += RDM_1.transpose()
        RDM_1_sym *= 0.5
        return RDM_1_sym

    def symmetrize_RDM_2(RDM_2):
        """symmetrize 2-RDM"""
        RDM_2_sym = np.zeros_like(RDM_2)
        RDM_2_sym += RDM_2
        RDM_2_sym += RDM_2.transpose(2, 3, 0, 1)
        RDM_2_sym *= 0.5
        return RDM_2_sym

    def map_t_1_from_RDM(RDM_1):
        """map T_1 amplitude from symmetrized RDM_1"""
        T_1 = np.zeros_like(RDM_1)
        T_1 += RDM_1
        T_1 -= np.einsum('p,q,pq->pq', self.sin_theta, self.sin_theta, np.eye(self.M))
        T_1 /= np.einsum('q,p->pq', self.cos_theta, self.sin_theta)
        return T_1

    def map_t_2_from_RDM(RDM_1, RDM_2):
        """map T_2 amplitude from symmetrized RDM_1 and RDM_1"""
        T_2 = np.zeros_like(RDM_2)
        T_2 += RDM_2
        T_2 -= 2 * np.einsum('pr,qs->pqrs', RDM_1, RDM_1)
        T_2 += np.einsum('ps,qr->pqrs', RDM_1, RDM_1)
        T_2 /= np.einsum('r,s,p,q->pqrs', self.cos_theta, self.cos_theta, self.sin_theta,
    self.sin_theta)
        return T_2

    # symmetrize density matrix
    RDM_1_sym = symmetrize_RDM_1(RDM_1)
    RDM_2_sym = symmetrize_RDM_2(RDM_2)

    # map T amplitude from symmetrize 1-RDM and 2-RDM
    T_1_sym = map_t_1_from_RDM(RDM_1_sym)
    T_2_sym = map_t_2_from_RDM(RDM_1_sym, RDM_2_sym)

    # check if the physcial rdms are symmetrized as expected
    assert np.allclose(RDM_1_sym, RDM_1_sym.transpose())
    assert np.allclose(RDM_2_sym, RDM_2_sym.transpose(2, 3, 0, 1))

    return RDM_1_sym, RDM_2_sym, T_1_sym, T_2_sym
```

Listing 4.8: Python script that implements constraint one

Constraint two: set physical boundary of one-body reduced density matrix (1-RDM) and correct the total number of electrons

As we know, if the 1-RDM is N-representable, its corresponding eigenvalue should be between 0 and 1. Thus, we introduce the following constraint: If the eigenvalue of 1-RDM become negative, fix it to be zero and if the eigenvalue of 1-RDM is above 1, fix it to be 1. The singles cluster amplitude is determined by inversely mapping from the corrected 1-RDM. After that, we apply an algorithm to correct the total number of the electrons. The explicit Python script to implement this constraint is shown in List 4.9.

```python
def _correct_occupation_number(n_el, RDM_1):
    """correct occupation number from 1-RDM"""
    # diagonalize 1-RDM to get occupation number and natural orbitals
    occupation_number, natural_orbital = np.linalg.eigh(RDM_1)
    # set physical boundary of the occupation number
    for index, N_occ in enumerate(occupation_number):
        if N_occ > 1:
            occupation_number[index] = 1
        if N_occ < 0:
            occupation_number[index] = 0

    # correct total number of electron
    tmp = occupation_number * (np.ones_like(occupation_number) - occupation_number)
    X = sum(occupation_number)
    Y = sum(tmp)
    L_lambda = (n_el - X) / Y # n_el is the total number of electrons
    occupation_number_correct = occupation_number + L_lambda * tmp

    # transfrom the corrected occupation number to the corrected 1-RDM through orbital rotation
    RDM_1_correct = np.dot(natural_orbital, np.dot(np.diag(occupation_number_correct), natural_orbital.transpose()))

    # reverse mapping the correct 1-RDM to T_1 amplitude
    T_1_correct = np.zeros_like(RDM_1_correct)
    T_1_correct += RDM_1_correct
    T_1_correct -= np.einsum('p,q,pq->pq', self.sin_theta, self.sin_theta, np.eye(self.M))
    T_1_correct /= np.einsum('q,p->pq', self.cos_theta, self.sin_theta)

    return occupation_number_correct, RDM_1_correct, T_1_correct
```

Listing 4.9: Python script that implements constraint two

Constraint three: positivity constraint for the direct two-body cumulant C_{pQ}^{pQ}

We firstly derive the positivity constraint for two-body cumulant C_{pQ}^{pQ} that has mixed $(\alpha\beta)$ spin components. Starting from the positivity condition defined in Eq. (4.48). By setting $\hat{o}_1 \equiv \hat{Q}\hat{p}$, we derive the P-condition:

$$\left\langle \hat{p}^\dagger \hat{Q}^\dagger \hat{Q} \hat{p} \right\rangle \geq 0. \tag{4.51}$$

By setting $\hat{o}_1 \equiv \hat{Q}^\dagger \hat{p}^\dagger$, we derive the Q-condition:

$$\left\langle \hat{p} \hat{Q} \hat{Q}^\dagger \hat{p}^\dagger \right\rangle \geq 0. \tag{4.52}$$

By setting $\hat{o}_1 \equiv \hat{Q}^\dagger \hat{p}$ or $\hat{o}_1 \equiv \hat{Q}\hat{p}^\dagger$, we derive the G-condition:

$$\left\langle \hat{p}^\dagger \hat{Q} \hat{Q}^\dagger \hat{p} \right\rangle \geq 0, \tag{4.53}$$

$$\left\langle \hat{p} \hat{Q}^\dagger \hat{Q} \hat{p}^\dagger \right\rangle \geq 0. \tag{4.54}$$

Making use of the general expression of the thermal properties in the TFCC theory

($\left\langle \hat{O} \right\rangle = \left\langle (\hat{O}e^{\hat{T}})_{f.c.} \right\rangle$), we can derive a set of P, Q, G cumulants as:

$$P^{pQ}_{rS} \equiv \left\langle \hat{p}^\dagger \hat{Q}^\dagger \hat{S} \hat{r} \right\rangle = C^{pQ}_{rS} + d^p_r d^Q_S \tag{4.55}$$

$$Q^{pQ}_{rS} \equiv \left\langle \hat{p} \hat{Q} \hat{S}^\dagger \hat{r}^\dagger \right\rangle = C^{pQ}_{rS} + \bar{d}^p_r \bar{d}^Q_S \tag{4.56}$$

$$G1^{pQ}_{rS} \equiv \left\langle \hat{p} \hat{Q}^\dagger \hat{S} \hat{r}^\dagger \right\rangle = -C^{pQ}_{rS} + \bar{d}^p_r d^Q_S \tag{4.57}$$

$$G2^{pQ}_{rS} \equiv \left\langle \hat{p}^\dagger \hat{Q} \hat{S}^\dagger \hat{r} \right\rangle = -C^{pQ}_{rS} + \bar{d}^Q_S d^p_r \tag{4.58}$$

where

$$C^{pQ}_{pQ} \equiv \cos\theta_p \cos\theta_Q \sin\theta_p \sin\theta_Q t^{a_p a_Q}_{b_p b_Q}, \tag{4.59}$$

$$d^p_q \equiv \cos\theta_p \sin\theta_q t^{a_p}_{b_q} + \sin\theta_p \sin\theta_q \delta_{pq}, \tag{4.60}$$

$$\bar{d}^p_p \equiv \delta_{pq} - d^p_q. \tag{4.61}$$

The positivity conditions in Eq. (4.51), Eq. (4.52), Eq. (4.53) and Eq. (4.54) can be obtained by taking the diagonal elements of the P,Q,G cumlants in Eq. (4.55), Eq. (4.56), Eq. (4.57) and Eq. (4.58):

$$P^{pQ}_{pQ} \equiv \left\langle \hat{p}^\dagger \hat{Q}^\dagger \hat{Q} \hat{p} \right\rangle = C^{pQ}_{pQ} + n_p n_Q \tag{4.62}$$

$$Q^{pQ}_{pQ} \equiv \left\langle \hat{p} \hat{Q} \hat{Q}^\dagger \hat{p}^\dagger \right\rangle = C^{pQ}_{pQ} + \bar{n}_p \bar{n}_Q \tag{4.63}$$

$$G1^{pQ}_{pQ} \equiv \left\langle \hat{p}^\dagger \hat{Q} \hat{Q}^\dagger \hat{p} \right\rangle = -C^{pQ}_{pQ} + n_p \bar{n}_Q \tag{4.64}$$

$$G2^{pQ}_{pQ} \equiv \left\langle \hat{p} \hat{Q}^\dagger \hat{Q} \hat{p}^\dagger \right\rangle = -C^{pQ}_{pQ} + \bar{n}_p n_Q \tag{4.65}$$

,where $n_p \equiv d^p_p$ and $\bar{n}_p \equiv \bar{d}^p_p$. Substituting Eq. (4.62), Eq. (4.63), Eq. (4.64) and Eq. (4.65) into Eq. (4.51), Eq. (4.52), Eq. (4.53) and Eq. (4.54), we can derive the inequalities for the direct cumulant C^{pQ}_{pQ}:

$$C^{pQ}_{pQ} + n_p n_Q \geq 0, \tag{4.66}$$

$$C^{pQ}_{pQ} + \bar{n}_p \bar{n}_Q \geq 0, \tag{4.67}$$

$$-C^{pQ}_{pQ} + n_p \bar{n}_Q \geq 0, \tag{4.68}$$

$$-C^{pQ}_{pQ} + \bar{n}_p n_Q \geq 0. \tag{4.69}$$

From the inequalities in Eq. (4.66), Eq. (4.67), Eq. (4.68) and Eq. (4.69), we can derive a physical boundary of the two-body direct cumulant (C^{pq}_{pq}):

$$-[\min(n_p n_Q, \bar{n}_p \bar{n}_Q)] \leq C^{pQ}_{pQ} \leq min(n_p \bar{n}_Q, n_Q \bar{n}_p) \tag{4.70}$$

This bound can be enforced by the Python script shown in List 4.10.

```python
def _correct_two_body_density_matrix(self, RDM_1, T_2):
    """implement correction to 2-RDM that satisfy N-representability condition"""
    def cal_upper_bound(diag_1_RDM, diag_1_RDM_bar):
        """calculate upper bound of two body cumulant"""
        upper_bound = np.zeros([self.M, self.M])

        for p, q in it.product(range(self.M), repeat=2):
            upper_bound[p, q] = min(diag_1_RDM[p] * diag_1_RDM_bar[q], diag_1_RDM[q] *
    diag_1_RDM_bar[p])

        return upper_bound

    def cal_lower_bound(diag_1_RDM, diag_1_RDM_bar):
        """calculate upper bound of two body cumulant"""
        lower_bound = np.zeros([self.M, self.M])

        for p, q in it.product(range(self.M), repeat=2):
            lower_bound[p, q] = -min(diag_1_RDM[p] * diag_1_RDM[q], diag_1_RDM_bar[p] *
    diag_1_RDM_bar[q])

        return lower_bound

    # evaluate n_p and 1 - n_p
    diag_1_RDM = np.diag(RDM_1)
    diag_1_RDM_bar = np.ones_like(diag_1_RDM) - diag_1_RDM

    # evaluate two body cumulant
    C_2 = self._calculate_two_body_direct_cumulant(T_2)

    # evaulate lower bound
    lower_bound = cal_lower_bound(diag_1_RDM, diag_1_RDM_bar)

    # evaluate upper bound
    upper_bound = cal_upper_bound(diag_1_RDM, diag_1_RDM_bar)

    # correct two body cumulant if it exceed the physical boundary
    for p, q in it.product(range(self.M), repeat=2):
        if C_2[p, q] > upper_bound[p, q]:
            C_2[p, q] = upper_bound[p, q]
        elif C_2[p, q] < lower_bound[p, q]:
            C_2[p, q] = lower_bound[p, q]
        else:
            pass

    # map matrix element of C_2 to T_2
    T_2_correct = C_2 / np.einsum('p,q,p,q->pq', self.cos_theta, self.cos_theta, self.
    sin_theta, self.sin_theta)

    return T_2_correct
```

Listing 4.10: Python script that implements constraint three

Constraint four: positivity constraints for the exchange cumulant C_{qP}^{pQ}

As in Eq. (4.51), Eq. (4.52), Eq. (4.53) and Eq. (4.54), the corresponding same spin ($\alpha\alpha$) components should also be positive:

$$\left\langle \hat{p}^\dagger \hat{q}^\dagger \hat{q} \hat{p} \right\rangle \geq 0, \tag{4.71}$$

$$\left\langle \hat{p} \hat{q} \hat{q}^\dagger \hat{p}^\dagger \right\rangle \geq 0, \tag{4.72}$$

$$\left\langle \hat{p}^\dagger \hat{q} \hat{q}^\dagger \hat{p} \right\rangle \geq 0, \tag{4.73}$$

$$\left\langle \hat{p} \hat{q}^\dagger \hat{q} \hat{p}^\dagger \right\rangle \geq 0. \tag{4.74}$$

Making using of the spin symmetry and the constraints P,Q,G cumulants for $\alpha\beta$ components (given in Eq. (4.62), Eq. (4.63), Eq. (4.64) and Eq. (4.65)), we can derive the corresponding constraints for the $(\alpha\alpha)$ components:

$$\left\langle \hat{p}^\dagger \hat{q}^\dagger \hat{q} \hat{p} \right\rangle = P_{pQ}^{pQ} - P_{qP}^{pQ} \geq 0, \tag{4.75}$$

$$\left\langle \hat{p} \hat{q} \hat{q}^\dagger \hat{p}^\dagger \right\rangle = Q_{pQ}^{pQ} - Q_{qP}^{pQ} \geq 0, \tag{4.76}$$

$$\left\langle \hat{p}^\dagger \hat{q} \hat{q}^\dagger \hat{p} \right\rangle = G1_{pQ}^{pQ} - G1_{qP}^{pQ} \geq 0, \tag{4.77}$$

$$\left\langle \hat{p} \hat{q}^\dagger \hat{q} \hat{p}^\dagger \right\rangle = G2_{pQ}^{pQ} - G2_{qP}^{pQ} \geq 0. \tag{4.78}$$

Substituting Eq. (4.55) and Eq. (4.56) into Eq. (4.75) and Eq. (4.76) we can derive the upper bound of the exchange cumulant:

$$C_{qP}^{pQ} \leq C_{pQ}^{pQ} + min(d_p^p d_q^q - d_q^p d_p^q, \bar{d}_p^p \bar{d}_q^q - \bar{d}_q^p \bar{d}_p^q). \tag{4.79}$$

Substituting Eq. (4.57) and Eq. (4.58) into Eq. (4.77) and Eq. (4.78) we can derive the lower bound of the exchange cumulant:

$$C_{qP}^{pQ} \geq C_{pQ}^{pQ} + \max(\bar{d}_q^p d_p^q, d_q^p \bar{d}_p^q) - \bar{d}_p^p d_q^q. \tag{4.80}$$

The explicit Python script to implement this constraint is shown in List 4.11.

```python
def _correct_exchange_two_body_cumulant(self, RDM_1, T_2, natural_orbital_flag=True):
    """correct exchange part of the two body cumulant when it exceed the physical boundary
    """
    def cal_upper_bound():
        """calculate upper bound of the exchange cumulant"""
        upper_bound = np.zeros([self.M, self.M])
        upper_bound += C_2_direct

        # min of the two matrices
        X = np.einsum('pp,qq->pq', d_1, d_1) - np.einsum('pq,qp->pq', d_1, d_1)
        Y = np.einsum('pp,qq->pq', d_1_bar, d_1_bar) - np.einsum('pq,qp->pq', d_1_bar,
    d_1_bar)

        upper_bound += np.minimum(X, Y)


        return upper_bound

    def cal_lower_bound():
        """calculate lower bound of the exchange cumulant"""
        lower_bound = np.zeros([self.M, self.M])
        lower_bound += C_2_direct
        lower_bound -= np.einsum('pp,qq->pq', d_1, d_1_bar)

        X = np.einsum('pq,qp->pq', d_1_bar, d_1)
        Y = np.einsum('pq,qp->pq', d_1, d_1_bar)
        lower_bound += np.maximum(X, Y)

        return lower_bound



    # calculate two body cumulant
    C_2_direct = self._calculate_two_body_direct_cumulant(T_2)
    C_2_exchange = self._calculate_two_body_exchange_cumulant(T_2)

    # transform cumulants in natural orbital basis
    if natural_orbital_flag:
        n, v = np.linalg.eigh(RDM_1)
        C_2_direct = np.einsum('lp,lk,kq->pq', v, C_2_direct, v)
        C_2_exchange = np.einsum('lp,lk,kq->pq', v, C_2_exchange, v)
        d_1 = np.diag(n)

    else:
        d_1 = RDM_1

    d_1_bar = np.eye(self.M) - d_1

    # calculate upper bound
    upper_bound = cal_upper_bound()

    # calculate lower bound
    lower_bound = cal_lower_bound()

    # set constraint on two body exchange cumulant when it exceed the physical boundary
    for p, r in it.product(range(self.M), repeat=2):
        if C_2_exchange[p, r] > upper_bound[p, r]:
            C_2_exchange[p, r] = upper_bound[p, r]
        elif C_2_exchange[p, r] < lower_bound[p, r]:
            C_2_exchange[p, r] = lower_bound[p, r]
        else:
            pass

    # inverse transform to the MO basis
    if natural_orbital_flag:
        C_2_exchange = np.einsum('pl,lk,qk->pq', v, C_2_exchange, v)

```

```
    # reverse map C_2_exchange to T_2
    T_2_exchange = C_2_exchange / np.einsum('p,q,q,p->pq', self.cos_theta, self.sin_theta,
    self.cos_theta, self.sin_theta)

    return T_2_exchange
```

Listing 4.11: Python script that implements constraint four

In this way, we manage to describe the N-representability problem and our attempts to resolve the problem by systematically applying constraints to the thermal reduced density matrices. In section 4.2, we will show some results of the thermal properties calculations applying the TFCC approach described in this section. We will show that the N-representability conditions play important roles for the TFCC approach to get accurate result for thermal properties calculations. Although the approach fail to produce satisfactory results for real molecular compounds, we gained insights through the analysis of the results of these numerical calculations.

4.2 Result and discussion

4.2.1 Test on model magnetic systems

We firstly test the TFCC approach on the model magnetic systems. The Hamiltonian of the model magnetic system is defined as:

$$\hat{H}_{magnet} \equiv \sum_{p} \epsilon_p E_p^p + \sum_{pq} V_{pq}^{pq} E_{pq}^{pq} \tag{4.81}$$

where

$$V_{pq}^{pq} = \begin{cases} V_{ontop}, if\ p = q, \\ \frac{V_{coup}}{|p-q|}, if\ p \neq q, \end{cases} \tag{4.82}$$

and E_p^p and E_{pq}^{pq} are the unitary group generators defined in Eq. (F.2) and Eq. (F.3).

The model magnetic Hamiltonian in Eq. (4.81) can be regarded as a special form of the full electronic Hamiltonian where the two-electron integrals are diagonal and the reference Slater determinant is its eigenfunction. The model is dictated by three parameters: ϵ_p, V_{coup} and V_{ontop}. Fig. 4.2 gives an intuitive picture of these three parameters: ϵ_p models the orbital energies of one-electron non-interacting term in the model Hamiltonian.[3] V_{coup} models the Coulomb interaction between different electrons. V_{ontop} models the additional repulsion interaction when there is a pair of α and β electrons on a same spatial orbital.

[3]We further assume that the orbital energies have equal spacing.

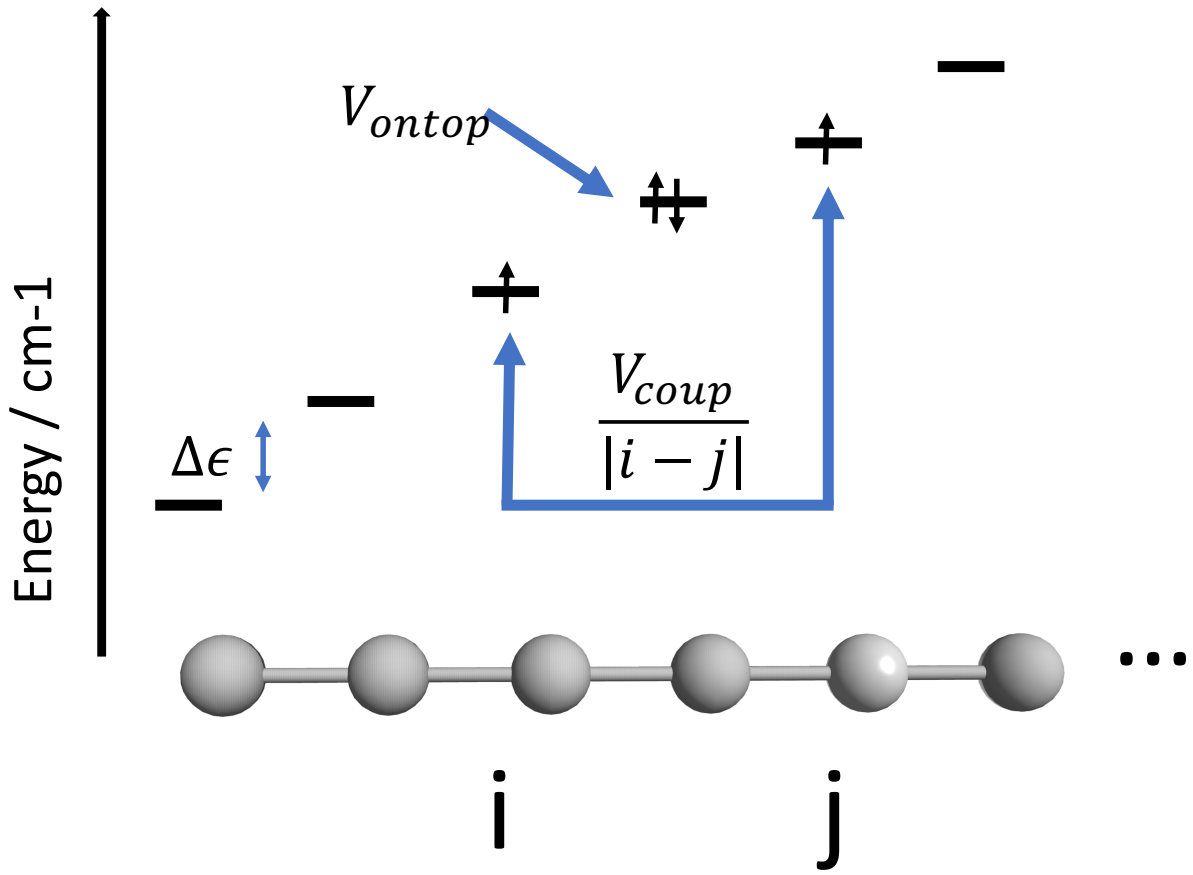


Figure 4.2: A diagram illustrates the three parameters in the model magnetic Hamiltonian in Eq. (4.81)

We tested two of magnetic models: weakly coupling model and strongly coupling model, with the model parameters listed Table 4.1.[4]

Parameters (cm^{-1})	weakly coupling model	strongly coupling model
$\Delta\epsilon$	20.0	20.0
V_{ontop}	10.0	10.0
V_{coup}	10.0	20.0

Table 4.1: List of model parameters for the weakly coupling and strongly coupling models.

We feed these model parameters into the TFCC approach that is described in section 4.1.1 to calculate the thermal properties.

In Fig. 4.3, we show the plot of thermal properties (internal energy, entropy, specific heat and occupation number) for the weakly coupling model. The TFCC result is benchmarked

[4]There 6 electrons (3 α and 3 β) and 6 spatial orbitals in both models.

with the SOS approach. [5] As we can see, the TFCC approach has good agreement with the SOS approach for the weakly coupling model. Meanwhile, we also calculate the minimum of the P,Q,G cumulants (described in left hand side of Eq. (4.66), Eq. (4.67), Eq. (4.68) and Eq. (4.69)) as functions of temperature as shown in Fig. 4.4. All the three minimum cumulants stay positive at all temperatures, which means that the P,Q,G conditions hold along the imaginary time propagation. This is expected since the thermal reduced density matrices are supposed to be N-representable to obtain accurate results for thermal properties.

In Fig. 4.5, we show the plot of thermal properties (internal energy, entropy, specific heat and occupation number) for the strongly coupling model. Unlike the weakly coupling case, the TFCC approach has large deviations with the SOS approach for the strongly coupling model. The entropy seems more accurate than the thermal internal energy at higher temperature which can be explained that there are some cancellation of errors between the Helmholtz free energy and the thermal internal energy when calculating the entropy ($S = \frac{A-U}{T}$). Subsequently, as shown in Fig. 4.6, the P,Q,G conditions no longer hold along the imaginary time propagation. Interestingly, the TFCC approach fails immediately at the point when the P,Q,G condition is violated. [6]

[5] The program is developed by Nooijen group.

[6] The numerical integration step has been test to be converge and sudden change at low temperature is due to a surge of the chemical potential which probe that the density matrices are not N-representable at low temperature.

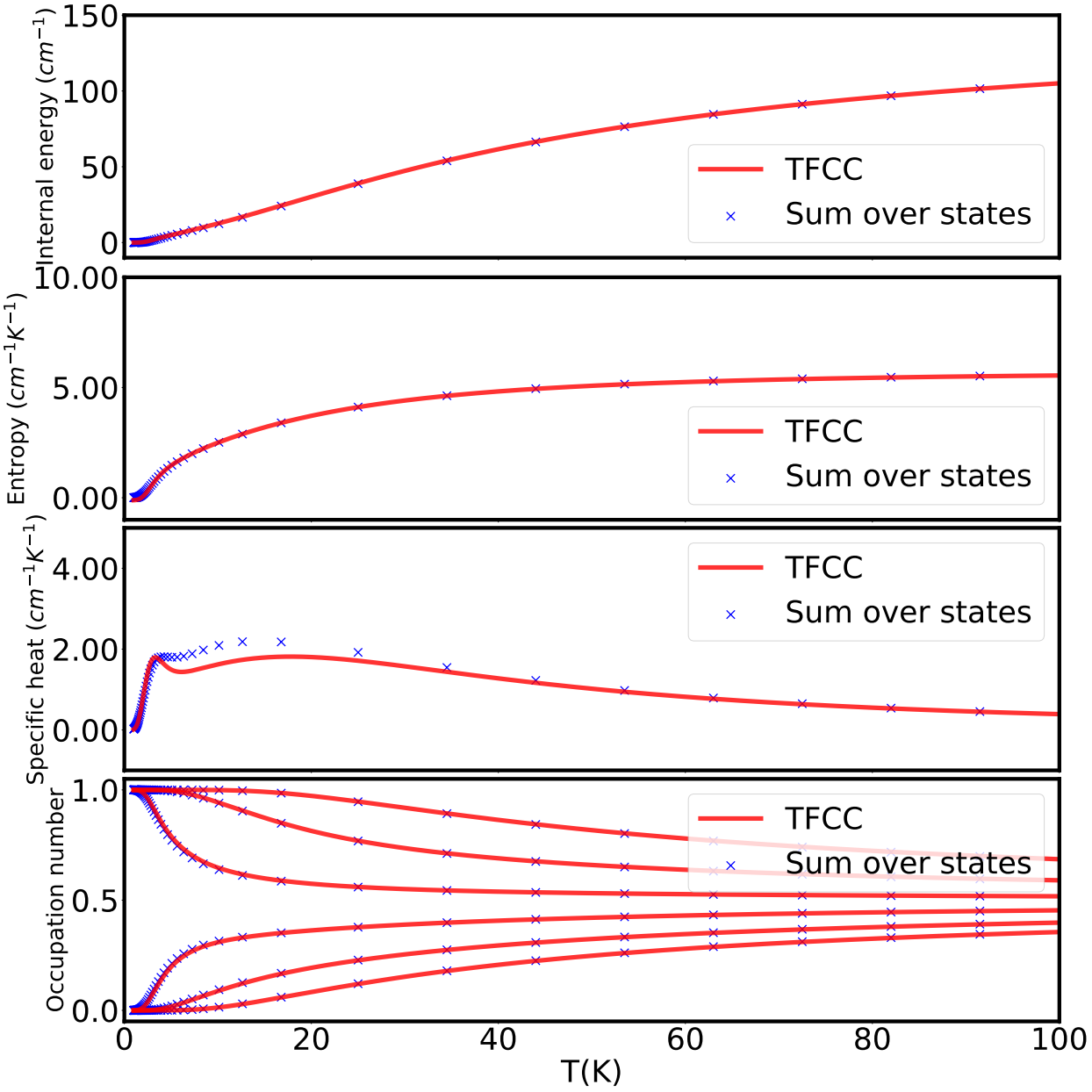


Figure 4.3: Plot of the thermal properties for the weakly coupling model

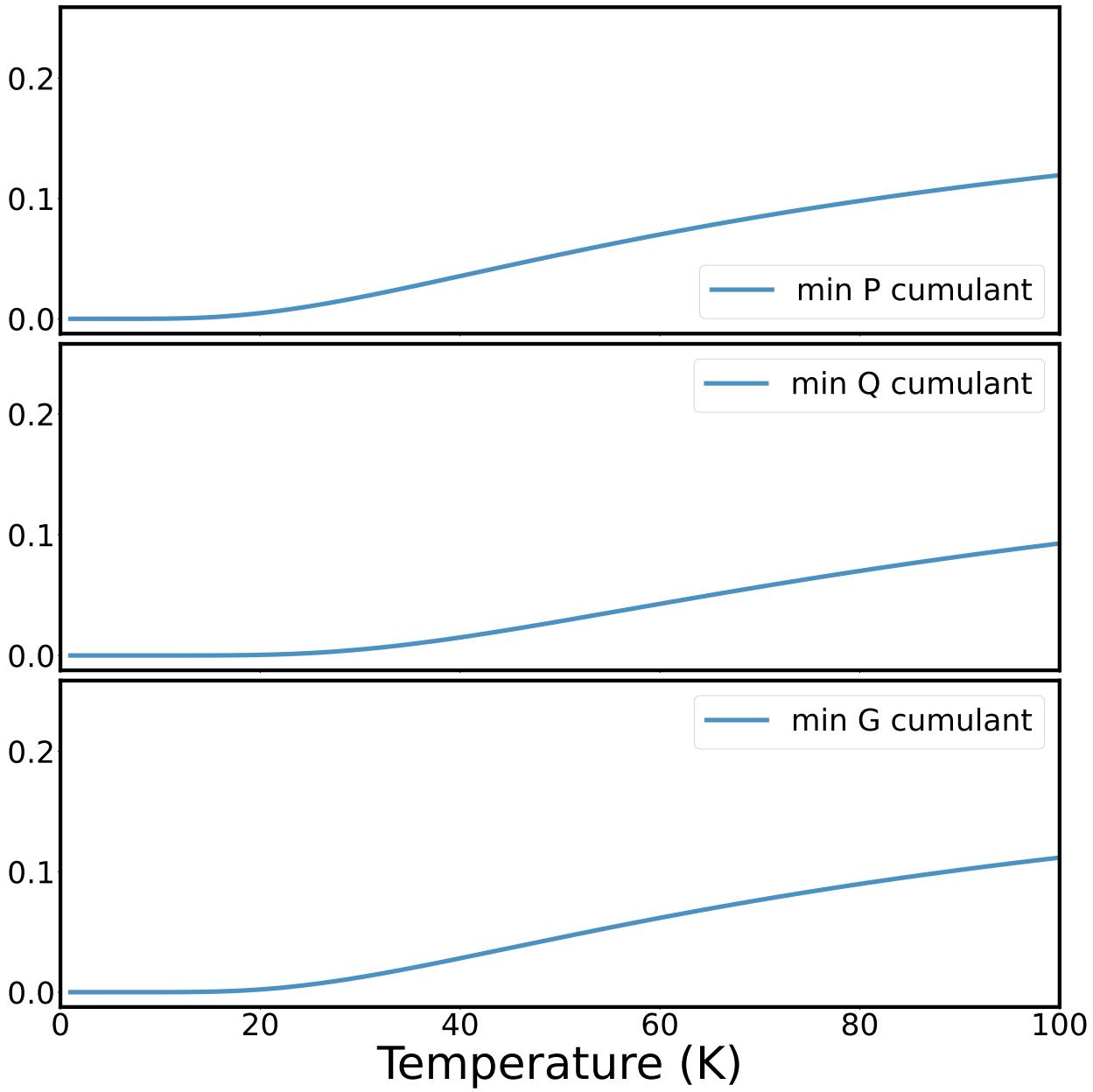


Figure 4.4: Plot of the minimum matrix elements of P, Q, G cumulants as functions of temperature for the weakly coupling model

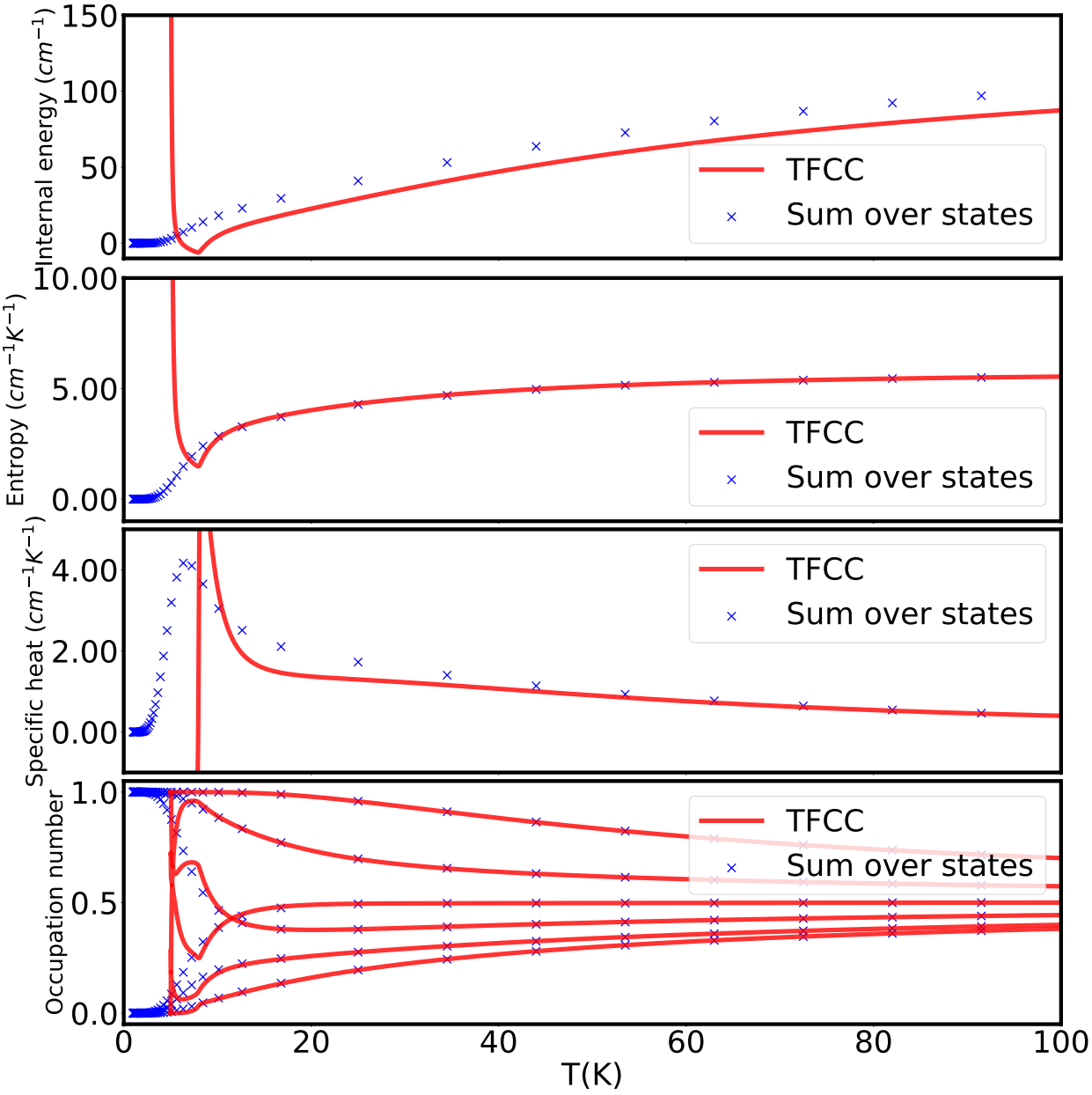


Figure 4.5: Plot of the thermal properties for the strongly coupling model

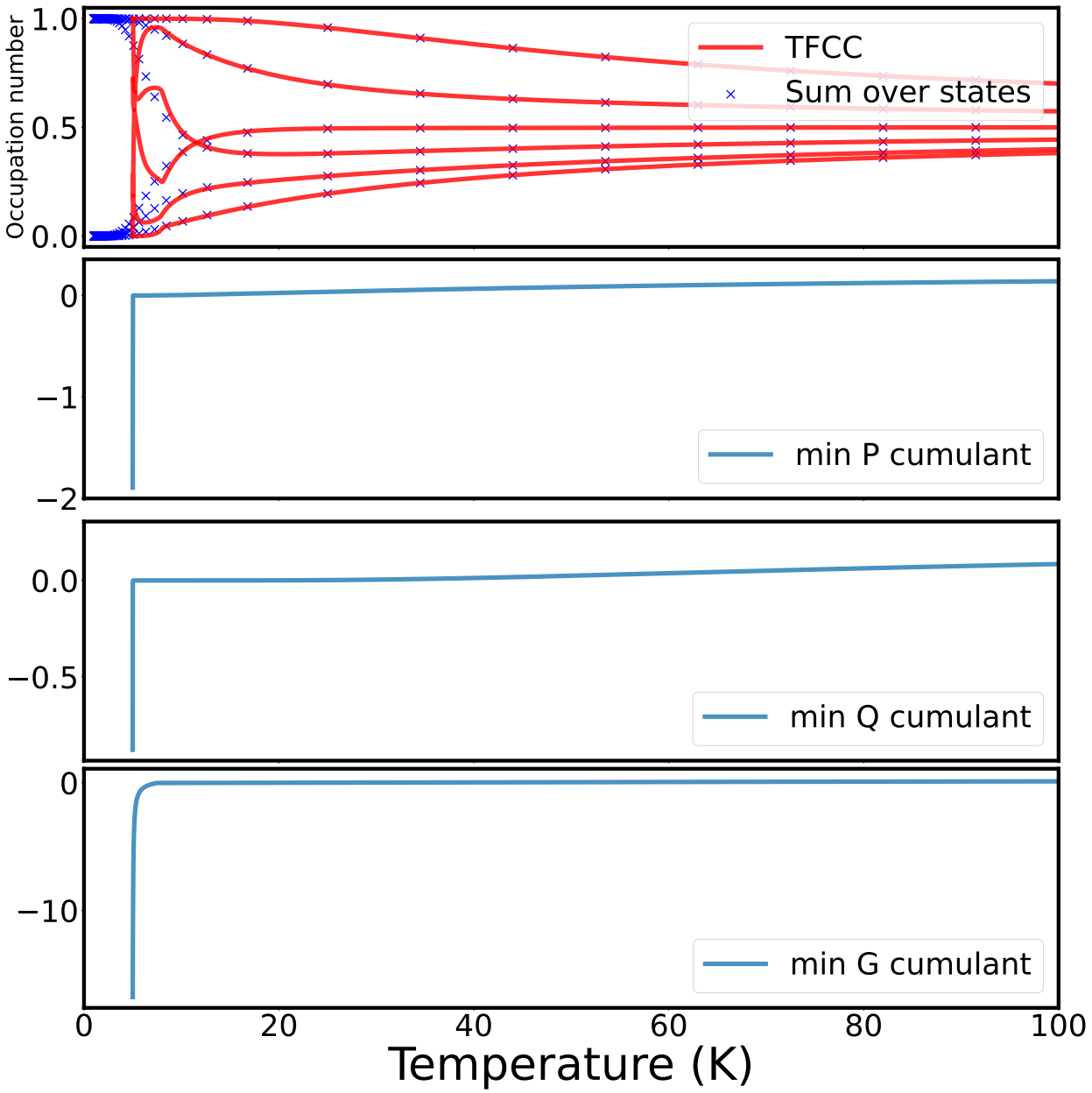


Figure 4.6: Plot of the occupation number and minimum matrix elements of P, Q, G cumulants as functions of temperature for the strongly coupling model

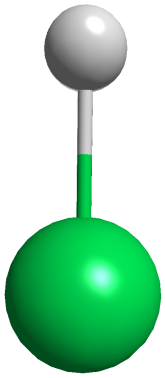
Based on our investigations, we demonstrate that the N-representability conditions serve as criteria for assessing whether the TFCC approach can yield accurate results. We also found that the seemingly promising TFCC method fails in strongly coupled models without additional N-representability constraints. In section 4.2.2, we will evaluate a few small molecular compounds while applying all the N-representability constraints discussed in in section 4.1.3. Our findings will indicate that the positivity conditions alone are insufficient for achieving accurate results regarding the thermal properties of these compounds.

4.2.2 Test on small molecular systems

In this section, we test the TFCC approach on a few small molecular compounds. We will firstly exam the canonical TFCC approach described in section 4.1.1 and then test the CAS-TFCC that is described in section 4.1.2. In both approaches, we compare the results with N-representability constraints described in section 4.1.3 and that without the constraints.

1. TFCC approach in full orbital space

Fig. 4.7 and Fig. 4.8 show the structure and coordinates of the two small molecular compounds (HF molecule and H_2O molecule) that we investigated.

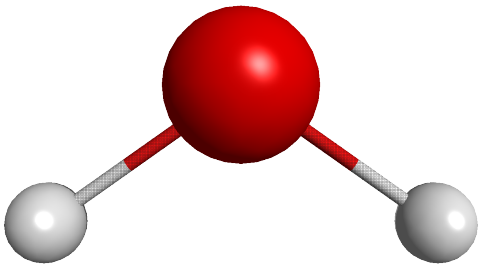


(a)

Atom	x (Å)	y (Å)	z (Å)
H	0.00	0.00	0.00
F	0.00	0.00	1.10

(b)

Figure 4.7: Representation of (a) structure (b) coordinates for HF molecule.



(a)

Atom	x (Å)	y (Å)	z (Å)
O	0.00	0.071	0.00
H	−0.90	−0.56	0.00
H	0.90	−0.56	0.00

(b)

Figure 4.8: Representation of (a) structure (b) coordinates for H_2O molecule.

We perform the TFCC imaginary time propagations (with cluster amplitudes truncate at singles and doubles) for both molecules (1) without the N-representability constraints (2) with the N-representability constraints. We also run calculations with cluster amplitude truncate at singles which is equivalent to the thermal HF calculations. We calculate the thermal properties: (1) thermal internal energy (2) occupation number on-the-fly. In both molecules, we used the 6-31g basis. The zero temperature limit of the thermal internal energy obtained from the TFCC calculation is compared with the CCSD(T) ground state energy.

Fig. 4.9 and Fig. 4.10 display the thermal internal energy plots as functions of temperature for HF and H_2Omolecules obtained using the TFCC approach. For both molecules, the results without N-representability constraints exhibit an unphysical trend: as the temperature decreases, the energy initially drops to a minimum and then begins to rise. In contrast, the results with constraints show that the energy remains constant after reaching its minimum. The zero-temperature limit without constraints yields a ground state energy slightly higher than that with constraints for both molecules. However, as shown in Table 4.2, the ground state energies from both approaches (with and without constraints) are significantly lower than the CCSD(T) results for both molecules, with energy differences far exceeding the threshold for chemical accuracy (0.016 Hartree). Additionally, we present the thermal HF results as a mean-field approximation. At higher temperatures, the TFCC results converge closer to the mean-field results, but the deviation increases as the temperature drops for both molecules. As expected, the mean-field approximation fails to provide an accurate ground state energy at the zero-temperature limit which is expected since it does not incorporate the electron correlation effect.

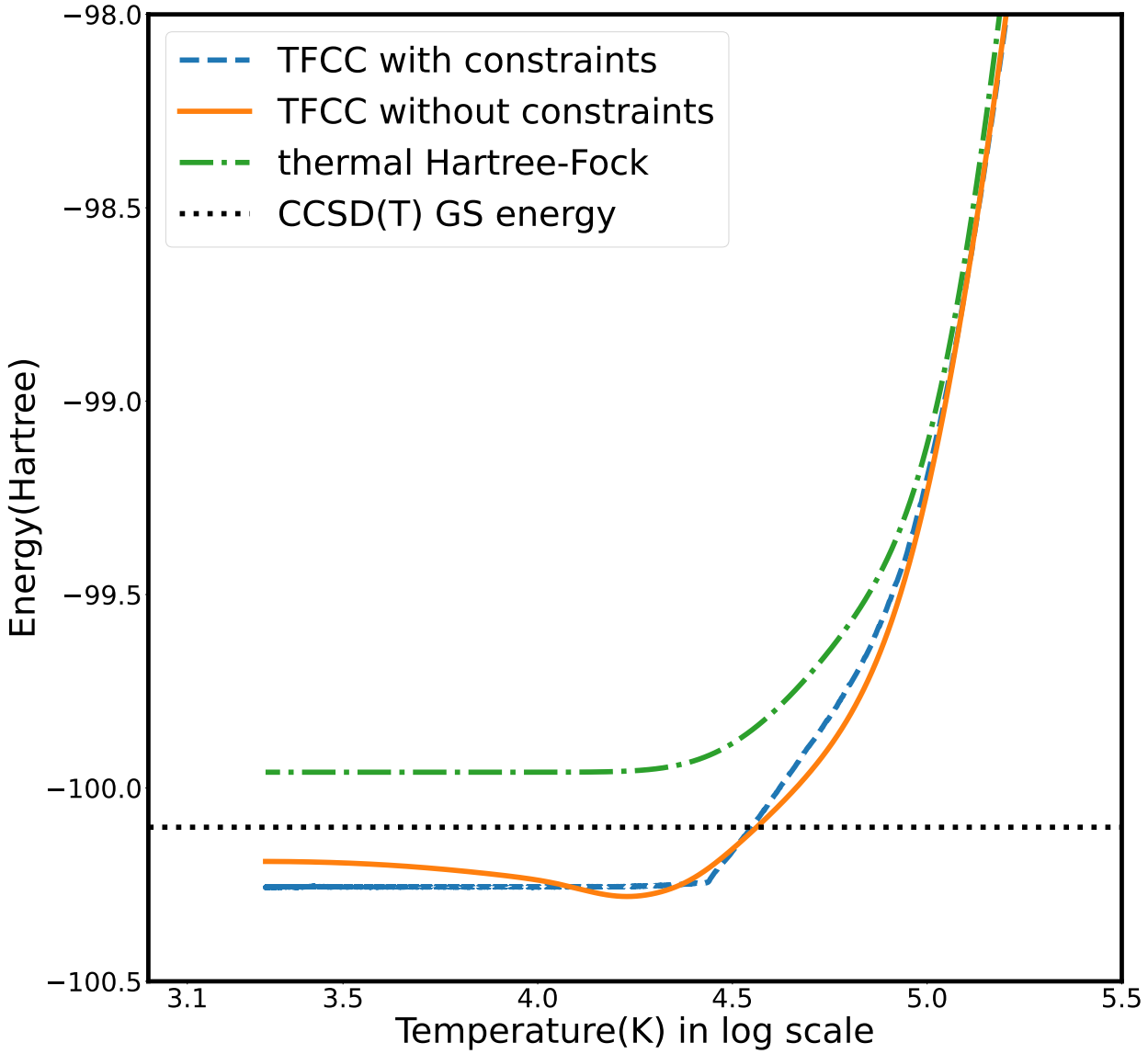


Figure 4.9: Plot of thermal internal energy for HF (6-31g basis)

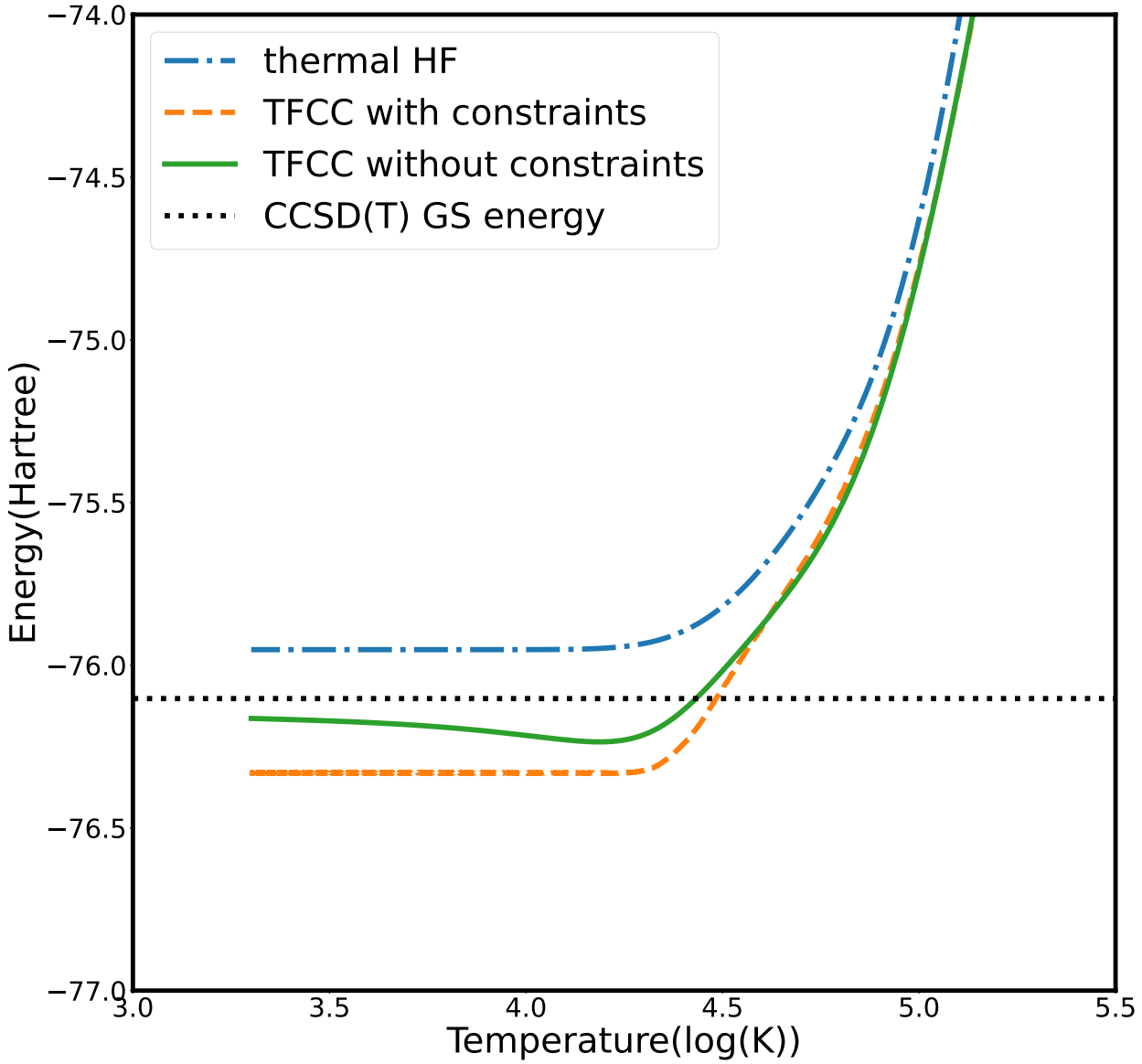


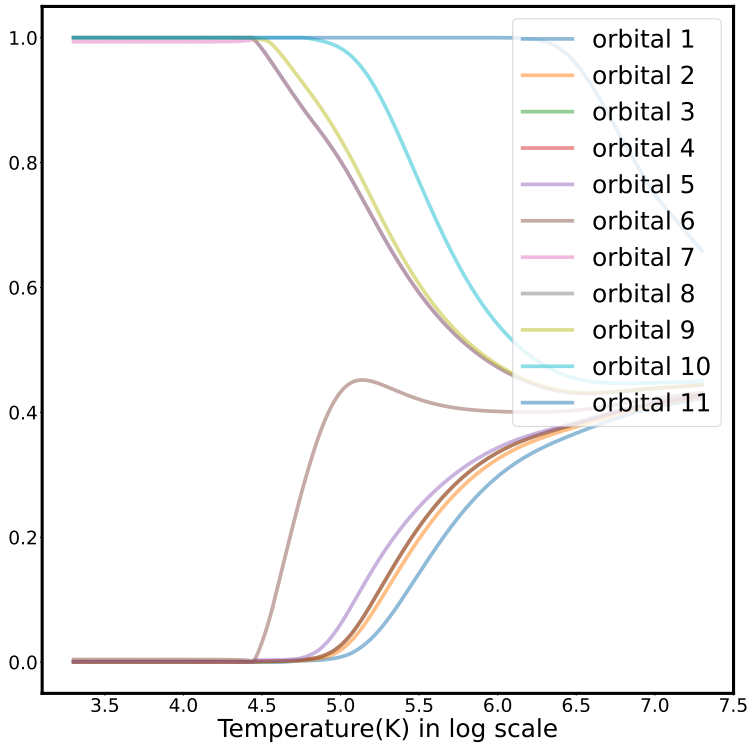
Figure 4.10: Plot of thermal internal energy for H_2O (6-31g basis)

molecule	TFCC without constraints	TFCC with constraints	CCSD(T)	Thermal HF
HF	−100.1900	−100.2565	−100.1016	−99.9593
H_2O	−76.1635	−76.3310	−76.1024	−75.9521

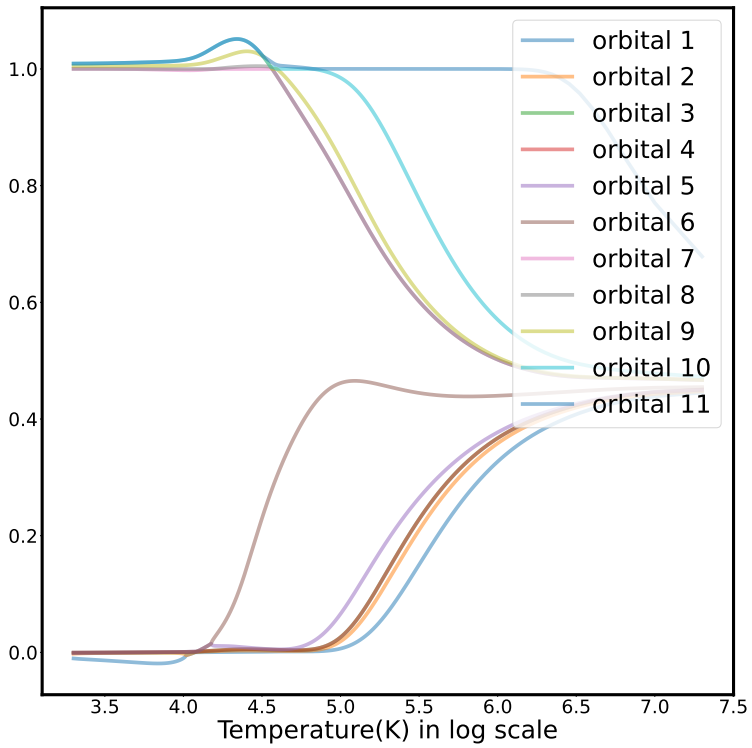
Table 4.2: Compare the ground state energies obtained from different approaches of HF and H_2O molecules (all energies are in unit Hartree)

Fig. 4.11 and Fig. 4.12 show the plot of occupation number of MOs as functions of temperature for the HF and H_2O molecules calculated from the TFCC approach. Both molecules exhibit the similar trends: 1.At high temperatures, the MOs are equally populated.

As the temperature decreases, the population of high-lying orbitals declines while that of low-lying orbitals increases. 2. At lower temperatures, the results without constraints show unphysical behavior, with some orbitals exhibiting negative or greater-than-one occupation numbers, indicating that the corresponding 1-RDMs are not N-representable. 3. In contrast, the occupation numbers for the results with constraints remain constant within the range of 0 to 1 at low temperatures.

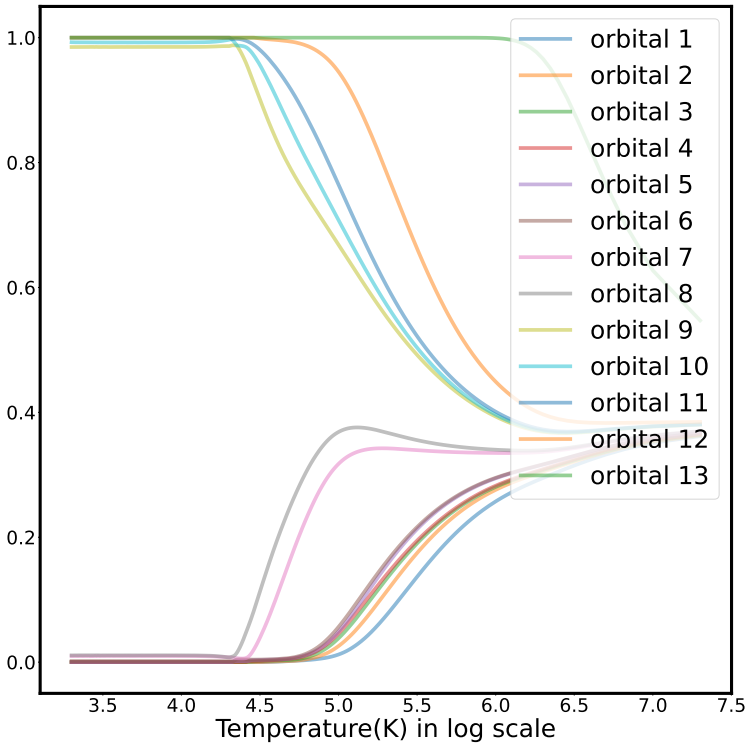


(a)

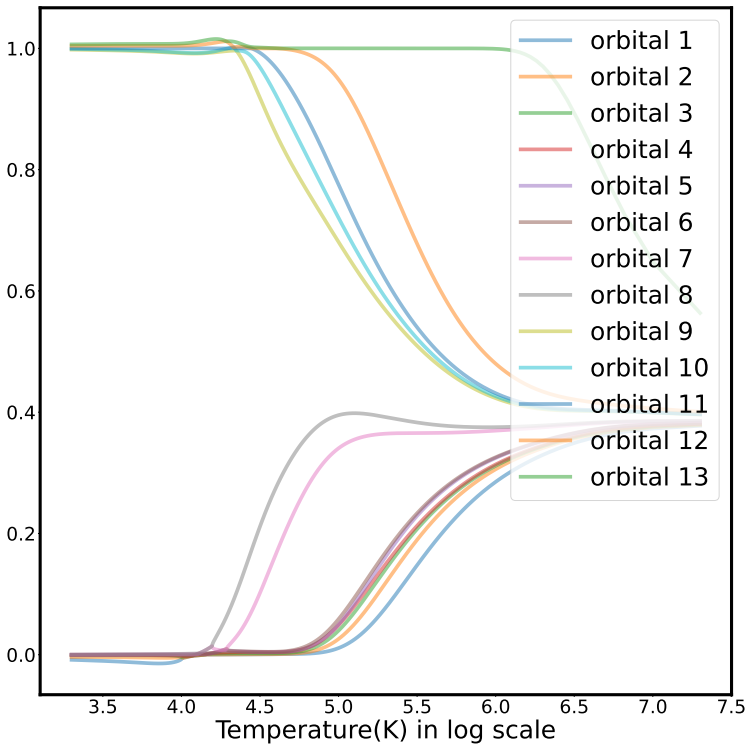


(b)

Figure 4.11: Plots of occupation number as a function of temperature (a) with N-representability constraints (b) without N-representability constraints for HF molecule.



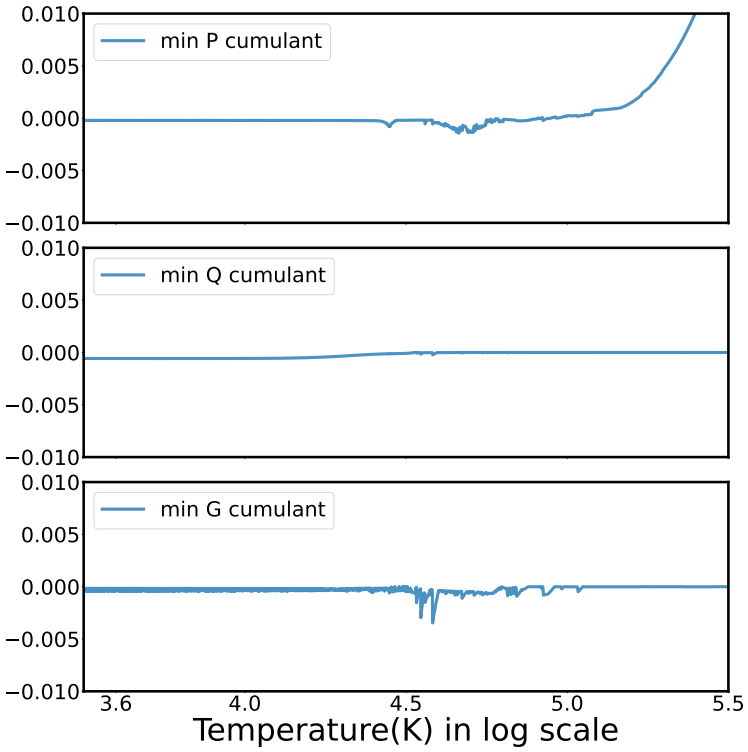
(a)



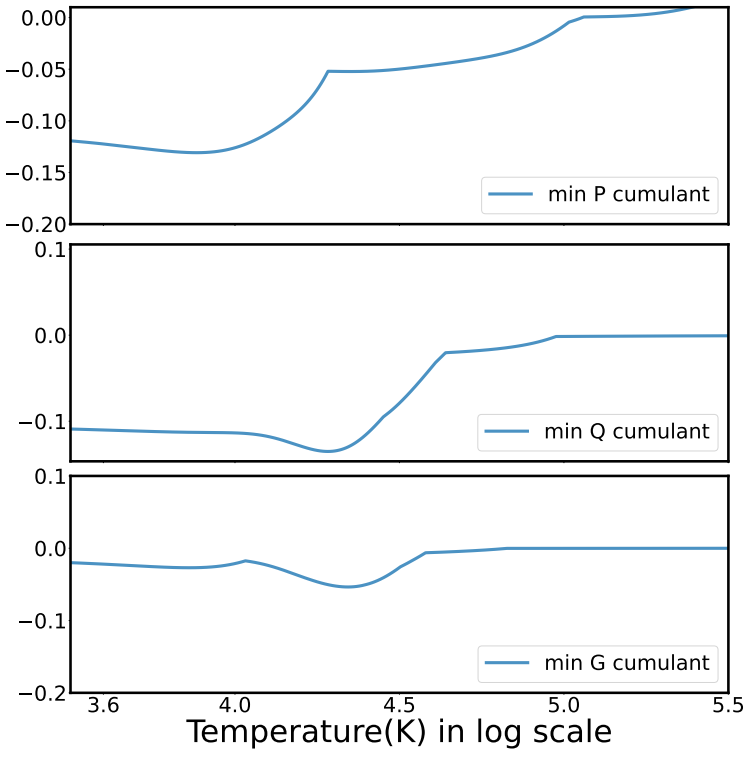
(b)

Figure 4.12: Plots of occupation number as a function of temperature (a) with N-representability constraints (b) without N-representability constraints for H_2O molecule.

Fig. 4.13 and Fig. 4.14 show the plot of minimum of P,Q,G cumulants as functions of temperature for the HF and H_2O molecules. As we can see, for both molecules, the P,Q,G conditions are violated along the imaginary time propagation for results without the constraints, while the P,Q,G conditions hold at all temperature for results with the constraints. This outcome is expected, as the purpose of introducing N-representability constraints is to enforce positivity conditions. However, as previously illustrated, these constraints are insufficient for producing accurate ground state energies in the low-temperature limit.

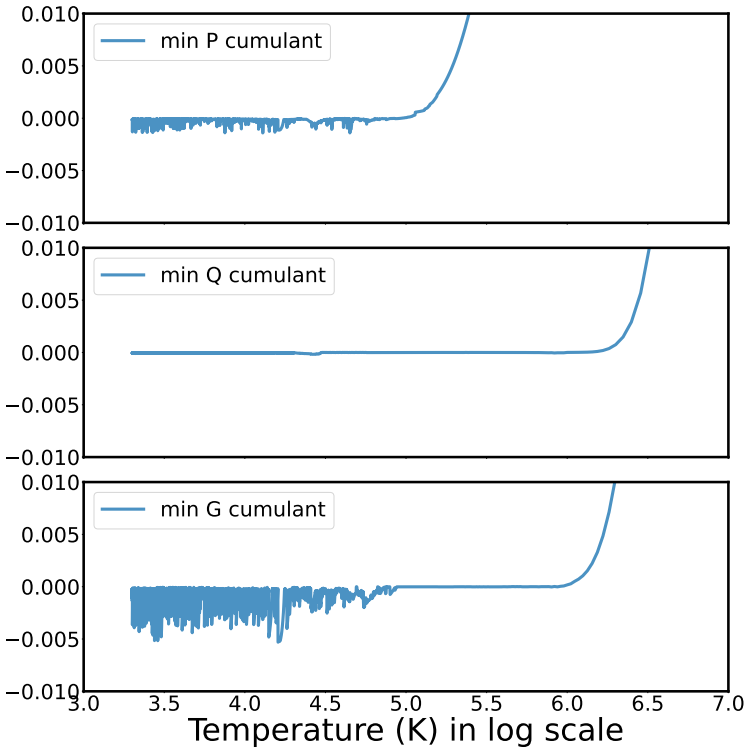


(a)

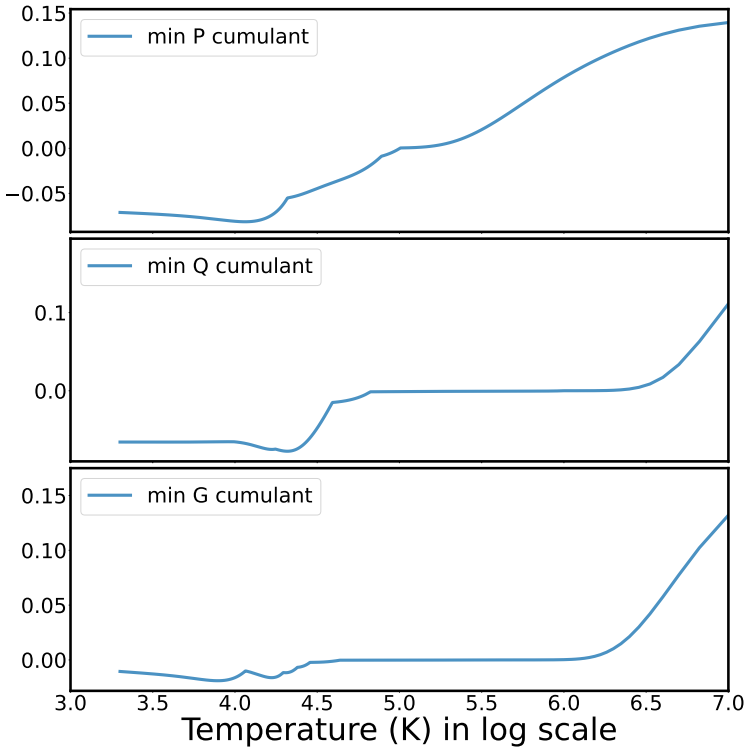


(b)

Figure 4.13: Plots of the minimum P,Q,G cumulants ($\alpha\beta$ component) (a) with N-representability constraints (b) without N-representability constraints for HF molecule.



(a)



(b)

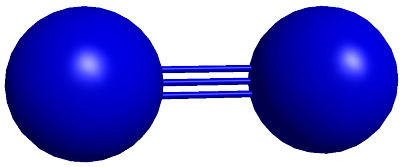
Figure 4.14: Plots of the minimum P,Q,G cumulants ($\alpha\beta$ component) (a) with N-representability constraints (b) without N-representability constraints for H_2O molecule.

2. CAS-TFCC approach

We further exam the CAS-TFCC approach that is described in section 4.1.2 on a few small molecular compounds. By construction of the effective model Hamiltonian in CAS, we can incorporate this correlation effect with low computational cost and easily comparing with the TFCC result of the SOS within the CAS that can be regarded as numerically exact.

To benchmark with the numerical exact results, we start by performing restricted HF calculations and selecting the active electrons and active orbitals. We then perform the CASSCF calculation to optimization the MOs with the respect the ground state for the give configuration. Once the optimized orbitals are obtained, we construct the configurational interaction (CI) Hamiltonian that spans all possible configurations (including states with a any number of (active) electrons) within the CAS and diagonalize it. The thermal properties can then be obtained through the SOS, including a chemical potential term $\mu\hat{N}$ to fix the average number of electrons.

We firstly test two small diatomic compounds: N_2 and O_2 molecules. These compounds have multi-configurational ground states but with well separated ground states to the excited states. The goal is to test the accuracy of the TFCC approach on the effect of static correlation at the low temperature limit. The structures and coordinates of the two compounds are shown in Fig. 4.15 and Fig. 4.16 respectively.

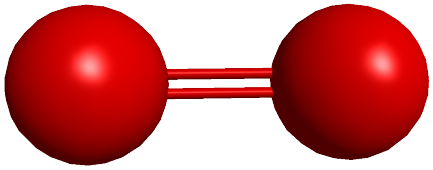


(a)

Atom	x (Å)	y (Å)	z (Å)
N	0.00	0.00	0.00
N	0.00	0.00	1.10

(b)

Figure 4.15: Representation of (a) structure (b) coordinates for N_2 molecule.



(a)

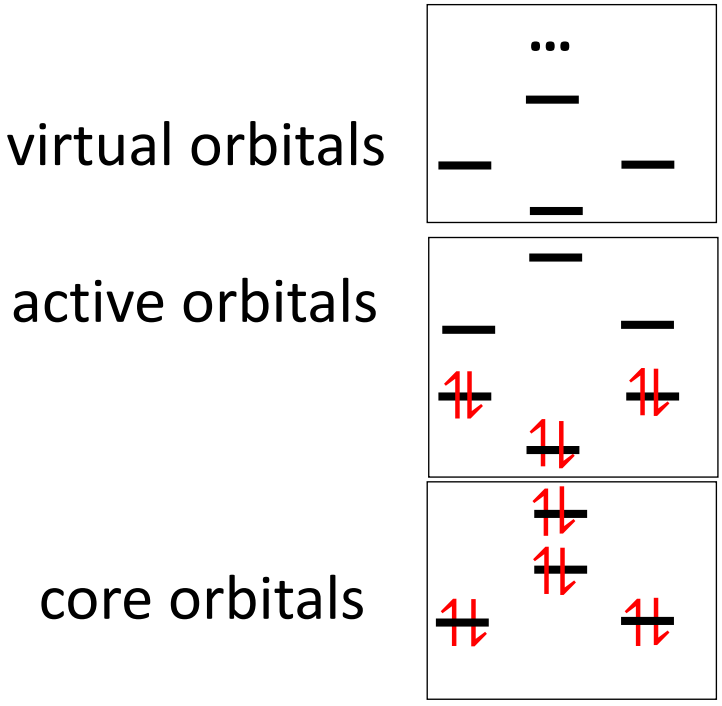
Atom	x (Å)	y (Å)	z (Å)
O	0.00	0.00	0.00
O	0.00	0.00	1.20

(b)

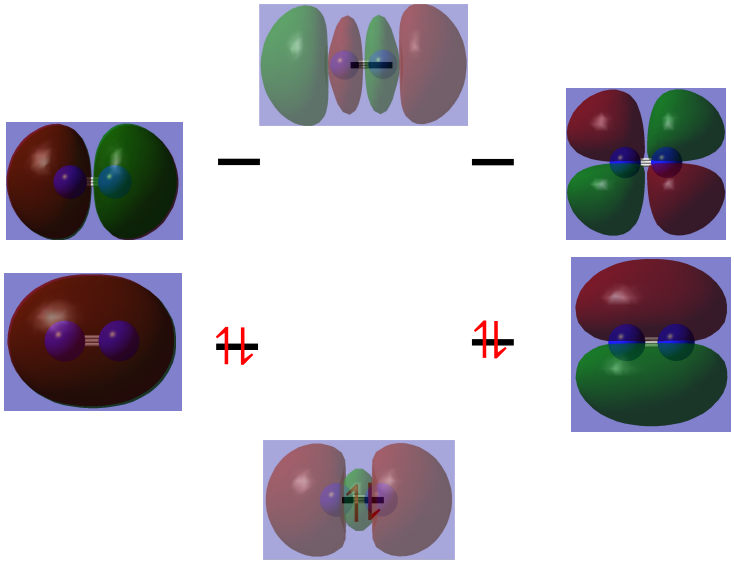
Figure 4.16: Representation of (a) structure (b) coordinates for O_2 molecule.

The resulting occupation scheme and active space are for N_2 and O_2 molecules are shown in Fig. 4.17 and Fig. 4.18 respectively. [7] For the N_2 molecule, we choose the active space to have six electrons (three α electrons and three β electrons) and six spatial orbitals. For the O_2 molecule, we choose the active space to have six electrons (four α electrons and two β electrons) and eight spatial orbitals. In both calculations, we use the ccpvdz basis.

[7] In the HF calculation of O_2 molecule, it has a triplet state. Though the `PySCF` CASSCF calculation is spin-adapted, the resultant wavefunction is projected against $\hat{S}_z$ of the spin-adapted wavefunction such that $S_z = 1$. This is achieved by specify the number of α electrons and number of β electrons in the active space settings.

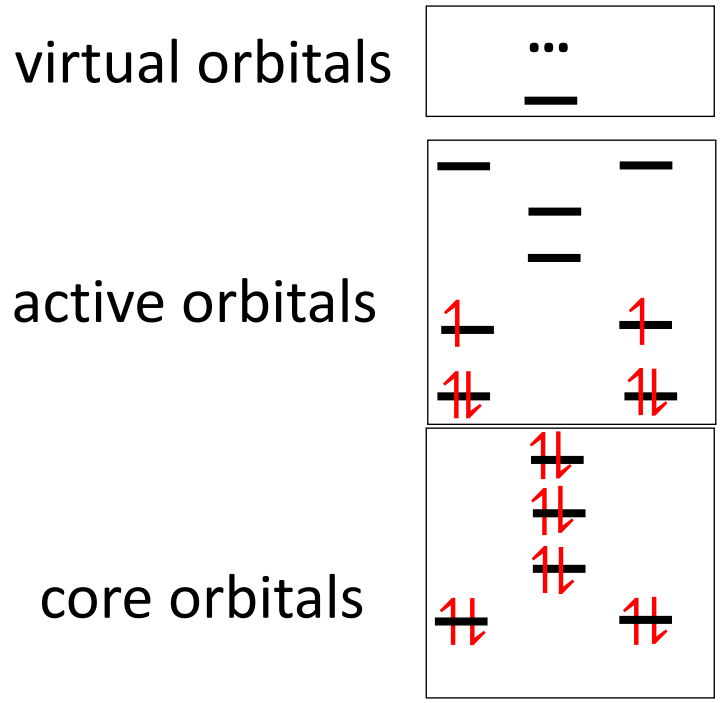


(a)

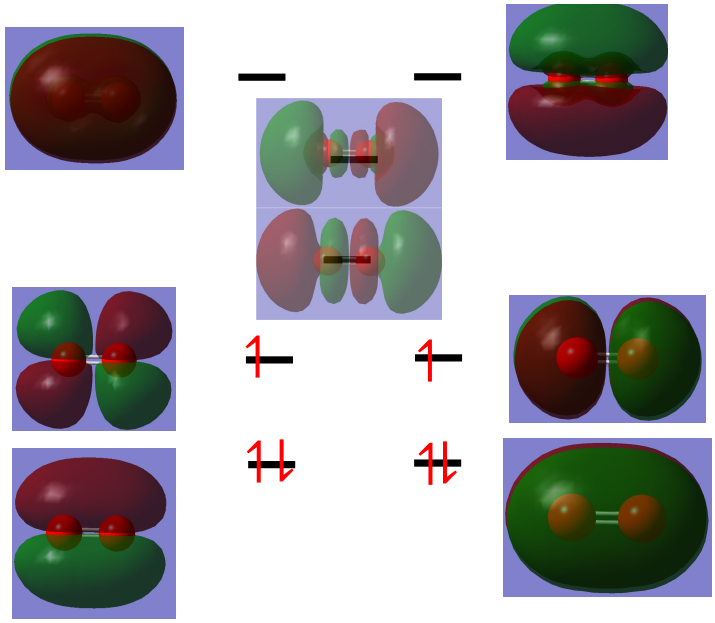


(b)

Figure 4.17: Illustration of (a) occupation scheme (b) active orbitals for N_2 molecule.



(a)



(b)

Figure 4.18: Illustration of (a) occupation scheme (b) active orbitals for O_2 molecule.

We perform the CAS-TFCC calculation and plot the thermal internal energy for the two molecular compounds in Fig. 4.19 and Fig. 4.20 respectively. As we can see, for both molecules, the calculation without applying the N-representability constraints fails at low temperature. In both cases, the energies have abnormally sudden drops at the low tem-

perature limit. In contrast, the CAS-TFCC calculations incorporating N-representability constraints show significant improvement at low temperatures. Since both molecules have well separated ground state energy, the thermal internal energies are converged to the ground state energy below 10^4 K. Comparing to the FCI SOS method, the TFCC approach manage to calculate thermal internal energy accurately at high temperature region ($T > 10^6$ K) for both molecules.

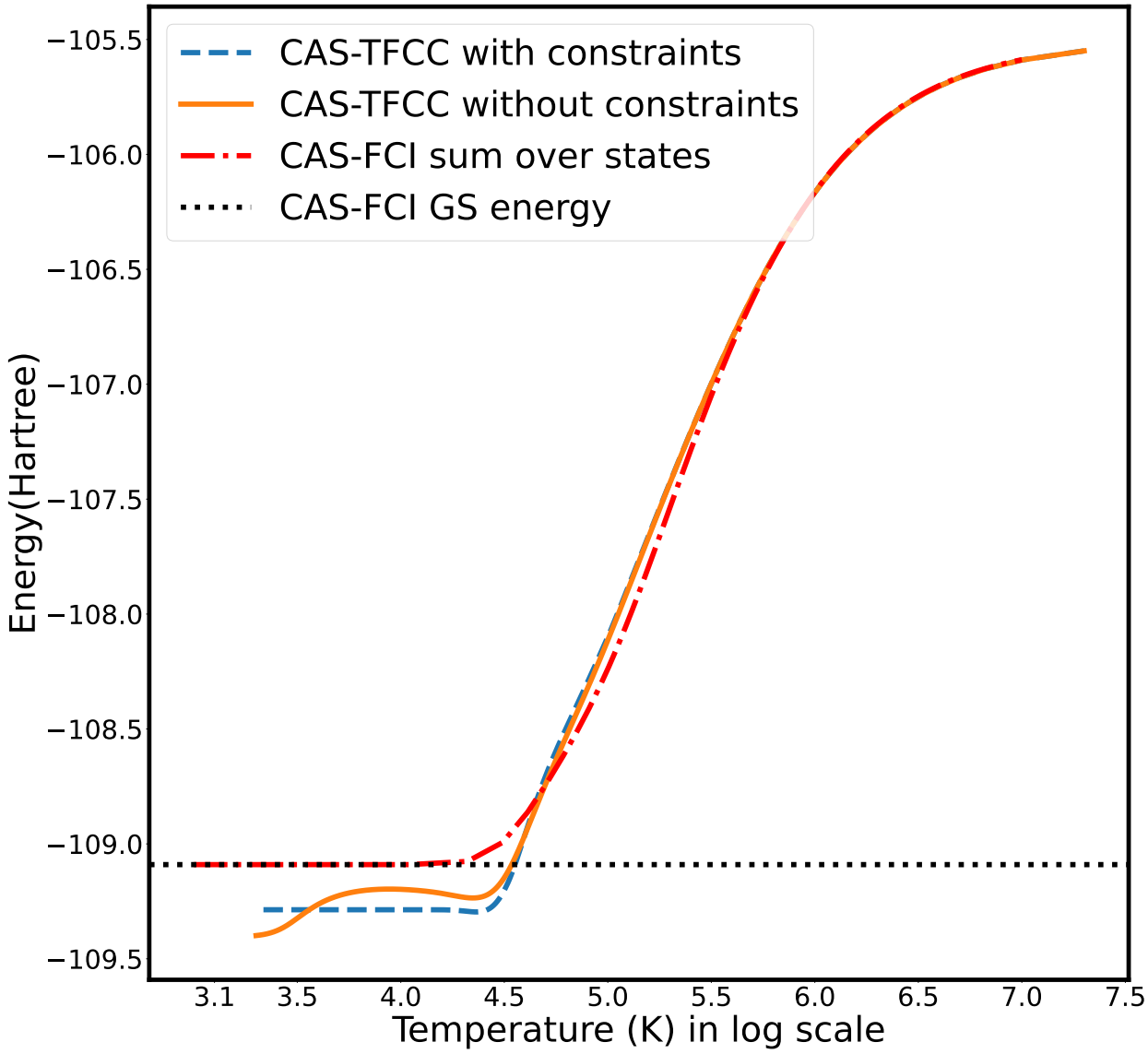


Figure 4.19: Plot of thermal internal energy for N_2 (ccpvdz basis)

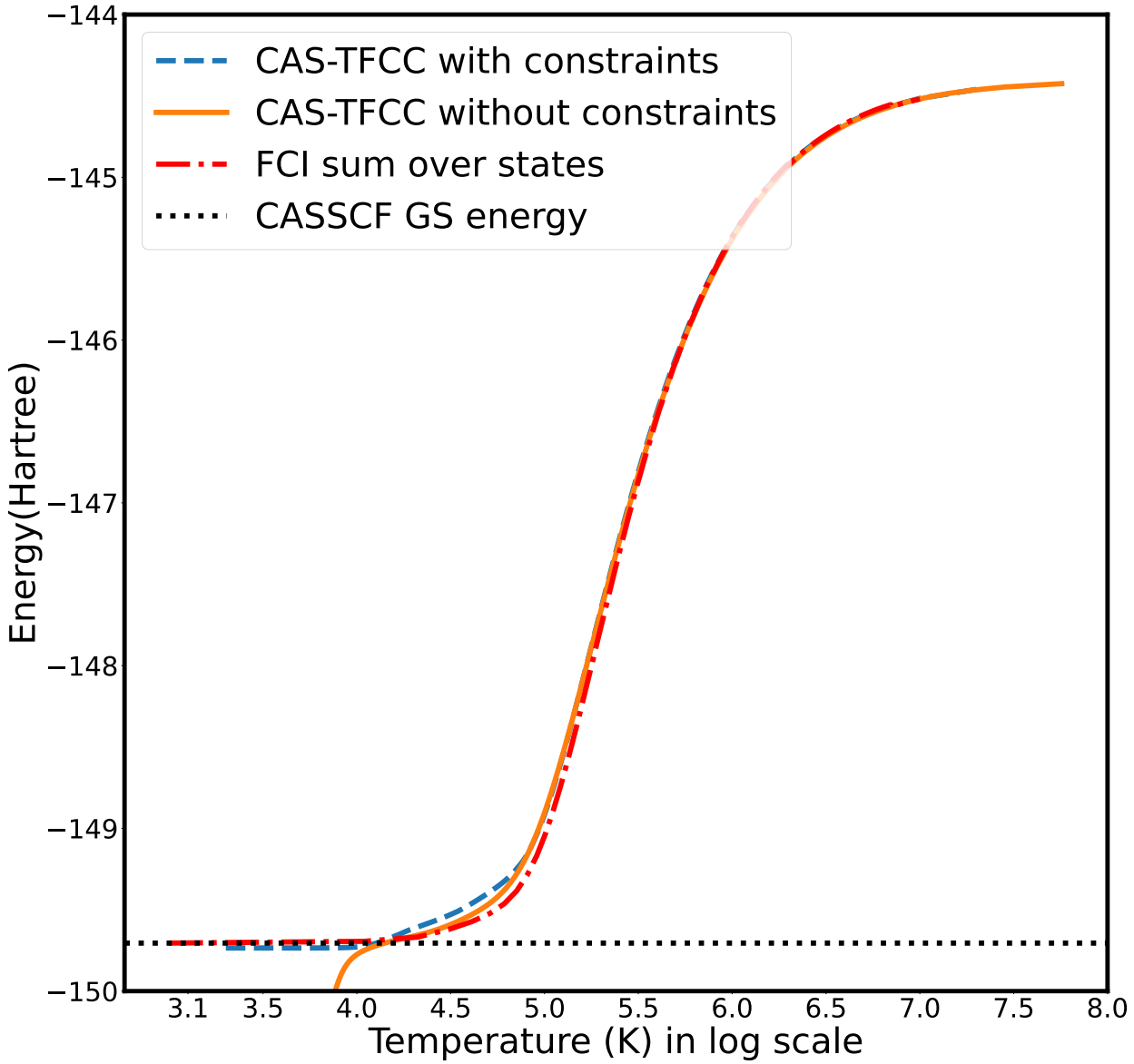


Figure 4.20: Plot of thermal internal energy for O_2 (ccpvdz basis)

Table 4.3 compares the ground state energies obtained from the low-temperature limit of the CAS-TFCC approach with those from the exact diagonalization of the CAS-FCI Hamiltonian. The ground state energy from the CAS-FCI calculation serves as the numerical benchmark for the effective model Hamiltonian defined by the CAS.

For N_2 molecule, ground state energy obtained from the zero temperature limit of the CAS-TFCC approach with the N-representibility constraints is ≈ 0.2 Hartree lower than the CAS-FCI ground state energy, which overestimates the correlation effect and has an error far beyond chemical accuracy (0.0016 Hartree).

For O_2 molecule, the zero temperature limit of the CAS-TFCC calculation with the N-representability produce a ground state energy ≈ 0.01 Hartree lower than the CAS-FCI

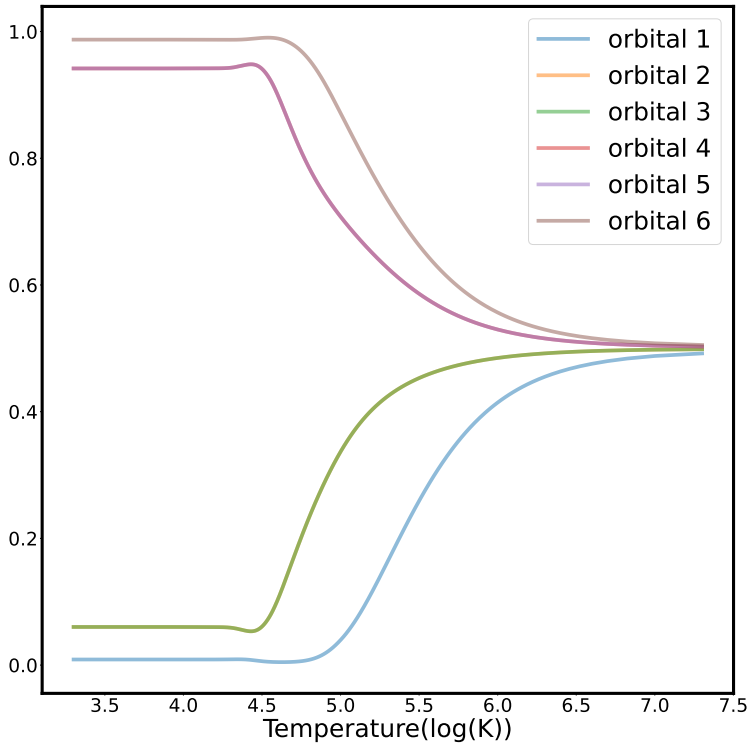
result. It is more accurate comparing to that of the N_2 molecule but still outside the chemical accuracy.

Overall, in both cases, the ground state energies obtained from the zero-temperature limit of the CAS-TFCC approach are significantly lower than expected. Nevertheless, the results with N-representability constraints demonstrate marked improvements.

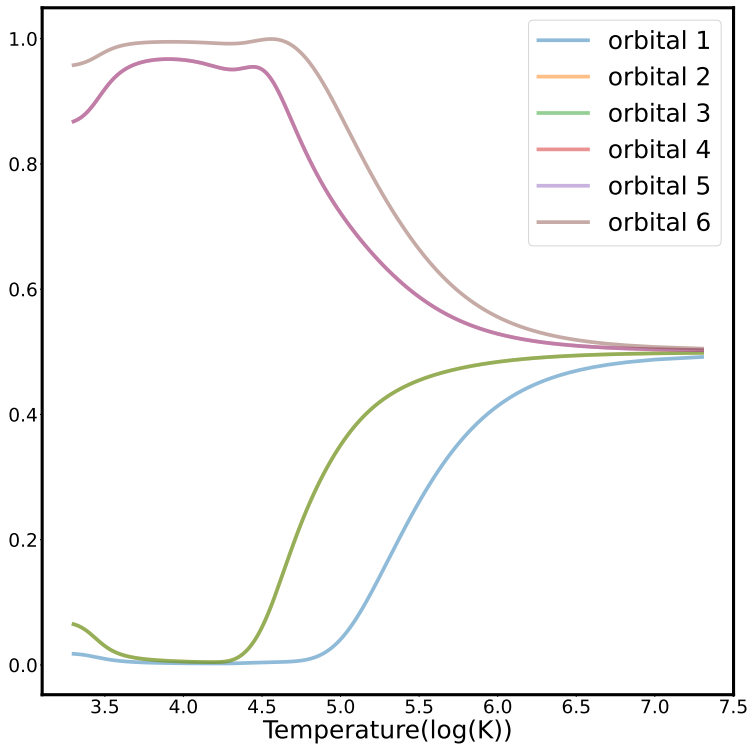
molecule	CAS-TFCC without constraint	CAS-TFCC with constraint	CAS-FCI
N_2	-109.3989	-109.3090	-109.0902
O_2	N.A.	-149.7050	-149.6952

Table 4.3: Compare the ground state energies obtained from different approaches of N_2 and O_2 molecules (all energies are in unit Hartree)

Fig. 4.21 and Fig. 4.22 show the plot of occupation number of active MOs as functions of temperature for the N_2 and O_2 molecules calculation from the CAS-TFCC approach. For both molecules, the results incorporating N-representability constraints exhibit trends similar to those observed for HF and H_2O molecules with the plain TFCC approach, as described previously. In contrast, the results obtained without these constraints show abrupt and unphysical changes at low temperatures for both molecules.

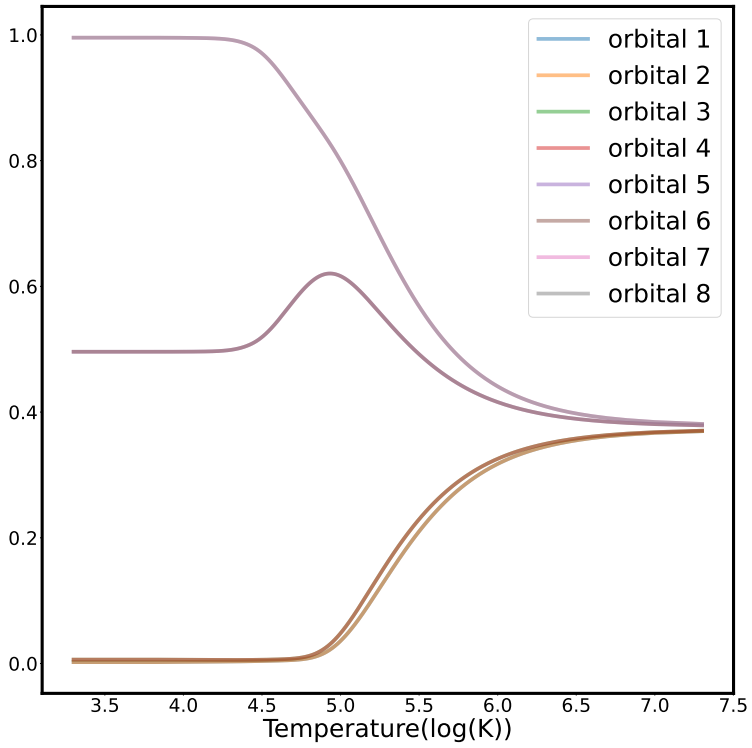


(a)

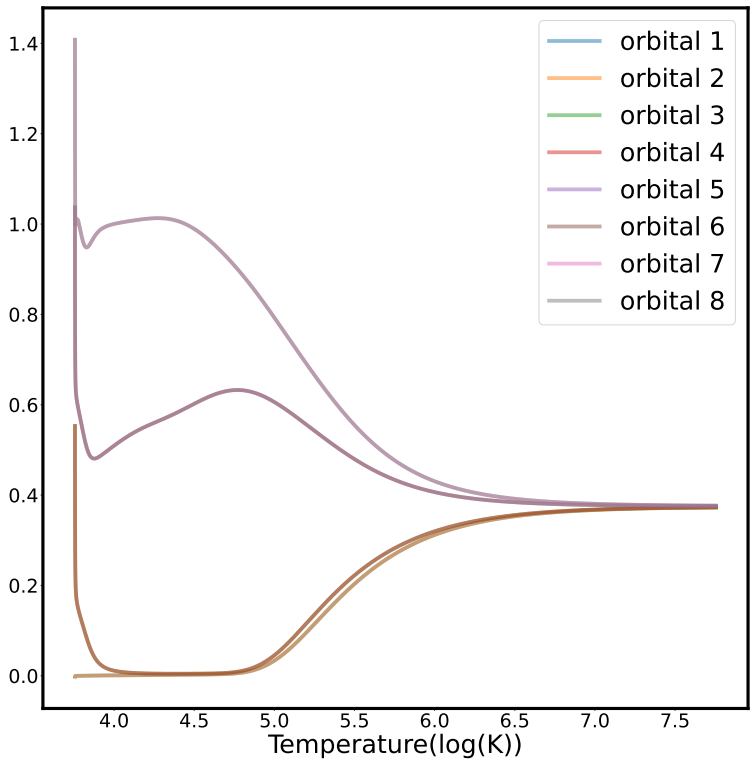


(b)

Figure 4.21: Plots of occupation number as a function of temperature (a) with N-representability constraints (b) without N-representability constraints for N_2 molecule.



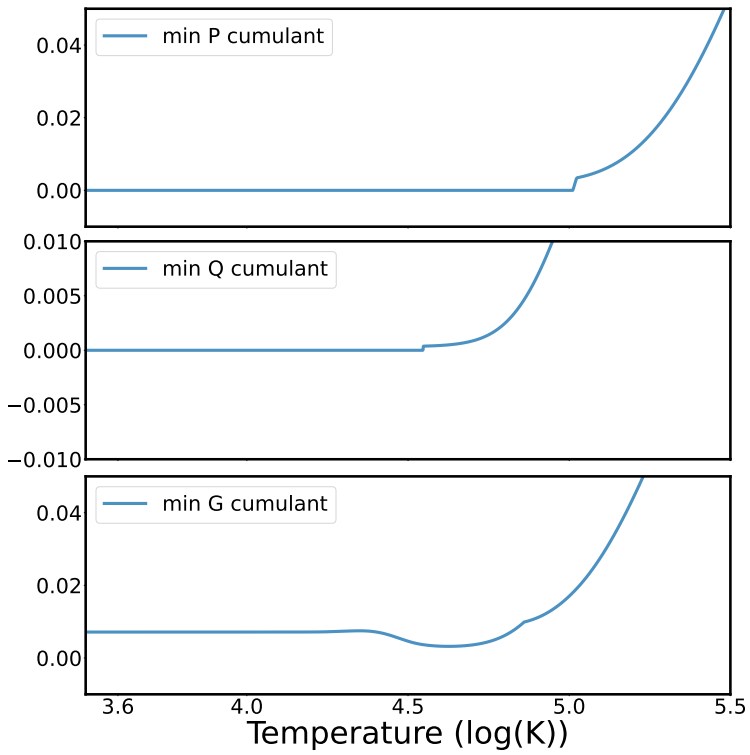
(a)



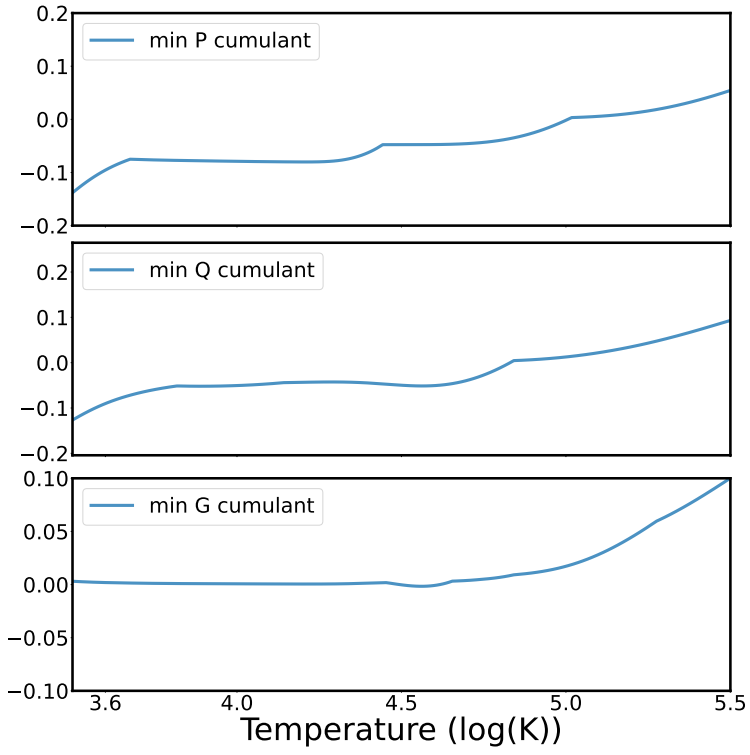
(b)

Figure 4.22: Plots of occupation number as a function of temperature (a) with N-representability constraints (b) without N-representability constraints for O_2 molecule.

Fig. 4.23 and Fig. 4.23 show the plot of minimum of P,Q,G cumulants as functions of temperature for the N_2 and O_2 molecules. As we can see, for both molecules, the P,Q,G conditions are violated at low temperatures for the results without applying the constraints which is consistent with the abnormal behaviour for the occupation number at low temperature. Conversely, the results that incorporate the constraints maintain the P, Q, and G conditions, as expected. As noted in previous cases, the violation of these positivity conditions indicates that the approach is failing at low temperatures.

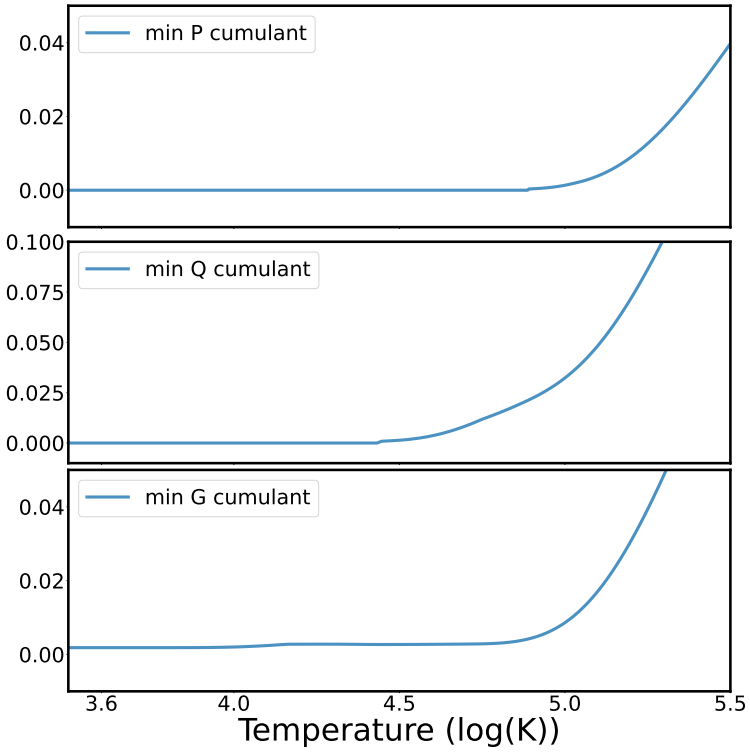


(a)

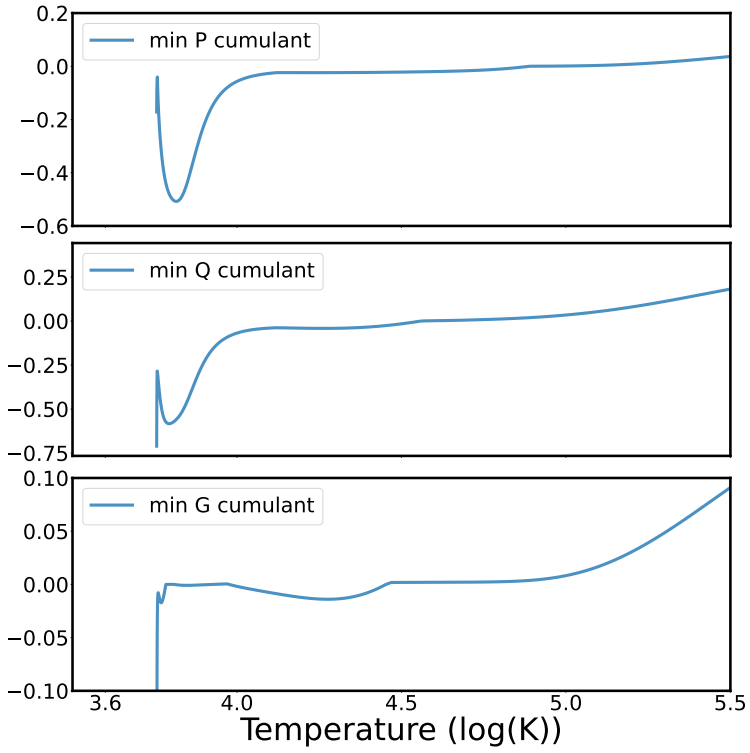


(b)

Figure 4.23: Plots of the minimum P,Q,G cumulants ($\alpha\beta$ component) (a) with N-representability constraints (b) without N-representability constraints for N_2 molecule.



(a)

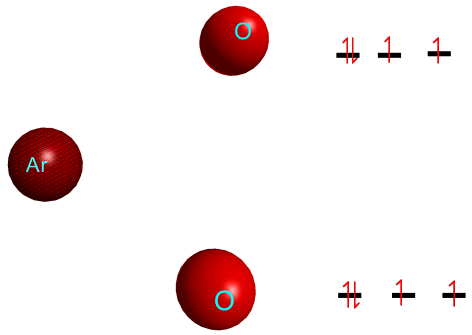


(b)

Figure 4.24: Plots of the minimum P,Q,G cumulants ($\alpha\beta$ component)(a) with N-representability constraints (b) without N-representability constraints for O_2 molecule.

We then tested more challenging models: the ArO_2 and ArON compounds. In these systems, there are not only multi-configurational ground states but also multiple low-lying states due to spin symmetry. The objective of testing these systems is to evaluate the accuracy of the TFCC approach in capturing the effects of static correlation across a wider temperature range.

Fig. 4.25 and Fig. 4.26 show the configuration and coordinates of ArO_2 and ArON molecules. In both molecules, the Ar atom forms a closed shell configuration and the two adjacent atoms serve as the ligands. The six $2p$ orbitals of the two ligands form the active orbitals. The two ligands are stretched away from the Ar atom to reduce the bonding / anti-bonding interactions with the Ar atom and thus create multiple low-lying state in the CAS. For the ArO_2 compound, there are eight active electrons (six α electrons and two β electrons). For the ArON compound, there are seven active electrons (six α electrons and one β electron). In the CASSCF calculation, the orbitals are optimized to an equal-weighted averaged high spin configuration states. [8].



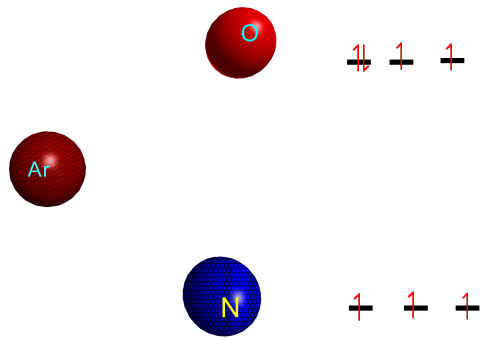
(a)

Atom	x (Å)	y (Å)	z (Å)
Ar	0.00	0.00	1.21
O	−1.29	0.00	−1.27
O	1.29	0.00	1.27

(b)

Figure 4.25: Illustration of (a) configuration (b)coordinate for ArO_2 molecule.

[8]For ArO_2 there are nine states that have high spin configuration and for ArON there are three states that have high spin configuration



(a)

Atom	x (Å)	y (Å)	z (Å)
Ar	0.00	0.00	1.09
O	−1.16	0.00	−1.14
N	1.16	0.00	1.14

(b)

Figure 4.26: Illustration of (a) configuration (b)coordinate for ArON molecule.

Fig. 4.27 and Fig. 4.28 show the plot of thermal internal energy as a function of temperature for the ArO_2 and the ArON compounds. In both cases, the TFCC approach begins to deviate from the SOS results at higher temperatures, in contrast to the behavior observed for the O_2 and N_2 compounds. Additionally, the thermal internal energy converges to the ground state at lower temperatures due to the presence of multiple low-lying states in these systems. [9] In the temperature region of $T > 10^6$ K, the TFCC produces consistent results with the SOS results for both compounds.

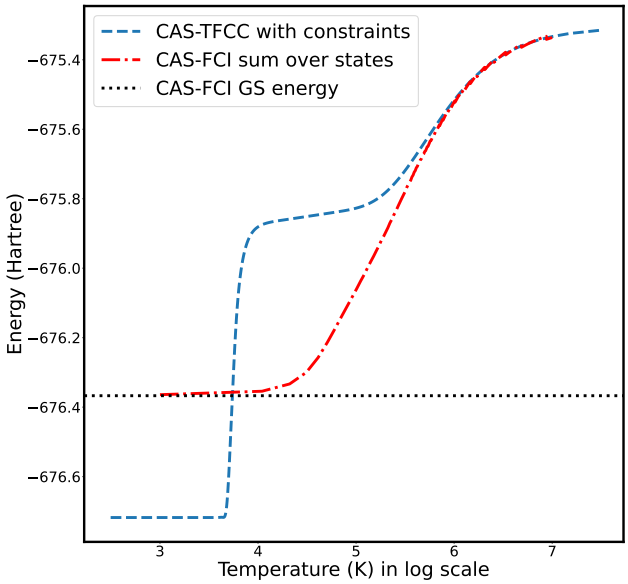


Figure 4.27: Plot of thermal internal energy for ArO_2 (ccpvdz basis)

[9]For the ArO_2 compound, there are 81 low-lying states, while for ArON, there are 9 low-lying states, attributable to spin degeneracy.

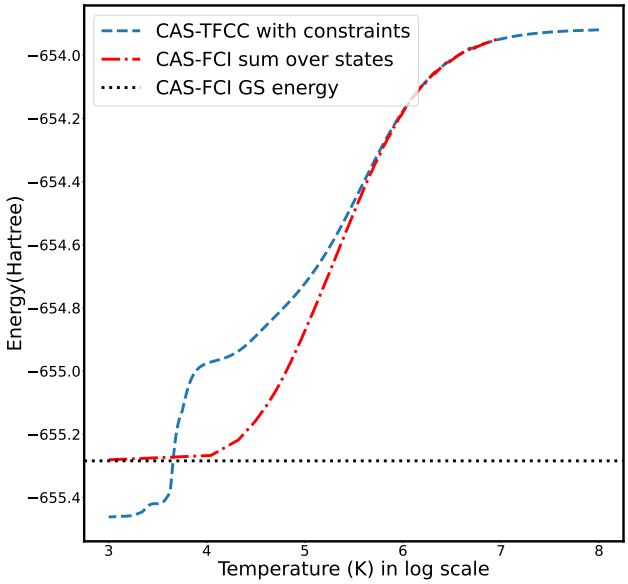


Figure 4.28: Plot of thermal internal energy for ArON (ccpvdz basis)

Table 4.4 shows the comparison of the ground state energy obtained from the low temperature limit of the TFCC approach and the exact diagonalisation (ED) of the CAS-FCI Hamiltonian for the ArO_2 and ArON compounds. In both compounds, the TFCC approach produce ground state much lower than the ED results (≈ 0.3 Hartree for ArO_2, ≈ 0.2 Hartree for ArON). In general, the TFCC approach fails to produce accurate results on thermal internal energies for the temperature range that is below 10^6 K for both compounds.

molecule	CAS-TFCC with constraints	CAS-FCI
ArO_2	-676.7178	-676.3671
ArON	-655.4621	-655.2844

Table 4.4: Compare the ground state energies obtained from different approaches of ArO_2 and ArON molecules (all energies are in unit Hartree)

In general, the results for the CAS-TFCC approach show slight improvement comparing to the canonical TFCC approach. However, these enhancements are still insufficient for practical applications. Substantial changes are necessary for the TFCC approach to effectively handle strongly correlated molecular compounds. Developing more sophisticated N-representability constraints presents a non-trivial challenge. We encourage readers interested in this issue to pursue further research in this area.

4.3 Summary of this chapter

In this chapter, we implement the general TFCC approach to tackle the thermal electronic structure problem, testing it on various model magnetic systems and small molecular com-

pounds.

Both the plain TFCC approach and the CAS-TFCC method are implemented and evaluated. The latter reduces computational costs by restricting the calculations to active orbitals, making it easier to benchmark against numerically exact results. However, both approaches struggle to produce accurate results for thermal properties due to the N-representability issue. To address this, we apply a series of constraints on the cluster amplitudes during the imaginary time integration to ensure the reduced density matrices remain N-representable. While the results with these constraints show notable improvements over those without, they still fall short of satisfactory performance for both the canonical and CAS TFCC approaches.

In general, the TFCC approach, especially with low-order truncation of cluster amplitudes (i.e., singles and doubles), fails to deliver accurate results for the thermal electronic structure problem without significant modifications to the scheme described in this chapter. More sophisticated N-representability constraints are essential to enhance this method. Machine learning algorithms such as the restricted Boltzmann machine [74, 75] might shed some light on this problem.

Chapter 5

Application: quantum dynamics simulations for the vibronic problems

reprinted with the permission from *J. Chem. Phys.* (**2024**) 160, 094105. *Copyright* 2024, *American Institute of Physics*

5.1 Abstract

A time-dependent vibrational electronic coupled-cluster (VECC) approach is proposed to simulate photo-electron/UV-VIS absorption spectra, as well as time-dependent properties for non-adiabatic vibronic models, going beyond the Born-Oppenheimer approximation. A detailed derivation of the equations of motion and a motivation of the ansatz are presented. The VECC method employs second-quantized bosonic construction operators and a mixed linear and exponential ansatz to form a compact representation of the time-dependent wave-function. Importantly, the method does not require a basis set, has only few user-defined inputs, and has a classical (polynomial) scaling with respect to the number of degrees of freedom (of the vibronic model), resulting in a favourable computational cost. In benchmark applications to small models and molecules the VECC method provides accurate results, compared to Multi-Configurational Time-dependent Hartree (MCTDH) calculations when predicting short-time dynamical properties (i.e. photo-elecron / UV-VIS absorption spectra) for non-adiabatic vibronic models. To illustrate the capabilities the VECC method is also applied successfully to a large vibronic model for hexahelicene with 14 electronic states and 63 normal modes, developed in the group by Santoro (D. Aranda and F. Santoro, Journal of Chemical Theory and Computation 17, 1691, 2021).

5.2 Introduction

The description of non-adiabatic nuclear dynamical processes is a very active area of investigation. It is at the heart of photochemical processes such as the investigation of intersystem

crossings, [76, 77, 78, 79, 80] like those found in the process of singlet fission. [81, 82, 83, 84, 85, 86, 87, 88, 89, 90, 91, 92, 93, 94, 95]

In such molecular processes there can be large changes in nuclear geometries and the coupling to the electronic ground state is often important. The most widely applicable approaches in this context employ on-the-fly dynamics (invoking electronic structure calculations of energy gradients and non-adiabatic couplings as needed). Various on-the-fly schemes can be used to approximate the nuclear dynamics on multiple electronic states, for example: Ehrenfest dynamics, [96, 97, 98] surface hopping, [99, 100, 101] ab initio multiple spawning (AIMS), [102, 103, 104, 105] and its generalization, [106] as well as Gaussian wave-packet methods (at various levels of sophistication). [100, 107, 108, 109, 110, 111, 112, 113, 114]

Our primary interest here is the description of electronic spectroscopy including vibrational fine-structure. The most widely used approaches to include nuclear fine-structure are based on single-surface displaced harmonic oscillator potentials (that include Duschinsky rotations). Commonly one obtains these potentials through calculations based on the Frank-Condon principle. [115, 116, 117, 118, 119, 120, 121, 122] However, many systems contain a dense collection of close-lying excited states and the underlying Born-Oppenheimer and harmonic approximations may not be sufficiently accurate to describe the resulting spectra. In a typical scenario, as shown in Fig. 5.1, a molecule absorbs light and is vertically excited from the ground state PES to an excited state PES, where the excited state wave-function evolves over time. Near crossing points between these excited PESs (conical intersections), one finds large state population transfer, and the full wave-function becomes a linear combination of the different excited electronic states. Studying this excited-state dynamics process helps to understand photo-chemical reaction pathways [123, 124, 125, 126] as well as interpret electronic spectra. [52, 53, 127, 128, 129, 130, 131] For a recent overview see reference [132].

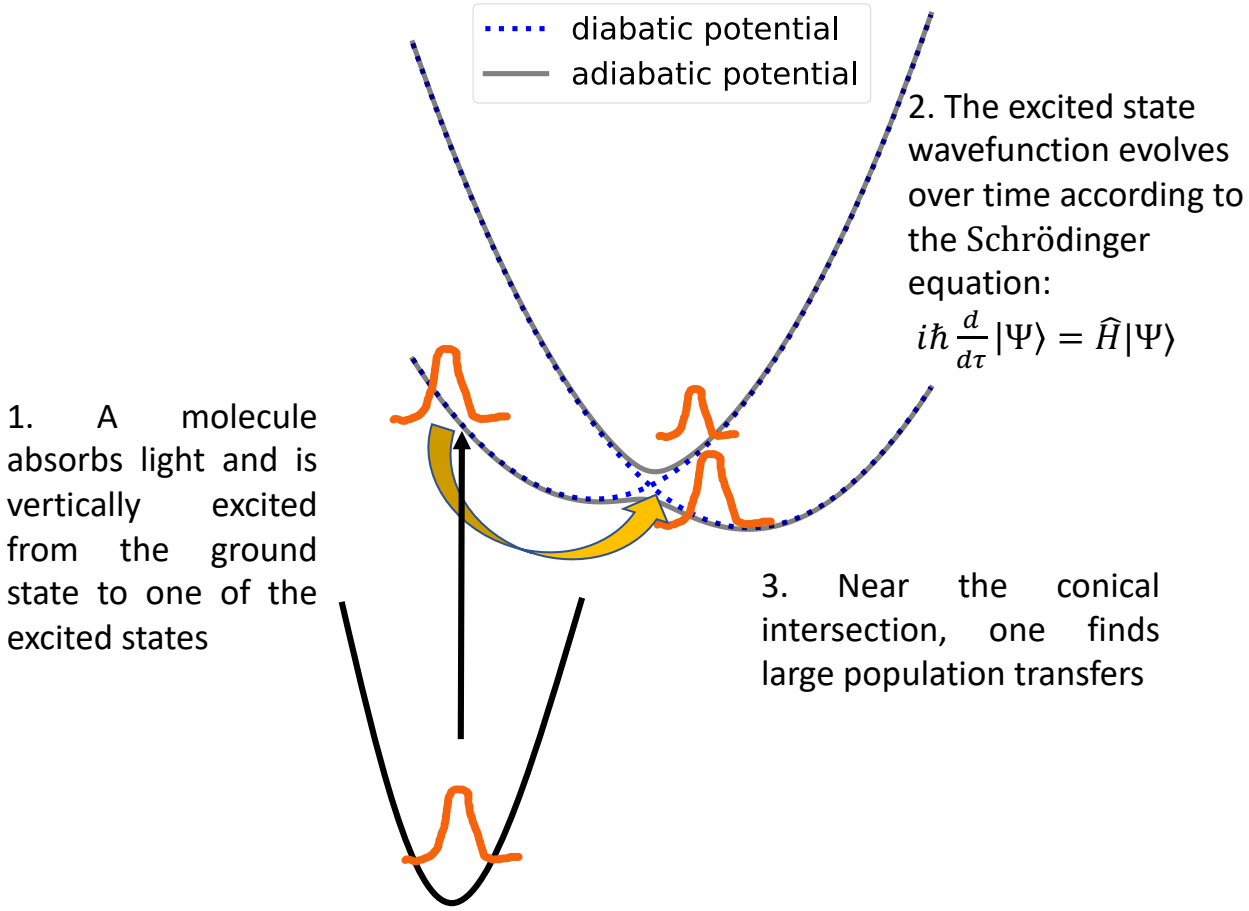


Figure 5.1: Diagram illustrates how excited state wave-function evolves over time.

Focusing on electronic spectroscopy, a more accurate description requires the inclusion of multiple coupled electronic states, but the potential energy surfaces need only be accurate over limited spatial extent, close to the ground state equilibrium geometry, as the low-resolution simulation of spectroscopic processes only requires relatively short propagation times of about 100 fs. One approach for simulating short-time phenomena is the use of a vibronic model in a diabatic basis, where each electronic matrix element can be represented by a short Taylor series expansion (quadratic, or even linear) in the ground state normal mode basis. Diabatic vibronic models are very useful for extracting short-time dynamics and spectroscopic information. [52, 53, 55, 133, 134, 135, 136, 137, 138] Standard electronic structure methods for excited states can "in-principle" be used to obtain vibronic models, but in practice require modification to extract the necessary vibronic information. Some of these standard methods include: time-dependent Density Functional Theory (TD-DFT) methods, [139, 140, 141] MBPT based methods [142, 143, 144], equation of motion coupled-cluster (EOMCC) methods and similarity transformed EOMCC approaches. [145, 146, 147, 148, 149]

A variety of approaches are available to construct vibronic models in the diabatic rep-

resentation. One approach is diabatization-by-ansatz, e.g. [135, 150, 151, 152, 153, 154], requiring only adiabatic energies at selected geometries. A more reliable option for models with many electronic states are diabatization procedures which aim to optimize the resulting diabatic states based on the overlap of adiabatic states (at close lying geometries), or non-adiabatic couplings. [53, 55, 56, 57, 58, 130, 132, 133, 137, 155, 156, 157]

After constructing a diabatic vibronic model, one can proceed with the calculation of the absorption spectrum. [1] One approach is using a time-independent Lanczos method. [52, 130, 135, 158, 159] This approach can effectively simulate spectra for small to medium-size systems. [2] One can also use wave-packet dynamics. These methods involve the calculation of the time auto-correlation function (ACF) after initial vertical excitation, using the time-dependent Schrödinger equation:

$$i\hbar \frac{\mathrm{d}}{\mathrm{d}\tau} |\Psi(\tau)\rangle = \hat{H}^{vibronic} |\Psi(\tau)\rangle \,. \tag{5.1}$$

The MCTDH [59, 60, 160, 161] approach (and Gaussian wave-packet variations [107, 162]) are among the most successful wave-packet dynamics methods. In particular, the multi-layer version of MCTDH [61, 62, 63, 163, 164] can be a highly efficient approach, but it does require some judicious choices from the user, and convergence of the approach may be hard to demonstrate convincingly. While the family of MCTDH methods are highly efficient, they can still be rather costly due to the high dimensionality of the underlying primitive Hilbert space. The challenges faced by the family of MCTDH methods motivates us to design an alternative wave-packet dynamics approach.

The idea of this work is to design a second-quantized exponential ansatz that parameterizes the wave-function in a compact manner and to extract the time-correlation function by propagating amplitude equations. The advantage of this approach is that it does not require the introduction of a vibrational (H.O.) basis and the number of parameters scales with the classical degrees of freedom.

In this paper, we develop a new method named "Vibrational Electronic Coupled Cluster (VECC)" to (approximately) solve the wave-packet dynamics problem. VECC is an application of the more general thermal normal-ordered exponential ansatz (TNOE) approach developed by M. Nooijen and S. Bao. [25] TNOE is a general second-quantized operator method for solving both time-dependent and statistical mechanical problems of bosonic and fermionic many-body systems. VECC can be regarded as a special form of the TNOE family of methods, in which we parameterize the time-dependent wave-function using a second-quantized exponential ansatz.

Attempts to utilize CC methods for solving the bosonic many-body problem can be dated back to the 1990s. Prasad developed a time-dependent CC method for single-surface multi-dimensional vibrational problem, in which a polynomial expansion of anharmonic potential is applied. [165] Mukherjee and co-workers proposed the thermal cumulant approach for the statistical mechanics of the multi-dimensional vibrational problem. [2] In recent years, there

[1] based on the vibronic Hamiltonian and transition moments (dipole or more general)

[2] because the simple form of the vibronic Hamiltonian allows one to use (primitive) harmonic-oscillator basis sets.

is a resurgence of this subject. Hirata et. al. [166, 167] use a similar operator approach, while, earlier, Christiansen [168] introduces a basis set in his vibrational coupled cluster (VCC) both aiming at obtaining accurate vibrational frequencies and fundamental transitions. However, all these methods mentioned above focus on the single-surface vibrational problem. In this paper, we extend the CC method to the multi-surface non-adiabatic dynamics vibronic problem.

This paper is organized as follows: In section 5.3, we outline the vibrational electronic coupled-cluster (VECC) theory. In section 5.4 the VECC method is used to simulate photo-electron/UV-VIS absorption spectra for a handful of molecular compounds. We also share an exploration of calculating diabatic state populations using VECC. In section 5.5 we summarize the VECC approach and in a few final remarks we discuss some of the choices and insights that provide further perspective on the approach, its limitations and possible improvements.

5.3 Theory

In this section, we introduce the formal VECC theory. The primary goals we aim to achieve with the VECC theory are the simulation of photo-electron/UV-VIS absorption spectra and the calculation of time-dependent diabatic state populations for gas phase molecular systems.

5.3.1 General overview of VECC Theory

Our starting pointing is a vibronic model Hamiltonian that is represented in diabatic electronic states and with the potential truncated up to quadratic terms. Model parameters can be obtained using standard electronic structure methods and diabatization protocols. [53, 55, 56, 57, 58, 130, 132, 133, 135, 137, 150, 151, 152, 153, 154, 155, 156, 157] The general vibronic model Hamiltonian can be expressed as a sum over electronic states and bosonic construction operators as follows:

$$\begin{aligned}\hat{H} = \sum_{ab} |a\rangle \langle b| \Bigg(& h_b^a + \sum_i h_b^{ai}\{\hat{a}_i^\dagger\} + \sum_i h_{bi}^a\{\hat{a}_i\} \\ & + \sum_{ij} h_{bj}^{ai}\{\hat{a}_i^\dagger \hat{a}_j\} + \frac{1}{2}\sum_{ij} h_b^{aij}\{\hat{a}_i^\dagger \hat{a}_j^\dagger\} + \frac{1}{2}\sum_{ij} h_{bij}^a\{\hat{a}_i \hat{a}_j\} \Bigg),\end{aligned} \tag{5.2}$$

where labels a, b denote electronic surfaces and labels i, j denote vibrational modes.

In VECC theory, we first apply a bosonic second-quantized coupled-cluster (CC) ansatz to parameterize the time-dependent wave-function. This CC ansatz is then substituted into the time-dependent Schrödinger equation (TDSE) to form coupled-cluster (CC) equations-of-motion (EOM) which are first order differential equations over time. Time dependent properties can be determined by solving CC EOM numerically.

Among the time-dependent properties, of particular interest is the time-autocorrelation function (ACF). The ACF is defined as the overlap between initial wave-function and the wave-function at time τ.

$$\begin{aligned} C(\tau) &= \langle \psi(t=0) | \psi(t=\tau) \rangle \\ &= \langle \psi(t=0) | \, e^{-i\hat{H}\tau} \, | \psi(t=0) \rangle \, . \end{aligned} \tag{5.3}$$

This property is of interest because the vibrationally-resolved electronic spectra of non-adiabatic vibronic models can be generated through Fourier transformation of the ACF (provided that the initial wave-function is designed carefully).

$$C(\tau) \xRightarrow{\text{Fourier transform}} \text{Spectra.} \tag{5.4}$$

To calculate the ACF we need to evaluate the quantum propagator $e^{-i\hat{H}\tau}$, whose Hamiltonian $\hat{H}$ (defined in Eq. (5.2)) has multiple electronic surfaces. This is problematic because the exponential parameterization for multiple surfaces is non-trivial. We will first examine simpler cases, such that the result can be generalized to multiple surfaces.

In section 5.3.2 we start with simplified single-surface quadratic vibrational models, which serve as a prototype problem for exploring four different realizations of the VECC ansatz. The preferred realization is then generalized to full multi-surface vibronic models in section 5.3.3. Additional modifications are made to the ansatz to improve the accuracy of the wave-function propagation, as well as simplify the VECC. Our approach for calculating time-dependent properties using this new VECC method is outlined in section 5.3.4. We focus on the ACF and the diabatic state population, although in principle any time-dependent properties can be obtained.

5.3.2 Exploring four single-surface approaches

Consider a molecule sited at the minima of its ground state PES. Its dimensionless normal modes are based on the ground state Hessian. The excited-state surface (near the vertical ground state geometry) is parameterized as a multidimensional displaced harmonic oscillator (D.H.O.) that includes Duschinsky rotations. The Hamiltonian that describes this multi-dimension D.H.O. can be expressed as:

$$\hat{H} = E_x + \sum_i \frac{1}{2} \hbar \omega_i (\hat{p}_i^2 + \hat{q}_i^2) + \sum_{ij} V_{ij} \hat{q}_i \hat{q}_j + \sum_i \alpha_i \hat{q}_i, \tag{5.5}$$

where E_x, ω_i, α_i, V_{ij} are the vertical energy, frequencies, linear displacements, and quadratic adjustment parameters respectively. The dimensionless momentum and coordinate operators $\hat{p}_i$ and $\hat{q}_i$ can be expressed in second-quantized form:

$$\hat{q}_i = \frac{1}{\sqrt{2}} (\hat{a}_i^\dagger + \hat{a}_i), \tag{5.6}$$

$$i\hat{p}_i = \frac{1}{\sqrt{2}}(\hat{a}_i^\dagger - \hat{a}_i). \tag{5.7}$$

Substituting Eqs. (5.6) and (5.7) into Eq. (5.5) we can express the multi-dimensional D.H.O. in a second-quantized form:

$$\begin{aligned}\hat{H} = &\left(E_x + \frac{1}{2}\sum_{ii} V_{ii} + \frac{1}{2}\sum_i \hbar\omega_i\right) + \sum_i \frac{\alpha_i}{\sqrt{2}}\{\hat{a}_i\} \\ &+ \sum_i \frac{\alpha_i}{\sqrt{2}}\{\hat{a}_i^\dagger\} + \sum_{ij}\left(\hbar\omega_i\delta_{ij} + V_{ij}\right)\{\hat{a}_i^\dagger \hat{a}_j\} \\ &+ \sum_{ij}\frac{V_{ij}}{2}\{\hat{a}_i^\dagger \hat{a}_j^\dagger\} + \sum_{ij}\frac{V_{ij}}{2}\{\hat{a}_i \hat{a}_j\},\end{aligned} \tag{5.8}$$

where the notation "{}" denotes normal ordering with respect to a vacuum state that satisfies $\hat{a}_i |0\rangle = 0$. [3]

Using the definition of the Hamiltonian in Eq. (5.8), we will explore four different single-surface approaches for solving the TDSE. The guiding principle when designing these approaches is to strike a balance between accuracy and robustness. To achieve this we compare simulated ACF and absorption spectra of each approach against ED for a small model system.

1. Single-exponential approach ($|\psi\rangle = e^{\hat{T}} |0\rangle$)

The first and most apparent ansatz is the single-exponential ansatz:

$$|\psi\rangle = e^{\hat{T}} |0\rangle , \tag{5.9}$$

where $\hat{T}$ is truncated at SD:

$$\hat{T} = t_0 + \sum_i t^i \hat{a}_i^\dagger + \frac{1}{2}\sum_{ij} t^{ij} \hat{a}_i^\dagger \hat{a}_j^\dagger. \tag{5.10}$$

Substituting this ansatz into the TDSE, closed-form CC VECC can be formulated

$$i\frac{\mathrm{d}}{\mathrm{d}\tau} e^{\hat{T}} |0\rangle = \hat{H} e^{\hat{T}} |0\rangle . \tag{5.11}$$

Multiplying by $e^{-\hat{T}}$ on both sides of Eq. (5.11) gives us

$$\begin{aligned} i\frac{\mathrm{d}\hat{T}}{\mathrm{d}\tau} |0\rangle &= \left(e^{-\hat{T}} \hat{H} e^{\hat{T}}\right) |0\rangle \\ &= \left(\hat{H} e^{\hat{T}}\right)_{conn.} |0\rangle , \end{aligned} \tag{5.12}$$

[3] The initial state in the simulation of absorption spectra is represented by $|0\rangle \mu$, where μ is a constant representing the electronic transition moment. For this reason we can focus on an initial state represented by $|0\rangle$.

where the subscript "conn." denotes connected. It can be proved that all disconnected contributions explicitly cancel out in $e^{-\hat{T}}\hat{H}e^{\hat{T}}$ by writing the string of operators in normal ordering and applying the Baker–Campbell–Hausdorff (BCH) series expansion. This is in analogy to the usage of SR-CC theory in electronic structure. [169][4]

Next, we introduce a projection manifold $\langle 0|\,\Omega_\mu^\dagger$

$$\Omega_\mu^\dagger = \{\mathbb{1}, \hat{a}_i, \hat{a}_i\hat{a}_j\}, \tag{5.13}$$

and project on both sides of Eq. (5.12)

$$i\,\langle 0|\,\Omega_\mu^\dagger \frac{\mathrm{d}\hat{T}}{\mathrm{d}\tau}\,|0\rangle = \langle 0|\,\Omega_\mu^\dagger \left(\hat{H}e^{\hat{T}}\right)_{conn.}|0\rangle\,. \tag{5.14}$$

Coupled-cluster amplitudes can then be determined by numerically solving the set of ODEs in Eq. (5.14). The ACF in these single surface cases is obtained from the projection against $\langle 0|$, or the $\Omega_\mu^\dagger = \mathbb{1}$ component.

To evaluate the single-exponential approach we will compare to ED, which is a numerically converged solution in a (large) finite basis. First we calculate an ACF. We then use the `autospec84` module in the MCTDH suite to Fourier transform the ACF resulting in a simulated absorption spectra. [59] For the single-exponential approach, the simulated absorption spectra agrees extremely well with the ED result.

The appealing feature of this single-exponential ansatz approach, is that it is numerically exact for these quadratic model Hamiltonians. The formal proof of this conclusion is that the CC residual equations are in closed form and the CC amplitudes truncate explicitly at singles and doubles. As shown in Eq. (5.15), when applying Wick's theorem to evaluate triple residual, there are no surviving contractions, provided that $\hat{H}$ is at most quadratic.

$$\langle 0|\,\hat{a}_i\hat{a}_j\hat{a}_k\left(\hat{H}e^{\hat{T}}\right)_{conn.}|0\rangle = 0 \tag{5.15}$$

Although with this appealing feature of numerical exact for the single surface quadratic Hamiltonian, we find difficulties to generalize the single-exponential ansatz approach to the full vibronic coupling problem due to the non-unitary property of it. In the single-exponential ansatz, we essentially parameterize the quantum propagator $e^{-i\hat{H}\tau}$, as it acts on the reference state

$$e^{\hat{T}}\,|0\rangle \equiv e^{-i\hat{H}\tau}\,|0\rangle\,. \tag{5.16}$$

The quantum propagator $e^{-i\hat{H}\tau}$ is an unitary operator while the exponential ansatz is non-unitary. For single-surface harmonic vibrational problems, the norm of time-dependent wavefunction and the energy expectation value are conserved, as they are numerically exact. The constant term t_0 in the operator $\hat{T}$ (Eq. (5.10)) plays a vital role in this regard.

However, we found that the non-unitary property of the single-exponential ansatz is potentially problematic when extending to full vibronic models. Due to non-vanishing disconnected contributions in the CC residual equations, the resulting CC EOM are no longer

[4]For explicit proof of the connectness of the CC equations, please see appendix G.

closed, and therefore the single-exponential ansatz (with singles and doubles truncation) becomes an approximate method rather than numerically exact. When applying the single-exponential ansatz to the full vibronic models, we observed divergence of the norm and energy expectation values. [5] As a consequence, both the simulated CC amplitude and the ACF diverges from our ED result (obtained using a converged finite basis).

To resolve this divergence issue, we propose another ansatz (Linear CI) that has a unitary parameterization and therefore when extending to full vibronic models the norm and energy expectation values are conserved.

2. Linear CI approach ($|\psi\rangle = \hat{Z}\,|0\rangle$))

The second ansatz we introduce is the linear configurational interaction (CI) ansatz,

$$|\psi\rangle = \hat{Z}\,|0\rangle\,, \tag{5.17}$$

whose CI operator is truncated at SD:

$$\hat{Z} = z_0 + \sum_i z^i \hat{a}_i^\dagger + \frac{1}{2}\sum_{ij} z^{ij}\hat{a}_i^\dagger \hat{a}_j^\dagger. \tag{5.18}$$

Applying the linear CI ansatz to the TDSE, we form the EOM:

$$i\,\langle 0|\,\Omega_\mu^\dagger \frac{\mathrm{d}\hat{Z}}{\mathrm{d}\tau}\,|0\rangle = \langle 0|\,\Omega_\mu^\dagger \hat{H}\hat{Z}\,|0\rangle\,. \tag{5.19}$$

As shown in Fig. 5.2b, it turns out that CISD is a poor approximation to the exact solution of the Schrödinger equation. The CISD absorption spectra has large deviations when compared to ED. This result is expected, since the CISD approximation is essentially equivalent to exact diagonalization of the full Hamiltonian in a H.O. basis truncated to only two-fold excitations. Such a basis set is too small to produce converged results for energy eigenvalues. Unlike the single-exponential ansatz, which is fully connected and numerically exact, the linear CI ansatz is not explicitly connected and also very approximate. In contrast to CCSD, in CISD, the triples residuals are non-zero in the singles and doubles approximation. In Eq. (5.19), the right hand side of the equation is not connected and as a result the exact CI equations do not rigorously truncate ever for Bosonic systems.

Although the linear CI ansatz has insufficient accuracy, its unitary property plays an important role when extending to general vibronic models, since it dramatically improves the numerical robustness of time integration.

Recall that our goal is to design an ansatz that keeps a balance between accuracy and robustness. We have seen that the single-exponential ansatz is accurate but not robust (for multi-surface models), while the linear CI ansatz is robust but not accurate. Therefore, we propose another ansatz that combines the good features of these two ansätze, attempting to improve both accuracy and robustness.

[5] Divergence was not guaranteed, but with enough regularity ($>$ 90% of our testing) divergence was observed after propagating the ACF longer than 50fs (in the full vibronic models)

3. Mixed CC/CI approach ($|\psi\rangle = e^{\hat{T}}\hat{Z}\,|0\rangle$)

The mixed CC/CI ansatz is a hybridization of the single-exponential ansatz and the linear CI ansatz. It is defined as follows

$$|\psi\rangle = e^{\hat{T}}\hat{Z}\,|0\rangle\,, \tag{5.20}$$

where

$$\hat{T} = \sum_i t^i \hat{a}_i^\dagger, \tag{5.21}$$

and

$$\hat{Z} = z_0 + \sum_i z^i \hat{a}_i^\dagger + \frac{1}{2}\sum_{ij} z^{ij}\hat{a}_i^\dagger \hat{a}_j^\dagger. \tag{5.22}$$

Let us note that we limit $\hat{T}$ to single "excitations" only as otherwise the approach would become exact again. Substituting this ansatz into the TDSE and projecting with $\langle 0|\,\Omega_\mu^\dagger e^{-\hat{T}}$ (where $\Omega_\mu^\dagger$ is defined in Eq. (5.13)) results in new EOM:

$$\langle 0|\,\Omega_\mu^\dagger \left(i\frac{\mathrm{d}\hat{T}}{\mathrm{d}\tau}\hat{Z} + i\frac{\mathrm{d}\hat{Z}}{\mathrm{d}\tau}\right)|0\rangle = \langle 0|\,\Omega_\mu^\dagger \bar{H}\hat{Z}\,|0\rangle\,, \tag{5.23}$$

where

$$\bar{H} = e^{-\hat{T}}\hat{H}e^{\hat{T}} = \left(\hat{H}e^{\hat{T}}\right)_{conn.}. \tag{5.24}$$

The left hand side of Eq. (5.23) has two unknown terms ($\frac{\mathrm{d}\hat{T}}{\mathrm{d}\tau}$ and $\frac{\mathrm{d}\hat{Z}}{\mathrm{d}\tau}$) and therefore does not have a unique solution. Since the manner in which these terms are specified is essentially redundant, there is freedom to choose the manner in which we partition the right hand side, or "net residual", of Eq. (5.23) in terms of the $\hat{T}$ and $\hat{Z}$ residuals. With this freedom, we choose to specify the EOM for $\hat{T}$ first, and then by definition the EOM for $\hat{Z}$ is the remaining part of Eq. (5.23)

We specify the EOM for $\hat{T}$ in the same manner as traditional CC singles EOM (as shown in Eq. (5.14)) and can then form EOM for $\hat{T}$:

$$i\frac{\mathrm{d}t^i}{\mathrm{d}\tau} = \bar{H}^i. \tag{5.25}$$

By substituting Eq. (5.25) into Eq. (5.23), we can form EOM for $\hat{Z}$:

$$i\,\langle 0|\,\Omega_\mu^\dagger \frac{\mathrm{d}\hat{Z}}{\mathrm{d}\tau}\,|0\rangle = \langle 0|\,\Omega_\mu^\dagger \hat{G}\hat{Z}\,|0\rangle\,, \tag{5.26}$$

where

$$\hat{G} = \bar{H} - \sum_i \bar{H}^i. \tag{5.27}$$

To determine the $\hat{T}$ and $\hat{Z}$ amplitudes as functions of time, we solve the coupled ODEs

in Eq. (5.25) and Eq. (5.26) through the numerical real time integration. Each iteration of the numerical integration is comprised of three stages. First, we perform the similarity transform of the Hamiltonian in Eq. (5.24). Then, we equate the $\bar{H}^i$ element of the similarity transformed Hamiltonian $\bar{H}$ to $\frac{\mathrm{d}\hat{T}^i}{\mathrm{d}\tau}$ based on Eq. (5.25). Lastly, we determine $\frac{\mathrm{d}\hat{Z}}{\mathrm{d}\tau}$ using Eq. (5.26) and propagate the differential EOM.

As shown in Fig. 5.2c, the mixed CC/CI ansatz is no longer numerically exact. As in the case of linear CI ansatz, the EOMs for Z in Eq. (5.26) are not in a closed form and the $\hat{Z}$ amplitude equation does not strictly truncate at any excitation level. However, it is not surprising that the mixed CC/CI ansatz can reach considerable accuracy when compared to ED. This is because the linear coupling constants are the dominant terms in the vibrational model Hamiltonian, and the $\hat{T}$ amplitude, which has an exponential parameterization, accounts for the linear coupling contributions in the CC EOM. Meanwhile, $\hat{Z}$'s amplitude mainly takes account of remaining quadratic coupling contributions in the time-dependent wave-function, which are much smaller than the linear coupling contributions.

When applied to vibronic models, the mixed CC/CI ansatz improves the robustness when compared to the single-exponential ansatz, because the $\hat{Z}$ component of the ansatz has a linear parameterization which is unitary.

However, it turns out that the mixed CC/CI ansatz can still have numerical divergence issues when being directly extended to full vibronic models. In the next section, we introduce one final refinement based on mixed CC/CI ansatz that further improves both accuracy and robustness.

4. Modified projection manifold approach ($\langle 0| \Omega_\mu^\dagger e^{\hat{T}^\dagger}$)

For the final approach we adopt the mixed CC/CI ansatz described in the previous section, but modify the projection manifold by introducing the operator $e^{\hat{T}^\dagger}$

$$\langle 0| \Omega_\mu^\dagger e^{\hat{T}^\dagger} e^{-\hat{T}}, \tag{5.28}$$

which is applied to both sides of the EOM in Eq. (5.23)

$$\langle 0| \Omega_\mu^\dagger e^{\hat{T}^\dagger} \left(i\frac{\mathrm{d}\hat{T}}{\mathrm{d}\tau}\hat{Z} + i\frac{\mathrm{d}\hat{Z}}{\mathrm{d}\tau} \right) |0\rangle = \langle 0| \Omega_\mu^\dagger e^{\hat{T}^\dagger} \bar{H}\hat{Z} |0\rangle \tag{5.29}$$

We keep the EOM for $\hat{T}$ amplitudes the same as Eq. (5.25) and then substitute them into Eq. (5.29) to form EOM for $\hat{Z}$ amplitudes.

$$i \langle 0| \Omega_\mu^\dagger \frac{\mathrm{d}\hat{Z}}{\mathrm{d}\tau} |0\rangle = \langle 0| \Omega_\mu^\dagger e^{\hat{T}^\dagger} \hat{G}\hat{Z} |0\rangle - i \langle 0| \Omega_\mu^\dagger \left(e^{\hat{T}^\dagger} - \mathbb{1} \right) \frac{\mathrm{d}\hat{Z}}{\mathrm{d}\tau} |0\rangle \tag{5.30}$$

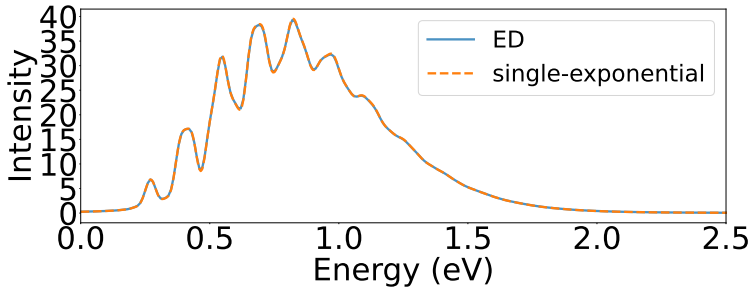
The numerical integration procedure, similar to the previous section, is comprised of three stages for each iteration. A complication, however, is that there are more terms in the $\hat{Z}$ residual equations. To evaluate the $\frac{\mathrm{d}\hat{Z}}{\mathrm{d}\tau}$ term, we need to solve the equation in a descending sequence, from highest order of truncation to lowest order truncation. This is because the higher order $\frac{\mathrm{d}\hat{Z}}{\mathrm{d}\tau}$ operators contribute to the lower rank sector when multiplied by $e^{\hat{T}^\dagger}$, and they need to be consecutively substituted into lower order $\hat{Z}$ residuals.

Comparing to the EOM of $\hat{Z}$ in the previous section Eq. (5.26), the introduction of the modified projection manifold complicates the EOM of $\hat{Z}$.

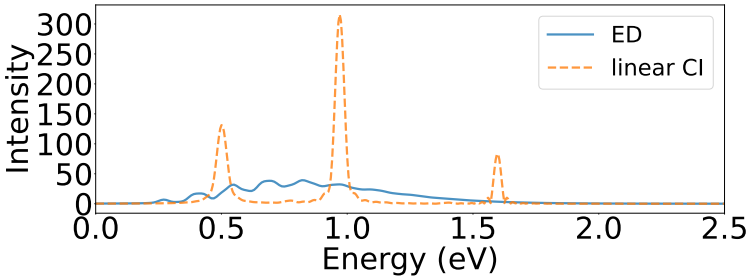
It is gratifying that modifying the projection manifold using $e^{\hat{T}^\dagger}$ notably improves agreement with ED as seen in Fig. 5.2d. Interestingly, the formal parameterization of the wavefunction has not improved, but the values for the parameters have improved.

If one does not adjust the projection manifold one may get ill defined equations for the time-derivatives, and they can easily start to diverge in multistate problems. This is the situation one needs to avoid, and adjustment of the projection manifold to capture the position of the wave packet appears to be effective, and robust.

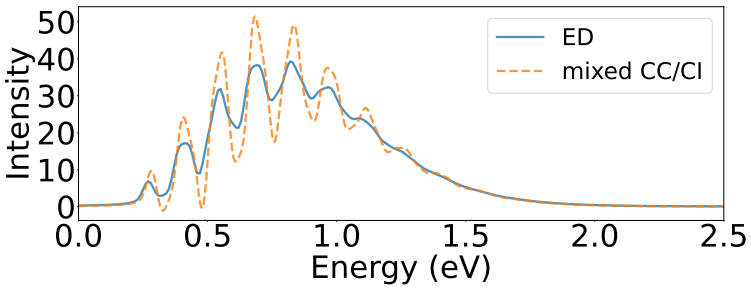
The scheme described in this section will be adopted and extended to the full vibronic models. We will elaborate in more detail the reason why the parameters can be improved by introducing the modified projection manifold insection 5.3.3. In a full vibronic model, when introducing multiple electronic surfaces, the partition of $\hat{T}$ and $\hat{Z}$ residual becomes more complicated. In the following sections, we will describe how to tackle these complications and optimize the choice of the partitioning of $\hat{T}$ residual.



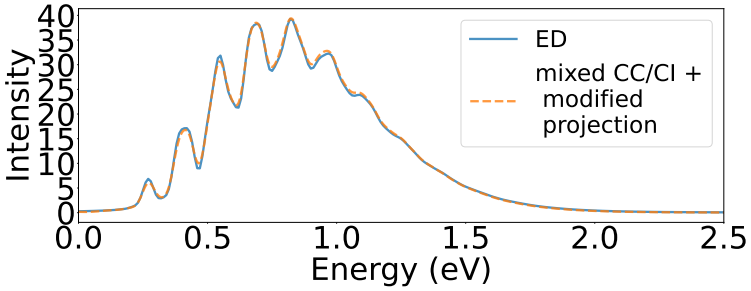
(a) Single-exponential ansatz



(b) Linear CI ansatz



(c) Mixed CC/CI ansatz



(d) Mixed CC/CI ansatz with modified projection manifold

Figure 5.2: Comparison of the different absorption spectra produced by the single-surface approaches. Spectra are benchmarked using ED.

5.3.3 Approach for full vibronic models

In this section we develop the VECC parameterization for general multi-surface vibronic models, and we will discuss the detailed EOMs for all the parameters. Given a vibronic

model Hamiltonian, as described in Eq. (5.2), our goal is to develop a computational method that can efficiently simulate the non-adiabatic dynamics of the model, with a focus on the ACF and diabatic state population. In the following sections, we will discuss how to extend the robust mixed CC/CI ansatz (defined in section 5.3.2) from single-surface vibrational models to full vibronic models.

We choose to truncate $\hat{T}$ at singles for two reasons: First, we show that T_2 has minor effect for single-surface quadratic vibrational-models (compare to ED). The same argument can also be applied for the fully vibronic coupling case. Second, as will be shown later, adding T_2 in the ansatz will complicate the expression of the diabatic state population, as well as other time-dependent properties. For consistency reasons we use only singles in $\hat{T}$ also when calculating ACF.

We firstly outline a straightforward extension. Then, we improve on this extension using an Ehrenfest parameterization. Finally, we present additional manipulations, which result in a significantly simplified computational procedure for the propagation of the amplitudes.

1. Extending the single-surface approach to multiple surfaces

The full wave-function of non-adiabatic vibronic models can be expressed as a linear combination of electronic states, which are each initiated in a single diabatic electronic state b

$$|\Psi(\tau)\rangle = \sum_b \chi_b \, |\psi(\tau)\rangle_b \,, \tag{5.31}$$

where the weight of each electronic state χ_b is the transition dipole moment, which we assume to be independent of geometry, as is reasonable for vibronic models.

At $\tau = 0$ we assume, for each electronic surface, that all vibrational modes are in their ground vibrational state

$$|\psi(\tau = 0)\rangle_b = |b, 0\rangle \,, \tag{5.32}$$

where the labels b and 0, in the RHS ket $|b, 0\rangle$, denote electronic surface b and ground vibrational levels (using GS normal modes) respectively. The initial state of the quantum dynamics propagation can then be defined as: [6]

$$|\Psi(\tau = 0)\rangle = \sum_b \chi_b \, |b, 0\rangle \,. \tag{5.33}$$

The wave-function of each electronic state, b is parameterized using the mixed CC/CI ansatz

$$|\psi(\tau)\rangle_b = \sum_x e^{\hat{T}(\tau)} \hat{Z}_x(\tau) \, |x, 0\rangle \,, \tag{5.34}$$

where

$$\hat{T} = \sum_i t^i \hat{a}_i^\dagger, \tag{5.35}$$

[6] This initial condition can be further generalized to adapt to different experimental setups, but these generalizations are beyond the scope of this chapter.

and

$$\hat{Z}_x = z_x^0 + \sum_i z_x^i \hat{a}_i^\dagger + \frac{1}{2}\sum_{ij} z_x^{ij} \hat{a}_i^\dagger \hat{a}_j^\dagger. \tag{5.36}$$

As in the case of the single-surface vibrational problem in Eq. (5.20), this ansatz consists of two components: $\hat{T}$ and $\hat{Z}$. The $\hat{T}$ operator is truncated at singles and has an exponential parameterization. Importantly it has no electronic-surface dependence. The operator $\hat{Z}$ is truncated to singles and doubles and has a linear CI-like parameterization. It has components specific for each diabatic electronic state. Let us emphasize that the time propagation for each state $|\psi(\tau)\rangle_b$ is independent. The time-correlation function combining the information from the individual state propagations and transition dipoles is assembled later.

Substituting Eq. (5.34) into the TDSE and projecting against $\langle y, 0| \, \Omega_\mu^\dagger e^{-\hat{T}}$ gives the following EOM:

$$\langle y, 0| \, \Omega_\mu^\dagger \left(i\frac{\mathrm{d}\hat{T}}{\mathrm{d}\tau}\hat{Z}_y + i\frac{\mathrm{d}\hat{Z}_y}{\mathrm{d}\tau} \right) |y, 0\rangle = \sum_x \langle y, 0| \, \Omega_\mu^\dagger \bar{\boldsymbol{H}} \hat{Z}_x \, |x, 0\rangle \, , \tag{5.37}$$

where

$$\bar{\boldsymbol{H}} = e^{-\hat{T}} \hat{\boldsymbol{H}} e^{\hat{T}} = \left(\hat{\boldsymbol{H}} e^{\hat{T}} \right)_{conn.} . \tag{5.38}$$

In Eq. (5.38) we transform each individual electronic component $\hat{H}_b^a$ with the same purely vibrational operator $e^{\hat{T}}$ and the result is connected.

As in the case of the single-surface approach, we modify the projection manifold by inserting $e^{\hat{T}^\dagger}$ to produce new EOM:

$$\langle y, 0| \, \Omega_\mu^\dagger e^{\hat{T}^\dagger} \left(i\frac{\mathrm{d}\hat{T}}{\mathrm{d}\tau}\hat{Z}_y + i\frac{\mathrm{d}\hat{Z}_y}{\mathrm{d}\tau} \right) |y, 0\rangle = \sum_x \langle y, 0| \, \Omega_\mu^\dagger e^{\hat{T}^\dagger} \bar{H}_x^y \hat{Z}_x \, |x, 0\rangle \, . \tag{5.39}$$

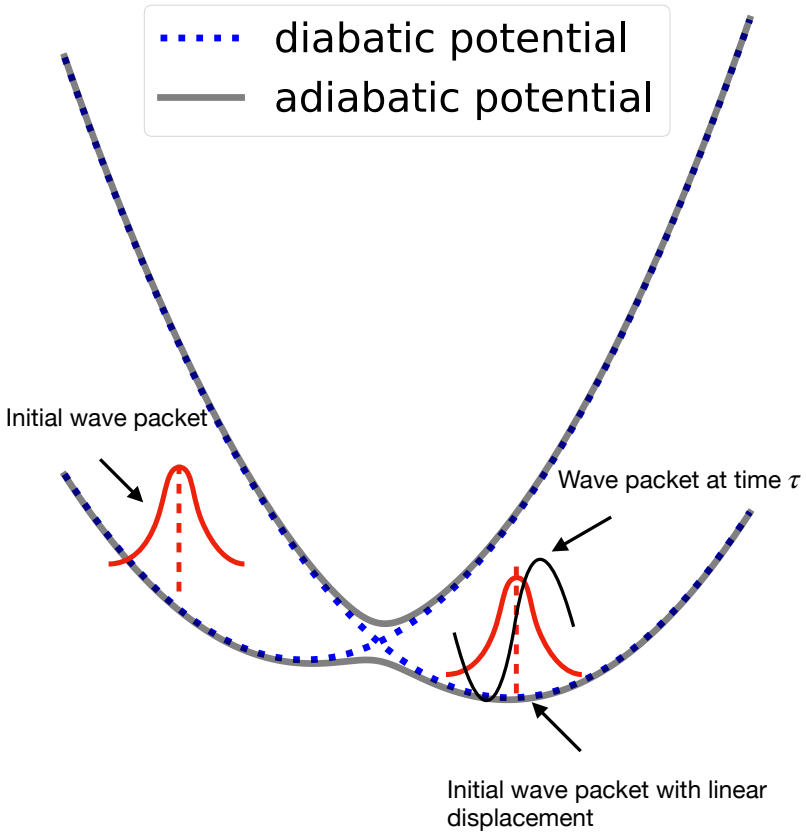


Figure 5.3: By introducing $e^{\hat{T}^\dagger}$, we shift the center of the initial wave-function, or reference state, to align it with the current wave-function at time τ.

As illustrated in Fig. 5.3, the goal of introducing this modification of the projection manifold is the same as in the single-surface case. It shifts the center of the reference state to align with the center of the moving wave-packet, thereby incorporating contributions of higher level excitations in the linear $\hat{Z}$ ansatz.

In the mixed CC/CI parametrization, the exponential part $e^{\hat{T}_1} |0, x\rangle$ serves as a moving Gaussian wave-packet that includes a linear displacement or (passively) the geometry change effect. Likewise, when acting on the bra state $\langle 0, x| e^{T_1^\dagger}$, it brings the linear displacement.

Because the excitation operators $\hat{\Omega}_\mu^\dagger$ commute with $e^{\hat{T}_1^\dagger}$, the states $\langle 0, x| \hat{\Omega}_\mu^\dagger e^{\hat{T}_1^\dagger}$ represent excitations out of a moving reference state, which follows the time-dependent wavefunction. This is a more suitable projection manifold than exciting from the initial state, which can easily lead to near singular equations, because of near zero overlap at later times. This explains why the values of the parameters in the mixed CC/CI approach are improved by introducing the modified projection manifold.

This modification improves both the accuracy and robustness.

Similar to the single-surface vibrational problem, the parameterization of the mixed CC/CI ansatz here is redundant. One is free to choose how to partition the $\hat{T}$ and $\hat{Z}$ residuals from the "net residual" in the right hand side of Eq. (5.39). One straightforward choice is to parameterize $\hat{T}$ as the diagonal matrix elements of $\bar{H}$ (for the initial state b) as a direct analogy to the single-reference case (see Eq. (5.25)):

$$i\frac{\mathrm{d}t^i}{\mathrm{d}\tau} = \bar{H}^i_{bb}. \tag{5.40}$$

By definition the EOM for $\hat{Z}$ are the remaining components of Eq. (5.39).

We have therefore extended our mixed CC/CI ansatz from single-surfaces to general multi-surface vibronic models. By evaluating the equations in this section we can efficiently simulate the non-adiabatic dynamics of the model.

While straightforward, this computational method has problems due to our partitioning of the $\hat{T}$ and $\hat{Z}$ residuals. In Eq. (5.34), the sum over x is a sum over all electronic states. $\hat{T}$ has no electronic label while $\hat{Z}$ has electronic surface dependence. At this stage the $\hat{T}$ operator only captures the diagonal surface contributions from the initial state b, while the $\hat{Z}$ operator captures both the diagonal and off-diagonal contributions of the time dependent wave-function. This is not ideal as the dominant contributions (the exponential operator which includes infinite fold excitations in the Taylor series expansion) do not incorporate the surface crossing contributions of the time dependent wave-function.

To tackle this, we devise an improved parameterization of the $\hat{T}$ (and therefore $\hat{Z}$) residuals in the following section. This parameterization accommodates the switching of electronic surfaces of the moving wave-packet which, to some extent, allows $\hat{T}$ to incorporate surface-crossing contributions of the time-dependent wave-function.

2. Ehrenfest parameterization of $\hat{T}$ residuals

The $\hat{T}$ component in the ansatz (Eq. (5.34)) has an exponential parameterization which incorporates high level excitations from its Taylor series expansion. Therefore if the $\hat{T}$ component is the dominant contribution of the time-dependent wave-function we should expect more accurate results. Our goal then, is to partition a large portion of the "net residual" on the $\hat{T}$ residual. To achieve this goal, we borrow the idea of Ehrenfest dynamics. Ehrenfest dynamics has been applied to ab-initio molecular dynamics, in which forces on nuclear motion are evaluated by taking weighted averages over all PES contributions when solving the Newtonian EOM [96].

In our case, we parameterize the $\hat{T}$ residual as a "weighted average" over all electronic states, where the weight is the approximated CI coefficient of each electronic state in the time-dependent wave-function. In this way, the $e^{\hat{T}}$ component of the ansatz describes the "average motion" of the wave-packet over all electronic states.

Our Ehrenfest parameterization of the $\hat{T}$ residual is:

$$i\frac{\mathrm{d}t^i}{\mathrm{d}\tau} = C\sum_y \left(c_y^0\right)^* R_y^i, \tag{5.41}$$

where R_y^i is defined as the singles residual, containing only the constant order contributions of $\hat{Z}$:

$$R_y^i = \sum_x \langle y,0|\, \hat{a}_i e^{\hat{T}^\dagger} \bar{H} z_x^0 \,|x,0\rangle\,. \tag{5.42}$$

By setting the coefficients to be the zero order component of $\hat{Z}$ ($c_y^0 = z_y^0$) they essentially parameterize the Hermitian conjugate of the zero order component of the wave-function:

$$\langle\psi_0| \approx \sum_x \langle x,0|\,(z_x^0)^* = \sum_x \langle x,0|\,(c_x^0)^*. \tag{5.43}$$

In practice, our choice of the c_y^0 coefficients is different due to considerations discussed in the next section. The coefficient C is the real, positive normalization constant

$$C = \left(\sum_y \left(c_y^0\right)^* c_y^0\right)^{-1}. \tag{5.44}$$

By taking the electronic state average to parameterize the $\hat{T}$ residual, the surface crossing contribution of the time-dependent wave-function is incorporated. For vibronic models with strong coupling, the wave-packet might be switched from its initial PES to another PES (or some linear combination) during the propagation. The Ehrenfest dynamics parameterization of $\hat{T}$ residual can accommodate this change of surfaces through the weighted average over all electronic states. When a switch occurs, the surface that the wave-packet switched to will have dominant weight in the time-dependent wave-function.

Using the Ehrenfest parameterization of $\hat{T}$, by substituting Eq. (5.41) into Eq. (5.39), we

formulate the new EOMs for $\hat{Z}$

$$\begin{aligned} i \left\langle y,0\right| \Omega_\mu^\dagger \frac{\mathrm{d}\hat{Z}_y}{\mathrm{d}\tau} \left|y,0\right\rangle = & \sum_x \left\langle y,0\right| \Omega_\mu^\dagger e^{\hat{T}^\dagger} \hat{\boldsymbol{G}} \hat{Z}_x \left|x,0\right\rangle \\ & - i \left\langle y,0\right| \Omega_\mu^\dagger \left(e^{\hat{T}^\dagger} - \mathbb{1}\right) \frac{\mathrm{d}\hat{Z}_y}{\mathrm{d}\tau} \left|y,0\right\rangle \end{aligned} \tag{5.45}$$

where

$$\hat{G} \equiv \bar{\boldsymbol{H}} - i\frac{\mathrm{d}\hat{T}}{\mathrm{d}\tau}\mathbf{1} \tag{5.46}$$

The formulation described above gives an efficient computational method to simulate wave-packet dynamics of non-adiabatic vibronic models. By introducing the idea of Ehrenfest dynamics to partition the $\hat{T}$ residual, we have improved the choice of the $\hat{T}$ residual parameterization. Because $\hat{T}$'s EOM (Eq. (5.41)) are coupled to $\hat{Z}$'s EOM (Eq. (5.45)), both the $\hat{T}$ and $\hat{Z}$ components of the ansatz incorporate the vibronic coupling effects.

Next, we introduce a minor modification of the current scheme. The motivation to introduce this modification is purely technical; the modification does not affect the end result, but rather simplifies the software implementation and increases the computational efficiency.

3. Simplification of the EOM through similarity transformation

As been discussed previously, the modified projection manifold can improve both robustness and accuracy of the VECC method. However, there are some practical challenges with implementing the modification. The $e^{\hat{T}^\dagger}$ operator will dramatically increase the number of terms in the CC residual equations. This has two side effects. It increases the difficulty of manually deriving the CC residual equations and the corresponding EOM. It also results in more terms being present in the CC residual equations, which makes the computational method more expensive. In order to reduce the chance of human errors in deriving the working equations as well as reduce the computational cost, we introduce a modification of the scheme described in the last section.

We insert resolutions of identity $\left(e^{-\hat{T}^\dagger} e^{\hat{T}^\dagger}\right)$ into Eq. (5.39):

$$\begin{aligned} & \langle y,0|\Omega_\mu^\dagger e^{\hat{T}^\dagger} \left(i\frac{\mathrm{d}\hat{T}}{\mathrm{d}\tau} \left(e^{-\hat{T}^\dagger} e^{\hat{T}^\dagger}\right) \hat{Z}_y + i\frac{\mathrm{d}\hat{Z}_y}{\mathrm{d}\tau} \right) \left|y,0\right\rangle = \\ & \sum_x \left\langle y,0\right| \Omega_\mu^\dagger e^{\hat{T}^\dagger} \bar{\boldsymbol{H}} \left(e^{-\hat{T}^\dagger} e^{\hat{T}^\dagger}\right) \hat{Z}_x \left|x,0\right\rangle . \end{aligned} \tag{5.47}$$

We can simplify Eq. (5.47) by defining four new quantities

$$\tilde{\bar{\boldsymbol{H}}} \equiv e^{\hat{T}^\dagger} \left(\bar{\boldsymbol{H}}\right) e^{-\hat{T}^\dagger} = \left(e^{\hat{T}^\dagger} \bar{\boldsymbol{H}}\right)_{conn.} \tag{5.48a}$$

$$\hat{\rho} \equiv e^{\hat{T}^\dagger} \left(i\frac{\mathrm{d}\hat{T}}{\mathrm{d}\tau}\right) e^{-\hat{T}^\dagger} = \left(e^{\hat{T}^\dagger} i\frac{\mathrm{d}\hat{T}}{\mathrm{d}\tau}\right)_{conn.} \tag{5.48b}$$

$$\hat{C}_x \left|x,0\right\rangle \equiv \left(e^{\hat{T}^\dagger}\hat{Z}_x\right)\left|x,0\right\rangle = \left(e^{\hat{T}^\dagger}\hat{Z}_x\right)_{conn.}\left|x,0\right\rangle \tag{5.48c}$$

$$\hat{D}_y \left|y,0\right\rangle \equiv \left(e^{\hat{T}^\dagger} - \mathbb{1}\right) i\frac{\mathrm{d}\hat{Z}_y}{\mathrm{d}\tau}\left|y,0\right\rangle \tag{5.48d}$$

that can be used to formulate more compact EOM for $\hat{Z}$:

$$\begin{aligned} i\left\langle y,0\right| \Omega_\mu^\dagger \frac{\mathrm{d}\hat{Z}_y}{\mathrm{d}\tau}\left|y,0\right\rangle = \sum_x \left\langle y,0\right| \Omega_\mu^\dagger \left(\tilde{\tilde{\boldsymbol{H}}} - \hat{\rho}\right)\hat{C}_x \left|x,0\right\rangle \\ - \left\langle y,0\right| \Omega_\mu^\dagger \hat{D}_y \left|y,0\right\rangle . \end{aligned} \tag{5.49}$$

All four quantities can be regarded as similarity transformations, although the last two may not be immediately obvious. It uses $e^{\hat{T}^\dagger}\left|0\right\rangle = \left|0\right\rangle$. In addition, $\tilde{\tilde{\boldsymbol{H}}}$ can be regarded as a doubly-transformed Hamiltonian, first by $e^{\hat{T}}$ from the right, then by $e^{\hat{T}^\dagger}$ from the left. Another detail is that $\hat{C}_x$ from Eq. (5.48c) has the form $c_x^0 + \hat{c}_x^1 + \hat{c}_x^2$ where the constant term c_x^0 defines the weights of electronic states in the Ehrenfest parameterization of $\hat{T}$ amplitude in Eq. (5.41). To numerically integrate the cluster amplitudes we pre-calculate all four intermediate quantities and then use them to calculate the $\hat{Z}$ residuals, as seen in Eq. (5.49).

This new scheme has two main advantages. The first is that we simplify the EOM of $\hat{Z}$. Eq. (5.49) resembles a linear CI equation which has fewer terms in its residual than the exponential form in Eq. (5.45). Consequently, the chance for mistakes when manually deriving the working equations of $\hat{Z}$ is reduced. Secondly, by pre-calculating the intermediate quantities in Eq. (5.48) we avoid repeatedly evaluating them in the CC residuals, which reduces the computational cost compared to the original scheme.

It is important to highlight that the purpose of this similarity transformation scheme is purely technical. The new scheme is mathematically equivalent to the previous scheme and both will produce identical results. In our opinion, this new concise formulation of VECC theory also bears some aesthetic value. In this way, we have finalized the formal VECC theory for non-adiabatic nuclear dynamics. In the next section we will discuss how to compute time dependent properties using VECC theory.

5.3.4 Calculating time-dependent properties with VECC

As previously described, the general procedure for calculating time-dependent properties using VECC is fourfold: 1. the time-dependent wave-function is parameterized using an ansatz; 2. EOM are formed by substituting that ansatz into the TDSE; 3. cluster amplitudes are obtained by solving these EOM numerically. 4. properties of interest can be mapped from the cluster amplitudes.

In section 5.3.3 we parameterized the time-dependent wave-function using the mixed-CC/CI ansatz. In the previous two sections we outlined the EOM of interest and the expressions for the $\hat{T}$ and $\hat{Z}$ (cluster) amplitudes. In this section we describe the procedure for numerically evaluating those amplitudes and how they are mapped to properties of interest.

We specify the initial conditions of the amplitudes:

$$\hat{T}(\tau = 0) = \mathbf{0}, \tag{5.50a}$$

$$\hat{Z}_x(\tau = 0) = \delta_{x,b}, \tag{5.50b}$$

where the surface label b denotes the electronic surface of interest. Time-integration of the $\hat{T}$ and $\hat{Z}$ amplitudes (as given in Eq. (5.41) and Eq. (5.49)) is performed one surface (b) at a time. Because these amplitudes parameterize the time-dependent wave-function $|\Psi(\tau)\rangle$, time-dependent properties can be mapped through the amplitudes. We will first look at the ACF.

1. Calculation of time-autocorrelation function (ACF)

To compute the ACF, we first construct the matrix elements of the quantum propagator

$$U_{ab} \equiv \langle a, 0| \, e^{-i\hat{H}\tau} \, |b, 0\rangle \,, \tag{5.51}$$

in a "column by column" fashion. Each column b is obtained by numerical time integration starting from it's initial conditions (as specified in Eqs. (5.50a) and (5.50b)). [7]

$$U_{ab} = \langle a, 0| \, e^{\hat{T}} \sum_y \hat{Z}_y \, |y, 0\rangle = z_a^0 \quad \text{for } b \in \{b_1, b_2, \cdots\} \tag{5.52}$$

By substituting the expression of the $\mathbf{U}$ matrix from Eq. (5.52) into the definition of the ACF in Eq. (5.3), we can map it to the CC amplitudes:

$$\begin{aligned} C(\tau) &= \langle \Psi(t = 0) | \Psi(t = \tau) \rangle \\ &= \sum_{ab} \chi_a \, \langle a, 0| \, e^{-i\hat{H}\tau} \, |b, 0\rangle \, \chi_b \\ &\equiv \sum_{ab} \chi_a U_{ab}(\tau) \chi_b, \end{aligned} \tag{5.53}$$

where χ_b denotes the transition dipole moment of the diabatic electronic state b. [8] Thus, by calculating $U_{ab}(\tau)$ we can straightforwardly obtain the ACF for a system of interest.

[7] In practice, to better mimic the experimental setups, we turn off the cross contribution or $\forall a \neq b U_{ab} = 0$.

[8] In Eq. (5.53), we assume that the transition dipole moment is along one dimension. In practice, we can have transition dipole moment data that is along the x,y,z dimensions. We then calcuate the ACF along one direction at a time using Eq. (5.53) and then take that average of the three dimensions (divided by three).

2. General expression for expectation value $\langle O(\tau)\rangle$

In general, the time-dependent expectation value for a quantum operator $\hat{O}$ is defined as

$$\langle O(\tau)\rangle = \frac{\langle\psi(\tau)|\hat{O}|\psi(\tau)\rangle}{\langle\psi(\tau)|\psi(\tau)\rangle}. \tag{5.54}$$

The evaluation of this expression for a general operator is nontrivial. The first challenge is that in conventional coupled-cluster theory for electronic structure, the cluster expansion series for both the numerator and denominator are formally infinite (when directly applying the CC ansatz into them). Another concern is that the CC amplitudes are not small in general. However, in VECC theory we use a series of mathematical manipulations to evaluate terms without truncation, and in a simple manner. The essential idea is to introduce a similarity transformation to cancel out the disconnected contributions in the expression, resulting in a finite expansion of the CC amplitudes. In this section, we derive a mathematical expression for a general time-dependent property as given by Eq. (5.54) in a concise form (finite expansion).

We begin by evaluating the denominator in Eq. (5.54), using the VECC ansatz from Eq. (5.34):

$$\langle\psi(\tau)|\psi(\tau)\rangle = \sum_{x,y} \langle y,0|\, \hat{Z}_y^\dagger e^{\hat{T}^\dagger} e^{\hat{T}} \hat{Z}_x \,|x,0\rangle\,. \tag{5.55}$$

Let us note here that we assume a single propagated wave function in this section, and do not propagate a superposition of states starting from an initial state for each surface. This simplifies the procedure and serves our current purposes. We insert a resolution of the identity

$$\langle\psi(\tau)|\psi(\tau)\rangle = \sum_{x} \langle x,0|\, \hat{Z}_x^\dagger \left(e^{\hat{T}} e^{-\hat{T}}\right) e^{\hat{T}^\dagger} e^{\hat{T}} \hat{Z}_x \,|x,0\rangle\,, \tag{5.56}$$

resulting in the term $e^{-\hat{T}} e^{\hat{T}^\dagger} e^{\hat{T}}$, which we can evaluate by expanding using a BCH series

$$e^{\hat{s}_1} \equiv e^{-\hat{T}} e^{\hat{T}^\dagger} e^{\hat{T}} \quad \text{where} \quad \left(\hat{T} \equiv \sum_i t^i \hat{a}_i^\dagger\right), \tag{5.57}$$

such that

$$\begin{aligned} \hat{s}_1 &= \hat{T}^\dagger + \left[\hat{T}^\dagger, \hat{T}\right] + \frac{1}{2!}\left[\left[\hat{T}^\dagger, \hat{T}\right], \hat{T}\right] + \cdots \\ &= \sum_i (t^i)^* \hat{a}_i + s_0 \\ &= \hat{T}^\dagger + s_0 \quad \text{where} \quad s_0 \equiv \sum_i (t^i)^* t^i \end{aligned} \tag{5.58}$$

Notice that this (infinite order) formula is particularly simple when using $\hat{T}$ truncated at singles and this is the prime reason that we use only singles in the $\hat{T}$ operator.

Substituting the BCH series from Eq. (5.58) into Eq. (5.56), results in

$$\begin{aligned}\langle\psi(\tau)|\psi(\tau)\rangle &= \sum_x \langle x,0|\,\hat{Z}_x^\dagger e^{\hat{T}}\left(e^{\hat{T}^\dagger}e^{s_0}\right)\hat{Z}_x\,|x,0\rangle \\ &\equiv e^{s_0}\sum_x \langle x,0|\,\hat{Z}_x^\dagger e^{\hat{T}}e^{\hat{T}^\dagger}\hat{Z}_x\,|x,0\rangle\,.\end{aligned} \tag{5.59}$$

We continue by inserting more resolutions of identity

$$e^{s_0}\sum_x \langle x,0|\,\hat{Z}_x^\dagger e^{\hat{T}}\left(\sum_n |x,n\rangle\langle x,n|\right)e^{\hat{T}^\dagger}\hat{Z}_x\,|x,0\rangle \tag{5.60}$$

such that

$$\langle\psi(\tau)|\psi(\tau)\rangle \equiv e^{s_0}\sum_x\sum_n C_{n,x}^\dagger C_{n,x} \tag{5.61}$$

where

$$C_{n,x} \equiv \langle x,n|\,e^{\hat{T}^\dagger}\hat{Z}_x\,|x,0\rangle\,. \tag{5.62}$$

We can easily expand Eq. (5.60) by applying Wick's theorem. In this fashion we have obtained an expression for the denominator as a finite expansion of the CC amplitudes. Next we apply similar mathematical tricks to evaluate the numerator.

We begin by substituting the VECC ansatz (from Eq. (5.34)) into the expression of the numerator in Eq. (5.54) as follows:

$$\langle\psi(\tau)|\,\hat{O}\,|\psi(\tau)\rangle = \sum_{x,y}\langle y,0|\,\hat{Z}_y^\dagger e^{\hat{T}^\dagger}\hat{O}e^{\hat{T}}\hat{Z}_x\,|x,0\rangle\,. \tag{5.63}$$

We introduce similarity transformations (in the same fashion as we did previously) by inserting a resolution of the identity, transforming $e^{\hat{T}^\dagger}\hat{O}e^{\hat{T}}$ into $e^{\hat{T}^\dagger}e^{\hat{T}}\bar{O}$ where

$$\bar{O} \equiv e^{-\hat{T}}\hat{O}e^{\hat{T}} = \left(\hat{O}e^{\hat{T}}\right)_{conn.}. \tag{5.64}$$

Following that, $e^{\hat{T}^\dagger}e^{\hat{T}}\bar{O}$ is replaced with $e^{\hat{T}}e^{\hat{T}^\dagger}e^{s_0}\bar{O}$ by inserting another resolution of the identity and using the same BCH expansion from Eq. (5.58) ($e^{-\hat{T}}e^{\hat{T}^\dagger}e^{\hat{T}} \to e^{\hat{T}^\dagger}e^{s_0}$). In this manner we can re-express Eq. (5.63) as:

$$\begin{aligned}\langle\psi(\tau)|\,\hat{O}\,|\psi(\tau)\rangle &= \sum_{x,y}\langle y,0|\,\hat{Z}_y^\dagger e^{\hat{T}}e^{\hat{T}^\dagger}e^{s_0}\bar{O}\hat{Z}_x\,|x,0\rangle \\ &\equiv e^{s_0}\sum_{x,y}\langle y,0|\,\hat{Z}_y^\dagger e^{\hat{T}}e^{\hat{T}^\dagger}\bar{O}\hat{Z}_x\,|x,0\rangle\,.\end{aligned} \tag{5.65}$$

Then, as in Eq. (5.60), we insert an additional resolution of identity:

$$e^{s_0} \sum_{x,y} \langle y,0| \hat{Z}_y^\dagger e^{\hat{T}} \left(\sum_n |y,n\rangle \langle y,n| \right) e^{\hat{T}^\dagger} \bar{O} \hat{Z}_x |x,0\rangle , \tag{5.66}$$

such that

$$\langle \psi(\tau)| \hat{O} |\psi(\tau)\rangle = e^{s_0} \sum_{x,y,n} C_{n,y}^\dagger \langle y,n| e^{\hat{T}^\dagger} \bar{O} \hat{Z}_x |x,0\rangle . \tag{5.67}$$

where the term $\langle y,n| e^{\hat{T}^\dagger} \bar{O} \hat{Z}_x |x,0\rangle$ in Eq. (5.67) has the explicit form of the right hand side in the CC EOM from Eq. (5.39). We can evaluate this term using VECC residual equations of the form in Eq. (5.42) simply by substituting the matrix elements of $\bar{O}$ in place of $\bar{H}$.

Thus, we have derived an expression for both the denominator and numerator of a general time-dependent property, as expressed in Eq. (5.54), with finite truncation of the VECC amplitudes.

We will further simplify Eq. (5.67), by applying the similarity transformation scheme discussed in section 5.3.3. We start by inserting resolutions of the identity:

$$\begin{aligned} &\langle \psi(\tau)| \hat{O} |\psi(\tau)\rangle \\ &= e^{s_0} \sum_{x,y,n} C_{n,y}^\dagger \langle y,n| e^{\hat{T}^\dagger} \bar{O} \left(e^{-\hat{T}^\dagger} e^{\hat{T}^\dagger} \right) \hat{Z}_x |x,0\rangle . \end{aligned} \tag{5.68}$$

As before, we define similarity transformed intermediate quantities (in this case we only define the two quantities for the right hand side):

$$\tilde{\bar{O}} \equiv e^{\hat{T}^\dagger} \bar{O} e^{-\hat{T}^\dagger}, \tag{5.69a}$$

$$\hat{C}_x |x,0\rangle \equiv e^{\hat{T}^\dagger} \hat{Z}_x |x,0\rangle = \left(e^{\hat{T}^\dagger} \hat{Z}_x \right)_{conn.} |x,0\rangle . \tag{5.69b}$$

Substituting these intermediate quantities into Eq. (5.67)

$$\langle \psi(\tau)| \hat{O} |\psi(\tau)\rangle = e^{s_0} \sum_{x,y,n} C_{n,y}^\dagger \langle y,n| \tilde{\bar{O}} \hat{C}_x |x,0\rangle . \tag{5.70}$$

Following the arguments in section 5.3.3 by pre-calculating the intermediate quantities, one can simplify Eq. (5.67) and reduce the computational cost. Additionally, Eq. (5.70) is mathematically equivalent to Eq. (5.67) and the expectation value is invariant with respect to the insertion of the resolution of the identity.

Substituting the numerator expression in Eq. (5.70) and the denominator expression in Eq. (5.61) into Eq. (5.54) we can express the expectation value of a generic time-dependent property (in a finite expansion of the VECC amplitudes) as follows:

$$\left\langle \hat{O}(\tau) \right\rangle = \frac{\sum_{x,y,n} C^{\dagger}_{n,y} \left\langle y, n \right| \tilde{\hat{O}} \hat{C}_x \left| x, 0 \right\rangle}{\sum_{x,n} C^{\dagger}_{n,x} C_{n,x}}. \tag{5.71}$$

Thus, we derived an expression in a concise form.

In the next section we will focus on calculating diabatic state populations, although in general the scheme discussed in this section can be applied to calculate an arbitrary expectation value of time-dependent properties. The implementation of approaches to calculate time-dependent properties other than the diabatic state population is beyond the scope of this paper, but it opens the possibilities for future work.

3. Calculation of diabatic state population

If we are interested in a specific property (e.g. the diabatic state population) we simply choose a form for the operator $\hat{O}$

$$\hat{O} \equiv \sum_{n} \left| a, n \right\rangle \left\langle a, n \right|, \tag{5.72}$$

and substitute it into our concise form in Eq. (5.71) resulting in an expression for the diabatic state population:

$$P_a(\tau) = \frac{\sum_{n} C^{\dagger}_{n,a} C_{n,a}}{\sum_{x,n} C^{\dagger}_{n,x} C_{n,x}}. \tag{5.73}$$

In this way, we have derived a concise expression for the diabatic state population. In our implementation of VECC we use Eq. (5.73) to calculate the diabatic state population. In practice, we begin by determining the $\hat{T}$ and $\hat{Z}$ amplitudes through numerical real-time integration. At each time step, the diabatic state population is mapped from the $\hat{T}$ and $\hat{Z}$ amplitudes in an "on-the-fly" fashion.

5.4 Result and discussion

The VECC approach (described in section 5.3.3) is implemented in the open source code `t-amplitudes`. [170] We evaluate the VECC method at both doubles (SD) and triples (SDT) truncation of the $\hat{Z}$ amplitude and with singles (S) truncation of the $\hat{T}$ amplitude. The explicit working equations used in `t-amplitudes` are generated by the equation generator developed by Raymond et al , whose open source software package `termfactory` is available on GitHub. [171] In the implementation, CC amplitudes are obtained through numerical real-time integration, and time-dependent properties are mapped from those CC amplitudes. Third-party Python libraries `NumPy` and `SciPy` are utilized in this implementation to solve

numerical ODEs and tensor products. [172, 173] The code is optimized to reach high performance.

We simulated the vibrationally-resolved electronic spectra and the diabatic state population for various models. All results are computed using the implementation of the VECC method as described in section 5.3.4. These results are benchmarked against MCTDH and ED.

5.4.1 Summary of vibronic models

In section 5.4.2 we explore representative vibronic spectra and diabatic state population of small two by two models, which have two electronic surfaces and two normal modes. (explicit model parameters shown in the appendix H). Since two by two models have a small number of degrees of freedom, we can afford to compare VECC results against ED in a converged basis set.

The latter can be regarded as numerical exact results. This allows for convenient testing of the VECC method for spectra and diabatic state population simulation for a variety of vibronic models. We will also use these models to test the convergence of VECC method in terms of excitation level of the $\hat{Z}$ operators, in a so-called matrix-based VECC implementation which is only applicable to small models (See appendix H.1 and discussion in section 5.4.2).

In section 5.4.3, we investigate the photo-electron spectra and diabatic state population of "small" molecules, specifically water (H_2O), and ammonia (NH_3) (model parameters available in the appendix H.1). For these models we anticipate good agreement with the (converged) MCTDH results for spectra.

However, we will show that the diabatic state population is still challenging to converge with low ranking (up to triple truncation) $\hat{Z}$ operators.

The goal of this section is to demonstrate the validity of the VECC method for real molecular systems.

Then in section 5.4.4 we investigate the absorption spectra for "larger" molecules, specifically the widely-tested pyrazine ($C_4H_4N_2$), and hexahelicene ($C_{26}H_{16}$), and we use model parameters available in the literature (see below). In these complicated models, we are more focused on qualitative comparison with the MCTDH results. The intention is to highlight the efficiency of the VECC method, while capturing the qualitative spectra.

Due to the qualitative focus and the large number of electronic states for systems such as hexahelicene we chose not to investigate their diabatic state populations.

The two by two models are described by the Hamiltonian:

$$\begin{aligned}\hat{H} &= \hat{K} + \hat{V} \\ &= \begin{bmatrix} E_a + h_0 + \lambda_1 q_1 & 0 \\ 0 & E_b + h_0 + \lambda_2 q_1 \end{bmatrix} + \begin{bmatrix} 0 & \gamma q_2 \\ \gamma q_2 & 0 \end{bmatrix}, \\ h_0 &= \frac{1}{2}\Big(\omega_1 q_1^2 + \omega_2 q_2^2\Big),\end{aligned} \tag{5.74}$$

where E_a and E_b are vertical energies corresponding to the two electronic states, ω_1 and ω_2 are the frequencies for the two vibrational modes, λ_1 and λ_2 are linear displacements corresponding to the two PESs and γ dictates the strength of the Peierls (off-diagonal) vibronic couplings.

Of the various two by two models we tested we discuss three: model A, model B and model C. The models differ only in the linear displacement parameters λ_1 and λ_2. All model parameters are presented in the appendix H.1. These models are typical strong vibronic models since they have a small energy gap between the two electronic states and sizeable Peierls vibronic-coupling constants.

The water and ammonia models were generated using code developed by the Nooijen group. Constructing these models begins by obtaining excited states energies. This was accomplished using electronic structure calculations, specifically an IP-EOMCCSD method. [174, 175, 176, 177, 178, 179, 180] Next, a diabatization procedure was applied using the VIBRON software package. [54] These calculations were performed by Julia Endicott. [181, 182]

The water model (3 states, 3 modes) is a typical weak-coupling system. The energy gap between each electronic state is very large $\sim 3\,\text{eV}$. The vibronic couplings are dominated by Holstein couplings (diagonal matrix elements) and there is only one Peierls coupling (off-diagonal elements).

The ammonia model (3 states, 6 modes) is a typical strong-coupling system. Two of the three states are degenerate JT states whose energy levels are higher than the non-degenerate state. All of the three states are coupled with each other through Peierls couplings. While the two degenerate JT states are strongly coupled with each other, the non-degenerate state is weakly coupled with the two degenerate JT states due to the large energy separation ($\sim 6\,\text{eV}$) between them.

The pyrazine and hexahelicene models were obtained from the literature. The widely-tested pyrazine model was obtained from the reference by Raab et al. [128] This model has 2 electronic states and 24 vibrational modes. The two electronic states have $\sim 1\,\text{eV}$ energy separation. The vibronic-coupling constants are truncated to bilinear couplings. The model parameters, time of propagation, and settings of the Fourier transform are obtained from the reference.

The hexahelicene model was obtained from the reference by Aranda et al. [56] This model has 14 electronic states and 63 vibrational modes. All electronic states in this model are close lying, with $\sim 0.2\,\text{eV}$ energy separation. Vertical energies were computed using TD-DFT with only linear vibronic-coupling constants (LVC). We benchmarked our VECC calculation against the multi-layer (ML)-MCTDH calculation provided in the reference.

5.4.2 two by two models

To illustrate the accuracy of VECC, we compare to ED for the two by two models, which are typical of strong-coupling systems.

Although VECC demonstrates highly accurate spectral simulation of model A and model B, even when using low ranking cluster operators ($\hat{T}$ truncates at S and $\hat{Z}$ truncates at SD

and SDT), the results (shown in the appendix H.2) do not demonstrate convergence. In this section we use model C to explore the convergence behaviour, in terms of the excitation level of $\hat{Z}$ operator, of the VECC approach.

To test the convergence behaviour we use a matrix-VECC approach in which Z-coefficients are propagated up to an arbitrary maximum excitation level `MaxExc`. This approach is computational expensive, compared to the operator-VECC, but it allows for easy testing of higher order excitations. By constructing the matrix elements of the doubly transformed Hamiltonian (plus some additional terms) over H.O. basis states, up to some maximum total excitation level (`MaxExc`) we can propagate Z-amplitudes as a matrix-vector product, while the T_1 amplitudes are solved as before. Both approaches are mathematically equivalent (e.g. $\hat{Z}$:SDT $\equiv$ `MaxExc=3`). The complete matrix-VECC scheme is elaborated in the appendix H.3.

Simulated spectra and diabatic state populations of model C are shown in Fig. 5.4 and Fig. 5.5, respectively. It is clear that VECC reaches convergence at `MaxExc=8`, while ED (not including T_1) requires `MaxExc=80`. This demonstrates that by increasing the excitation order of $\hat{Z}$, the result eventually converges towards to the exact solution.

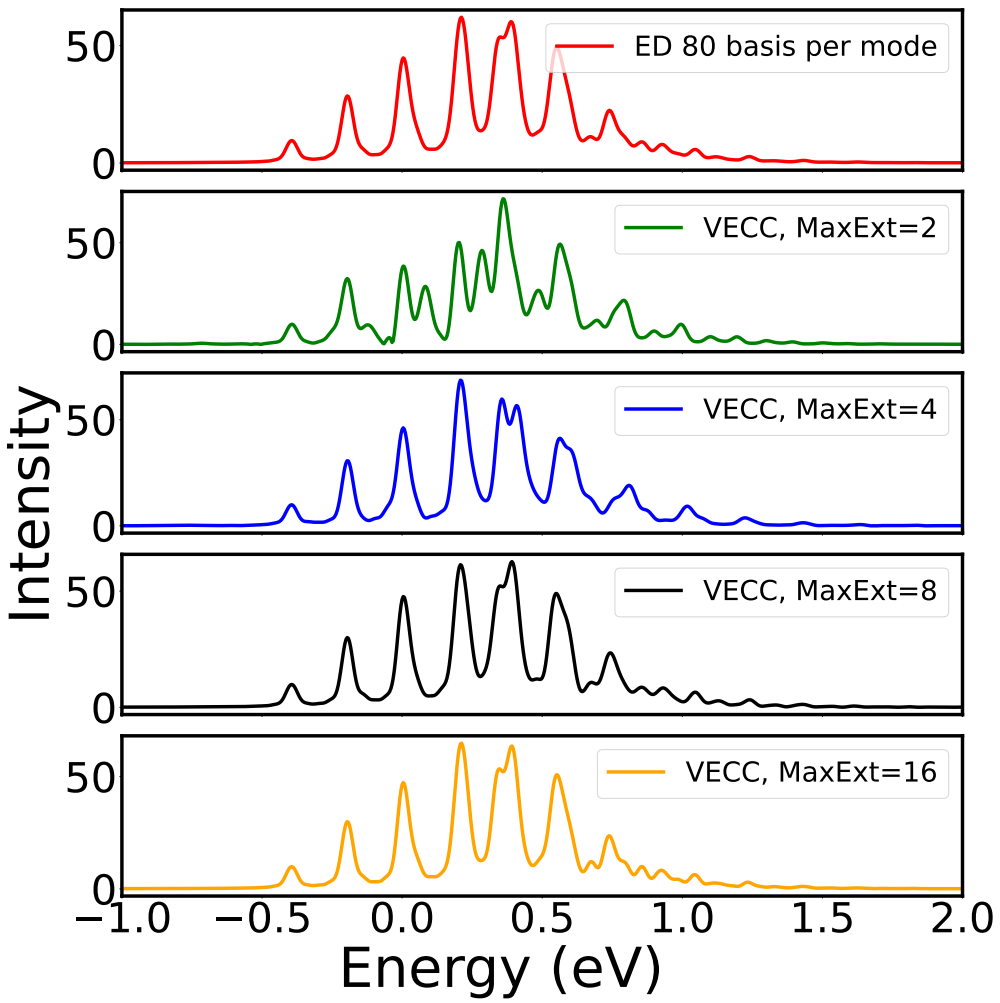


Figure 5.4: Simulated spectra of model-C using VECC and ED. The convergence of VECC is compared against ED for various excitation levels of the $\hat{Z}$ operator.

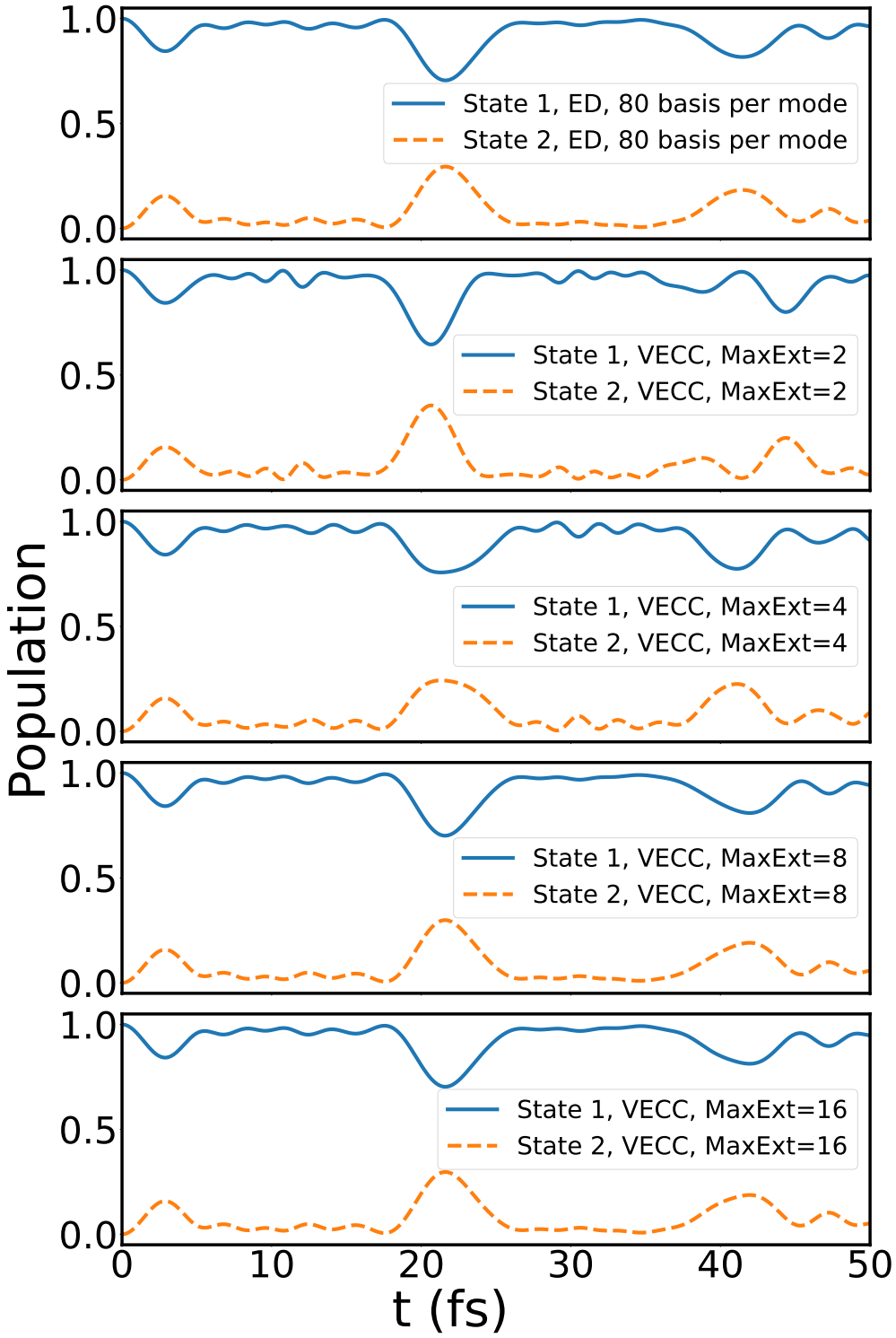


Figure 5.5: Simulated diabatic state population of model-C using VECC and ED. The convergence of VECC is compared against ED for various excitation levels of the $\hat{Z}$ operator.

5.4.3 Small molecules

To further examine the performance of the VECC method, we simulate the photo-electron spectra and diabatic state population of the water and ammonia vibronic models.

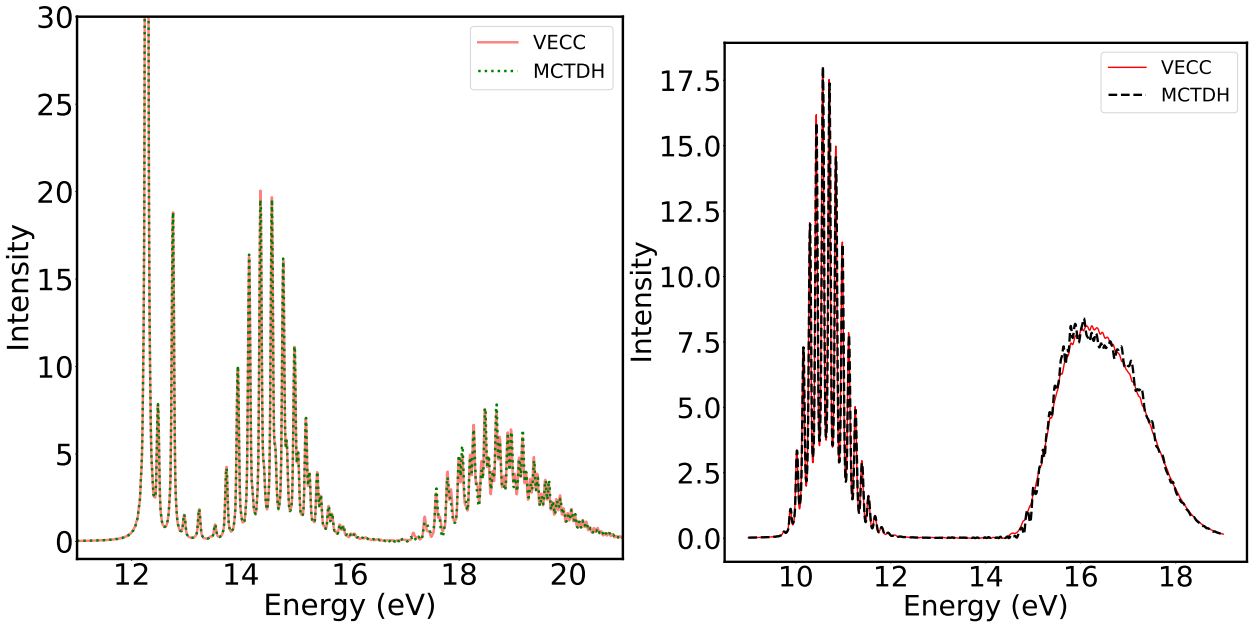
1. Simulation of photo-electron spectra

As shown in Fig. 5.6, we simulate the spectra for water and ammonia molecules and benchmark with the MCTDH method. In both calculations we use $n = 1$ and $\tau = 40$fs when running `autospec` to generate spectra from the ACF. Fig. 5.6a shows the simulated spectra of the water molecule, which is a typical weak-coupling system. The spectra has three bands; each band roughly matching the energy level of one excited electronic state. The bands are broadened by excitations of vibrational levels. In general the spectra match very well, although there are tiny discrepancies on a few peak intensities. We regard them as insignificant. [9]

Fig. 5.6b shows the simulated spectra of the ammonia molecule, which is a typical strong-coupling system. The spectra of the ammonia molecule, has two bands. The higher energy band closely matches the energy level of the two degenerate JT states, and the lower energy band corresponds to the remaining non-degenerate state. For the lower energy band, VECC almost exactly matches MCTDH. In the higher energy band, VECC produces similar peak shape and width compared to MCTDH, but produces slightly different fine-structures, that may be hard to converge.

In general, we show that the VECC method can produce accurate vibrationally-resolved electronic spectra. The VECC method has some difficulties predicting fine-structures consistent with MCTDH for vibronic models with strong coupling. However, the accuracy is acceptable and consistent with experimental spectra, yielding semi-quantitative results. Moreover, the VECC method has a significant advantage in terms of computational runtime compared to the MCTDH method, as well as its ease of use.

[9] Since these two methods are fundamentally different, we do not anticipate that they should produce the exact same result. In particular MCTDH results are subject to truncations of a finite basis set.



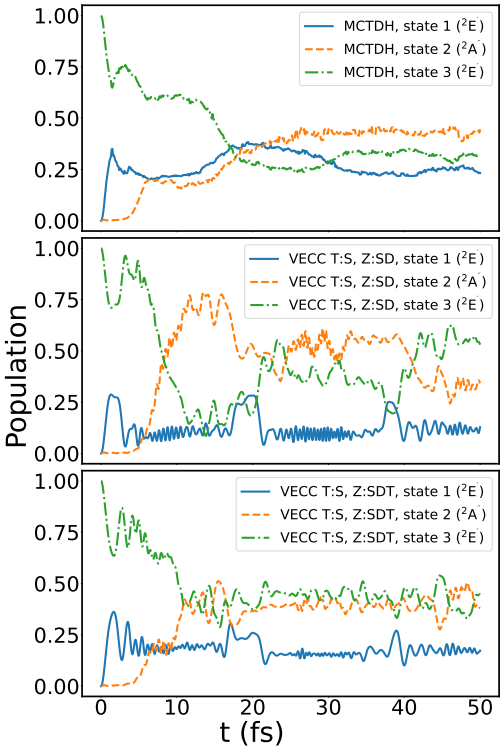
(a) Photo-electron spectra of water after 100 fs propagation.

(b) Photo-electron spectra of ammonia after 100 fs propagation.

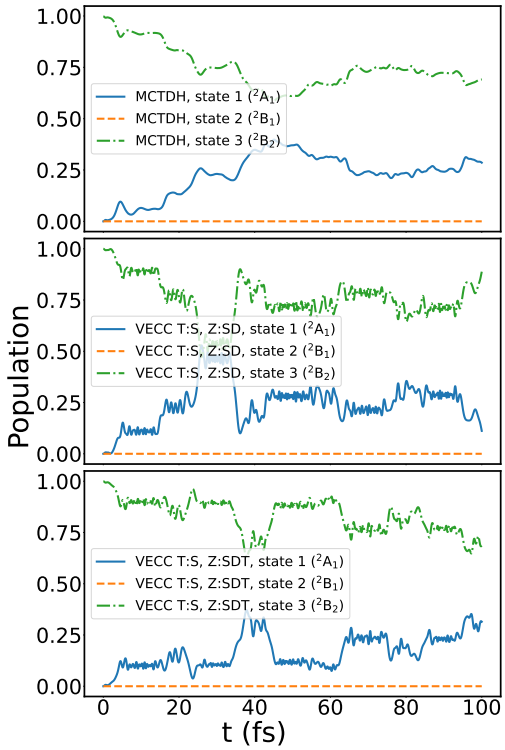
Figure 5.6: Simulated absorption spectra of water and ammonia molecular compounds using VECC and MCTDH. Both are generated through a Fourier transform of their time-autocorrelation functions using `autospec84`.

2. Simulation of diabatic state population

Next we turn to the calculation of diabatic state populations. Fig. 5.7 shows the evolution of the diabatic state populations for ammonia and water. In both plots (in Fig. 5.7a and Fig. 5.7b), we show results for both double and triple truncation of $\hat{Z}$. Though not fully converged with triple $\hat{Z}$, the result tends to converge towards the MCTDH by increase the excitation orders of $\hat{Z}$. In general, the VECC approach qualitatively matches the trend of time evolution of state population of the MCTDH result but with longer periods of quantum coherence, as well as stronger Rabi oscillations.



(a) Diabatic state population of ammonia after 50fs propagation.



(b) Diabatic state population of water after 100fs propagation.

Figure 5.7: Simulated diabatic state population of water and ammonia models using VECC and MCTDH. The symmetry label of each state is listed in parentheses.

The cause of this discrepancy is likely associated with the Ehrenfest parameterization described in section 5.3.3. In this parameterization, we chose $\hat{T}$ to be independent of electronic states and weight-averaged over all electronic states. As shown in Eq. (5.75a) and Eq. (5.75b), each diabatic state is determined by a linear cluster expansion based on a common reference state.

$$|\text{ref}\rangle = e^{\hat{T}(\tau)} \sum_b |b, 0\rangle \tag{5.75a}$$

$$|D_b\rangle = \hat{Z}_b(\tau)\,|\text{ref}\rangle \tag{5.75b}$$

For example, if we choose to truncate the $\hat{Z}$ amplitude at doubles (for each vibration mode) the different diabatic states could differ by, at most, two-fold excitations (in terms of the vibrational degrees of freedom). This has the side effect of preserving the large overlap between the different diabatic states throughout the time evolution. Thus, the VECC populations oscillate more strongly than the MCTDH populations. In general, we need higher excitation of $\hat{Z}$ amplitude to converge the state population calculation in the VECC method which is consistent with the result for the simple two by two models.

5.4.4 Large molecules

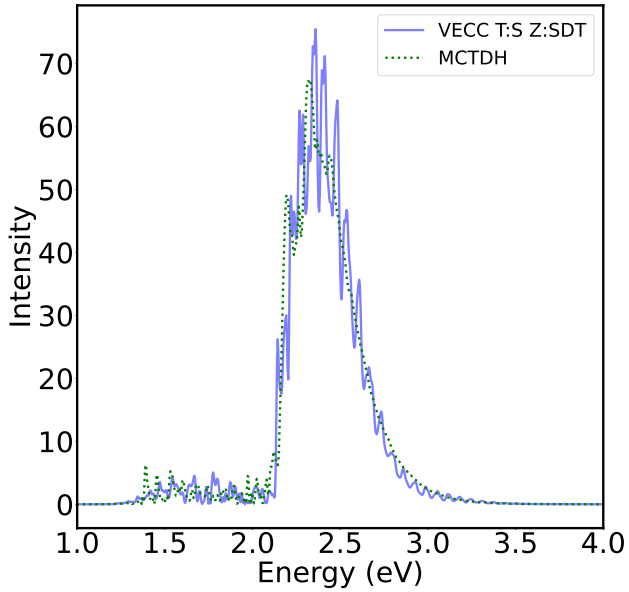
The benchmarks for spectra of small molecular compounds demonstrate that the VECC method is capable of accurately simulating vibronic spectra. To evaluate the efficiency of the VECC method, we benchmark absorption spectra for larger molecular compounds. As shown in Fig. 5.8 and Fig. 5.9, we simulated the absorption spectra of two large molecular compounds pyrazine and hexahelicene. In both calculations, to generate spectra from ACF, we use the same empirical broadening parameters as described in the correspond original references. [56, 128]

The absorption spectra of pyrazine, shown in Fig. 5.8 was simulated using VECC and MCTDH. The spectra has two bands: the lower energy band ranges from 1.4 eV to 2.0 eV and the higher energy band ranges from 2.0 eV to 3.0 eV. The VECC spectra roughly matches the MCTDH spectra in both bands. Compared to MCTDH, the VECC method produces sharper peaks and richer fine-structures in the higher energy band. The cause of the discrepancies between the two methods can be complicated. Note that, as shown in the reference by Raab et al, the MCTDH spectra fails to match the experimental spectra without introducing empirical broadening of the peaks in the Fourier transform. [128]

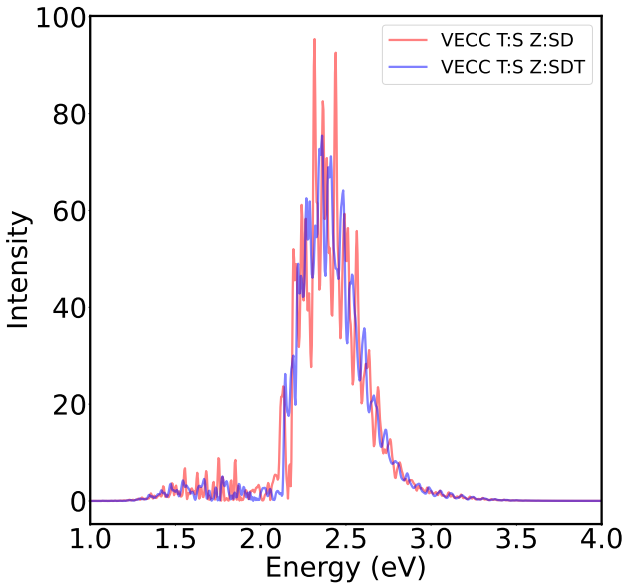
In Fig. 5.8b we can see that as truncation order of the Z amplitudes increase, the spectra converges towards the MCTDH spectra, especially with regards to the peak intensities. The spectra results are close to each other in general. We therefore conclude that we have sufficient convergence in our VECC calculation, in terms of the truncation level of the CC amplitudes.

VECC shows tremendous advantage in terms of computation runtime compared to MCTDH, between two to three orders of magnitude faster. It takes $>$ 1 day (using an Intel Xeon E5-2667) to simulate the spectra of the pyrazine vibronic model with MCTDH. [10] The VECC method, takes $\sim$ 1 minute with doubles (SD) truncation of the $\hat{Z}$ amplitude and $\sim$ 2.5 minutes with triples (SDT) truncation of the $\hat{Z}$ amplitude (using an Apple M2).

[10] using the same input file settings as in the reference by Raab et al. [128]



(a) Benchmark of absorption spectras generated by VECC against MCTDH, after 300 fs propagation



(b) Comparison of absorption spectra simulated by VECC, at different CC truncation levels, after 300 fs propagation.

Figure 5.8: We simulate the absorption spectra of pyrazine (2 states, 24 modes) using the VECC and MCTDH methods. The model and Fourier transform parameters were obtained from the reference by Raab et al. [128]

The other large vibronic model we investigated was hexahelicene. Fig. 5.9 compares the absorption spectra produced from the VECC method, the reference ML-MCTDH spectra and the experimental spectra as reported in. [56] (ML stands for multi-layer. The explicit multi-layer setting of the MCTDH calcuation is elaborated in the corresponding reference.)

In the spectra of hexahelicene, there are mainly two bands: the lower energy band ranges from 3.5 eV to 5.0 eV and the higher energy band ranges from 5.0 eV to 6.0 eV. In the simulated spectra the vertical energies, zero point energy, and intensities are shifted according to reference. [56]

In the lower energy band, the VECC peak positions and intensities roughly match those of ML-MCTDH. Moreover, as shown in the reference [56], the Frank-Condon Herzberg-Teller model with vertical gradient (FCHT|VG) method fails at this region where its prediction of the peak positions and intensities has qualitative different from the experimental spectra. The correct prediction of peak positions and intensities illustrates that the VECC method manages to successfully incorporate the effect of vibronic coupling.

In the higher energy band, the peak positions from the VECC method are consistent with that of the ML-MCTDH method. However, the peak intensities from the VECC calculation are slightly lower. Interestingly, the ML-MCTDH method seems to overestimate the peak intensities in the higher energy band, and the VECC result is in fact closer to the experimental spectra.

The SDT and SD truncation results of the VECC method only show slight differences. In comparison to the SD result, the peak intensities of the SDT result seem to converge towards the ML-MCTDH method. The results indicate that the calculation has reached sufficient convergence even at SD truncation of the CC amplitudes. We think it is a desirable feature of the VECC approach that both SD and SDT results can be obtained with reasonable computational costs, such that one can assess convergence.

The benchmark studies of absorption spectra for these two compounds verify the robustness of the VECC method for simulating spectra of large molecular compounds.

Compared to the ML-MCTDH method, which requires complicated settings of basis function and multi-layer tree structures, using the VECC method is much simpler, requiring only two inputs: vibronic model parameters and a choice of $\hat{T}$ and $\hat{Z}$ truncation levels. With the attractive features of improved scaling and user friendly inputs, the VECC method is well positioned to be widely applied to simulations of photo-electron and UV-VIS absorption spectra.

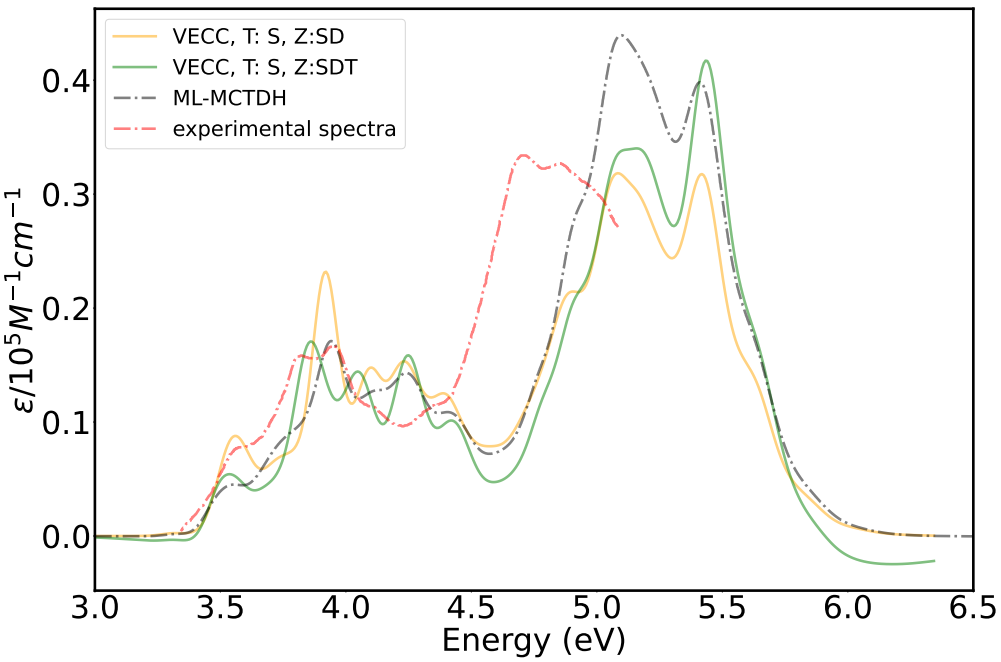


Figure 5.9: Simulated and experimental absorption spectra of hexahelicene (14 states, 63 modes). Comparing the VECC method against the ML-MCTDH method used in Aranda et al, [56] after 300 fs propagation.

5.5 Concluding remarks

5.5.1 In Summary

In this work, our goal is to develop a novel computational method that can efficiently simulate non-adiabatic dynamics based on a diabatic vibronic Hamiltonian. Non-adiabatic dynamics has wide applications in simulations of photo-electron/UV-VIS spectra and diabatic state populations.

To achieve this goal we developed the VECC method, which can be regarded as a special form of the TNOE approach proposed by M. Nooijen and S. Bao. [25] A key benefit of the VECC method is that it allows us to solve the quantum dynamics problem without the need for introducing basis sets. In the VECC method, we apply a second-quantized CC ansatz to parameterize the time-dependent wave-function. To solve the quantum dynamics problem, we substitute the CC ansatz into the TDSE to form CC VECC. The computational cost of evaluating these CC VECC scales classically as the size of the system. In this way, the VECC method dramatically reduces the computational cost compared to conventional basis set based methods that have exponential scaling over the size of the system.

From our benchmark studies we verified that the VECC method is capable of simulating photo-electron and UV/VIS absorption spectra efficiently and accurately. It is likely that the accuracy of the parameterized (gas-phase) vibronic model is the primary candidate for discrepancies with experiment. Thus, the VECC method in conjunction with vibronic models

is well positioned to be widely applied to simulations of experimental spectra, which can facilitate the characterization of molecular compounds and understanding of their optical properties.

It is clear that the current implementation of VECC has some limitations. The electronic transition moments are assumed to be constant. In our experience such an approach is well-justified for vibronic models as the diabatic states do not change much with geometry. Additionally, we cannot presently simulate hot bands, but using the mixed CC/CI approach this should not be too complicated to include. Importantly, the VECC approach has difficulties predicting accurate diabatic state populations for vibronic models with strong coupling, especially for longer times. One obvious obstacle is that VECC diabatic state populations experience stronger quantum coherence and for longer durations, when compared to MCTDH. We attribute the primary cause of this loss in accuracy to our use of an Ehrenfest parameterization in section 5.3.3 which assumes a single common important geometry (or moving Gaussian wave packet) for all electronic states. Another limitation of the VECC method described in this work, is that we restrict our diabatic potential to a form of polynomial expansion that is truncated at quadratic terms. This limits the application of the VECC method in circumstances which requires higher-order expansions of the PES and different forms of the potential (e.g. bond breaking).

Overall the VECC method performs quite impressively when simulating absorption spectra and presents significant improvements in computational runtime when compared to MCTDH. It is also convenient to use in contrast with ML-MCTDH which requires a lot of delicate input from users of the program. Although with a few limitations, the VECC method proposed in this paper is one of the first attempts to apply the CC method to the multi-surface excited state dynamics problem. This work opens a new field and has great potential for more future exploration.

5.5.2 Final Remarks

In this section we offer some insights regarding choices made during the development of the VECC theory, as well as discuss connections with established methods from the literature.

The most straightforward exponential parameterization for wave-functions associated with vibronic models would include a single operator $\hat{T} = \sum_{a,b} \hat{T}_b^a$, where each electronic component $\hat{T}_b^a$ has some normal mode component. However, the matrix nature of such operators ($\hat{T}$) is problematic when evaluating the TDSE. Computing $\frac{d}{d\tau} e^{\hat{T}}$ is complicated, as we cannot use the standard chain rule, and the corresponding similarity-transformed Hamiltonian ($e^{-\hat{T}} \hat{H} e^{\hat{T}}$) is not a connected operator. While we explored some of these possibilities in early work (unpublished), we abandoned them in favor of exponential operators that have no electronic dependence (or at most diagonal dependence). As can be seen in Eq. (5.24) and Eq. (5.38) their resulting similarity-transformed Hamiltonians are connected operators.

For single surface Hamiltonians, it suffices to use only creation operators in $\hat{T}$, and one can achieve exact results with the single-exponential ansatz (for up to quadratic Hamiltonians and second order terms in $\hat{T}$). It is somewhat surprising that one can use non-unitary

parameterizations to achieve exact results. We found that the complex "constant" term (t_0) is necessary to preserve the normalization and energy conservation properties. The value of this parameter is simply calculated from the propagation of the equation of motion. However, as mentioned previously, extending such an exponential operator to multiple surfaces introduces many complications. Therefore we explored other parameterizations and showed that a mixed-CC/CI parameterization ($e^{\hat{T}}\hat{Z}$) is sufficiently accurate in the single-surface case, and convenient and robust for the multi-surface case.

The multi surface vibronic problem is quite sensitive to divergences while propagating the amplitude equations, which came as a surprise to us. The robust mixed-CC/CI parameterization (see Eqs. (5.34-5.36)) was necessary to overcome these divergences. However, this is a redundant parameterization where we have the freedom to choose the form of $\hat{T}$ or $\hat{Z}$. For the mixed-CC/CI ansatz we chose to truncate $\hat{T}$ at singles (Eq. (5.35)). In principle, we could choose to truncate $\hat{T}$ at singles and doubles. However, truncating at singles simplifies the calculation of properties for multiple surfaces (See Eq. (5.58) in section 5.3.4). We do not anticipate this choice to significantly affect results, because when $\hat{T}$ is truncated at singles we achieve sufficient accuracy for the single surface case, as shown in Figs. 5.2c and 5.2d. We also impose a state averaged equation for $\hat{T}$, and this essentially describes translations of the coordinate system. In the spirit of Ehrenfest dynamics, the state-averaged equation results in the same coordinates being used for each state. If one takes the view that $\hat{T}$ causes a translation, it is natural to project against states that are also translated and this leads to modified projection manifold, or equivalently the doubly transformed Hamiltonian $\hat{G} = e^{\hat{T}^\dagger}e^{-\hat{T}}\hat{H}e^{\hat{T}}e^{-\hat{T}^\dagger}$. However, it appears that a drawback of this Ehrenfest parameterization is that it causes longer periods of quantum coherence and stronger Rabi oscillations when calculating diabatic state populations.

We think the mixed CC/CI parameterization can be further understood by outlining the similarity with a Gaussian wave packet approach. If we consider the VECC wave-function

$$|\Psi(t)\rangle = \sum_x e^{T_1}\hat{Z}_x\,|0,x\rangle \tag{5.76}$$

It could alternatively be represented in real space as

$$|\Psi(q,t)\rangle = \sum_x [z_x^0 + \sum_i z_x^i(q_i - Q_i) + \sum_{i,j} z_x^{ij}(q_i - Q_i)(q_j - Q_j) + \cdots] e^{-\frac{1}{2}\sum_i (q_i - Q_i)^2}\,|x\rangle \tag{5.77}$$

The central coordinate $Q(t)$ of the Gaussian is generated by our e^{T_1} and is the same for all electronic states. This Gaussian function is multiplied by a general state-specific polynomial, which would be quadratic for the SD model and cubic for the SDT model. Associating a swarm of cartesian polynomials with a moving Gaussian is an appealing picture, reminicent of atomic orbital basis sets used in electronic structure theory, but now in all vibrational dimensions. This conceptually convenient representation also naturally leads to the modified time-evolving projection manifold we use. The derivation of equations would appear to be more convenient using our second-quantized approach, avoiding the use of integrals.

This model could be improved by using state-specific centers Q_x. Likewise the current

VECC approach might be improved by using state-specific T_1 amplitudes, e.g.

$$|\Psi(\tau)\rangle = \sum_x e^{\hat{T}_{1,x}(\tau)} \hat{Z}_x(\tau) \, |0, x\rangle \tag{5.78}$$

The difficulties with such a method would be developing equations for the amplitudes, in particular when the electronic state has little population. These problems have been solved in Ab initio multiple spawning and Gaussian wave-packet approaches, [102, 103, 104, 105, 106, 107, 108, 109] . This can provide inspiration for generalizations of our current Ehrenfest based VECC approach.

Chapter 6

Application: statistical mechanics simulations for the vibronic problems

reprinted with the permission from *J. Chem. Theory. Comput.* (**2024**) XXX, XXX. *Copyright* 2024, *American Chemical Society*

6.1 Abstract

A VE-TFCC approach is developed to calculate thermal properties of non-adiabatic vibronic coupling systems. The TF theory and a mixed linear exponential ansatz based on second-quantized Bosonic construction operators are introduced to propagate the thermal density operator as a "pure state" in the Bogoliubov representation. Through this compact representation of the thermal density operator, the approach is basis-set free and scales classically (polynomial) as the number of degrees of freedoms (DoF) in the system. The VE-TFCC approach is benchmarked with small test models and a real molecular compound (CoF_4^- anion) against the conventional sum over states (SOS) method and applied to calculate thermochemistry properties of a gas phase reaction: $CoF_3 + F^- \longrightarrow CoF_4^-$. Results show that the VE-TFCC approach, in conjunction with vibronic models, provide an effective protocol for calculating thermodynamic properties of vibronic coupling systems.

6.2 Introduction

Thermochemistry properties play an important role in understanding reaction mechanisms, optoelectronic properties and structural properties of compounds [183, 184]. As current experimental thermochemistry data is insufficient and has limited accuracy [185], computational methods that can simulate chemical systems at thermal equilibrium and accurately calculate thermochemistry properties are useful as an alternative approach to this problem. Conventional methods for evaluating thermodynamics properties of polyatomic systems are rooted in the BOA. For a system in an electronic state that is energetically far from the

other states: (1) geometry optimization is first performed to find a stable (at a local minima) structure, at which the following six calculations are evaluated, (2) the normal modes are obtained using a hessian calculation, (3) rotational contributions to thermal properties are calculated under the R.R. approximation, including nuclear spin symmetry factor, (4) translational contributions to the thermal properties are calculated under the free particle approximation. (5) vibrational contributions are calculated using the hessian results under the H.O. approximation, (6) the electronic spin multiplicity contribution to entropy is evaluated using $R \log W | W = 2S + 1$, and finally (7) the thermochemistry properties can be calculated by adding all these components together with the electronic structure contribution at the optimized structure [185]. The accuracy of the calculated thermal properties depends on: (1) the accuracy of the electronic structure calculation, which is determined by the level of treating electron correlation and basis set; [45, 186] (2) the validity of the R.R. and H.O. approximations; [1] (3) and more fundamentally, the validity of the BOA.

While this conventional protocol works well for most common systems, it fails for systems in degenerate or pseudo-degenerate electronic states. [2] These systems are widely seen in transition metal compounds or ions of main-group element compounds. To handle these systems, one needs to involve the group Born-Oppenheimer approximation (GBOA): the electronic Hamiltonian operator is resolved in a set of close-lying electronic states that are energetically far from all the rest, and the states in the set are coupled by vibrational DoF, i.e., vibronic coupling. [191]

To construct the Hamiltonian matrix elements one may use the conventional adiabatic representation of the electronic Hamiltonian eigenstates, which feature non-smooth PESs and singular non-adiabatic coupling-matrix elements of nuclear momentum and kinetic operators. Alternatively, a diabatization procedure can be used to construct a vibronic Hamiltonian in a diabatic representation. We may unitarily transform the adiabatic states to a set of diabatic states. The diabatic states slowly evolve with respect to nuclear vibrations. Therefore, their matrix elements of the nuclear momentum and kinetic operators are finite and can be neglected after division by the heavy nuclear masses. Their diagonal and off-diagonal electronic Hamiltonian matrix elements are also smooth differentiable functions of nuclear coordinates. [52, 53, 54, 55, 56, 57, 58] The resulting matrix elements in the vibronic Hamiltonian using diabatization are differentiable, which can be more easily diagonalized and is more convenient for propagating quantum dynamics. [3]

Given a vibronic Hamiltonian in the diabatic representation, one can obtain thermal properties by taking the statistical average of any physical observable. The most direct approach is SOS where both the Hamiltonian operator ($\hat{H}$) and the thermal density operator ($e^{-\beta \hat{H}}$) are resolved in a truncated H.O. basis. The thermal properties can then be calculated through the trace over all matrix elements in the truncated H.O. basis. Alternatively, one can use the generalized MCTDH for density operator propagations [64, 65] or Path Integral Monte Carlo (PIMC) based approaches [192, 193]. However, all of these methods require

[1] Anharmonic corrections can be introduced using various methods, e.g., HEAT [187, 188, 189] and W4 [190].

[2] The (pseudo-)degeneracy signals the breakdown of BOA.

[3] The cost of using the diabatic states (diabats) is the loss of their clear meaning of electronic energy levels, as their PESs may well cross and their energy order is altered.

basis sets and have an exponential scaling over the DoFs of the vibronic models, and hence the application is limited to the small to medium size molecules.

The motivation of this work is to develop a more efficient computational method to directly calculate thermal energetic properties of vibronic models that has better scaling. The essence of this method is to introduce a second-quantized-based many-body quantum field theoretical approach to form a compact representation of the thermal density operator. In this way, one can access the thermal properties by contraction rules and time-independent Wick's theorem thus avoiding explicit consideration of the exponentially large Hilbert space in the conventional basis set approaches. The first attempts to obtain thermal properties of quantum many-body systems using this type of approach can be dated back to the 1990s [2, 3, 4, 5]. Recently, there has been a resurgence of interest in this topic. Many attempts have been made to obtain a time-dependent coupled cluster (TDCC) or many-body perturbation theory (MBPT) formulation for directly calculating thermal properties of quantum many-body systems [6, 7, 8, 9, 10, 11, 12, 13, 14, 25, 26, 27, 28, 29, 30]. However, most of these works focus on either pure electronic systems or single-surface pure vibrational systems. In this work, we develop an approach for multi-surface vibronic coupling systems. This work can be viewed as a statistical mechanics formulation of our previous work on the VECC method for real time non-adiabatic dynamics [31]. It is a specific application of the TNOE approach developed by Nooijen and Bao [25] for vibronic models. To simplify the TNOE formulation, we introduced TF dynamics and a thermal density operator in the Bogoliubov representation, inspired by the works by Harsha et al. [26, 27, 28, 29, 30]. For a thermal density operator in the Bogoliubov representation the TNOE ansatz reduces to the simple exponential ansatz and the approach becomes single-reference like. By treating the thermal density operator as a state, it can be propagated using TF dynamics.

The rest of this chapter is organized as follows. In section 6.3, the general VE-TFCC theory is presented. We begin by defining the prototypical single-surface vibrational problem in section 6.3.1 and then generalize it to the vibronic coupling problem in section 6.3.2. In section 6.4, we benchmark the VE-TFCC method on calculating thermal properties. We test the method on two by two model systems with both weak and strong vibronic couplings to show the validity of the method. We also test the method using a real molecular compound: the CoF_4^- anion. Finally, we calculate the thermochemistry data of a gas phase reaction, $CoF_3 + F^- \longrightarrow CoF_4^-$, as an example of a real world application of this method.

6.3 Theory

The objective of developing the VE-TFCC approach is to efficiently simulate vibronic coupling systems at thermal equilibrium. In this approach, cluster amplitudes are obtained through imaginary time integration and thermal averaged properties are directly mapped from the cluster amplitudes. This is a statistical mechanics analog to the VECC approach [31] for quantum dynamics simulations of vibronic coupling systems, in which time-dependent properties are also mapped from the cluster amplitudes that are obtained through real time integration. The major differences between the two approaches are: (1) the cluster amplitudes are integrated over imaginary time in VE-TFCC, instead of real time as in VECC;

(2) the initial amplitudes at very large temperature ($\beta \approx 0$) requires special consideration. To develop the theory we start with the TNOE representation of the full thermal density matrix and thermal properties and subsequently relate this to the thermofield formulation.

The thermal density operator,

$$\hat{D} = e^{-\beta \hat{H}} \tag{6.1}$$

satisfies an imaginary time EOM:

$$-\frac{\mathrm{d}}{\mathrm{d}\beta}\hat{D} = \hat{H}\hat{D} \tag{6.2}$$

which is the imaginary time analog of the TDSE.

In reference [25], we proposed a general theory, in which a TNOE ansatz is introduced to parameterize the thermal density operator:

$$\hat{D} \equiv \{e^{\hat{S}(\beta)}\}\hat{D}_0, \tag{6.3}$$

$$\hat{S} \equiv s_0(\beta) + \sum_{\mu} s_\mu(\beta)\{\hat{\Omega}_\mu\}. \tag{6.4}$$

Throughout this work, curly brackets $\{\}$ indicates the normal ordering of the second-quantized operators in the brackets, with respect to the reference density operator $\hat{D}_0$[4]. The operator $\hat{\Omega}_\mu$ represents strings of second-quantized construction operators truncated up to order μ, $\mu \in \{1, 2, \cdots\}$.

Substituting Eq. (6.3) into Eq. (6.2), and projecting the resultant equation against $\{\hat{\Omega}_\mu\}\hat{D}_0$ and $\hat{D}_0$, we correspondingly obtain

$$-\frac{\mathrm{d}}{\mathrm{d}\beta}\left\langle \{\Omega_\mu^\dagger\}\{\hat{S}(\beta)\}\right\rangle = \left\langle \{\Omega_\mu^\dagger\}\left(\{\hat{H}\}\{e^{\hat{S}(\beta)}\}\right)_{conn.}\right\rangle, \tag{6.5}$$

$$-\frac{\mathrm{d}}{\mathrm{d}\beta}s_0(\beta) = \left\langle \left(\{\hat{H}\}\{e^{\hat{S}(\beta)}\}\right)_{conn.}\right\rangle. \tag{6.6}$$

where the subscript "conn." stands for "connected". These equations allow us to formulate the EOM of the $\hat{S}$ amplitude. The amplitudes are initialized at high temperature (small β) because the classical (H.O.) approach is exact in this limit. Solving the equations in imaginary time to obtain the amplitudes at all β, we can then calculate the thermal average of an observable as

$$\left\langle \hat{O}\right\rangle = \frac{\mathrm{Tr}\left(\hat{O}\hat{D}\right)}{\mathrm{Tr}\left(\hat{D}\right)} = O_0 + \left\langle \left(\{\hat{O}\}\{e^{\hat{S}(\beta)}\}\right)_{conn.}\right\rangle, \tag{6.7}$$

where the two components in the last equality arises from the fact that an arbitrary operator can be decomposed into a constant part and a normal ordered part, i.e., $\hat{O} \equiv O_0 + \{\hat{O}\}$.

It is feasible to develop a computational method, based on the TNOE formulation, to solve the $\hat{S}$ amplitudes by numerically integrating over imaginary time. However, there is a

[4]Whose parameters can be obtained from some external source.

pragmatic issue with directly implementing this computational method. The main concern is that the $\hat{S}$ operator consists of both excitation and de-excitation second-quantized operators, which complicates the working equations. To simplify the original TNOE formation, we modify it by introducing the TF theory and the Bogoliubov representation of the thermal density operator.

This modification is inspired by the studies on TF dynamics which is originally devised by physicists [20, 21, 22] and firstly introduced to quantum chemistry by Mukerjee and his coworkers [2]. Recently, it is re-introduced by Harsha et al. [26, 27, 28, 29, 30] The idea is to square the dimension of the Hilbert space by introducing ancillary DoFs which then allows us to obtain thermal properties by evolving a pure state in the expanded space and then taking the partial trace over the ancillary degrees of freedom. With suitable definitions of the ansatz and some algebraic manipulations, the resulting EOM adopts a single-reference CC formulation, without the explicit normal ordering. We begin by formulating the theory for the single-surface vibrational problem and then generalize it to the multi-surface full vibronic coupling problem.

6.3.1 Single-surface formulation: vibrational TFCC theory

Consider a generic (quadratic) vibrational Hamiltonian with linear displacements, quadratic squeezing, and bilinear couplings:

$$\hat{H} = E_0 + \sum_i \hbar\omega_i(\hat{p}_i^2 + \hat{q}_i^2) + \sum_i \alpha_i \hat{q}_i + \sum_{ij} \Lambda_{ij}\hat{q}_i\hat{q}_j, \tag{6.8}$$

where $\hat{p}_i$ and $\hat{q}_i$ are dimensionless momentum and position operators. We can express the $\hat{p}_i$ and $\hat{q}_i$ using Bosonic construction operators:

$$\hat{q}_i = \frac{1}{\sqrt{2}}(\hat{i}^\dagger + \hat{i}), \tag{6.9}$$

$$i\hat{p}_i = \frac{1}{\sqrt{2}}(\hat{i}^\dagger - \hat{i}). \tag{6.10}$$

Substituting into Eq. (6.8) gives:

$$\hat{H} = E_x + \sum_i \omega_i\{\hat{i}^\dagger\hat{i}\} + \sum_i \lambda_i(\hat{i}^\dagger + \hat{i}) + \sum_{ij} \Lambda_{ij}\{\hat{i}^\dagger\hat{j}\} + \frac{1}{2}\sum_{ij} \Lambda_{ij}(\hat{i}^\dagger\hat{j}^\dagger + \hat{i}\hat{j}), \tag{6.11}$$

where

$$E_x = E_0 + \frac{1}{2}\sum_i \Lambda_{ii} + \frac{1}{2}\sum_i \hbar\omega_i, \tag{6.12}$$

and

$$\lambda_i = \frac{\alpha_i}{\sqrt{2}}. \tag{6.13}$$

The theory can be formulated for more general Hamiltonians, including cubic and quartic

constants, as long as $\hat{H}$ has a finite polynomial representation in terms of normal modes. For vibronic models we typically restrict ourselves to up to quadratic terms, and this is assumed here. We partition the Hamiltonian into a mean field term $\hat{h}_0$ and a perturbation $\hat{V}$:

$$\hat{H} \equiv \hat{h}_0 + \hat{V} \tag{6.14}$$

where the mean field term consists of the frequency term:

$$\hat{h}_0 \equiv \sum_i \omega_i \{\hat{i}^\dagger \hat{i}\} \tag{6.15}$$

and the perturbation consists of the remaining components:

$$\hat{V} \equiv E_x + \sum_i \lambda_i (\hat{i}^\dagger + \hat{i}) + \sum_{ij} \Lambda_{ij} \{\hat{i}^\dagger \hat{j}\} + \frac{1}{2} \sum_{ij} \Lambda_{ij} (\hat{i}^\dagger \hat{j}^\dagger + \hat{i}\hat{j}). \tag{6.16}$$

In this way, we have defined a model Hamiltonian for single-surface vibrational systems (whose potential is truncated up to second order) in second quantization. To calculate thermal properties, we can take the trace over the thermal density operator $\left\langle \hat{O} \right\rangle = \frac{\mathrm{Tr}\left(\hat{O} e^{-\beta \hat{H}}\right)}{\mathrm{Tr}\left(e^{-\beta \hat{H}}\right)}$. However, this straightforward way to calculate thermal properties turns out to be problematic in practice due to the high computational cost. To reduce the computational cost, we introduce an alternative way to directly calculate thermal properties that is mathematically equivalent. This alternative approach is known as thermofield theory and it allows us to design a more efficient algorithm to compute thermal properties for vibrational systems.

1. Formal thermofield (TF) theory

Now we introduce the formal TF theory. In essence, TF allows us to obtain $\left\langle \hat{O} \right\rangle$ by calculating the expectation value of the observable operator for a pure state, i.e.,

$$\mathrm{Tr}_{physical}\left(\hat{O}\hat{D}\right) \equiv \mathrm{Tr}_{physical}\left(\hat{O} e^{-\beta \hat{H}}\right) = \langle \Psi(\beta)| \hat{O} |\Psi(\beta)\rangle \tag{6.17}$$

To define the thermal state $|\Psi(\beta)\rangle$, we enlarge the original physical Hilbert space using an ancillary Hilbert space. The original Hilbert space of the physical Hamiltonian is denoted by the harmonic oscillator eigenstates $\{|m\rangle\}$, and the ancillary space by the same number and same type of states $\{|\tilde{n}\rangle\}$. The thermal state $|\Psi(\beta)\rangle$ lies in the compound space that consist of the direct product of the physical and ancillary Hilbert spaces. The compound space is described by the basis:

$$|m, \tilde{n}\rangle \equiv |m\rangle |\tilde{n}\rangle . \tag{6.18}$$

The thermal state in this compound space is defined as:

$$|\Psi(\beta)\rangle \equiv e^{-\beta \hat{H}/2} |U\rangle , \tag{6.19}$$

where

$$|U\rangle \equiv \sum_m |m, \tilde{m}\rangle . \tag{6.20}$$

At $\beta = 0$ the thermal state is $|\Psi(\beta)\rangle = |U\rangle$, which is uniform and has 'diagonal' elements only. By definition there is a one-to-one correspondence between the physical state $|m\rangle$ and its ancillary image $|\tilde{m}\rangle$. In other words, the physical state $|m\rangle$ is entangled with the ancillary state $|\tilde{m}\rangle$. Eq. (6.19) can be rigorously proved as follows:

$$\begin{aligned}
\langle\Psi(\beta)|\,\hat{O}\,|\Psi(\beta)\rangle &= \sum_{m,n} \langle m,\tilde{m}|\, e^{-\beta\hat{H}/2}\hat{O}e^{-\beta\hat{H}/2}\,|n,\tilde{n}\rangle \\
&= \sum_{m,n} \langle m|\, e^{-\beta\hat{H}/2}\hat{O}e^{-\beta\hat{H}/2}\,|n\rangle\,\delta_{mn} \\
&= \mathrm{Tr}_{physical}\left(e^{-\beta\hat{H}/2}\hat{O}e^{-\beta\hat{H}/2}\right) \\
&= \mathrm{Tr}_{physical}\left(\hat{O}e^{-\beta\hat{H}}\right) \\
&= \mathrm{Tr}_{physical}\left(\hat{O}\hat{D}\right)
\end{aligned} \tag{6.21}$$

.

The introduction of the ancillary space results in a trace over the physical space, which then gives an ensemble average.

The definition of the thermal state in Eq. (6.19) can be further simplified by expressing the uniform state $|U\rangle$ in a concise form. To achieve this, we introduce the Bosonic construction operators $\hat{i}$, $\hat{i}^\dagger$ in physical space and the dual (associated) operators $\tilde{i}$, $\tilde{i}^\dagger$ in ancillary space that satisfy the usual commutation relations. In addition, the operators in physical space commute with the operators in ancillary space. Then the uniform state $|U\rangle$ can be concisely expressed as

$$|U\rangle \equiv \sum_m |m,\tilde{m}\rangle = \sum_m \frac{1}{\sqrt{m!}}(\hat{i}^\dagger)^m \frac{1}{\sqrt{m!}}(\tilde{i}^\dagger)^m \left|0,\tilde{0}\right\rangle = \sum_m \frac{1}{m!}(\hat{i}^\dagger\tilde{i}^\dagger)^m \left|0,\tilde{0}\right\rangle = e^{\hat{u}}\left|0,\tilde{0}\right\rangle, \tag{6.22}$$

where

$$\hat{u} \equiv \sum_i \hat{i}^\dagger\tilde{i}^\dagger. \tag{6.23}$$

In this way, the definition of the thermal state in Eq. (6.19) can be simplified to:

$$|\Psi(\beta)\rangle \equiv e^{-\beta\hat{H}/2}e^{\hat{u}}\left|0,\tilde{0}\right\rangle. \tag{6.24}$$

By introducing the thermal state $|\Psi(\beta)\rangle$, we can express an ensemble thermal average over a physical operator as an expectation value of a pure quantum state in the enlarged compound space. This allows us to design efficient algorithms to find a heuristic approximation to the thermal state $|\Psi(\beta)\rangle$. In practice, we apply an exponential ansatz to approximate the thermal state ($|\Psi(\beta)\rangle \equiv e^{\hat{T}(\beta)}\,|ref\rangle$) in the same fashion as our approximation of the many-electron wavefunction in CC theory. Now, we elaborate on this formulation.

2. Coupled cluster formulation of thermofield theory

Here, we introduce the coupled cluster formulation of thermofield theory, namely TFCC

theory. By defining a "mean-field" approximated thermal state $|\theta(\beta)\rangle$ as the reference state at an arbitrary finite temperature β [5]:

$$|\theta(\beta)\rangle \equiv e^{-\beta\hat{h}_0/2}\,|U\rangle\,, \tag{6.25}$$

we can derive a coupled cluster theory, that resembles the single-reference formulation, on top of this reference state without explicitly introducing normal ordering.

It can be verified (see appendix B) that a set of operators $\hat{a}_i$, $\hat{a}_i^\dagger$, $\hat{b}_i$ and $\hat{b}_i^\dagger$, which are linear combinations of the original Bosonic construction operators $\hat{i}$, $\hat{i}^\dagger$, $\tilde{i}$ and $\tilde{i}^\dagger$ and span the same physical and ancillary spaces, satisfy

$$\hat{a}_i\,|\theta(\beta)\rangle = \hat{b}_i\,|\theta(\beta)\rangle = 0, \tag{6.26}$$

$$\langle\theta(\beta)|\,\hat{a}_i^\dagger = \langle\theta(\beta)|\,\hat{b}_i^\dagger = 0. \tag{6.27}$$

These operators are Bosonic construction operators and satisfy the canonical commutation relation by definition:

$$[\hat{a}_i, \hat{a}_j^\dagger] = \delta_{ij}, \tag{6.28}$$

$$[\hat{b}_i, \hat{b}_j^\dagger] = \delta_{ij}. \tag{6.29}$$

The new set of operators are obtained by the Bogoliubov transformation [23, 24] of the original set of operators (the explicit derivation is given in appendix B):

$$\begin{bmatrix}\hat{a}_i\\ \hat{b}_i^\dagger\end{bmatrix} = \begin{bmatrix}\cosh\theta_i & -\sinh\theta_i\\ -\sinh\theta_i & \cosh\theta_i\end{bmatrix}\begin{bmatrix}\hat{i}\\ \tilde{i}^\dagger\end{bmatrix}, \tag{6.30}$$

$$\begin{bmatrix}\hat{a}_i^\dagger\\ \hat{b}_i\end{bmatrix} = \begin{bmatrix}\cosh\theta_i & -\sinh\theta_i\\ -\sinh\theta_i & \cosh\theta_i\end{bmatrix}\begin{bmatrix}\hat{i}^\dagger\\ \tilde{i}\end{bmatrix}, \tag{6.31}$$

where the hyperbolic functions $\cosh\theta_i$ and $\sinh\theta_i$ in the transformation matrix can be related to the Bose-Einstein occupation number corresponding to the reference state based on the zeroth order hamiltonian in Eq. (6.15):

$$\cosh\theta_i = \left(1 - e^{-\beta\hbar\omega_i}\right)^{-\frac{1}{2}}, \tag{6.32}$$

$$\sinh\theta_i = e^{-\beta\hbar\omega_i/2}\left(1 - e^{-\beta\hbar\omega_i}\right)^{-\frac{1}{2}}. \tag{6.33}$$

In this way, the definitions of the thermal state and the Bogoliubov transformation are complete. Under the conditions described in Eq. (6.26) and Eq. (6.27), the reference state $|\theta(\beta)\rangle$ can be regarded as the quasi-particle vacuum state, which makes coupled cluster formulation on top of it single-reference like. In the remaining part of this section, we will elaborate on this formulation.

First, we propagate the thermal density operator as a (pure) state in the Bogoliubov

[5] $\hat{h}_0$ is defined in Eq. (6.15)

representation. It can be represented as follows:

$$|\Phi(\tau)\rangle \equiv \hat{D}\,|U\rangle = e^{-\tau\hat{H}}\,|U\rangle\,. \tag{6.34}$$

Notice that compared to the original definition of the thermal state $|\Psi(\tau)\rangle$ in Eq. (6.19), the power of the exponential is different by a factor of two ($\left|\Phi(\frac{\tau}{2})\right\rangle = |\Psi(\tau)\rangle$). Using the cyclic rule, we can easily prove that

$$\mathrm{Tr}_{physical}\left(\hat{O}\hat{D}\right) = \langle\Psi(\tau)|\,\hat{O}\,|\Psi(\tau)\rangle = \langle U|\,\hat{O}\,|\Phi(\tau)\rangle\,. \tag{6.35}$$

In analog to Eq. (6.2), we can derive an EOM for the TF state $|\Phi(\tau)\rangle$:

$$-\frac{\mathrm{d}}{\mathrm{d}\tau}\,|\Phi(\tau)\rangle = \hat{H}\,|\Phi(\tau)\rangle\,. \tag{6.36}$$

To formulate the TFCC theory, we apply the TNOE ansatz to parameterize the TF state: [6]

$$|\Phi(\tau)\rangle \equiv \{e^{\hat{S}(\tau)}\}e^{-\beta\hat{h}_0}\,|U\rangle\,. \tag{6.37}$$

Comparing to the original TNOE ansatz defined in Eq. (6.3), $e^{-\beta\hat{h}_0}\,|U\rangle$ can be regarded as the "reference density operator" at a specific temperature β.

Substituting the ansatz defined in Eq. (6.37) into Eq. (6.36), we have

$$-\frac{\mathrm{d}}{\mathrm{d}\tau}\{e^{\hat{S}(\tau)}\}e^{-\beta\hat{h}_0}\,|U\rangle = \hat{H}\{e^{\hat{S}(\tau)}\}e^{-\beta\hat{h}_0}\,|U\rangle\,. \tag{6.38}$$

Next, we project both hands sides of the equation the uniform state $\langle U|\,\Omega_\mu^\dagger$:

$$-\langle U|\,\Omega_\mu^\dagger\frac{\mathrm{d}\{e^{\hat{S}(\tau)}\}}{\mathrm{d}\tau}e^{-\beta\hat{h}_0}\,|U\rangle = \langle U|\,\Omega_\mu^\dagger\hat{H}\{e^{\hat{S}(\tau)}\}e^{-\beta\hat{h}_0}\,|U\rangle\,. \tag{6.39}$$

Splitting $e^{-\beta\hat{h}_0}$ into the product $e^{-\beta\hat{h}_0/2}e^{-\beta\hat{h}_0/2}$ and making use of the cyclic property:

$$-\langle U|\,e^{-\beta\hat{h}_0/2}\Omega_\mu^\dagger\frac{\mathrm{d}\{e^{\hat{S}(\tau)}\}}{\mathrm{d}\tau}e^{-\beta\hat{h}_0/2}\,|U\rangle = \langle U|\,e^{-\beta\hat{h}_0/2}\Omega_\mu^\dagger\hat{H}\{e^{\hat{S}(\tau)}\}e^{-\beta\hat{h}_0/2}\,|U\rangle\,. \tag{6.40}$$

Using the definition of $|\theta(\beta)\rangle$ from Eq. (6.25), Eq. (6.40) reduces to

$$-\langle\theta(\beta)|\,\Omega_\mu^\dagger\frac{\mathrm{d}\{e^{\hat{S}(\tau)}\}}{\mathrm{d}\tau}\,|\theta(\beta)\rangle = \langle\theta(\beta)|\,\Omega_\mu^\dagger\hat{H}\{e^{\hat{S}(\tau)}\}\,|\theta(\beta)\rangle\,, \tag{6.41}$$

where both the Hamiltonian operator and the normal-ordered exponential operator are physical operators, satisfying the condition for using the cyclic property of the trace.

Next, we transform both operators ($\hat{H}$, $\{e^{\hat{S}(\tau)}\}$) into the Bogoliubov representation.

[6] To make direct comparison to the work by MN and SB [25], we introduce the TNOE ansatz. However, we showed previously that we can arrived at the same TFCC EOM without the resort of the TNOE ansatz in chapter 3.2.

To transform the Hamiltonian operator, we rank the terms of the original single-surface quadratic vibrational Hamiltonian in Eq. (6.11) according to their Bosonic operators:

$$\begin{aligned}\hat{H} &\equiv h^0 + \hat{h}^1 + \hat{h}_1 + \hat{h}_1^1 + \hat{h}^2 + \hat{h}_2 \\ &= h^0 + \sum_i h^i \hat{i}^\dagger + \sum_i h_i \hat{i} + \sum_{ij} h_j^i \{\hat{i}^\dagger \hat{j}\} + \frac{1}{2}\sum_{ij} h^{ij} \hat{i}^\dagger \hat{j}^\dagger + \frac{1}{2}\sum_{ij} h_{ij} \hat{i}\hat{j},\end{aligned} \tag{6.42}$$

where superscripts are associated with the Bosonic creation operators while subscripts are associated with the Bosonic annihilation operators. Based on the Bogoliubov transformation defined in Eqs. (6.30) and (6.31), the corresponding inverse Bogoliubov transformation can be easily obtained:

$$\begin{bmatrix} \hat{i} \\ \tilde{i}^\dagger \end{bmatrix} = \begin{bmatrix} \cosh\theta_i & \sinh\theta_i \\ \sinh\theta_i & \cosh\theta_i \end{bmatrix} \begin{bmatrix} \hat{a}_i \\ \hat{b}_i^\dagger \end{bmatrix}, \tag{6.43}$$

$$\begin{bmatrix} \hat{i}^\dagger \\ \tilde{i} \end{bmatrix} = \begin{bmatrix} \cosh\theta_i & \sinh\theta_i \\ \sinh\theta_i & \cosh\theta_i \end{bmatrix} \begin{bmatrix} \hat{a}_i^\dagger \\ \hat{b}_i \end{bmatrix}. \tag{6.44}$$

Substituting Eqs. (6.43) and (6.44) into the physical Hamiltonian from Eq. (6.42), we can transform the physical Hamiltonian into the Bogoliubov representation

$$\hat{H} \underset{\text{B.T.}}{\rightarrow} \tilde{H}, \tag{6.45}$$

where

$$\begin{aligned}\tilde{H} &\equiv \tilde{h}^0 + \tilde{h}^1 + \tilde{h}_1 + \tilde{h}_1^1 + \tilde{h}^2 + \tilde{h}_2 \\ &= \tilde{h}^0 + \sum_p \tilde{h}^p \hat{c}_p^\dagger + \sum_p \tilde{h}_p \hat{c}_p + \sum_{pq} \tilde{h}_q^p \{\hat{c}_p^\dagger \hat{c}_q\} + \frac{1}{2}\sum_{pq} \tilde{h}^{pq} \hat{c}_p^\dagger \hat{c}_q^\dagger + \frac{1}{2}\sum_{pq} \tilde{h}_{pq} \hat{c}_p \hat{c}_q.\end{aligned} \tag{6.46}$$

Despite similar looking terms in Eqs. (6.42) and (6.46), $\tilde{H}$ is written in the $2M$-dimensional Bogoliubov representation, i.e., the summations of p and q are from 1 to $2M$, while $\hat{H}$ is written in the M-dimensional physical representation. For example, $\tilde{h}_1^1$ is given by:

$$\begin{aligned}\tilde{h}_1^1 &= \sum_i^M \sum_j^M \Big(\cosh\theta_i \cosh\theta_j h_j^i \hat{a}_i^\dagger \hat{a}_j + \cosh\theta_i \sinh\theta_j h^{ij} \hat{a}_i^\dagger \hat{b}_j \\ &\qquad + \sinh\theta_i \cosh\theta_j h_{ij} \hat{b}_i^\dagger \hat{a}_j + \sinh\theta_i \sinh\theta_j h_i^j \hat{b}_i^\dagger \hat{b}_j \Big) \\ &\equiv \sum_p^{2M} \sum_q^{2M} \tilde{h}_q^p c_p^\dagger c_q,\end{aligned} \tag{6.47}$$

where

$$\boldsymbol{c}^\dagger = \left[\hat{a}_1^\dagger, \ldots, \hat{a}_i^\dagger, \ldots, \hat{a}_M^\dagger, \hat{b}_{M+1}^\dagger, \ldots, \hat{b}_{M+i}^\dagger, \ldots, \hat{b}_{2M}^\dagger\right], \tag{6.48}$$

$$\boldsymbol{c} = \left[\hat{a}_1, \ldots, \hat{a}_i, \ldots, \hat{a}_M, \hat{b}_{M+1}, \ldots, \hat{b}_{M+i}, \ldots, \hat{b}_{2M}\right], \tag{6.49}$$

and the renormalized matrix elements of Bogoliubov transformed Hamiltonian $\tilde{h}_q^p$ have the following structure

$$\begin{bmatrix} \boldsymbol{x}\boldsymbol{h}_1^1\boldsymbol{x}^\intercal & \boldsymbol{x}\boldsymbol{h}^2\boldsymbol{y}^\intercal \\ \boldsymbol{y}\boldsymbol{h}_2\boldsymbol{x}^\intercal & \boldsymbol{y}\boldsymbol{h}_1^1\boldsymbol{y}^\intercal \end{bmatrix} \tag{6.50}$$

where

$$\boldsymbol{x} = [\cosh\theta_1, \ldots, \cosh\theta_i, \ldots, \cosh\theta_M]\,, \tag{6.51}$$

$$\boldsymbol{y} = [\sinh\theta_1, \ldots, \sinh\theta_i, \ldots, \sinh\theta_M]\,. \tag{6.52}$$

Expressions for each term of $\tilde{H}$ in Eq. (6.46) are available in appendix I.1. Equations 6.46–6.52 describe the physical Hamiltonian in the Bogoliubov representation.

Similarly, we can transform the TNOE operator into the Bogoliubov representation.

$$\{e^{\hat{S}(\tau)}\} \underset{\text{B.T.}}{\rightarrow} \{e^{\tilde{S}(\tau)}\}, \tag{6.53}$$

which, because of Eqs. (6.26) and (6.27), becomes a conventional exponential operator $e^{\hat{T}}$ that only contains excitation operators: [7]

$$\{e^{\tilde{S}(\tau)}\} \rightarrow e^{\hat{T}(\tau)}, \tag{6.54}$$

$$\hat{T}(\tau) = t^0(\tau) + \sum_p t^p(\tau)\hat{c}_p^\dagger + \frac{1}{2}\sum_{pq} t^{pq}(\tau)\hat{c}_p^\dagger\hat{c}_q^\dagger. \tag{6.55}$$

Correspondingly, the projected EOM in Eq. (6.41) is reduced to

$$-\langle\theta(\beta)|\,\Omega_\mu^\dagger \frac{\mathrm{d}}{\mathrm{d}\tau} e^{\hat{T}(\tau)}\,|\theta(\beta)\rangle = \langle\theta(\beta)|\,\Omega_\mu^\dagger(\tilde{H}e^{\hat{T}(\tau)})\,|\theta(\beta)\rangle\,. \tag{6.56}$$

In a final step we can modify the projection manifold in Eq. (6.56) to $\langle\theta(\beta)|\,\Omega_\mu^\dagger e^{-\hat{T}}$ and formulate a closed form for the EOM in this TFCC form:

$$-\frac{\mathrm{d}t^\mu(\tau)}{\mathrm{d}\tau} = \langle\theta(\beta)|\,\Omega_\mu^\dagger e^{-\hat{T}(\tau)}\tilde{H}e^{\hat{T}(\tau)}\,|\theta(\beta)\rangle = \langle\theta(\beta)|\,\Omega_\mu^\dagger(\tilde{H}e^{\hat{T}(\tau)})_{conn.}\,|\theta(\beta)\rangle \tag{6.57}$$

where the subscript "conn." denotes the equation is connected. The derivation of Eq. (6.57) is based on two assumptions: (1) the Bosonic construction operators are τ-independent:

$$\begin{aligned} \frac{\mathrm{d}\hat{T}(\tau)}{\mathrm{d}\tau} &= \sum_\mu \left[\frac{\mathrm{d}t^\mu(\tau)}{\mathrm{d}\tau}\hat{\Omega}_\mu(\tau) + t^\mu(\tau)\frac{\mathrm{d}\hat{\Omega}_\mu(\tau)}{\mathrm{d}\tau}\right] \\ &= \sum_\mu \frac{\mathrm{d}t^\mu(\tau)}{\mathrm{d}\tau}\hat{\Omega}_\mu(\tau); \end{aligned} \tag{6.58}$$

[7] All terms containing de-excitation operators vanish when acting on the quasi-particle vacuum state $|\theta(\beta)\rangle$

(2) the thermal state $|\theta(\beta)\rangle$ is also τ-independent:

$$\frac{\mathrm{d}}{\mathrm{d}\tau}|\theta(\beta)\rangle = 0. \tag{6.59}$$

Eq. (6.57) is the EOM of the TFCC formulation which resembles the canonical SR-CC theory. The cluster amplitude $\hat{T}$ can be determined through imaginary time integration and thermally averaged properties can be calculated using the cluster amplitudes. The expectation value of an arbitrary physical operator $\hat{O}$ is defined in Eq. (6.7). We can derive TFCC expressions for the numerator and denominator using the cyclic invariance of placing the sandwiched operators in tracing matrices and calculating $\langle U|\cdot|U\rangle$-type expectation values:

$$\begin{aligned}
\mathrm{Tr}_{physical}\left(\hat{D}\right) &= \langle U|\Phi(\tau)\rangle \\
&= \langle U|\, e^{\hat{T}(\tau)}e^{-\beta\hat{h}_0}\,|U\rangle \\
&= \langle U|\, e^{-\beta\hat{h}_0/2}e^{\hat{T}(\tau)}e^{-\beta\hat{h}_0/2}\,|U\rangle \\
&\underset{\text{B.T.}}{\rightarrow} \langle\theta(\beta)|\, e^{\hat{T}(\tau)}\,|\theta(\beta)\rangle \\
&= e^{t^0(\tau)}.
\end{aligned} \tag{6.60}$$

The $t^0(\tau)$ is the same as in Eq. (6.55).

$$\begin{aligned}
\mathrm{Tr}_{physical}\left(\hat{O}\hat{D}\right) &= \langle U|\,\hat{O}\,|\Phi(\tau)\rangle \\
&= \langle U|\,\hat{O}e^{\hat{T}(\tau)}e^{-\beta\hat{h}_0}\,|U\rangle \\
&= \langle U|\, e^{-\beta\hat{h}_0/2}\hat{O}e^{\hat{T}(\tau)}e^{-\beta\hat{h}_0/2}\,|U\rangle \\
&\underset{\text{B.T.}}{\rightarrow} \langle\theta(\beta)|\,\tilde{O}e^{\hat{T}(\tau)}\,|\theta(\beta)\rangle \\
&= \langle\theta(\beta)|\, e^{\hat{T}(\tau)}e^{-\hat{T}(\tau)}\tilde{O}e^{\hat{T}(\tau)}\,|\theta(\beta)\rangle \\
&= e^{t^0(\tau)}\,\langle\theta(\beta)|\,(\tilde{O}e^{\hat{T}(\tau)})_{conn.}\,|\theta(\beta)\rangle\,.
\end{aligned} \tag{6.61}$$

In the last equality in Eq. (6.61), we use $\langle\theta(\beta)|\, e^{\hat{T}(\tau)} = e^{t^0(\tau)}\,\langle\theta(\beta)|$ [8]. As before, the Bogoliubov transformation is indicated by $\underset{\text{B.T.}}{\rightarrow}$. Using Eqs. (6.60) and (6.61), we obtain a general expression for thermal properties in the TFCC formulation:

$$\left\langle\hat{O}\right\rangle = \frac{\mathrm{Tr}_{physical}\left(\hat{O}\hat{D}\right)}{\mathrm{Tr}_{physical}\left(\hat{D}\right)} = \langle\theta(\beta)|\,(\tilde{O}e^{\hat{T}(\tau)})_{conn.}\,|\theta(\beta)\rangle \tag{6.62}$$

Note that our TFCC formulation is slightly different from the original work on TF dynamics by Harsha et al. [27] In the original formulation, response theory and Λ-equations are

[8] This comes from $e^{\hat{T}^\dagger(\tau)}\,|\theta(\beta)\rangle = e^{t^0(\tau)}\,|\theta(\beta)\rangle$, as $\hat{T}^\dagger(\tau)\,|\theta(\beta)\rangle = t^0(\tau)\,|\theta(\beta)\rangle$, which results from Eq. (6.26).

applied to calculate the physical properties, in the same way as the canonical coupled cluster theory. However, in our formulation, the physical properties are directly mapped through the cumulant expression of the thermal density matrices, which is based upon our previous work of the TNOE approach. [9] [25]

To verify the soundness of this formulation, we use Eq. (6.62) to calculate $\left\langle \hat{i}^\dagger \hat{j} \right\rangle$ of a two modes uncoupled vibrational model, whose Hamiltonian reads

$$\hat{H} = E_0 + \sum_{k=1}^{2} \left(\lambda_k (\hat{k}^\dagger + \hat{k}) + \omega_k \{\hat{k}^\dagger \hat{k}\} \right), \tag{6.63}$$

with $i, j = 1, 2$, over a wide range of temperature. Perfect agreement with numerically exact values, obtained by summing over states, is seen in Fig. 6.1, illustrating the validity of our method for calculating thermal properties.

[9] Let us note that properties calculated directly in TFCC are in general different from properties obtained using response theory, or alternatively, properties calculated as derivatives.

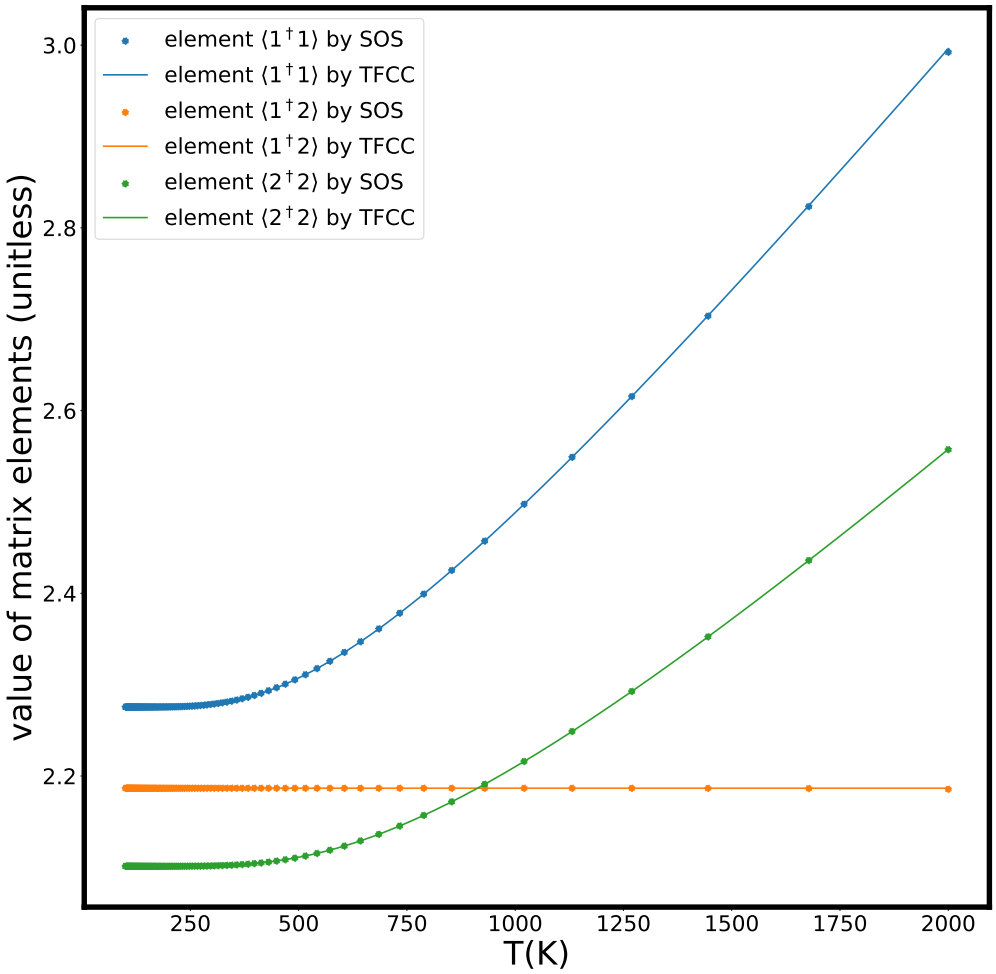


Figure 6.1: Compared to the sum over states method with a converged basis set, the thermal one-body reduced density matrix calculated using the expression from the TFCC method produces numerical exact result for the single-surface vibrational problem when truncated up to quadratic terms.

This concludes the formulation of the TFCC theory for the single-surface vibrational problem. A powerful feature of TFCC, for the single-surface problem with potential truncated up to quadratics, is that it is numerically exact because the EOM are in a closed form. Although it will not be numerically exact for higher order potentials, the theory can in principle be applied to simulate chemical systems at thermal equilibrium under BOA with a PES in a generic polynomial form.

3. Initialization of the cluster amplitude

Now, we discuss a practical aspect in the numerical imaginary time integration of the coupled cluster amplitudes. Unlike the real time dynamics case, the initial condition of the cluster amplitudes for the imaginary integration is ill-defined at $\tau = 0$. This is because at $\tau = 0$, the thermal density operator is defined as:

$$\lim_{\tau \to 0} \hat{D}(\tau) = \lim_{\tau \to 0} e^{-\tau \hat{H}} = \mathbb{1}, \tag{6.64}$$

and the Hilbert space of the Bosonic vibrational Hamiltonian has an infinite dimension. The expression of the density matrix is defined as:

$$\begin{aligned}\lim_{\tau\to 0} d_\mu(\tau) &\equiv \left\langle \Omega_\mu^\dagger \right\rangle \\ &= \lim_{\tau\to 0} \frac{\mathrm{Tr}_{physical}\left(\Omega_\mu^\dagger \hat{D}(\tau)\right)}{\mathrm{Tr}_{physical}\left(\hat{D}(\tau)\right)} = \frac{\mathrm{Tr}_{physical}\left(\Omega_\mu^\dagger \mathbb{1}\right)}{\mathrm{Tr}_{physical}\left(\mathbb{1}\right)} = \frac{\sum_{m=0}^{\infty}\langle m|\,\Omega_\mu^\dagger\,|m\rangle \to \infty}{\sum_{m=0}^{\infty}\langle m|\,\mathbb{1}\,|m\rangle \to \infty}.\end{aligned} \tag{6.65}$$

The $\frac{\infty}{\infty}$ expression is ill-determined. Meanwhile the thermal density matrices can be mapped to the coupled cluster amplitudes through the cumulant expression in Eq. (6.62):

$$d_\mu(\tau) = \langle\theta(\beta)|\,(\Omega_\mu^\dagger e^{\hat{T}(\tau)})_{conn.}\,|\theta(\beta)\rangle\,. \tag{6.66}$$

From Eqs. (6.65) and (6.66), we see that at $\tau = 0$, the initial coupled cluster amplitudes are ill-defined. Consequently, we can not initialize the numerical imaginary time integration for the coupled cluster amplitudes.

Fortunately, it is possible to obtain approximated coupled cluster amplitudes at a large but finite temperature with external sources as the initialization. The analytical thermal density matrices for a general displaced H.O. are known and can be used to approximate the initial coupled cluster amplitude at high temperature. The underlying reason for this approximation is that the bilinear couplings between modes and the quadratic squeezing within respective modes can be treated as small perturbations to the vibrational Hamiltonian in Eq. (6.8). Also, at high temperature thermal properties tend to converge towards their classical limits, which are less dependent on the perturbations.

Following this logic, we proposed a procedure to initialize coupled cluster amplitudes at a high yet finite temperature. First, we approximate the initial physical thermal density matrices using the analytical thermal density matrix ($\approx C_\mu(\tau_0)$) of the displaced H.O. at an initial temperature τ_0:

$$d_\mu(\tau_0) = \left\langle \Omega_\mu^\dagger(\tau_0) \right\rangle \approx C_\mu(\tau_0), \tag{6.67}$$

Then, we transform $\Omega_\mu^\dagger$ to the quasi-particle representation $\tilde{\Omega}_\mu^\dagger$ through Eqs. (6.43) and (6.44). Now, the vector of the physical density matrix elements can be expressed as a linear transformation of a vector of the quasi-particle density matrix elements:

$$\tilde{\boldsymbol{d}}_\mu(\tau_0) = \boldsymbol{X}\,\boldsymbol{d}_{\boldsymbol{\mu}}(\tau_0) \tag{6.68}$$

The matrix elements of $\boldsymbol{X}$ are determined by the transformations in Eqs. (6.43) and (6.44). In the last step, all coupled cluster amplitude can be mapped from the cumulant expression of the quasi-particle thermal density matrix elements:

$$\tilde{d}_\mu(\tau_0) = \langle\theta(\beta)|\,(\tilde{\Omega}_\mu^\dagger e^{\hat{T}(\tau_0)})_{conn.}\,|\theta(\beta)\rangle\,. \tag{6.69}$$

From $\tilde{d}_\mu(\tau_0)$ the initial CC amplitudes are obtained.

6.3.2 Vibronic multi-surface formulation: VE-TFCC theory

In this section, we extend the TFCC approach derived for the single-surface vibrational problems to the multi-surface vibronic coupling problems. The generic vibronic Hamiltonian that includes multiple electronic states and vibrational modes, and whose potential is truncated up to second order reads

$$\hat{\boldsymbol{H}} \equiv \sum_{xy} |x\rangle \, \hat{H}_{xy} \, \langle y| \,, \tag{6.70}$$

$$\hat{H}_{xy} = h_y^x + \sum_i h_y^{xi} \hat{i}^\dagger + \sum_i h_{yi}^x \hat{i} + \sum_{ij} h_{yj}^{xi} \{\hat{i}^\dagger \hat{j}\} + \frac{1}{2} \sum_{ij} h_y^{xij} \hat{i}^\dagger \hat{j}^\dagger + \frac{1}{2} \sum_{ij} h_{yij}^x \hat{i}\hat{j}, \tag{6.71}$$

where $|x\rangle$ and $|y\rangle$ represent diabatic electronic states. The matrix elements in the Hamiltonian take the forms of:

$$\begin{aligned} h_y^x &= \left(E_x + \frac{1}{2} \sum_i \omega_i + \frac{1}{2} \sum_i \gamma_{yii}^x \right) \delta_{xy} \\ h_y^{xi} &= h_{yi}^x = \frac{\alpha_{yi}^x}{\sqrt{2}} \\ h_y^{xij} &= h_{yij}^x = \gamma_{yij}^x \\ h_{yj}^{xi} &= \omega_i \delta_{xy} \delta_{ij} + \gamma_{yij}^x, \end{aligned} \tag{6.72}$$

where E_a, ω_i, α_{yi}^x, γ_{yii}^x, and $\gamma_{yi\neq j}^x$ denote vertical energies, frequencies, linear couplings, quadratic squeezings, and bilinear couplings, respectively. These parameters can be obtained from *ab initio* electronic structure calculations.

To discuss the general formulation of calculating properties for vibronic Hamiltonians in a thermofield context we assume that a generic property is defined in a similar way as the Hamiltonian, and we write

$$\hat{\boldsymbol{O}} \equiv \sum_{xy} |x\rangle \, \hat{O}_{xy} \, \langle y| \,, \tag{6.73}$$

the formal definition of the thermal property is then given by

$$\begin{aligned} \left\langle \hat{\boldsymbol{O}}(\tau) \right\rangle &= \frac{1}{Q(\tau)} \sum_{w,n} \langle w, \boldsymbol{n}| \, \hat{\boldsymbol{O}} e^{-\tau \hat{\boldsymbol{H}}} \, |w, \boldsymbol{n}\rangle \\ &= \frac{1}{Q(\tau)} \sum_{w,n,m} \langle w, \boldsymbol{n}, \tilde{\boldsymbol{n}}| \, \hat{\boldsymbol{O}} e^{-\tau \hat{\boldsymbol{H}}} \, |w, \boldsymbol{m}, \tilde{\boldsymbol{m}}\rangle \,. \end{aligned} \tag{6.74}$$

Here the partition function $Q(\tau)$ is simply given by the numerator with $\hat{\boldsymbol{O}}$ replaced by the identity operator.

In analogy to the single-surface vibrational problem, we define a vibrational thermal reference state for each electronic diabat as:

$$|w, \theta(\beta)\rangle \equiv e^{-\beta \hat{h}_0/2} \, |w, U\rangle \tag{6.75}$$

where the label x denotes diabatic electronic states, and $|U\rangle = \sum_m |m, \tilde{m}\rangle$ denotes the uniform state as before. The zeroth order Hamiltonian $\hat{h}_0$ is the same for each electronic state and only depends on the vibrational degrees of freedom. In this way we can translate all aspects of vibrational thermofield theory to the current situation. All symbols inherit their meanings from the single-surface vibrational problem. Each vibronic thermal reference state is simply a direct product of an electronic diabat, and a vibrational thermal state in the composite space $e^{-\beta\hat{h}_0/2}\sum_m |m, \tilde{m}\rangle$. As a result of this direct product, each reference thermal state is a quasi-particle vacuum state, using the same Bogoliubov transformation as before:

$$\hat{a}_i |w, \theta(\beta)\rangle = \hat{b}_i |w, \theta(\beta)\rangle = 0, \tag{6.76}$$

$$\langle w, \theta(\beta)| \hat{a}_i^\dagger = \langle w, \theta(\beta)| \hat{b}_i^\dagger = 0. \tag{6.77}$$

Note that the Bogoliubov transformation is independent of the electronic DoF.

Using the thermal reference state, the property can be reformulated as

$$\left\langle \hat{\boldsymbol{O}}(\tau) \right\rangle = \frac{1}{Q(\tau)} \sum_w \langle w, \theta(\beta)| \hat{\boldsymbol{O}} e^{-\tau\hat{\boldsymbol{H}}} e^{\beta\hat{h}_0} |w, \theta(\beta)\rangle . \tag{6.78}$$

We can define states $\left|\phi^{(x)}\right\rangle$ and their equation of motion:

$$\left|\phi^{(w)}(\tau)\right\rangle \equiv e^{-\tau\hat{\boldsymbol{H}}} e^{\beta\hat{h}_0} |w, \theta(\beta)\rangle \tag{6.79}$$

$$-\frac{d}{d\tau}\left|\phi^{(w)}(\tau)\right\rangle = \hat{\boldsymbol{H}}\left|\phi^{(w)}(\tau)\right\rangle . \tag{6.80}$$

Such that the thermal property is obtained as

$$\left\langle \hat{\boldsymbol{O}}(\tau) \right\rangle = \frac{1}{Q(\tau)} \sum_w \langle w, \theta(\beta)| \hat{\boldsymbol{O}} \left|\phi^{(w)}(\tau)\right\rangle . \tag{6.81}$$

The states $\left|\phi^{(w)}(\tau)\right\rangle$ are then represented in the VE-TFCC representation

$$\left|\phi^{(w)}(\tau)\right\rangle = e^{\hat{T}^{(w)}(\tau)} \hat{\boldsymbol{Z}}(\tau) |w, \theta(\beta)\rangle , \tag{6.82}$$

where

$$\hat{\boldsymbol{Z}}(\tau) \equiv \sum_x \hat{Z}_x^{(w)}(\tau) |x\rangle \langle w| . \tag{6.83}$$

and the relevant amplitudes can be obtained from individual τ propagations, initializing the states at high temperature, in analogy with the single surface propagations discussed before. Importantly we can obtain free energies, as well as thermal reduced density matrices from these propagations. It is not necessary to solve response equations. This is an important strength of the approach. Next, we will discuss the detailed parameterization and equations of motion.

1. Formulation of the detailed EOM in VE-TFCC

As in the single-surface vibrational problems, we formulate an EOM to propagate the thermostate based on a fixed ansatz. Thermal properties can then be determined through imaginary time integration over the cluster amplitudes. As before, we transform the physical diabatic Hamiltonian matrix elements into the Bogoliubov representation by applying Eqs. (6.43) and (6.44):

$$\hat{H}_{xy} \underset{\text{B.T.}}{\rightarrow} \tilde{H}_{xy}. \tag{6.84}$$

$\tilde{\boldsymbol{H}}$ in the doubled Bogoliubov representation reads:

$$\tilde{\boldsymbol{H}} \equiv \sum_{xy} |x\rangle \, \tilde{H}_{xy} \, \langle y| \,, \tag{6.85}$$

$$\tilde{H}_{xy} = \sum_{p} \tilde{h}^{xp}_{y} \hat{c}^{\dagger}_{p} + \sum_{p} \tilde{h}^{x}_{yp} \hat{c}_{p} + \sum_{pq} \tilde{h}^{xp}_{yq} \{\hat{c}^{\dagger}_{p} \hat{c}_{q}\} + \frac{1}{2} \sum_{pq} \tilde{h}^{xpq}_{y} \hat{c}^{\dagger}_{p} \hat{c}^{\dagger}_{q} + \frac{1}{2} \sum_{pq} \tilde{h}^{x}_{ypq} \hat{c}_{p} \hat{c}_{q}. \tag{6.86}$$

We then apply the mixed CC/CI (CI: configuration interaction) ansatz to parameterize the TF state associated with the initial surface w:

$$\left|\phi^{(w)}(\tau)\right\rangle \equiv e^{-\tau \tilde{\boldsymbol{H}}} e^{\beta \hat{h}_0} \left|w, \theta(\beta)\right\rangle, \tag{6.87}$$

$$\left|\phi^{(w)}(\tau)\right\rangle = e^{\hat{T}^{(w)}(\tau)} \sum_{x} \hat{Z}^{(w)}_{x}(\tau) \left|x, \theta(\beta)\right\rangle, \tag{6.88}$$

where

$$\hat{T}^{(w)}(\tau) \approx \sum_{p} t^{p(w)}(\tau) \hat{c}^{\dagger}_{p} + \frac{1}{2} \sum_{pq} t^{pq(w)}(\tau) \hat{c}^{\dagger}_{p} \hat{c}^{\dagger}_{q} + \cdots, \tag{6.89}$$

$$\hat{Z}^{(w)}_{x}(\tau) \approx z^{0(w)}_{x}(\tau) + \sum_{p} z^{p(w)}_{x}(\tau) \hat{c}^{\dagger}_{p} + \frac{1}{2} \sum_{pq} z^{pq(w)}_{x}(\tau) \hat{c}^{\dagger}_{p} \hat{c}^{\dagger}_{q} + \cdots, \tag{6.90}$$

where "$\approx$" denotes the truncation up to double excitations.

The introduction of multiple electronic states complicates the problem. We borrow the idea from our previous work (three of us: SB, NR and MN) [31] to introduce the mixed CC/CI ansatz. The explicit motivation for choosing this ansatz is elaborated in appendix section I.3. In this ansatz, the diabat-specific vibrational excitations are all included in the CI excitation operator $\hat{Z}^{(w)}_{x}$, which describes how the vibrational wave packet evolves from a single initial state $|w\rangle$ to all the diabats $\{|x\rangle\}$. We substitute the mixed CC/CI ansatz into the Schrödinger equation for the TF state $\left(-\frac{\mathrm{d}}{\mathrm{d}\tau}\left|\phi^{(w)}(\tau)\right\rangle = \tilde{\boldsymbol{H}}\left|\phi^{(w)}(\tau)\right\rangle\right)$ giving us:

$$-\frac{\mathrm{d}}{\mathrm{d}\tau}\left(e^{\hat{T}^{(w)}(\tau)} \sum_{x} \hat{Z}^{(w)}_{x}(\tau)\right) \left|x, \theta(\beta)\right\rangle = \tilde{\boldsymbol{H}} \left(e^{\hat{T}^{(w)}(\tau)} \sum_{x} \hat{Z}^{(w)}_{x}(\tau)\right) \left|x, \theta(\beta)\right\rangle. \tag{6.91}$$

In the last step, just as for the single-surface vibrational problem, we project the equation

against $\langle y,\theta(\beta)|\,\tilde{\Omega}_\mu^\dagger e^{-\hat{T}^{(w)}(\tau)}$, and the TFCC-EOM can be derived as:

$$-\langle y,\theta(\beta)|\,\tilde{\Omega}_\mu^\dagger\left(\frac{\mathrm{d}\hat{T}^{(w)}(\tau)}{\mathrm{d}\tau}\hat{Z}_y^{(w)}(\tau)+\frac{\mathrm{d}\hat{Z}_y^{(w)}(\tau)}{\mathrm{d}\tau}\right)|y,\theta(\beta)\rangle=\langle y,\theta(\beta)|\,\tilde{\Omega}_\mu^\dagger\sum_x\bar{H}_{yx}^{(w)}(\tau)\hat{Z}_x^{(w)}(\tau)\,|x,\theta(\beta)\rangle\,, \tag{6.92}$$

where

$$\bar{H}_{yx}^{(w)}(\tau)\equiv\left(\tilde{H}_{yx}e^{\hat{T}^{(w)}(\tau)}\right)_{conn.}. \tag{6.93}$$

$$\tilde{\Omega}_\mu^\dagger\equiv\{\mathbb{1},\hat{c}_p^\dagger,\hat{c}_p^\dagger\hat{c}_q^\dagger,\cdots\} \tag{6.94}$$

The EOM in Eq. (6.92) parametrically depends on the initial electronic label w. In practice, we use a diagonal approximation for the initial $\hat{Z}_x^{(w)}$:

$$\hat{Z}_x^{(w)}(\tau_0)\approx\delta_{xw}\hat{Z}_x(\tau_0) \tag{6.95}$$

and propagate the EOM for individual diabats ($|x\rangle$) separately, during which $\hat{Z}_x^{(w)}$ becomes off-diagonal. Note that in Eq. (6.93), $\hat{T}$ spans the vibrational DoF only and the similarity transformation is performed on each electronic block of the diabatic Hamiltonian matrix elements with the same vibrational $\hat{T}^{(w)}$ operator. In this way, we avoid the direct evaluation of a matrix exponential in the electronic DoF and thus each electronic block of the similarity transformed Hamiltonian in Eq. (6.93) stays connected. Thermal properties are calculated using the $\hat{T}^{(w)}(\tau)$ and $\hat{Z}_x^{(w)}(\tau)$ amplitudes on-the-fly.

A general multi-surface reduced density matrix in Bogoliubov representation can be defined as:

$$\begin{aligned}\tilde{D}_{yw}^{\mu}(\tau)&\equiv\mathrm{Tr}_{vibrational}\left(\langle y|\,\tilde{\Omega}_\mu^\dagger e^{-\tau\hat{\boldsymbol{H}}}\,|w\rangle\right)\\&=\langle y,\theta(\beta)|\,\tilde{\Omega}_\mu^\dagger e^{-\tau\hat{\boldsymbol{H}}}e^{\beta\hat{h}_0}\,|w,\theta(\beta)\rangle\\&=\langle y,\theta(\beta)|\,\tilde{\Omega}_\mu^\dagger\left|\phi^{(w)}(\tau)\right\rangle\\&=\langle y,\theta(\beta)|\,\tilde{\Omega}_\mu^\dagger e^{\hat{T}^{(w)}(\tau)}\sum_x\hat{Z}_x^{(w)}(\tau)\,|x,\theta(\beta)\rangle\,.\end{aligned} \tag{6.96}$$

The electronic density matrix ($\mu=0$) is simply:

$$\begin{aligned}\tilde{D}_{yw}^{0}(\tau)&=\langle y,\theta(\beta)|\,\mathbb{1}e^{\hat{T}^{(w)}(\tau)}\sum_x\hat{Z}_x^{(w)}(\tau)\,|x,\theta(\beta)\rangle\\&=\langle y,\theta(\beta)|\sum_x z_x^{0(w)}\,|x,\theta(\beta)\rangle\,.\end{aligned} \tag{6.97}$$

We can evaluate thermal density matrices in the Bogoliubov representation through the cumulant expression of the cluster amplitudes, similar to the single-surface vibrational problem. Then, we can inverse Bogoliubov transform these density matrices into the physical

representation (the explicit scheme of the transformation is shown in appendix section I.4):

$$\tilde{D}^{\mu}_{yw} \underset{\text{inverse B.T.}}{\rightarrow} \hat{D}^{\mu}_{yw} \tag{6.98}$$

To obtain the thermal properties, we directly sum over electronic states. The partition function can be defined as:

$$Q(\tau) \equiv \mathrm{Tr}\Big(\hat{D}\Big) = \sum_{x} (\hat{D}^{0}_{xx}(\tau)). \tag{6.99}$$

For a vibrational operator $\hat{O} \equiv \sum_{\mu} o_{\mu} \hat{\Omega}_{\mu}$, the thermal expectation value is defined as:

$$\Big\langle \hat{O} \Big\rangle \equiv \frac{\mathrm{Tr}\Big(\hat{O}\hat{D}\Big)}{\mathrm{Tr}\Big(\hat{D}\Big)} = \frac{\sum_{x\mu} o_{\mu} \hat{D}^{\mu}_{xx}}{Q(\tau)}. \tag{6.100}$$

In this way, we derived a cumulant expression that maps thermal properties from the amplitudes. The amplitudes can, in principle, be determined through imaginary time integration. However, there is a redundancy in the parameterization, as the number of equations equals the number of parameters in $\hat{\boldsymbol{Z}}$, but one also needs an equation for the amplitudes in $\hat{T}$. We introduce a technique to address this issue next.

2. Ehrenfest parameterization

The mixed CC/CI ansatz gives a redundant parameterization. As a consequence, the number of independent parameters is larger than the number of projected EOMs in Eq. (6.92). To solve this problem, we introduce the Ehrenfest parameterization of $\hat{T}(\tau)$ residuals in a similar way as in VECC theory for real time dynamics [31]. We take the weighted average over all electronic states[10] to accommodate population transfer between the electronic states, for each step of the imaginary time τ propagation:

$$-\frac{\mathrm{d}t^{\mu}(\tau)}{\mathrm{d}\tau} = \frac{\sum_{yx} z^{0}_{y}(\tau) \left\langle y, \theta(\beta) \right| \tilde{\Omega}^{\dagger}_{\mu} \bar{H}_{xy}(\tau) \hat{z}^{0}_{x}(\tau) \left| x, \theta(\beta) \right\rangle}{\sum_{x} (z^{0}_{x}(\tau))^{2}}. \tag{6.101}$$

The $\hat{Z}_{x}(\tau)$ residual can then be determined by substituting Eq. (6.101) into Eq. (6.92).

3. Initialization of the cluster amplitudes

Like in the single-surface vibrational problem, we need to initialize the cluster amplitudes for the vibronic problem, which are ill-defined at $\tau = 0$ (for the same reason). Following the same logic, we use high temperature H.O. thermal density matrices to initialize the amplitude for each diabat w. The procedure is briefly summarized below (explicit equations are given in appendix I.2).

The reduced thermal density matrix in the Bogoliubov representation is obtained from

[10] at thermal equilibrium

the cumulant expression of the cluster amplitude:

$$\begin{aligned}\tilde{d}^{\mu}_{yw}(\tau_0) &= \langle y,\theta(\beta)|\,\tilde{\Omega}^{\dagger}_{\mu}e^{\hat{T}(\tau_0)}\sum_x \hat{Z}_x(\tau_0)\,|x,\theta(\beta)\rangle \\ &\approx \langle y,\theta(\beta)|\,\tilde{\Omega}^{\dagger}_{\mu}e^{\hat{T}(\tau_0)}\hat{Z}_w(\tau_0)\,|w,\theta(\beta)\rangle\end{aligned} \tag{6.102}$$

This matrix is then reversely transformed to the physical space and then approximated by the high temperature classical limit:

$$\tilde{d}^{\mu}_{yw}(\tau_0) \to d^{\mu}_{yw}(\tau_0) \approx \delta_{yw}C^{\mu}_{w}(\tau_0). \tag{6.103}$$

The redundancy of the mixed CC/CI parameterization allows a flexibility to choose the initial parameterization of $\hat{T}(\tau)$ and $\hat{Z}_x(\tau)$ amplitudes. For simplicity, we choose:

$$z^{\mu}_{x}(\tau_0) = 0 \;\forall\; \mu \neq 0. \tag{6.104}$$

In this way, we have completed the formulation of the VE-TFCC approach for simulating vibronic coupling systems at thermal equilibrium. The key advantage of this approach compared to conventional approaches for statistical mechanics simulation is that it scales polynomially w.r.t. the number of DoF in the system. This is achieved by introducing *operator*-based mixed CC/CI ansatz to parameterized the thermal density operator. As a result, the approach is basis-set free and this avoids the usual curse of dimensionality.

6.4 Benchmarks and Application

The VE-TFCC approach is implemented in the open source code `hot-molecule` [194] which is an extension of our previous open source code `t-amplitudes` [170]. Standard Python libraries NumPy and SciPy are utilized to solve numerical ODEs and form tensor products [172, 173]. Libraries in open source software `Pibronic`[195] & `vmio`[196] developed by N. Raymond are used to handle I/O and processing of vibronic model parameters; formatted as standard MCTDH operator files (`*.op`).

In section 6.4.1, we employed the VE-TFCC method to calculate thermal properties for vibronic models with two electronic states and two normal modes, the same two by two models used in the reference [31]. These models are designed to simulate weak and strong vibronic couplings, respectively. Given the small number of DoF, we can benchmark VE-TFCC results against numerically exact SOS results. [11] In section 6.4.2, we benchmark the thermal internal energy of the vibronic model for a real molecular anion $CoF_4{}^-$ against a numerically exact block relaxation calculation in the low temperature limit. We also calculate thermochemistry data of the gas phase reaction:

$$CoF_3 + F^- \to CoF_4{}^-, \tag{6.105}$$

to showcase a real application of the method.

[11] obtained using a converged basis set for a wide range of temperature up to $T = 2000$ K.

6.4.1 Benchmark on two by two vibronic models

The two by two vibronic Hamiltonian reads:

$$\hat{H} = \begin{bmatrix} E_a + h_0 + \lambda_1 \hat{q}_1 & \gamma \hat{q}_2 \\ \gamma \hat{q}_2 & E_b + h_0 + \lambda_2 \hat{q}_1 \end{bmatrix} \tag{6.106}$$

$$h_0 = \frac{1}{2}\omega_1 \left(\hat{p}_1^2 + \hat{q}_1^2\right) + \frac{1}{2}\omega_2 \left(\hat{p}_2^2 + \hat{q}_2^2\right), \tag{6.107}$$

where E_a and E_b are energies of the two electronic states at the reference structure without distortion, ω_1 and ω_2 are the frequencies for the two vibrational modes that distort the structure, λ_1 and λ_2 are linear diagonal vibronic coupling constants, i.e., the Holstein couplings, along the q_1 coordinate of mode 1, and γ dictates the strength of the Peierls (off-diagonal) vibronic coupling along the q_2 coordinate of mode 2. Two models: model A and model B are tested. The model parameters are listed in Table 6.1.

Parameter	model A (eV)	model B (eV)
E^a	0.0	0.0
E^b	0.2	0.2
ω_1	0.2	0.2
ω_2	0.3	0.3
γ	0.2	0.2
λ_1	0.5	1.0
λ_2	-0.25	-0.5

Table 6.1: two by two model parameters.

1. Calculation of energy related thermal properties

Figs. 6.2 and 6.3 show the calculated internal energies, Helmholtz free energies, and entropies as functions of temperature for the two models, respectively.

For both models we perform two VE-TFCC calculations: The green curves are results obtained with $\hat{T}$ truncated at singles (S) and $\hat{Z}$ truncated at singles and doubles (SD). The blue curves are results with both $\hat{T}$ and $\hat{Z}$ truncated at SD. Comparing the two calculations in both models, we found that it is important to include doubles in $\hat{T}$ to produce accurate results. This is very different from the real time dynamics case in the VECC approach [31], where the contribution from doubles $\hat{T}$ is negligible, and is usually not included to facilitate the calculation of electronic populations.

In general, singles $\hat{T}$ determines the location of the center of the TF wave function, while doubles $\hat{T}$ accounts for the width. In the thermal case the vibronic model is located in the region of the conical intersection and the location of the center does not change much (or at all) with temperature. The width of the TF wave function grows with increasing temperature, and at high temperature the distribution reaches a uniform or very flat distribution. This cannot be described using a linear operator ($\hat{Z}$), and requires inclusion of the exponential

operator $\hat{T}$ truncated at SD. Interestingly, the results show that the doubles $\hat{T}_2$ are needed even at small β when it approximates the H.O. solution. As shown in the appendix I.2 the initial conditions based on H.O at high temperature require inclusion of doubles $\hat{T}_2$ (refer to Eq. (I.4)). The model calculations indicate that an Ehrenfest doubles $\hat{T}$, that is the same for each diabatic electronic state, captures the majority of the effect while the operator $\hat{Z}$ accounts for state-specific and off-diagonal effects. Good agreement between VE-TFCC and SOS is evident for $\hat{T}$ truncated at SD. The only minor deviation occurs at $T = 2000\ K$ for model A, the weak Holstein coupling model, in Fig. 6.2.

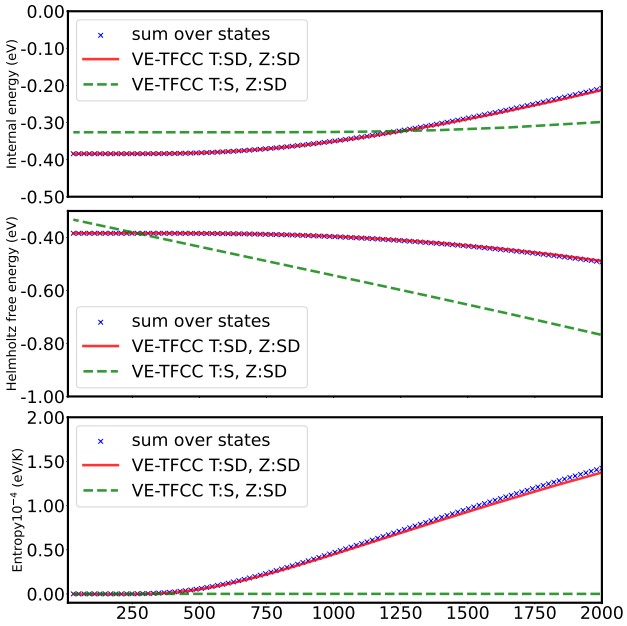


Figure 6.2: Simulated energy related thermal properties of model A, which has smaller linear displacements.

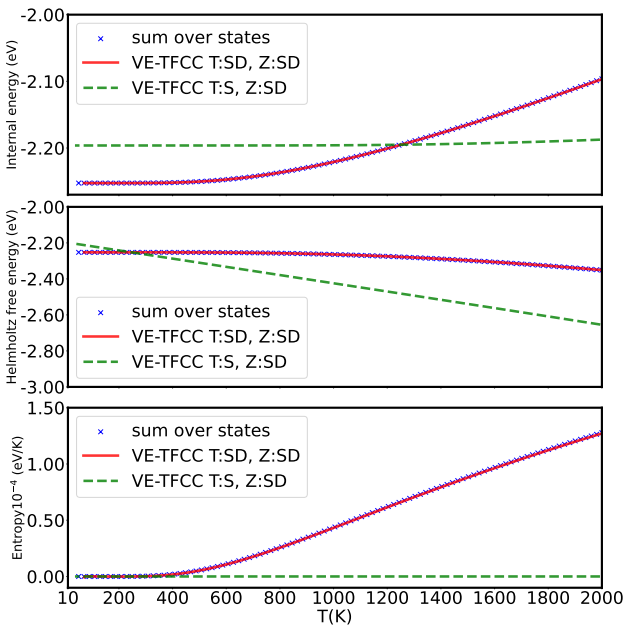


Figure 6.3: Simulated energy related thermal properties of model B, which has larger linear displacements.

2. Calculation of the variance of position

To further validate the robustness of the VE-TFCC approach, we investigate another thermal property, q-variance: $\langle \Delta \hat{q}_i \rangle \equiv \langle \hat{q}_i^2 \rangle - \langle \hat{q}_i \rangle^2$, for each normal mode $i = 1, 2$. The explicit scheme to calculate this property is given in appendix I.4. Figs. 6.4 and 6.5 show the calculated q-variance, as functions of temperature, for the two models.

The legends in Figs. 6.4 and 6.5 have the same meaning as in Figs. 6.2 and 6.3. The results show similar tends: $\hat{T}$ truncated at SD has good agreements with SOS, while $\hat{T}$ truncated at S has larger deviations. In general, for model B (larger linear displacement) VE-TFCC produces more accurate results than model A (smaller linear displacement), which is consistent with the results of the energy related thermal properties.

These results verify the conclusion drawn in previously: the doubles $\hat{T}$ plays an important role in obtaining accurate thermal properties using VE-TFCC.[12] The doubles $\hat{T}$ accounts for the width of the wavefunction and the q-variance is a measure of this width. As we can see in both models, the q-variance increases strongly as temperature increases for both the exact and SD solutions. However, in the results with $\hat{T}$ truncated at S, the q-variance often barely changes with temperature. This confirms that in the VE-TFCC approach doubles $\hat{T}$ are essential to capture the change of the width of the position distribution, as well as thermal energies as functions of temperature.

[12]It is not even possible to represent H.O. at initial temperature (τ_0) without introducing doubles $\hat{T}$ (refer to Eq. (I.4)).

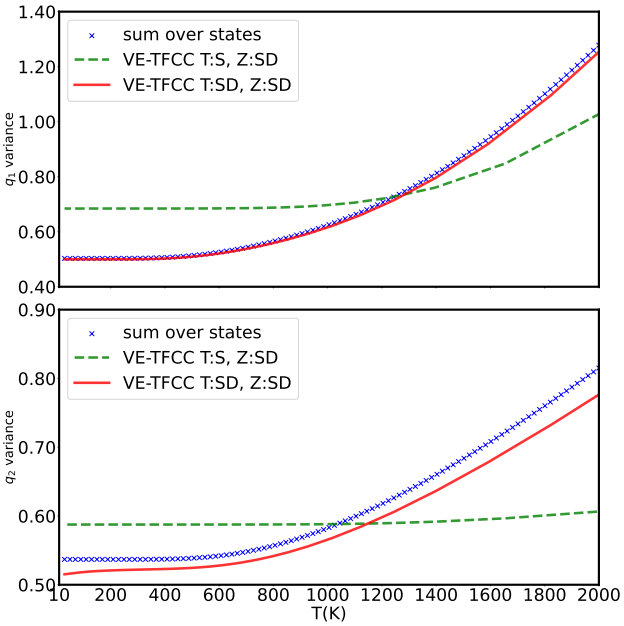


Figure 6.4: Simulated q-variance ($\langle \Delta \hat{q}_i \rangle$) of model A, which has smaller linear displacements.

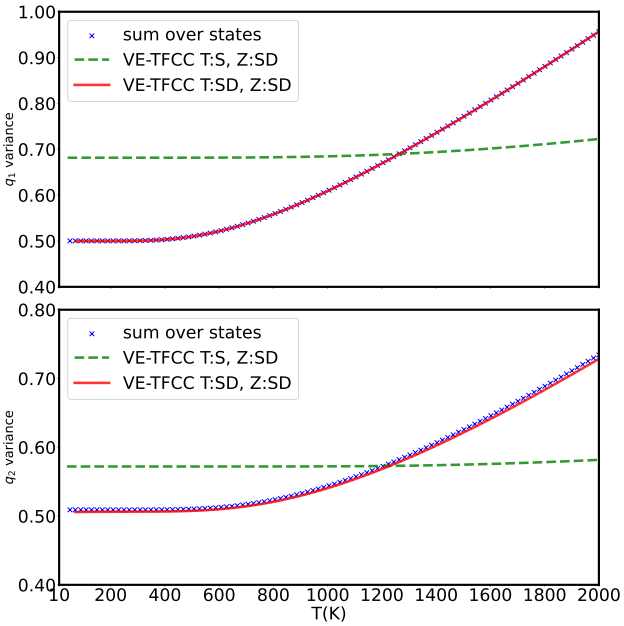
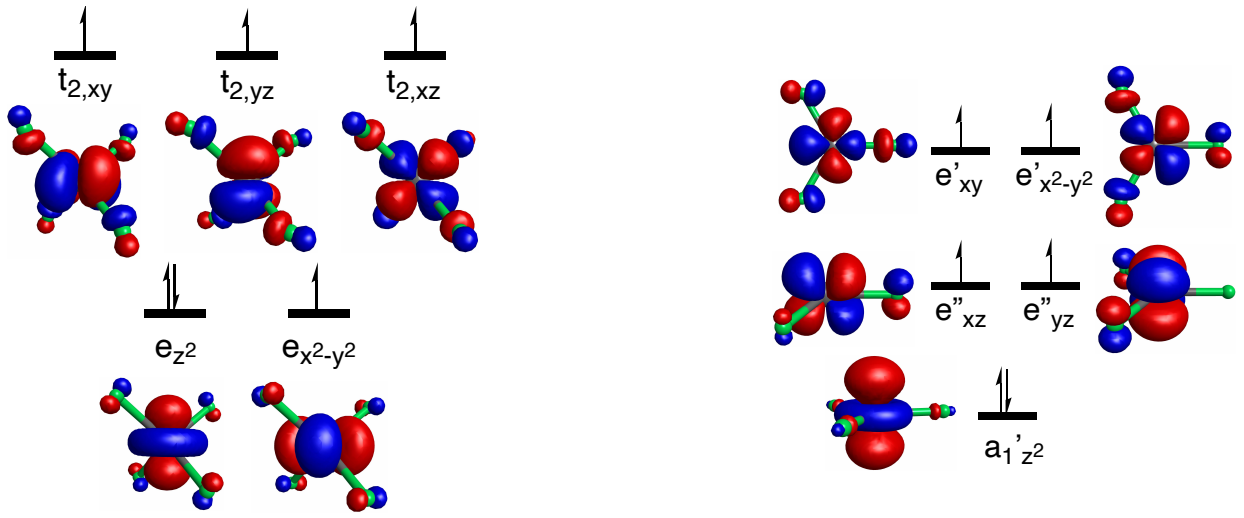


Figure 6.5: Simulated q-variance ($\langle \Delta \hat{q}_i \rangle$) of model B, which has larger linear displacements.

6.4.2 Benchmark on the vibronic model for CoF_4^- anion

To demonstrate the validity of the VE-TFCC method in calculating thermal properties of real molecular systems, we benchmarked against a block relaxation calculation using a 2-states 9-modes vibronic model of the CoF_4^- anion. The block relaxation calculation was performed

using the MCTDH package [160]. The parameters of the vibronic model are calculated by diabatizing electronic states obtained using general multi-configurational quasi-degenerate Perturbation theory (GMC-QDPT) [142, 143, 144] and the cc-pVTZ basis set [197]. The active space of the GMC-QDPT calculations consists of 5 orbitals dominated by Co 3d atomic orbitals (Fig. 6.6a) and 6 electrons. The GMC-QDPT calculations are performed using GAMESS-US [198]. The calculations show that the CoF_4^- anion adopts a high spin electronic configuration in its ^5E doubly-degenerate ground state, whose occupation scheme is shown in Fig. 6.6a. The two-fold degeneracy of the ground state is induced by the T_d symmetry of the anion, and it leads to JT interaction.



(a) (b)

Figure 6.6: Active orbitals and occupation schemes for (a) the ^5E ground state of CoF_4^- in T_d symmetry and (b) the $^5A_1^{'}$ ground state of CoF_3.

The diabatization protocol developed by Zeng [58] is employed to obtain the vibronic model parameters. The CoF_4^- structure is first optimized by equally averaging the two components of the ^5E ground state. Without imposing any constraint, the T_d symmetry is preserved in the optimization. The optimized structure (with $r_{CoF} = 1.79$ Å) is used to construct the vibronic model of the ^5E ground state. At the optimized structure, a numerical hessian calculation is performed using the averaged energies of the lowest two quintet states, which correlate to the two ^5E components. The resulting nine normal modes ($a_1' + e + t_2 + t_2$) do not have any imaginary frequencies. The CoF_4^- anion is then distorted along each pair of modes, with a small (0.05 eV) displacement in the positive and negative directions. At each distorted structure, two GMC-QDPT adiabats are obtained and orthogonally transformed to have maximum overlaps with the two ^5E components at the reference structure. The adiabatic energies are correspondingly transformed to diabatic Hamiltonian matrix elements. The "point by point" obtained diabatic Hamiltonian matrix elements are fitted against polynomials of the dimensionless reduced coordinates of the nine modes, including linear, quadratic, and bilinear terms. The fitting parameters indicate that the ^5E state features a substantial JT interaction along the e bending modes, which are illustrated in

Fig. 6.7. The $E \times e$ vibronic coupling is strong, as the linear coupling constant (0.042 eV) is twice the vibratonial frequency of the e mode (0.021 eV). Plotted in Fig. 6.8a and Fig. 6.8b are the $E \times e$ diabatic and adiabatic PESs, respectively. The adiabatic PESs exhibit typical Mexican hat shape with the conical intersection at the T_d high symmetry, while the diabatic PESs are smooth displaced parabolas, as expected.

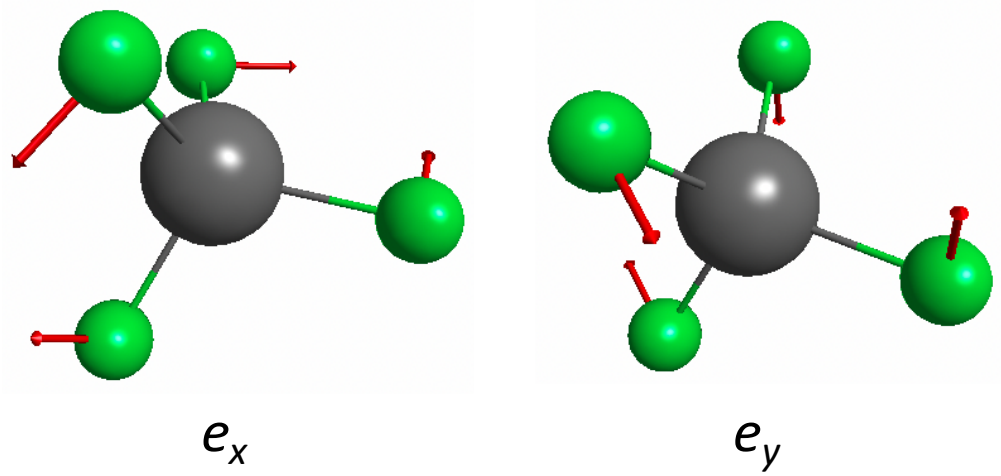
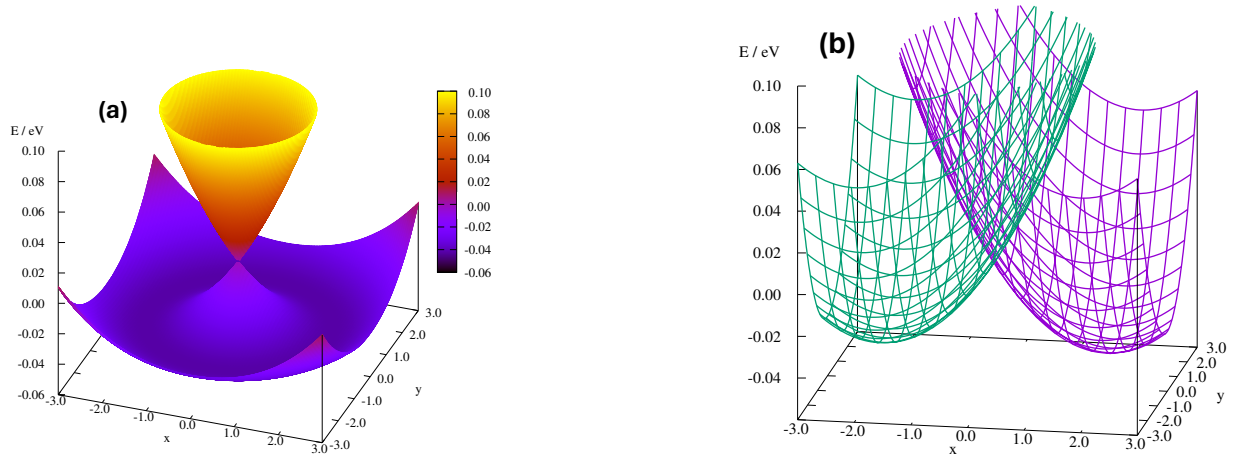


Figure 6.7: Illustration of the 168.46 cm^{-1} e bending modes of the CoF_4^- anion. The dimensionless reduced normal mode coordinates are labeled as x and y, corresponding to the e_x and e_y component modes.



(a) (b)

Figure 6.8: Plots of (a) adiabatic and (b) diabatic of E $\times$ e PESs of the CoF_4^- anion.

1. Comparison of internal energies from $T = 0$ to 1000 K

All nine modes and the two components of the ^{5}E state are included in our vibronic model for the CoF_4^- anion. Using this model, we calculate the thermal internal energy

of the anion and benchmark against a block relaxation calculation. In the block relaxation calculation, 600 lowest energy eigenvalues of the vibronic model are obtained, and the thermal internal energy is computed by summing over them, each weighted by the Boltzmann factor of specific temperature: The results are compared in Fig. 6.9. In this plot, the green dashed line represent the $9k_BT$ classical limit, where k_B denotes the Boltzmann constant. The black horizontal dashed line in the figure indicates the zero point energy (ZPE) for the nine normal modes.

$$\mathrm{ZPE} = \frac{1}{2}\sum_{i=1}^{N=9} \hbar\omega_i = 20.40\,\mathrm{kJ/mol}. \tag{6.108}$$

We also calculated the thermal internal energy of the harmonic oscillators of the nine normal modes:

$$E_{noJT}(T) = \sum_{i=1}^{N=9} \hbar\omega_i \left(\frac{1}{2} + \frac{e^{-\beta\hbar\omega_i}}{1-e^{-\beta\hbar\omega_i}}\right). \tag{6.109}$$

This is the vibrational energy of the ^{5}E ground state without considering any JT effect, static or dynamic, among the degenerate term symbol. We hence use "noJT" to label this series of results, which is shown by the red dashed curve in the figure.

As shown in Fig. 6.9, at $T < 200$ K, the VE-TFCC result converges towards the block relaxation result. This agreement validates the accuracy of the VE-TFCC method at low temperature. The zero temperature limit of the thermal internal energy deviates from the ZPE because of the JT stabilization. As the temperature increases the VE-TFCC result deviates from the block relaxation result. This is expected, since the block relaxation captures a finite number of low-lying vibronic eigenstates, which are insufficient to describe all thermally populated states at high temperature. At high temperature the VE-TFCC result is almost parallel with the classical limit. This parallel relation validates the accuracy of the VE-TFCC method at high temperature. They are not identical since the VE-TFCC internal energy is offset by the dynamical JT effect. The full vibronic treatment gives the dynamical JT effect.

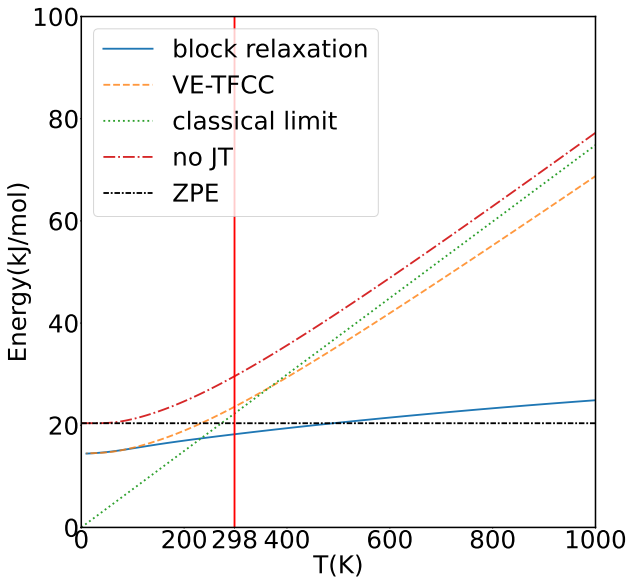


Figure 6.9: Comparison of the thermal internal energies for CoF_4^- anion calculated using different approximations.

The computational efficiency of VE-TFCC is evident, it takes $\sim$ 20 seconds to run on a Laptop Mac's M2 chip, while it takes $\sim$ 3 hours to run the block relaxation calculation, for all nine modes, with an Intel Xeon E5-2667 CPU.

For better comparison, we also perform the calculation that incorporated the static JT effect. In the static JT treatment, we assumed that the system is trapped in one stable JT-distorted structure in its ground state PES, with all degeneracy of electronic states being fully lifted, and invoked the Born-Oppenheimer approximation to describe the vibration of the system around this distorted structure, without allowing the system to hop to an electronic excited state. In short, it is a conventional computational chemistry treatment for a non-degenerate electronic state at a minimum of the JT-distorted ground state PES. The contributions of the other symmetry-related JT-distorted structures to the free energies are included as the entropy term of $k_B T \log(n)$, where n is the number of the stable JT-distorted structures. Note that we have ignored the symmetry number (due to the nuclear spin) in calculating rotational partition functions in both static and dynamic JT treatments. Besides, in the conventional thermochemistry treatment, symmetry equivalent structures are not considered. We consider these structures to make direct comparison with the corresponding vibronic model whose Hamiltonian preserves the high symmetry of the reference structure of the system (T_d in this case). The explicit calculation is elaborated next.

2. Thermochemistry comparison

VE-TFCC was used to calculate four thermochemical quantities, $\Delta_r U$, $\Delta_r S$, $\Delta_r A$, and $\Delta_r G$, for the gas phase reaction in Eq. (6.105). Results using the noJT, static JT, and dynamic JT methods, as well as the difference between the static JT and dynamic JT methods are presented in Table 6.2. The computational details are shown in appendix I.5.1.

Reaction energies at 0 K are summarized in the first row of Table 6.2. The difference

between the static and dynamic JT calculations is only 0.96 kJ/mol. The static JT treatment only leads to minute error in estimating the reaction energy at 0 K.

To examine the thermal effect, we also calculated the reaction energy at 298 K. Thermal corrections to internal energies, and their individual translational, rotational, and vibrational components[13] are tabulated in Table I.1 (in appendix I.5.2).

To consider the full vibronic correction (dynamic JT) to the reaction energy an additional 5.99 kJ/mol correction is added to the noJT value at 298 K in Fig. 6.9. The reaction energies at 298 K are shown in the second row of Table 6.2. The difference between the static and dynamic JT calculations is slightly larger at 298 K than at 0 K ($1.3 > 0.96$) but overall the change is minor.

To examine the reaction free energies we first need to obtain reaction entropies. The translational, rotational, and vibrational entropies[14] are tabulated in Table I.2 (in appendix I.5.3). The vibronic contribution to entropy obtained from the VE-TFCC calculation is 0.0064 kJ/mol/K. As tabulated in the third row of Table 6.2, the reaction entropies are -0.112, -0.099, and -0.109 kJ/mol/K for noJT, static JT, and dynamic JT, respectively. Using the previously calculated reaction energies and entropies, we obtain the reaction Helmholtz free energies $\Delta_r A = \Delta_r U - T\Delta_r S$ and the reaction Gibbs free energies $\Delta_r G = \Delta_r U - T\Delta_r S - RT$ at 298 K. Calculated free energies are tabulated in last two rows of Table 6.2. The vibronic contributions to the reaction free energies amount to -7.15 kJ/mol, more substantial than the -6 kJ/mol contribution to the reaction energy. Evidently, the vibronic contribution to entropy is not negligible for obtaining accurate thermodynamics data for chemical reactions. The 1.51 kJ/mol difference between dynamic and static JT treatments remains almost the same as in calculation of reaction energy.

quantity	no JT	static JT	dynamic JT	static − dynamic
$\Delta_r U$(0 K)	−471.34	−476.34	−477.30	0.96
$\Delta_r U$(298 K)	−471.18	−475.87	−477.17	1.3
$\Delta_r S$(298 K)	−0.112	−0.099	−0.109	0.01
$\Delta_r A$(298 K)	−437.74	−446.40	−444.89	−1.51
$\Delta_r G$(298 K)	−440.21	−448.88	−447.37	−1.51

Table 6.2: Summary of the thermochemistry data (Reaction energies and free energies are all in units of kJ/mol and the entropy is in units of kJ/mol/K.)

6.4.3 Analysis of thermochemistry calculations

In this section, we give a detailed analysis on the results of the thermochemistry calculations conducted in section 6.4.2. We focus on two aspects: (1) the accuracy of the electronic structure calculation, and (2) the effect of the vibronic coupling and the JT effect.

[13] obtained from standard thermochemistry calculations
[14] obtained from standard thermochemistry calculations

1. Accuracy of the electronic structure calculation

To examine the appropriateness of using the GMC-QDPT method for electronic structure calculations for the species in reaction Eq. (6.105), especially the necessity of multireference calculations, we performed CCSD(T)/aug-cc-pVTZ calculations for the JT-distorted CoF_4^- in D_{2d} symmetry and the $CoF_3 + F^-$ complex in C_{3v} symmetry. The F^- is placed 8 Å above the trigonal plane of CoF_3. The subtraction of the two energies gives an electronic reaction energy of -392.9 kJ/mol at 0 K without any vibrational or vibronic correction. This is ~ 80 kJ/mol higher than the GMC-QDPT analogue of -479.60 kJ/mol. In Table 6.3 these values are compared with the experimental value of -442 ± 25 kJ/mol [199] which has a large uncertainty. Still, the GMC-QDPT pure electronic reaction energy is closer to the experimental value than the CCSD(T) result, and the large deviation between CCSD(T) and experiment cannot be rectified by the inclusion of vibronic correction, which is within 10 kJ/mol for this reaction. One possible reason for the inferior performance of CCSD(T) is revealed by the T_2 amplitudes: two amplitudes of 0.12 and 0.13 for CoF_4^-, and four amplitudes from 0.12 to 0.14 for $CoF_3 + F^-$. These substantial amplitudes indicate fairly large multi-reference characters of the ground states in the reactant and product, and more so for the reactant. Therefore, the single-reference CCSD(T) may not describe the reactant and product accurately. Furthermore, it overestimates the correlation energy for the reactant more than for the product, and resulting in the less exoergicity electronic reaction energy. This examination confirms the importance of electronic structure question in calculating thermal equilibrium properties.

method	$\Delta_r E(0\text{ K})$ (kJ/mol)
CCSD(T)	-392.9
Experimental	-442.0 ± 25.0
GMC-QDPT	-479.60

Table 6.3: Comparison of electronic reaction energies at 0 K.

2. Fundamental different results of dynamical and static JT treatments.

The dynamic JT and the static JT treatments for the CoF_4^- anion produce similar results for the thermodynamics quantities (internal energy, free energy and entropy) at $T = 0$ and 298 K as shown in section 6.4.2. Despite this similarity it is important to clarify that the two treatments do not provide similar descriptions of CoF_4^-. In this subsection, we elaborate on their differences.

Since only the e bending mode delivers a substantial JT interaction for CoF_4^-, we ignore all the other modes and reduce the vibronic problem of the anion to an $E \times e$ problem, with the Hamiltonian

$$\hat{H} = \frac{1}{2}a_1 \begin{bmatrix} -\frac{\mathrm{d}^2}{\mathrm{d}x^2} - \frac{\mathrm{d}^2}{\mathrm{d}y^2} & 0 \\ 0 & -\frac{\mathrm{d}^2}{\mathrm{d}x^2} - \frac{\mathrm{d}^2}{\mathrm{d}y^2} \end{bmatrix} + \begin{bmatrix} H_{11} & H_{12} \\ H_{12} & H_{22} \end{bmatrix}, \tag{6.110}$$

where

$$\begin{aligned}\frac{1}{2}(H_{11}+H_{22}) &= \frac{1}{2}a_1(x^2+y^2)+a_2(x^3-3xy^2)+a_3(x^2+y^2)^2\\ \frac{1}{2}(H_{11}-H_{22}) &= a_4x+\frac{1}{2}a_5(x^2-y^2)\\ H_{12} &= -a_4y+a_5xy.\end{aligned} \tag{6.111}$$

with the coefficients (in eV)

$$\begin{aligned} a_1 &= 0.020\,89 & a_2 &= 0.000\,331\,6 & a_3 &= 0.000\,023\\ a_4 &= 0.043\,13 & a_5 &= 0.000\,103. \end{aligned}$$

The e modes have a vibron energy of a_1, and dimensionless reduced coordinates x and y. The 3rd order term $a_2(x^3-3xy^2)$ is included in $\frac{1}{2}(H_{11}+H_{22})$ to make the energy difference between the minima and the saddle points on the ground state PES (plotted in Fig. 6.10) consistent with the GMC-QDPT calculation. The 4th order term $a_3(x^2+y^2)^2$ is included in $\frac{1}{2}(H_{11}+H_{22})$ to bound it from below. Note that this model is not identical to the one investigated in section 6.4.2, since the previous model's potential is truncated at 2nd order. Still, the qualitative picture shall be similar.

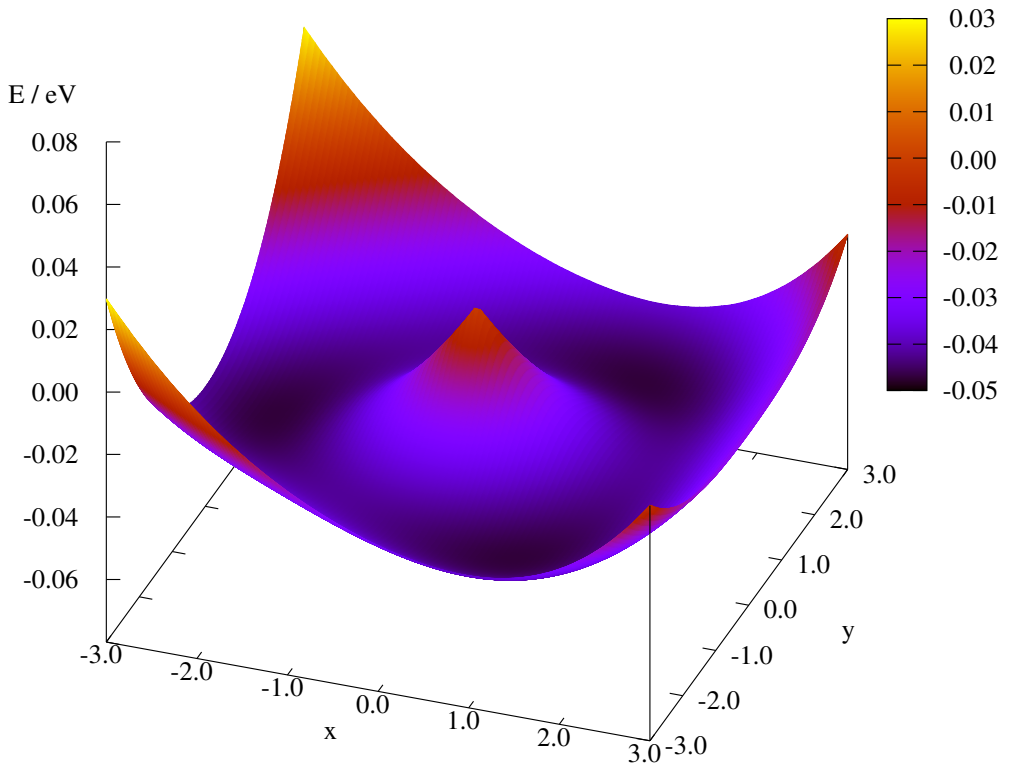


Figure 6.10: The ground state adiabatic PES of the E × e model in Eq. (6.111).

At one of the three symmetrically related minima of the PES, $(x_0, y_0) = (-2.24313, 0.0)$,

we calculated the hessian of the ground state PES and obtained the eigenvalues of $b_1 = 0.017\,91$ and $b_2 = 0.006\,22$ eV, which give the single surface vibrational Hamiltonian:

$$\hat{H} = \frac{1}{2}\left(-a_1\left(\frac{d^2}{dx^2} + \frac{d^2}{dy^2}\right) + b_1(x - x_0)^2 + b_2 y^2\right) - b_3, \tag{6.112}$$

where $b_3 = 0.047\,08$ eV. This is a 2-D H.O. Hamiltonian expanded around the minimum with the JT stabilization energy of b_3. The use of this local, Born-Oppenheimer-approximation-based Hamiltonian gives the static JT treatment, i.e., the vibrational wave packet is statically trapped around the minimum. The corresponding two vibrational frequencies are $\sqrt{a_1 \times b_1} = 0.01934$ eV and $\sqrt{a_1 \times b_2} = 0.01140$ eV. The two new vibrons are softer than the original ones with $a_1 = 0.02089$ eV energy. The ZPE of the H.O. Hamiltonian in Eq. (6.112) is $\frac{1}{2}(\sqrt{a_1 \times b_1} + \sqrt{a_1 \times b_2}) - b_3 = -0.031\,71$ eV, which is the ground state energy of the static JT treatment.

On the other hand, we use a 2-D H.O. basis set to resolve the E $\times$ e vibronic Hamiltonian and then diagonalize the resultant matrix to give the ground state of the dynamic JT treatment. The ground state energy $-0.032\,95$ eV is very close to the static JT analogue. This is consistent with the results in section 5.4.2, which were obtained by including all 9 modes but the Hamiltonian matrix elements are truncated to 2nd order only. Still, the dynamic treatment gives a lower ground state energy. [15]

Although having similar energy eigenvalues, the character of the ground eigenstates obtained from dynamic and static JT treatments are very different. In the static JT treatment, the ground state has its vibrational state localized within one minimum of the low-energy trough of the Mexican-hat-shaped PES, which is plotted in Fig. 6.10. However, the $0.005\,23$ eV barrier between the minimum and the saddle point within the trough is even smaller than the $\frac{1}{2}0.1140 = 0.0570$ eV zero point energy of the vibration in the direction to cross the barrier. The vibrational wave packet cannot be trapped within one minimum. The static JT approximation breaks for CoF_4^-.

Another way to see the failure of the static JT treatment is the $0.003\,71$ eV splitting between the degenerate E ground state and the A_1 first excited state of the E $\times$ e vibronic Hamiltonian, which is 1/3 of the relevant $0.011\,40$ eV vibron energy. This substantial splitting quantifies the interaction between the vibrational ground states localized in the three minima.

Fig. 6.11 shows the plot of the vibrational density of the first excited A_1 vibronic eigen state [16] (the green surface), and the normalized ground state density of the static JT treatment (the purple surface). If the static JT treatment is a good approximation, the green gaussian shall perfectly coincide with the purple lobe around the same minimum. However, the purple lobe is obviously higher. This indicate non-negligible antibonding interaction between the three Gaussians localized at the three minima. The static JT picture is fundamentally incorrect for CoF_4^-, despite its good approximation to ground state energy.

[15] Please note that we shall not use variational principle to argue that the dynamic JT treatment must give a lower ground state energy than the static JT treatment, since the two treatments use different Hamiltonians.

[16] scaled by 3 for direct comparison

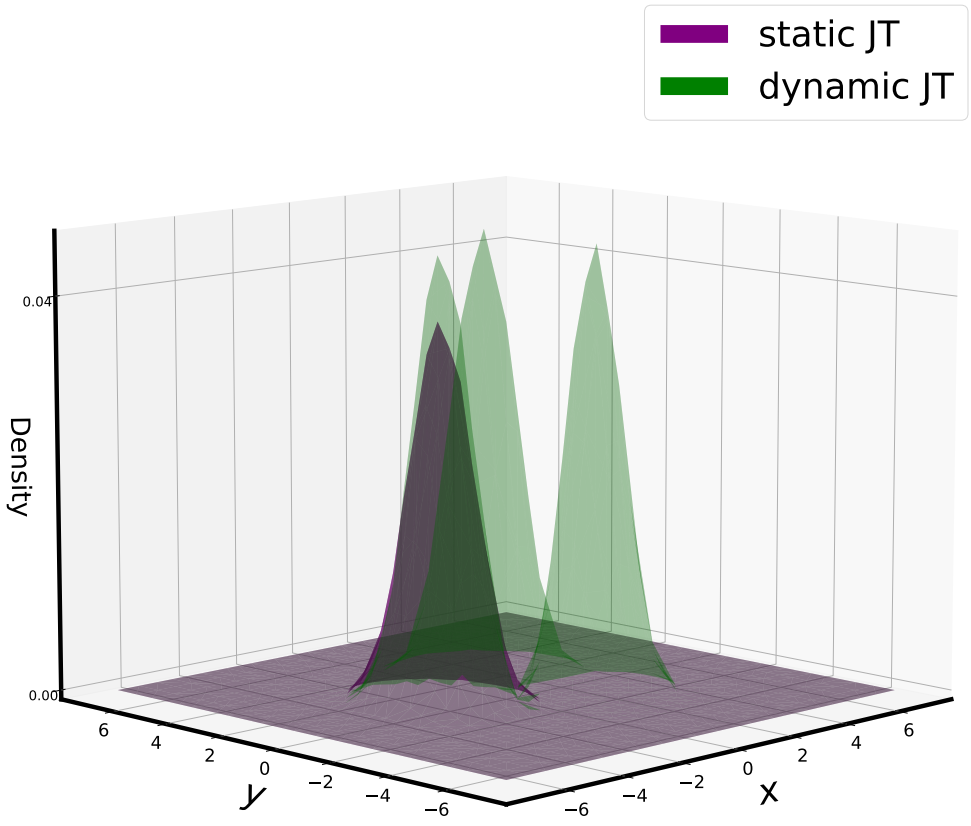


Figure 6.11: Plot of vibrational density of first excited A_1 state of dynamic JT and ground state of static JT.

6.5 Concluding Remarks

In this work, the VE-TFCC approach is developed to directly calculate thermal properties of vibronic coupling systems. The VE-TFCC approach can be regarded as a specific application of the more general TNOE approach developed by Nooijen and Bao [25]. In the latter approach, a normal-ordered exponential ansatz is introduced to parameterize the thermal density operator for a general quantum many-body Hamiltonian (either Bosonic or Fermionic). The thermal properties can be approximated through cumulant expansion of density matrices of low ranking cluster operators by applying unique contraction rules and the generalized Wick's theorem [200]. The VE-TFCC approach is also inspired by TF theory for quantum chemistry which was developed by Harsha et al. [26, 27, 28, 29, 30] In TF theory an ancillary space is introduced to construct the "thermal state" which represents the thermal density operator as a "pure state" in the compound space (physical and ancillary). In this way, the dimension of the Hilbert space is squared, allowing one to obtain thermal

properties for the physical space by evolving a pure state in the compound space and calculating thermal properties as expectation values. The VE-TFCC approach combines the ideas of the TNOE approach and TF theory. As a result, a single-reference-like coupled cluster approach is formulated to directly calculate thermal properties of vibronic coupling systems. In this approach, a second-quantized bosonic mixed linear-exponential ansatz is applied to parameterize the thermal density operator in the Bogoliubov representation. The resulting EOMs of the VE-TFCC approach resembles the VECC approach for real time dynamics in a previous work by three of us (SB, NR and MN) [31] and the thermal properties of vibronic coupling system can be obtained by imaginary time integration over the cluster amplitudes.

Some interesting features of the VE-TFCC approach include: i) Due to the compact representation of the thermal density operator in the VE-TFCC approach, it has a favorable computational cost. The approach is basis-set free and has polynomial scaling with respect to the number of DoF in the vibronic models similar to classical mechanics simulations, although it is a fully quantum mechanical method. ii) It is straightforward to calculate (approximate) thermal reduced density matrices, *without* response theory. The results will not be identical to energy derivative (or response) approaches, but they are solidly based in thermofield theory. iii) Although the approach requires the definition of a reference state and zeroth-order Hamiltonian, results are rigorously invariant under the choice of $\hat{h}_0$ or reference temperature β. iv) The initial conditions are based on a high-temperature classical (H.O.) description of the system. We think this is the weakest part of the theory. In our applications thus far, results are satisfactory. v) In the previous real time VECC approach it was sufficient to use singles $\hat{T}_1$, and to include $e^{\hat{T}_1^\dagger}$ in the modified projection manifold. This accounted for the fact that the center of the wave packet can move far away from the initial state. In the thermal case the center does not move much, but the width of the distribution is a critical feature. Besides, the operator $\hat{T}_2$ is crucial to initialize the propagation in the high temperature limit (refer to Eq. (I.4)). For these reasons the doubles operator $\hat{T}_2$ is of vital importance in the thermal case, but no modification to the projection manifold is necessary. vi) In VE-TFCC we propagate each diabatic state independently, obtaining corresponding (electronic) columns w of the thermal reduced density matrices $\hat{D}^{\mu}_{yw}$. The effect of radiationless transition between the two electronic states (either intersystem crossing or internal conversion) are captured by off-diagonal elements ($y \neq w$). At the initial high temperature only the starting state is populated, and by definition the reduced density matrices are diagonal. The state-averaged "Ehrenfest" approximation, for the $\hat{T}$ operator, facilitates the mixing of the other electronic states during the imaginary time propagation. This improves VE-TFCC's ability to capture state population transfer during the propagation. vii) The VE-TFCC approach is very user friendly. The user only needs to select the excitation level of the linear operator $\hat{Z}$, and the initial high temperature (small β), the rest is done by the program. viii) The approach is in principle also applicable to single surface anharmonic partition functions. The operator $\hat{Z}$ is not needed then, but it may be advantageous to use higher rank $\hat{T}$ operators. In addition, our implementation would need to be generalized to higher order than quadratic terms in the Hamiltonian terms. ix) The approach is not rigorously extensive, due to the linear CI part of the approximation. It is not clear at this moment how this would affect accuracy for larger systems. x) The current approach is applicable to finite systems only. The generalization to solids would be

interesting but there are likely significant issues to resolve.

The VE-TFCC approach is first tested by calculating a few thermal properties (internal energy, Helmholtz free energy and reaction entropy) for small vibronic models that have two electronic states and two normal modes and are constructed to simulate strong vibronic coupling. The accuracy of VE-TFCC is validated by benchmarking against numerical exact results. Then, as an application, VE-TFCC is employed to calculate thermochemistry properties of a gas phase chemical reaction that forms the CoF_4^- anion. Through the VE-TFCC simulation of the CoF_4^- vibronic model (2 states, 9 modes), we manage to calculate thermochemistry properties that incorporate the vibronic correction. Our results reveal that the vibronic correction is non-neligible. The VE-TFCC approach in conjunction with vibronic models provides a new protocol for calculating accurate thermochemistry properties of vibronic coupling systems.

Overall the VE-TFCC approach developed in this work is well positioned for applications in thermal equilibrium involving a number of low energy electronic states, as is common in many branches of chemistry and physics. It also provides a promising avenue for extending previous work[31] to capture finite temperature effects using real time dynamics, such as simulating hot-bands in spectroscopy.

Chapter 7

Concluding remarks and future orientations

7.1 Concluding remarks

In this thesis, we develop the general TNOE and TFCC approaches for statistical mechanics and quantum dynamics simulations in quantum chemistry. These approaches are applied to simulate the time-dependent and thermal properties of vibronic coupling systems, which play a crucial role in quantum chemistry. Vibronic coupling governs the transfer of electronic state populations during photo-electronic processes in molecular systems, and it also influences electronic transitions in vibrationally resolved electronic spectroscopy. By studying the quantum dynamics of these systems, we can gain insights into the optoelectronic properties of molecular compounds. Additionally, the effects of finite temperature on vibronic coupling systems are important for various applications. Most chemical reactions are thermodynamically driven, and the vibronic contributions to thermochemical properties, particularly in strongly coupled systems like JT systems, are significant. Furthermore, finite temperature effects impact hot bands in spectroscopy, making this an area of critical interest.

To simulate vibronic coupling systems, the first step is to construct the vibronic model Hamiltonian. Using standard diabatization protocols, we obtain the model parameters for the vibronic Hamiltonian from ab initio electronic structure calculations. With the vibronic model Hamiltonian established, our goal is to simulate its quantum dynamics and statistical mechanics.

We begin by developing a computational approach called the VECC method, designed to efficiently simulate the quantum dynamics of vibronic problems. In this approach, we apply the TNOE ansatz (reduced to the simple exponential ansatz in this case) to parameterize the time-dependent wavefunction. This allows us to calculate time-dependent properties on-the-fly through real-time integration of the cluster amplitudes in the exponential ansatz. However, the simplest implementation of the VECC method presents challenges due to the non-unitary nature of the exponential ansatz and the disconnectedness of the CC EOMs for a general diabatic vibronic coupling Hamiltonian. As a result, we encountered numerical instability during real-time integration, causing the cluster amplitudes to diverge. To address

these issues, we developed techniques such as the mixed CC-CI ansatz, Ehrenfest parameterization of the CC residuals, and modifications to the projection manifold. By applying these techniques, we successfully resolved the numerical problems associated with the naive implementation, enabling accurate simulations of spectroscopy and state populations for various vibronic models with impressive efficiency. A key advantage of the VECC method compared to conventional approaches for quantum dynamics simulations of vibronic problems is that it is basis-set free. Despite being a fully quantum mechanical approach, it scales classically (polynomially) with respect to the number of degrees of freedom in the vibronic model.

To simulate the statistical mechanics of vibronic coupling systems, we employ the general TFCC approach, referred to as the VE-TFCC approach. This method serves as a statistical mechanical formulation of the original VECC approach used for quantum dynamics simulations. Instead of real-time propagation, we conduct imaginary time evolution of the thermostate in the thermofield representation to calculate the thermal properties of these systems. Unlike the VECC approach, which focuses on real-time dynamics, we utilize the physical-ancillary dual space and Bogoliubov transformation to represent the thermal density operator ($e^{-\beta\hat{H}}$) as a "pure state". This allows the thermostate involves within this dual space, akin to the time-dependent wavefunction in the original physical space. Due to the disconnected nature of the CC EOMs, similar challenges arise in the exponential parameterization of the thermostate for diabatic vibronic model Hamiltonians, as seen in quantum dynamics. To address these issues, we adopt strategies such as the mixed CC/CI ansatz and the Ehrenfest parameterization of the CC residuals. This approach is applied to calculate the thermal properties of two-by-two model vibronic coupling systems, as well as a more realistic model: the CoF_4^- anion (which includes two states and nine modes). We also compute the thermochemistry data for the gas-phase reaction: $CoF_3 + F^- \rightarrow CoF_4^-$. The results from the VE-TFCC approach are benchmarked against conventional SOS methods. Like the quantum dynamics case, the VE-TFCC approach is basis-set-free and effectively avoids the curse of dimensionality. Benchmarking across various vibronic models demonstrates that the VE-TFCC approach exhibits impressive efficiency and accuracy.

Additionally, this general approach is applied to electronic structure problems, aiming to directly calculate the thermal properties of a statistical ensemble of electronic states under the BOA. However, it struggles to yield satisfactory results due to the N-representability problem. Attempts to address this issue by systematically imposing constraints on the cluster amplitudes during imaginary time propagation have also proven inadequate. Systematic analyses and investigations of model magnetic systems and small molecular compounds have provided valuable theoretical insights. Nevertheless, without a radical change in the current methodology, improvements in results remain elusive. Modern machine learning algorithms, such as the restricted Boltzmann machine [74, 75], may offer promising new avenues for tackling this problem.

7.2 Future orientations

It has been a dream for every quantum chemist since the dawn of quantum mechanics to fully understand molecular systems at a first-principles level. In the most platonic case, the

development of novel functional materials would resemble the design processes of bridges, skyscrapers, or cars, where computer simulations are extensively used at various stages to optimize the overall performance. However, unlike the macroscopic objects, the physics law that governs the microscopic world is the quantum mechanics. Therefore, quantum simulations are required to predict the properties of microscopic functional materials. Unfortunately, this task in general is a NP hard problem [201] and can not be efficiently solved on a classical computer. Nevertheless, it is feasible to find heuristic solutions to the subset of the problem based upon the specific structures of the problem. The computational methods developed in this thesis exemplify heuristic solutions for subsets of quantum simulation problems.

Fig. 7.1 illustrates the envisioned process for material discovery. Theory and experiments should be integrated such that prediction, design, synthesis, and characterization form a loop, dynamically evolving together. Modeling and simulation can play crucial roles at each stage. In the most ideal scenario, it would be feasible to create a digital twin of a physical laboratory, allowing everything to be simulated before actual experiments, akin to strategies in robotics automation and efforts towards self-driving chemistry labs [202]

In general, the current state-of-the-art computational methods for quantum chemistry are still far away from the dream envisioned by the pioneers of the quantum mechanics. Both more efficient algorithms and more powerful computers are required to fully resolve the problem. Fortunately, recent advancements in technologies such as general-purpose artificial intelligence (AI) and advanced computational architectures (e.g. graphics processing unit (GPU)s and noisy intermediate-scale quantum (NISQ) devices) might shed some new light on this old problem. Meanwhile, more advanced experimental tools need to be developed to better control microscopic systems and the nanotechnologies might play a role for this purpose.

With these advancements, humanity can look forward to a future with more sustainable clean energy sources and improved pharmaceuticals for combating diseases. However, we still have a long journey ahead: "*the great ocean of truth lay all undiscovered before me*".

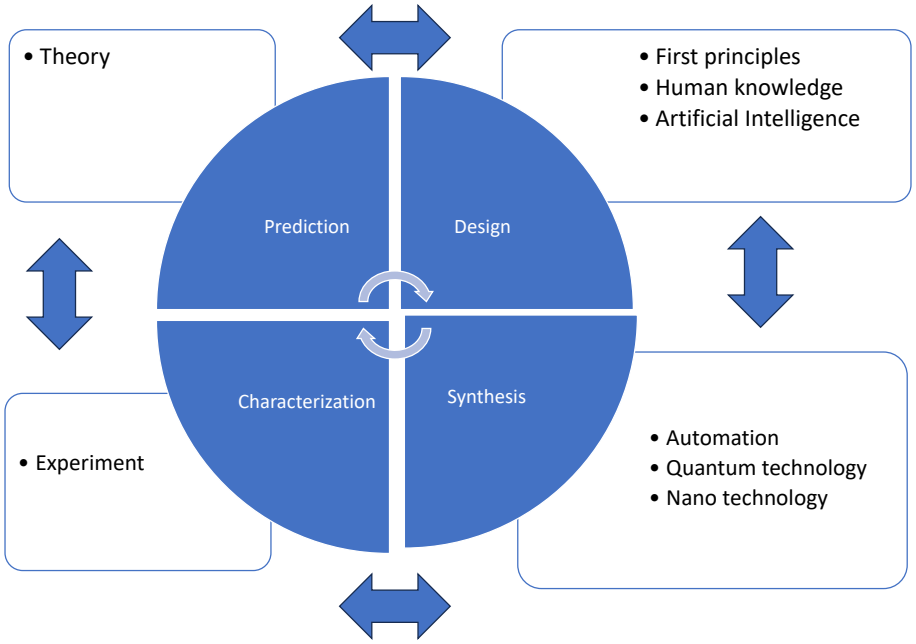


Figure 7.1: Illustration of the future orientations

References

[1] Paul Adrien Maurice Dirac. "Quantum mechanics of many-electron systems". In: *Proceedings of the Royal Society of London. Series A, Containing Papers of a Mathematical and Physical Character* 123.792 (1929), pp. 714–733.

[2] Goutam Sanyal, Seikh Hannan Mandal, and Debashis Mukherjee. "Thermal averaging in quantum many-body systems: a non-perturbative thermal cluster cumulant approach". In: *Chemical physics letters* 192.1 (1992), pp. 55–61.

[3] G Sanyal et al. "Systematic nonperturbative approach for thermal averages in quantum many-body systems: The thermal-cluster-cumulant method". In: *Physical Review E* 48.5 (1993), p. 3373.

[4] Sheikh Hannan Mandal, Rathindranath Ghosh, and Debashis Mukherjee. "A non-perturbative cumulant expansion method for the grand partition function of quantum systems". In: *Chemical physics letters* 335.3-4 (2001), pp. 281–288.

[5] Sheikh Hannan Mandal et al. "A non-perturbative path-integral based thermal cluster expansion approach for grand partition function of quantum systems". In: *Chemical physics letters* 352.1-2 (2002), pp. 63–69.

[6] Alec F White and Garnet Kin-Lic Chan. "A time-dependent formulation of coupled-cluster theory for many-fermion systems at finite temperature". In: *Journal of Chemical Theory and Computation* 14.11 (2018), pp. 5690–5700.

[7] Alec F White and Garnet Kin-Lic Chan. "Time-dependent coupled cluster theory on the keldysh contour for nonequilibrium systems". In: *Journal of Chemical Theory and Computation* 15.11 (2019), pp. 6137–6153.

[8] Alec F White and Garnet Kin-Lic Chan. "Finite-temperature coupled cluster: Efficient implementation and application to prototypical systems". In: *The Journal of Chemical Physics* 152.22 (2020), p. 224104.

[9] Ruojing Peng et al. "Conservation laws in coupled cluster dynamics at finite temperature". In: *The Journal of Chemical Physics* 155.4 (2021), p. 044103.

[10] So Hirata and Punit K Jha. "Converging finite-temperature many-body perturbation theory in the grand canonical ensemble that conserves the average number of electrons". In: *Annual Reports in Computational Chemistry*. Vol. 15. Elsevier, 2019, pp. 17–37.

[11] Punit K Jha and So Hirata. "Numerical evidence invalidating finite-temperature many-body perturbation theory". In: *Annual Reports in Computational Chemistry*. Vol. 15. Elsevier, 2019, pp. 3–15.

[12] Punit K Jha and So Hirata. "Finite-temperature many-body perturbation theory in the canonical ensemble". In: *Physical Review E* 101.2 (2020), p. 022106.

[13] So Hirata and Punit K Jha. "Finite-temperature many-body perturbation theory in the grand canonical ensemble". In: *The Journal of Chemical Physics* 153.1 (2020), p. 014103.

[14] Xiuyi Qin and So Hirata. "Finite-temperature many-body perturbation theory for anharmonic vibrations: Recursions, algebraic reduction, second-quantized reduction, diagrammatic rules, linked-diagram theorem, finite-temperature self-consistent field, and general-order algorithm". In: *The Journal of Chemical Physics* 159.8 (2023), p. 084114.

[15] Takeo Matsubara. "A new approach to quantum-statistical mechanics". In: *Progress of theoretical physics* 14.4 (1955), pp. 351–378.

[16] Pavel Pokhilko and Dominika Zgid. "Two-particle properties within finite-temperature self-consistent one-particle Green's function methods: theory and application". In: *APS March Meeting Abstracts*. Vol. 2021. 2021, pp. M21–008.

[17] Pavel Pokhilko et al. "Evaluation of two-particle properties within finite-temperature self-consistent one-particle Green's function methods: Theory and application to GW and GF2". In: *The Journal of Chemical Physics* 155.2 (2021), p. 024119.

[18] Pavel Pokhilko, Chia-Nan Yeh, and Dominika Zgid. "Iterative subspace algorithms for finite-temperature solution of Dyson equation". In: *The Journal of Chemical Physics* 156.9 (2022), p. 094101.

[19] Chia-Nan Yeh et al. "Fully self-consistent finite-temperature G W in Gaussian Bloch orbitals for solids". In: *Physical Review B* 106.23 (2022), p. 235104.

[20] Yasushi Takahashi and Hiroomi Umezawa. "Thermo field dynamics". In: *International journal of modern Physics B* 10.13n14 (1996), pp. 1755–1805.

[21] H Matsumoto et al. "Thermo field dynamics in interaction representation". In: *Progress of Theoretical Physics* 70.2 (1983), pp. 599–602.

[22] Hiroomi Umezawa, Hiroshi Matsumoto, and Masashi Tachiki. *Thermo field dynamics and condensed states*. Amsterdam: Elsevier Science Ltd, 1982.

[23] JG Valatin. "Comments on the theory of superconductivity". In: *Il Nuovo Cimento (1955-1965)* 7 (1958), pp. 843–857.

[24] NN Bogoljubov, Vladimir Veniaminovic Tolmachov, and DV Širkov. "A new method in the theory of superconductivity". In: *Fortschritte der physik* 6.11-12 (1958), pp. 605–682.

[25] Marcel Nooijen and Songhao Bao. "Normal ordered exponential approach to thermal properties and time-correlation functions: general theory and simple examples". In: *Molecular Physics* 119.21-22 (2021), e1980832. DOI: 10.1080/00268976.2021.1980832.

[26] Gaurav Harsha, Thomas M Henderson, and Gustavo E Scuseria. "Thermofield theory for finite-temperature quantum chemistry". In: *The Journal of Chemical Physics* 150.15 (2019), p. 154109.

[27] Gaurav Harsha, Thomas M Henderson, and Gustavo E Scuseria. "Thermofield theory for finite-temperature coupled cluster". In: *Journal of Chemical Theory and Computation* 15.11 (2019), pp. 6127–6136.

[28] Gaurav Harsha, Thomas M Henderson, and Gustavo E Scuseria. "Wave function methods for canonical ensemble thermal averages in correlated many-fermion systems". In: *The Journal of Chemical Physics* 153.12 (2020), p. 124115.

[29] Gaurav Harsha et al. "Thermal coupled cluster theory for SU (2) systems". In: *Physical Review B* 105.4 (2022), p. 045125.

[30] Gaurav Harsha, Thomas M Henderson, and Gustavo E Scuseria. "Thermofield theory for finite-temperature electronic structure". In: *The Journal of Physical Chemistry A* 127.14 (2023), pp. 3063–3071.

[31] Songhao Bao, Neil Raymond, and Marcel Nooijen. "Time dependent vibrational electronic coupled cluster (VECC) theory for non-adiabatic nuclear dynamics". In: *The Journal of Chemical Physics* 160.9 (Mar. 2024), p. 094105. ISSN: 0021-9606. DOI: 10.1063/5.0190034. eprint: https://pubs.aip.org/aip/jcp/article-pdf/doi/10.1063/5.0190034/19705218/094105_1_5.0190034.pdf. URL: https://doi.org/10.1063/5.0190034.

[32] Songhao Bao et al. "Vibrational electronic-thermofield coupled cluster (VE-TFCC) theory for quantum simulations of vibronic coupling systems at thermal equilibrium". In: *Journal of Chemical Theory and Computation* (2024). DOI: 10.1021/acs.jctc.4c00338.

[33] Max Born and Kun Huang. *Dynamical theory of crystal lattices*. Oxford university press, 1954.

[34] Max Born and R Oppenheimer. "Zür quantentheorie der molekeln". In: *Ann. Phys* 389.20 (1927), pp. 457–484.

[35] Scott Hopkins. *An Introduction to Spectroscopy and Quantum Structure*. Waterloo: University of Waterloo, 2011.

[36] Douglas R Hartree. "The wave mechanics of an atom with a non-Coulomb central field. Part I. Theory and methods". In: *Mathematical Proceedings of the Cambridge Philosophical Society*. Vol. 24. 1. Cambridge university press. 1928, pp. 89–110.

[37] John Clarke Slater. "The self consistent field and the structure of atoms". In: *Physical Review* 32.3 (1928), p. 339.

[38] JA Gaunt. "A theory of Hartree's atomic fields". In: *Mathematical Proceedings of the Cambridge Philosophical Society*. Vol. 24. 2. Cambridge University Press. 1928, pp. 328–342.

[39] John C Slater. "Note on Hartree's method". In: *Physical Review* 35.2 (1930), p. 210.

[40] Vladimir Fock. "Näherungsmethode zur Lösung des quantenmechanischen Mehrkörperproblems". In: *Zeitschrift für Physik* 61 (1930), pp. 126–148.

[41] Attila Szabo and Neil S Ostlund. *Modern quantum chemistry: introduction to advanced electronic structure theory*. Courier Corporation, 2012.

[42] Ilya G Ryabinkin et al. "Qubit coupled cluster method: a systematic approach to quantum chemistry on a quantum computer". In: *Journal of chemical theory and computation* 14.12 (2018), pp. 6317–6326.

[43] Jiří Čížek. "On the correlation problem in atomic and molecular systems. Calculation of wavefunction components in Ursell-type expansion using quantum-field theoretical methods". In: *The Journal of Chemical Physics* 45.11 (1966), pp. 4256–4266.

[44] J Čížek and J Paldus. "Correlation problems in atomic and molecular systems III. Rederivation of the coupled-pair many-electron theory using the traditional quantum chemical methodst". In: *International Journal of Quantum Chemistry* 5.4 (1971), pp. 359–379.

[45] Isaiah Shavitt and Rodney J Bartlett. *Many-body methods in chemistry and physics: MBPT and coupled-cluster theory*. New York: Cambridge university press, 2009.

[46] Werner Kutzelnigg and Debashis Mukherjee. "Normal order and extended Wick theorem for a multiconfiguration reference wave function". In: *The Journal of chemical physics* 107.2 (1997), pp. 432–449.

[47] Liguo Kong, Marcel Nooijen, and Debashis Mukherjee. "An algebraic proof of generalized Wick theorem". In: *The Journal of chemical physics* 132.23 (2010).

[48] So Hirata. "Finite-temperature many-body perturbation theory for electrons: Algebraic recursive definitions, second-quantized derivation, linked-diagram theorem, general-order algorithms, and grand canonical and canonical ensembles". In: *The Journal of Chemical Physics* 155.9 (2021).

[49] Raj Kumar Pathria. *Statistical mechanics*. Elsevier, 2016, pp. 1–22.

[50] David R Yarkony. "Nonadiabatic Derivative Couplings". In: *Encyclopedia of Computational Chemistry* 3 (2002).

[51] Tohru Azumi and Kazuo Matsuzaki. "What does the term "vibronic coupling" mean?" In: *Photochemistry and photobiology* 25.3 (1977), pp. 315–326.

[52] H Köppel, Wolfgang Domcke, and Lorenz S Cederbaum. "Multimode molecular dynamics beyond the Born-Oppenheimer approximation". In: *Advances in chemical physics* 57 (1984), pp. 59–246.

[53] Marcel Nooijen. "First-principles simulation of the UV absorption spectrum of ketene". In: *International journal of quantum chemistry* 95.6 (2003), pp. 768–783.

[54] M Nooijen and A Hazra. "VIBRON—A program for Vibronic Coupling and Franck–Condon calculations". In: *With contributions from JF Stanton and K. Sattelmeyer* (2003).

[55] Martha Yaghoubi Jouybari et al. "Ultrafast dynamics of the two lowest bright excited states of cytosine and 1-methylcytosine: A quantum dynamical study". In: *Journal of Chemical Theory and Computation* 16.9 (2020), pp. 5792–5808.

[56] Daniel Aranda and Fabrizio Santoro. "Vibronic spectra of π-conjugated systems with a multitude of coupled states: A protocol based on linear vibronic coupling models and quantum dynamics tested on hexahelicene". In: *Journal of Chemical Theory and Computation* 17.3 (2021), pp. 1691–1700.

[57] James A Green et al. "Fragment diabatization linear vibronic coupling model for quantum dynamics of multichromophoric systems: Population of the charge-transfer state in the photoexcited guanine–cytosine pair". In: *Journal of Chemical Theory and Computation* 17.8 (2021), pp. 4660–4674.

[58] Tao Zeng. "A diabatization protocol that includes spin-orbit coupling". In: *The Journal of Chemical Physics* 146.14 (2017), p. 144103.

[59] Michael H Beck et al. "The multiconfiguration time-dependent Hartree (MCTDH) method: a highly efficient algorithm for propagating wavepackets". In: *Physics reports* 324.1 (2000), pp. 1–105.

[60] GA Worth et al. "The Heidelberg MCTDH Package: A set of programs for multi-dimensional quantum dynamics". In: *User's Guide, Version* 8 (2000).

[61] Haobin Wang and Michael Thoss. "Multilayer formulation of the multiconfiguration time-dependent Hartree theory". In: *The Journal of chemical physics* 119.3 (2003), pp. 1289–1299.

[62] Uwe Manthe. "A multilayer multiconfigurational time-dependent Hartree approach for quantum dynamics on general potential energy surfaces". In: *The Journal of chemical physics* 128.16 (2008), p. 164116.

[63] Oriol Vendrell and Hans-Dieter Meyer. "Multilayer multiconfiguration time-dependent Hartree method: Implementation and applications to a Henon–Heiles Hamiltonian and to pyrazine". In: *The Journal of Chemical Physics* 134.4 (2011), p. 044135.

[64] A Raab, Irene Burghardt, and H-D Meyer. "The multiconfiguration time-dependent Hartree method generalized to the propagation of density operators". In: *The Journal of chemical physics* 111.19 (1999), pp. 8759–8772.

[65] A Raab and H-D Meyer. "A numerical study on the performance of the multiconfiguration time-dependent Hartree method for density operators". In: *The Journal of Chemical Physics* 112.24 (2000), pp. 10718–10729.

[66] David A Mazziotti. "3, 5-contracted Schrödinger equation: Determining quantum energies and reduced density matrices without wave functions". In: *International journal of quantum chemistry* 70.4-5 (1998), pp. 557–570.

[67] David A Mazziotti. "Contracted Schrödinger equation: Determining quantum energies and two-particle density matrices without wave functions". In: *Physical Review A* 57.6 (1998), p. 4219.

[68] David A Mazziotti. "Variational method for solving the contracted Schrödinger equation through a projection of the N-particle power method onto the two-particle space". In: *The Journal of chemical physics* 116.4 (2002), pp. 1239–1249.

[69] C Valdemoro, LM Tel, and E Pérez-Romero. "The contracted Schrödinger equation: some results". In: *Advances in quantum chemistry*. Vol. 28. Elsevier, 1997, pp. 33–46.

[70] Marcel Nooijen, Mark Wladyslawski, and Anirban Hazra. "Cumulant approach to the direct calculation of reduced density matrices: A critical analysis". In: *The Journal of chemical physics* 118.11 (2003), pp. 4832–4848.

[71] Qiming Sun et al. "PySCF: the Python-based simulations of chemistry framework". In: *Wiley Interdisciplinary Reviews: Computational Molecular Science* 8.1 (2018), e1340.

[72] Songhao Bao. *Thermal-Field*. https://github.com/bsonghao/Thermal-Field.git. 2021. URL: https://github.com/bsonghao/Thermal-Field.git.

[73] So Hirata et al. "Coupled-cluster singles and doubles for extended systems". In: *The Journal of chemical physics* 120.6 (2004), pp. 2581–2592.

[74] David Sherrington and Scott Kirkpatrick. "Solvable model of a spin-glass". In: *Physical review letters* 35.26 (1975), p. 1792.

[75] David H Ackley, Geoffrey E Hinton, and Terrence J Sejnowski. "A learning algorithm for Boltzmann machines". In: *Cognitive science* 9.1 (1985), pp. 147–169.

[76] Fernando Bernardi, Massimo Olivucci, and Michael A Robb. "Potential energy surface crossings in organic photochemistry". In: *Chemical Society Reviews* 25.5 (1996), pp. 321–328.

[77] Nina Ismail et al. "Ultrafast decay of electronically excited singlet cytosine via a π, π^* to no, π^* state switch". In: *Journal of the American Chemical Society* 124.24 (2002), pp. 6818–6819.

[78] Michael A Robb. *Theoretical chemistry for electronic excited states*. Vol. 12. Royal Society of Chemistry, 2018.

[79] John C Tully. "Perspective: Nonadiabatic dynamics theory". In: *The Journal of chemical physics* 137.22 (2012), 22A301.

[80] Michael S Schuurman and Albert Stolow. "Dynamics at conical intersections". In: *Annual review of physical chemistry* 69 (2018), pp. 427–450.

[81] S Singh et al. "Laser generation of excitons and fluorescence in anthracene crystals". In: *The Journal of Chemical Physics* 42.1 (1965), pp. 330–342.

[82] CE Swenberg and WT Stacy. "Bimolecular radiationless transitions in crystalline tetracene". In: *Chemical Physics Letters* 2.5 (1968), pp. 327–328.

[83] Nicholas Geacintov, Martin Pope, and F Vogel. "Effect of magnetic field on the fluorescence of tetracene crystals: exciton fission". In: *Physical Review Letters* 22.12 (1969), p. 593.

[84] RE Merrifield, P Avakian, and RP Groff. "Fission of singlet excitons into pairs of triplet excitons in tetracene crystals". In: *Chemical Physics Letters* 3.6 (1969), pp. 386–388.

[85] RE Merrifield. "Theory of magnetic field effects on the mutual annihilation of triplet excitons". In: *The Journal of Chemical Physics* 48.9 (1968), pp. 4318–4319.

[86] RC Johnson and RE Merrifield. "Effects of magnetic fields on the mutual annihilation of triplet excitons in anthracene crystals". In: *Physical Review B* 1.2 (1970), p. 896.

[87] A Suna. "Kinematics of exciton-exciton annihilation in molecular crystals". In: *Physical Review B* 1.4 (1970), p. 1716.

[88] RE Merrifield. "Magnetic effects on triplet exciton interactions". In: *Pure and Applied Chemistry* 27.3 (1971), pp. 481–498.

[89] Gérard Klein and René Voltz. "Formation and decay of superexcited states in dense organic matter under high energy radiation". In: *International Journal for Radiation Physics and Chemistry* 7.2-3 (1975), pp. 155–174.

[90] Ch E Swenberg and NE Geacintov. "Exciton interactions in organic solids". In: *Organic molecular photophysics* 1 (1973), pp. 489–564.

[91] Tao Zeng, Roald Hoffmann, and Nandini Ananth. "The low-lying electronic states of pentacene and their roles in singlet fission". In: *Journal of the American Chemical Society* 136.15 (2014), pp. 5755–5764.

[92] Tao Zeng, Nandini Ananth, and Roald Hoffmann. "Seeking small molecules for singlet fission: a heteroatom substitution strategy". In: *Journal of the American Chemical Society* 136.36 (2014), pp. 12638–12647.

[93] Tao Zeng and Prateek Goel. "Design of small intramolecular singlet fission chromophores: an azaborine candidate and general small size effects". In: *The Journal of Physical Chemistry Letters* 7.7 (2016), pp. 1351–1358.

[94] Tao Zeng. "Through-linker intramolecular singlet fission: general mechanism and designing small chromophores". In: *The Journal of Physical Chemistry Letters* 7.21 (2016), pp. 4405–4412.

[95] Robert Pollice et al. "Organic molecules with inverted gaps between first excited singlet and triplet states and appreciable fluorescence rates". In: *Matter* 4.5 (2021), pp. 1654–1682.

[96] Xiaosong Li et al. "Ab initio Ehrenfest dynamics". In: *The Journal of chemical physics* 123.8 (2005), p. 084106.

[97] Dmitry V Makhov et al. "Ab initio quantum direct dynamics simulations of ultrafast photochemistry with multiconfigurational Ehrenfest approach". In: *Chemical Physics* 493 (2017), pp. 200–218.

[98] Andrew J Jenkins et al. "The Ehrenfest method with fully quantum nuclear motion (Qu-Eh): Application to charge migration in radical cations". In: *The Journal of chemical physics* 149.9 (2018), p. 094108.

[99] John C Tully. "Molecular dynamics with electronic transitions". In: *The Journal of Chemical Physics* 93.2 (1990), pp. 1061–1071.

[100] Martin Richter et al. "SHARC: Ab initio molecular dynamics with surface hopping in the adiabatic representation including arbitrary couplings". In: *Journal of chemical theory and computation* 7.5 (2011), pp. 1253–1258.

[101] Clemens Rauer et al. "Cyclobutane thymine photodimerization mechanism revealed by nonadiabatic molecular dynamics". In: *Journal of the American Chemical Society* 138.49 (2016), pp. 15911–15916.

[102] Michal Ben-Nun, Jason Quenneville, and Todd J Martínez. "Ab initio multiple spawning: Photochemistry from first principles quantum molecular dynamics". In: *The Journal of Physical Chemistry A* 104.22 (2000), pp. 5161–5175.

[103] Hanneli R Hudock et al. "Ab initio molecular dynamics and time-resolved photoelectron spectroscopy of electronically excited uracil and thymine". In: *The Journal of Physical Chemistry A* 111.34 (2007), pp. 8500–8508.

[104] Monika Williams et al. "Unmasking the cis-stilbene phantom state via vacuum ultraviolet time-resolved photoelectron spectroscopy and ab initio multiple spawning". In: *The Journal of Physical Chemistry Letters* 12.27 (2021), pp. 6363–6369.

[105] Toshifumi Mori et al. "Role of Rydberg states in the photochemical dynamics of ethylene". In: *The Journal of Physical Chemistry A* 116.11 (2012), pp. 2808–2818.

[106] Basile FE Curchod et al. "Communication: GAIMS—Generalized Ab Initio Multiple Spawning for both internal conversion and intersystem crossing processes". In: *The Journal of Chemical Physics* 144.10 (2016), p. 101102.

[107] Irene Burghardt, Mathias Nest, and Graham A Worth. "Multiconfigurational system-bath dynamics using Gaussian wave packets: Energy relaxation and decoherence induced by a finite-dimensional bath". In: *The Journal of chemical physics* 119.11 (2003), pp. 5364–5378.

[108] Gareth W Richings et al. "Quantum dynamics simulations using Gaussian wavepackets: the vMCG method". In: *International Reviews in Physical Chemistry* 34.2 (2015), pp. 269–308.

[109] Georgia Christopoulou, Antonia Freibert, and Graham A Worth. "Improved algorithm for the direct dynamics variational multi-configurational Gaussian method". In: *The Journal of Chemical Physics* 154.12 (2021), p. 124127.

[110] Martin Richter et al. "Correction to "SHARC–Ab Initio Molecular Dynamics with Surface Hopping in the Adiabatic Representation Including Arbitrary Couplings"[J. Chem. Theory Comput. 2011, 7, 1253–1258]". In: *Journal of Chemical Theory and Computation* 8.1 (2012), pp. 374–374.

[111] Juan José Bajo et al. "Mixed quantum-classical dynamics in the adiabatic representation to simulate molecules driven by strong laser pulses". In: *The Journal of Physical Chemistry A* 116.11 (2012), pp. 2800–2807.

[112] Sebastian Mai et al. "Perturbational treatment of spin-orbit coupling for generally applicable high-level multi-reference methods". In: *The Journal of Chemical Physics* 141.7 (2014).

[113] Sebastian Mai, Philipp Marquetand, and Leticia González. "A general method to describe intersystem crossing dynamics in trajectory surface hopping". In: *International Journal of Quantum Chemistry* 115.18 (2015), pp. 1215–1231.

[114] Sebastian Mai et al. "General trajectory surface hopping method for ultrafast nonadiabatic dynamics". In: *Attosecond Molecular Dynamics* 13 (2018), p. 348.

[115] Stefan Grimme. "Calculation of the electronic spectra of large molecules". In: *Reviews in computational chemistry* 20 (2004), pp. 153–218.

[116] Anirban Hazra, Hannah H Chang, and Marcel Nooijen. "First principles simulation of the UV absorption spectrum of ethylene using the vertical Franck-Condon approach". In: *The Journal of chemical physics* 121.5 (2004), pp. 2125–2136.

[117] Marc Dierksen and Stefan Grimme. "An efficient approach for the calculation of Franck–Condon integrals of large molecules". In: *The Journal of chemical physics* 122.24 (2005), p. 244101.

[118] H-C Jankowiak, JL Stuber, and R Berger. "Vibronic transitions in large molecular systems: Rigorous prescreening conditions for Franck-Condon factors". In: *The Journal of chemical physics* 127.23 (2007), p. 234101.

[119] Alberto Baiardi, Julien Bloino, and Vincenzo Barone. "General time dependent approach to vibronic spectroscopy including Franck–Condon, Herzberg–Teller, and Duschinsky effects". In: *Journal of chemical theory and computation* 9.9 (2013), pp. 4097–4115.

[120] Bernardo de Souza et al. "Predicting phosphorescence rates of light organic molecules using time-dependent density functional theory and the path integral approach to dynamics". In: *Journal of chemical theory and computation* 15.3 (2019), pp. 1896–1904.

[121] Fiorella Villanueva Heldmaier et al. "UVPD spectroscopy of differential mobility-selected prototropic isomers of protonated adenine". In: *Physical Chemistry Chemical Physics* 23.35 (2021), pp. 19892–19900.

[122] Nour Mashmoushi et al. "UVPD Spectroscopy of Differential Mobility-Selected Prototropic Isomers of Rivaroxaban". In: *The Journal of Physical Chemistry A* 125.37 (2021), pp. 8187–8195.

[123] Ya Wang, Yang Liu, and Isaac B Bersuker. "Sudden polarization and zwitterion formation as a pseudo-Jahn–Teller effect: a new insight into the photochemistry of alkenes". In: *Physical Chemistry Chemical Physics* 21.20 (2019), pp. 10677–10692.

[124] Marc K Etherington et al. "Revealing the spin–vibronic coupling mechanism of thermally activated delayed fluorescence". In: *Nature Communications* 7.1 (2016), p. 13680.

[125] J Patrick Zobel, Anna M Wernbacher, and Leticia González. "Efficient Reverse Intersystem Crossing in Carbene-Copper-Amide TADF Emitters via an Intermediate Triplet State". In: *Angewandte Chemie International Edition* 62.15 (2023), e202217620.

[126] Shuyang Shi et al. "Highly efficient photo-and electroluminescence from two-coordinate Cu (I) complexes featuring nonconventional N-heterocyclic carbenes". In: *Journal of the American Chemical Society* 141.8 (2019), pp. 3576–3588.

[127] Gerhard Herzberg. *Electronic spectra and electronic structure of polyatomic molecules*. Vol. 3. van Nostrand, 1966.

[128] A Raab et al. "Molecular dynamics of pyrazine after excitation to the S 2 electronic state using a realistic 24-mode model Hamiltonian". In: *The Journal of chemical physics* 110.2 (1999), pp. 936–946.

[129] Anirban Hazra and Marcel Nooijen. "Comparison of various Franck–Condon and vibronic coupling approaches for simulating electronic spectra: The case of the lowest photoelectron band of ethylene". In: *Physical Chemistry Chemical Physics* 7.8 (2005), pp. 1759–1771.

[130] Anirban Hazra and Marcel Nooijen. "Vibronic coupling in the excited cationic states of ethylene: Simulation of the photoelectron spectrum between 12 and 18 eV". In: *The Journal of chemical physics* 122.20 (2005), p. 204327.

[131] Wolfgang Domcke, David R Yarkony, and Horst Köppel. *Conical intersections: theory, computation and experiment*. Vol. 17. World Scientific, 2011.

[132] Ketan Sharma, Terry A Miller, and John F Stanton. "Vibronically coupled states: Computational considerations and characterisation of vibronic and rovibronic spectroscopic parameters". In: *International Reviews in Physical Chemistry* 40.2 (2021), pp. 165–298.

[133] Johannes Neugebauer, Evert Jan Baerends, and Marcel Nooijen. "Vibronic coupling and double excitations in linear response time-dependent density functional calculations: Dipole-allowed states of N 2". In: *The Journal of chemical physics* 121.13 (2004), pp. 6155–6166.

[134] Johannes Neugebauer, Evert Jan Baerends, and Marcel Nooijen. "Vibronic structure of the permanganate absorption spectrum from time-dependent density functional calculations". In: *The Journal of Physical Chemistry A* 109.6 (2005), pp. 1168–1179.

[135] John F Stanton. "On the vibronic level structure in the NO 3 radical. I. The ground electronic state". In: *The Journal of chemical physics* 126.13 (2007), p. 134309.

[136] Michael S Schuurman and David R Yarkony. "On the vibronic coupling approximation: A generally applicable approach for determining fully quadratic quasidiabatic coupled electronic state Hamiltonians". In: *The Journal of chemical physics* 127.9 (2007), p. 094104.

[137] Kerstin Klein et al. "Quantitative vibronic coupling calculations: the formyloxyl radical". In: *Theoretical Chemistry Accounts* 129.3 (2011), pp. 527–543.

[138] AB Trofimov et al. "Vibronic coupling in the ground and excited states of the pyridine radical cation". In: *The Journal of Chemical Physics* 153.16 (2020), p. 164307.

[139] R Eric Stratmann, Gustavo E Scuseria, and Michael J Frisch. "An efficient implementation of time-dependent density-functional theory for the calculation of excitation energies of large molecules". In: *The Journal of chemical physics* 109.19 (1998), pp. 8218–8224.

[140] Mark E Casida and Miquel Huix-Rotllant. "Progress in time-dependent density-functional theory". In: *Annual review of physical chemistry* 63 (2012), pp. 287–323.

[141] Barry Moore and Jochen Autschbach. "Longest-wavelength electronic excitations of linear cyanines: the role of electron delocalization and of approximations in time-dependent density functional theory". In: *Journal of chemical theory and computation* 9.11 (2013), pp. 4991–5003.

[142] Haruyuki Nakano, Ryuma Uchiyama, and Kimihiko Hirao. "Quasi-degenerate perturbation theory with general multiconfiguration self-consistent field reference functions". In: *Journal of computational chemistry* 23.12 (2002), pp. 1166–1175.

[143] Makoto Miyajima, Yoshihiro Watanabe, and Haruyuki Nakano. "Relativistic quasidegenerate perturbation theory with four-component general multiconfiguration reference functions". In: *The Journal of chemical physics* 124.4 (2006), p. 044101.

[144] Ryo Ebisuzaki, Yoshihiro Watanabe, and Haruyuki Nakano. "Efficient implementation of relativistic and non-relativistic quasidegenerate perturbation theory with general multiconfigurational reference functions". In: *Chemical physics letters* 442.1-3 (2007), pp. 164–169.

[145] John F Stanton and Rodney J Bartlett. "The equation of motion coupled-cluster method. A systematic biorthogonal approach to molecular excitation energies, transition probabilities, and excited state properties". In: *The Journal of chemical physics* 98.9 (1993), pp. 7029–7039.

[146] Rodney J Bartlett and John F Stanton. "Applications of Post-Hartree—Fock Methods: A Tutorial". In: *Reviews in computational chemistry* (1994), pp. 65–169.

[147] Marcel Nooijen and Rodney J Bartlett. "A new method for excited states: Similarity transformed equation-of-motion coupled-cluster theory". In: *The Journal of chemical physics* 106.15 (1997), pp. 6441–6448.

[148] Marcel Nooijen and Rodney J Bartlett. "Similarity transformed equation-of-motion coupled-cluster study of ionized, electron attached, and excited states of free base porphin". In: *The Journal of chemical physics* 106.15 (1997), pp. 6449–6455.

[149] Marcel Nooijen and Rodney J Bartlett. "Similarity transformed equation-of-motion coupled-cluster theory: Details, examples, and comparisons". In: *The Journal of chemical physics* 107.17 (1997), pp. 6812–6830.

[150] H Köppel, W Domcke, and LS Cederbaum. "Theory of vibronic coupling in linear molecules". In: *The Journal of Chemical Physics* 74.5 (1981), pp. 2945–2968.

[151] Susanta Mahapatra, Wolfgang Eisfeld, and Horst Köppel. "Effects of multimode Jahn-Teller coupling on the photodetachment spectrum of nitrate anion (NO3-)". In: *Chemical physics letters* 441.1-3 (2007), pp. 7–15.

[152] Shirin Faraji et al. "Towards a higher-order description of Jahn–Teller coupling effects in molecular spectroscopy: The $\tilde{A}^2E''$ state of NO3". In: *Chemical Physics* 347.1-3 (2008), pp. 110–119.

[153] David MG Williams and Wolfgang Eisfeld. "Complete nuclear permutation inversion invariant artificial neural network (CNPI-ANN) diabatization for the accurate treatment of vibronic coupling problems". In: *The Journal of Physical Chemistry A* 124.37 (2020), pp. 7608–7621.

[154] Alexander B Trofimov et al. "Vibronic coupling in the ground and excited states of the imidazole radical cation". In: *The Journal of Chemical Physics* 157.17 (2022), p. 174309.

[155] Takatoshi Ichino, Jürgen Gauss, and John F Stanton. "Quasidiabatic states described by coupled-cluster theory". In: *The Journal of chemical physics* 130.17 (2009), p. 174105.

[156] Shirin Faraji, Spiridoula Matsika, and Anna I Krylov. "Calculations of non-adiabatic couplings within equation-of-motion coupled-cluster framework: Theory, implementation, and validation against multi-reference methods". In: *The Journal of chemical physics* 148.4 (2018), p. 044103.

[157] Flavia Aleotti et al. "Parameterization of a linear vibronic coupling model with multiconfigurational electronic structure methods to study the quantum dynamics of photoexcited pyrene". In: *The Journal of Chemical Physics* 154.10 (2021), p. 104106.

[158] Takatoshi Ichino et al. "The vibronic level structure of the cyclopentadienyl radical". In: *The Journal of chemical physics* 129.8 (2008), p. 084310.

[159] Michael S Schuurman, Richard A Young, and David R Yarkony. "On the multimode quadratic vibronic coupling problem: An open-ended solution using a parallel Lanczos algorithm". In: *Chemical Physics* 347.1-3 (2008), pp. 57–64.

[160] G. A. Worth et al. The MCTDH Package, Version 8.2, (2000). H.-D. Meyer, Version 8.3 (2002), Version 8.4 (2007). Used version: 8.4.23 (May 2022). See http://mctdh.uni-hd.de. University of Heidelberg, Germany.

[161] G. A. Worth et al. *The Heidelberg MCTDH Package: A set of programs for multi-dimensional quantum dynamics. User's Guide.* English. Version Version 8.5.16. 209 pp. published.

[162] Gareth W Richings and Graham A Worth. "A practical diabatisation scheme for use with the direct-dynamics variational multi-configuration Gaussian method". In: *The Journal of Physical Chemistry A* 119.50 (2015), pp. 12457–12470.

[163] Qingyong Meng and Hans-Dieter Meyer. "A multilayer MCTDH study on the full dimensional vibronic dynamics of naphthalene and anthracene cations". In: *The Journal of Chemical Physics* 138.1 (2013), p. 18908.

[164] Haobin Wang and Hans-Dieter Meyer. "On regularizing the ML-MCTDH equations of motion". In: *The Journal of chemical physics* 149.4 (2018), p. 044119.

[165] M Durga Prasad. "Time-dependent coupled cluster method: A new approach to the calculation of molecular absorption spectra". In: *The Journal of chemical physics* 88.11 (1988), pp. 7005–7010.

[166] Jacob A Faucheaux and So Hirata. "Higher-order diagrammatic vibrational coupled-cluster theory". In: *The Journal of chemical physics* 143.13 (2015), p. 134105.

[167] Jacob A Faucheaux, Marcel Nooijen, and So Hirata. "Similarity-transformed equation-of-motion vibrational coupled-cluster theory". In: *The Journal of chemical physics* 148.5 (2018), p. 054104.

[168] Ove Christiansen. "Vibrational coupled cluster theory". In: *The Journal of chemical physics* 120.5 (2004), pp. 2149–2159.

[169] T Daniel Crawford and Henry F Schaefer III. "An introduction to coupled cluster theory for computational chemists". In: *Reviews in computational chemistry* 14 (2007), pp. 33–136.

[170] Neil Raymond and Songhao Bao. *T-amplitudes*. https://git.uwaterloo.ca/ngraymon/t-amplitudes/. 2020. URL: https://git.uwaterloo.ca/ngraymon/t-amplitudes/.

[171] Neil Raymond and Lucas Harrison Price. *termfactory*. https://github.com/ngraymon/termfactory/. 2022. URL: https://github.com/ngraymon/termfactory.

[172] *NumPy*. https://github.com/numpy/numpy.git. June 22, 2022. URL: https://github.com/numpy/numpy.git.

[173] *SciPy*. https://github.com/scipy/scipy.git. Oct. 8, 2022. URL: https://github.com/scipy/scipy.git.

[174] Yannick J Bomble et al. "Equation-of-motion coupled-cluster methods for ionized states with an approximate treatment of triple excitations". In: *The Journal of chemical physics* 122.15 (2005), p. 154107.

[175] Monika Musia and Rodney J Bartlett. "EOM-CCSDT study of the low-lying ionization potentials of ethylene, acetylene and formaldehyde". In: *Chemical physics letters* 384.4-6 (2004), pp. 210–214.

[176] Monika Musial and Rodney J Bartlett. "Equation-of-motion coupled cluster method with full inclusion of connected triple excitations for electron-attached states: EA-EOM-CCSDT". In: *Journal of Chemical Physics* 119.4 (2003), pp. 1901–1908.

[177] John F Stanton and Jürgen Gauss. "Analytic energy derivatives for ionized states described by the equation-of-motion coupled cluster method". In: *The Journal of chemical physics* 101.10 (1994), pp. 8938–8944.

[178] Marcel Nooijen and Jaap G Snijders. "Coupled cluster Green's function method: Working equations and applications". In: *International journal of quantum chemistry* 48.1 (1993), pp. 15–48.

[179] Marcel Nooijen and Jaap G Snijders. "Coupled cluster approach to the single-particle Green's function". In: *International Journal of Quantum Chemistry* 44.S26 (1992), pp. 55–83.

[180] RJ Bartlett and JF Stanton. "Reviews in computational chemistry". In: *Inc. New York* (1994), p. 65.

[181] Julia Endicott. *Generating Vibronic Coupling Models and Simulating Photoelectron Spectra*. CHEM 494 project report. 2014. URL: http://scienide2.uwaterloo.ca/~nooijen/website_new_20_10_2011/vibron/VC/julia_thesis.pdf (visited on 08/08/2022).

[182] Marcel Nooijen. *Vibronic model parameters, calculated by IP-EOMCC method, for generating photo-electron spectra.* 2011. URL: http://scienide2.uwaterloo.ca/~nooijen/website_new_20_10_2011/vibron/VC/models.html (visited on 08/08/2022).

[183] Luc Vereecken and Joseph S Francisco. "Theoretical studies of atmospheric reaction mechanisms in the troposphere". In: *Chemical Society Reviews* 41.19 (2012), pp. 6259–6293.

[184] Alexis T Bell and Martin Head-Gordon. "Quantum mechanical modeling of catalytic processes". In: *Annual Review of Chemical and Biomolecular Engineering* 2 (2011), pp. 453–477.

[185] Amir Karton. "A computational chemist's guide to accurate thermochemistry for organic molecules". In: *Wiley Interdisciplinary Reviews: Computational Molecular Science* 6.3 (2016), pp. 292–310.

[186] JA Pople. "Two-dimensional chart of quantum chemistry". In: *The Journal of Chemical Physics* 43.10 (1965), S229–S230.

[187] Attila Tajti et al. "HEAT: High accuracy extrapolated ab initio thermochemistry". In: *The Journal of chemical physics* 121.23 (2004), pp. 11599–11613.

[188] Yannick J Bomble et al. "High-accuracy extrapolated ab initio thermochemistry. II. Minor improvements to the protocol and a vital simplification". In: *The Journal of chemical physics* 125.6 (2006), p. 064108.

[189] Michael E Harding et al. "High-accuracy extrapolated ab initio thermochemistry. III. Additional improvements and overview". In: *The Journal of chemical physics* 128.11 (2008), p. 114111.

[190] Amir Karton et al. "W4 theory for computational thermochemistry: In pursuit of confident sub-kJ/mol predictions". In: *The Journal of chemical physics* 125.14 (2006), p. 144108.

[191] Lorenz S Cederbaum. "Born–Oppenheimer approximation and beyond". In: *Conical Intersections: Electronic Structure, Dynamics and Spectroscopy* 15 (2004), pp. 3–40.

[192] Neil Raymond et al. "A path integral methodology for obtaining thermodynamic properties of nonadiabatic systems using Gaussian mixture distributions". In: *The Journal of Chemical Physics* 148.19 (2018), p. 194110.

[193] Dmitri Iouchtchenko et al. "Deterministic and quasi-random sampling of optimized Gaussian mixture distributions for vibronic Monte Carlo". In: *arXiv preprint arXiv:1912.11594* (2019).

[194] Songhao Bao. *hot-molecule.* GitHub repository, https://github.com/bsonghao/hot-molecule.git (accessed 2024-05-15). 2022-05-14.

[195] Neil Raymond. *Pibronic.* GitHub repository, https://github.com/ngraymon/Pibronic.git (accessed 2024-05-15). 2018-01-31.

[196] Neil Raymond. *vmio.* https://github.com/ngraymon/vmio.git. 2024. URL: https://github.com/ngraymon/vmio.git.

[197] Thom H Dunning Jr. "Gaussian basis sets for use in correlated molecular calculations. I. The atoms boron through neon and hydrogen". In: *The Journal of chemical physics* 90.2 (1989), pp. 1007–1023.

[198] Michael W Schmidt et al. "General atomic and molecular electronic structure system". In: *Journal of computational chemistry* 14.11 (1993), pp. 1347–1363.

[199] MV Korobov, LN Savinova, and LN Sidorov. "Stabilities of CoF4 and CrF5 in the gas phase". In: *The Journal of Chemical Thermodynamics* 25.9 (1993), pp. 1161–1168.

[200] Gian-Carlo Wick. "The evaluation of the collision matrix". In: *Physical review* 80.2 (1950), p. 268.

[201] Michael A Nielsen and Isaac L Chuang. *Quantum computation and quantum information*. Vol. 2. Cambridge university press Cambridge, 2001.

[202] Stanley Lo et al. "Review of low-cost self-driving laboratories in chemistry and materials science: the "frugal twin" concept". In: *Digital Discovery* 3.5 (2024), pp. 842–868.

[203] Arnout Ceulemans and LG Vanquickenborne. "The epikernel principle". In: *Stereochemistry and Bonding*. B-3030 Leuven, Belgium: Springer, 2005, pp. 125–159.

Appendix A

Proof of the (anti)-commutation rule of the Bogoliubov transform operators

A.1 Proof of commutation rules of the Bogoliubov transformed Bosonic operators

In this section, we will prove that the canonical commutation rules preserves for the Bogoliubov transformed Bosonic operators. Our starting point is the commutation rules of the operators before the Bogoliubov transformation:

$$\begin{aligned}
&[\hat{i}, \hat{j}^\dagger] = \delta_{ij}, \\
&[\tilde{i}, \tilde{j}^\dagger] = \delta_{ij}, \\
&[\tilde{i}, \tilde{j}] = [\tilde{i}^\dagger, \tilde{j}^\dagger] = 0, \\
&[\tilde{i}, \hat{j}] = [\tilde{i}^\dagger, \hat{j}^\dagger] = [\hat{i}, \tilde{j}^\dagger] = [\tilde{i}, \hat{j}^\dagger] = 0,
\end{aligned} \tag{A.1}$$

and Bogoliubov transformation defined in Eq. (3.69) and Eq. (3.70).

We apply the canonical commutation relation of the original operators in Eq. (A.1) to expand the commutator of the Bogoliubov transformed operators and we have:

$$\begin{aligned}
[\hat{a}_i, \hat{a}_j^\dagger] &= [\cosh\theta_i \hat{i} - \sinh\theta_i \tilde{i}^\dagger, \cosh\theta_j \hat{j}^\dagger - \sinh\theta_j \tilde{j}], \\
&= \cosh\theta_i \cosh\theta_j [\hat{i}, \hat{j}^\dagger] - \cosh\theta_i \sinh\theta_j [\hat{i}, \tilde{j}] - \sinh\theta_i \cosh\theta_j [\tilde{i}^\dagger, \hat{j}^\dagger] - \sinh\theta_i \sinh\theta_j [\tilde{j}, \tilde{i}^\dagger], \\
&= (\cosh^2\theta_i - \sinh^2\theta_i)\delta_{ij}, \\
&= \delta_{ij},
\end{aligned} \tag{A.2}$$

$$
\begin{aligned}
[\hat{a}_i, \hat{a}_j] &= [\cosh\theta_i \hat{i} - \sinh\theta_i \tilde{i}^\dagger, \cosh\theta_j \hat{j} - \sinh\theta_j \tilde{j}^\dagger], \\
&= \cosh\theta_i \cosh\theta_j [\hat{i}, \hat{j}] - \cosh\theta_i \sinh\theta_j [\hat{i}, \tilde{j}^\dagger] + \sinh\theta_i \cosh\theta_j [\hat{j}, \tilde{i}^\dagger] - \sinh\theta_i \sinh\theta_j [\tilde{j}^\dagger, \tilde{i}^\dagger], \\
&= 0,
\end{aligned}
\tag{A.3}
$$

$$
\begin{aligned}
[\hat{a}_i^\dagger, \hat{a}_j^\dagger] &= [\cosh\theta_i \hat{i}^\dagger - \sinh\theta_i \tilde{i}, \cosh\theta_j \hat{j}^\dagger - \sinh\theta_j \tilde{j}], \\
&= \cosh\theta_i \cosh\theta_j [\hat{i}^\dagger, \hat{j}^\dagger] + \cosh\theta_i \sinh\theta_j [\tilde{j}, \hat{i}^\dagger] - \sinh\theta_i \cosh\theta_j [\tilde{i}, \hat{j}^\dagger] - \sinh\theta_i \sinh\theta_j [\tilde{j}, \tilde{i}], \\
&= 0,
\end{aligned}
\tag{A.4}
$$

$$
\begin{aligned}
[\hat{b}_i, \hat{b}_j^\dagger] &= [-\sinh\theta_i \hat{i}^\dagger + \cosh\theta_i \tilde{i}, -\sinh\theta_j \hat{j} + \cosh\theta_j \tilde{j}^\dagger], \\
&= -\sinh\theta_i \sinh\theta_j [\hat{j}, \hat{i}^\dagger] - \sinh\theta_i \cosh\theta_j [\hat{i}^\dagger, \tilde{j}^\dagger] - \cosh\theta_i \sinh\theta_j [\tilde{i}, \hat{j}] + \cosh\theta_i \cosh\theta_j [\tilde{i}, \tilde{j}^\dagger], \\
&= (-\sinh^2\theta_i + \cosh^2\theta_i)\delta_{ij}, \\
&= \delta_{ij},
\end{aligned}
\tag{A.5}
$$

$$
\begin{aligned}
[\hat{b}_i, \hat{b}_j] &= [-\sinh\theta_i \hat{i}^\dagger + \cosh\theta_i \tilde{i}, -\sinh\theta_j \hat{j}^\dagger + \cosh\theta_j \tilde{j}], \\
&= \sinh\theta_i \sinh\theta_j [\hat{i}^\dagger, \hat{j}^\dagger] + \sinh\theta_i \cosh\theta_j [\tilde{j}, \hat{i}^\dagger] - \cosh\theta_i \sinh\theta_j [\tilde{i}, \hat{j}^\dagger] + \cosh\theta_i \cosh\theta_j [\tilde{i}, \tilde{j}], \\
&= 0,
\end{aligned}
\tag{A.6}
$$

$$
\begin{aligned}
[\hat{b}_i^\dagger, \hat{b}_j^\dagger] &= [-\sinh\theta_i \hat{i} + \cosh\theta_i \tilde{i}^\dagger, -\sinh\theta_j \hat{j} + \cosh\theta_j \tilde{j}^\dagger], \\
&= \sinh\theta_i \sinh\theta_j [\hat{i}, \hat{j}] - \sinh\theta_i \cosh\theta_j [\hat{i}, \tilde{j}^\dagger] + \cosh\theta_i \sinh\theta_j [\hat{j}, \tilde{i}^\dagger] + \cosh\theta_i \cosh\theta_j [\tilde{i}^\dagger, \tilde{j}^\dagger], \\
&= 0,
\end{aligned}
\tag{A.7}
$$

$$
\begin{aligned}
[\hat{a}_i, \hat{b}_j^\dagger] &= [\cosh\theta_i \hat{i} - \sinh\theta_i \tilde{i}^\dagger, -\sinh\theta_j \hat{j} + \cosh\theta_j \tilde{j}^\dagger], \\
&= -\cosh\theta_i \sinh\theta_j [\hat{i}, \hat{j}] + \cosh\theta_i \cosh\theta_j [\hat{i}, \tilde{j}^\dagger] - \cosh\theta_i \sinh\theta_j [\hat{j}, \tilde{i}^\dagger] - \sinh\theta_i \cosh\theta_j [\tilde{i}^\dagger, \tilde{j}^\dagger], \\
&= 0,
\end{aligned}
\tag{A.8}
$$

$$
\begin{aligned}
[\hat{a}_i^\dagger, \hat{b}_j^\dagger] &= [\cosh\theta_i \hat{i}^\dagger - \sinh\theta_i \tilde{i}, -\sinh\theta_j \hat{j} + \cosh\theta_j \tilde{j}^\dagger], \\
&= \cosh\theta_i \sinh\theta_j [\hat{j}, \hat{i}^\dagger] + \cosh\theta_i \cosh\theta_j [\hat{i}^\dagger, \tilde{j}^\dagger] + \cosh\theta_i \sinh\theta_j [\tilde{i}, \hat{j}] - \sinh\theta_i \cosh\theta_j [\tilde{i}, \tilde{j}^\dagger], \\
&= (\cosh\theta_i \sinh\theta_i - \sinh\theta_i \cosh\theta_i)\delta_{ij} \\
&= 0.
\end{aligned}
\tag{A.9}
$$

$$
\begin{aligned}
[\hat{a}_i, \hat{b}_j] &= [\cosh\theta_i \hat{i} - \sinh\theta_i \tilde{i}^\dagger, -\sinh\theta_j \hat{j}^\dagger + \cosh\theta_j \tilde{j}], \\
&= -\cosh\theta_i \sinh\theta_j [\hat{i}, \hat{j}^\dagger] + \cosh\theta_i \cosh\theta_j [\hat{i}, \tilde{j}] + \cosh\theta_i \sinh\theta_j [\tilde{i}^\dagger, \hat{j}^\dagger] + \sinh\theta_i \cosh\theta_j [\tilde{j}, \tilde{i}^\dagger], \\
&= (-\cosh\theta_i \sinh\theta_i + \sinh\theta_i \cosh\theta_i)\delta_{ij} \\
&= 0.
\end{aligned}
\tag{A.10}
$$

From Eq. (A.2), Eq. (A.3), Eq. (A.4), Eq. (A.5), Eq. (A.6), Eq. (A.7), Eq. (A.8), Eq. (A.9) and Eq. (A.10), we prove that the Bogoliubov transformed Bosonic operators preserves the commutation rule as the original operators.

A.2 Proof of anti-commutation rules of the Bogoliubov transformed Fermonic operators

In this section, we prove the canonical anti-commutation rule preserves for the Bogoliubov transformed Fermionic operators. Our starting point is the anti-commtation rule of the original operators before the Bogoliubov transformation:

$$
\begin{aligned}
&\{\hat{i}, \hat{j}^\dagger\} = \delta_{ij}, \\
&\{\tilde{i}, \tilde{j}^\dagger\} = \delta_{ij}, \\
&\{\tilde{i}, \tilde{j}\} = \{\tilde{i}^\dagger, \tilde{j}^\dagger\} = 0, \\
&\{\tilde{i}, \hat{j}\} = \{\tilde{i}^\dagger, \hat{j}^\dagger\} = \{\hat{i}, \tilde{j}^\dagger\} = \{\tilde{i}, \hat{j}^\dagger\} = 0,
\end{aligned}
\tag{A.11}
$$

and Bogoliubov transformation defined in Eq. (3.81) and Eq. (3.82).

We apply the anti-commutation relation of the original operators in Eq. (A.11) to expand the anti-commutator of the Bogoliubov transformed operators and we have:

$$\begin{aligned}\{\hat{a}_i, \hat{a}_j^\dagger\} &= \{\cos\theta_i\hat{i} - \sin\theta_i\tilde{i}^\dagger, \cos\theta_j\hat{j}^\dagger - \sin\theta_j\tilde{j}\} \\ &= \cos\theta_i\cos\theta_j\{\hat{i}, \hat{j}^\dagger\} - \cos\theta_i\sin\theta_j\{\hat{i}, \tilde{j}\} - \sin\theta_i\cos\theta_j\{\tilde{i}^\dagger, \hat{j}^\dagger\} + \sin\theta_i\sin\theta_j\{\tilde{j}, \tilde{i}^\dagger\} \\ &= (\cos^2\theta_i + \sin^2\theta_i)\delta_{ij} \\ &= \delta_{ij},\end{aligned} \tag{A.12}$$

$$\begin{aligned}\{\hat{a}_i, \hat{a}_j\} &= \{\cos\theta_i\hat{i} - \sin\theta_i\tilde{i}^\dagger, \cos\theta_j\hat{j} - \sin\theta_j\tilde{j}^\dagger\} \\ &= \cos\theta_i\cos\theta_j\{\hat{i}, \hat{j}\} - \cos\theta_i\sin\theta_j\{\hat{i}, \tilde{j}^\dagger\} - \sin\theta_i\cos\theta_j\{\hat{j}, \tilde{i}^\dagger\} + \sin\theta_i\sin\theta_j\{\tilde{i}^\dagger, \tilde{j}^\dagger\} \\ &= 0,\end{aligned} \tag{A.13}$$

$$\begin{aligned}\{\hat{a}_i^\dagger, \hat{a}_j^\dagger\} &= \{\cos\theta_i\hat{i}^\dagger - \sin\theta_i\tilde{i}, \cos\theta_j\hat{j}^\dagger - \sin\theta_j\tilde{j}\} \\ &= \cos\theta_i\cos\theta_j\{\hat{i}^\dagger, \hat{j}^\dagger\} - \cos\theta_i\sin\theta_j\{\tilde{j}, \hat{i}^\dagger\} - \sin\theta_i\cos\theta_j\{\tilde{i}, \hat{j}^\dagger\} + \sin\theta_i\sin\theta_j\{\tilde{i}, \tilde{j}\} \\ &= 0,\end{aligned} \tag{A.14}$$

$$\begin{aligned}\{\hat{b}_i, \hat{b}_j^\dagger\} &= \{\sin\theta_i\hat{i} + \cos\theta_i\tilde{i}^\dagger, \sin\theta_j\hat{j}^\dagger + \cos\theta_j\tilde{j}\} \\ &= \sin\theta_i\sin\theta_j\{\hat{i}, \hat{j}^\dagger\} + \sin\theta_i\cos\theta_j\{\hat{i}, \tilde{j}\} + \cos\theta_i\sin\theta_j\{\tilde{i}^\dagger, \hat{j}^\dagger\} + \cos\theta_i\cos\theta_j\{\tilde{j}, \hat{i}^\dagger\} \\ &= (\sin^2\theta_i + \cos^2\theta_i)\delta_{ij} \\ &= \delta_{ij},\end{aligned} \tag{A.15}$$

$$\begin{aligned}\{\hat{b}_i, \hat{b}_j\} &= \{\sin\theta_i\hat{i} + \cos\theta_i\tilde{i}^\dagger, \sin\theta_j\hat{j} + \cos\theta_j\tilde{j}^\dagger\} \\ &= \sin\theta_i\sin\theta_j\{\hat{i}, \hat{j}\} + \sin\theta_i\cos\theta_j\{\hat{i}, \tilde{j}^\dagger\} + \cos\theta_i\sin\theta_j\{\hat{j}, \tilde{i}^\dagger\} + \cos\theta_i\cos\theta_j\{\tilde{i}^\dagger, \hat{j}^\dagger\} \\ &= 0,\end{aligned} \tag{A.16}$$

$$\begin{aligned}\{\hat{b}_i^\dagger, \hat{b}_j^\dagger\} &= \{\sin\theta_i\hat{i}^\dagger + \cos\theta_i\tilde{i}, \sin\theta_j\hat{j}^\dagger + \cos\theta_j\tilde{j}\} \\ &= \sin\theta_i\sin\theta_j\{\hat{i}^\dagger, \hat{j}^\dagger\} + \sin\theta_i\cos\theta_j\{\tilde{j}, \hat{i}^\dagger\} + \cos\theta_i\sin\theta_j\{\tilde{i}, \hat{j}^\dagger\} + \cos\theta_i\cos\theta_j\{\tilde{i}, \hat{j}\} \\ &= 0,\end{aligned} \tag{A.17}$$

$$\begin{aligned}\{\hat{a}_i, \hat{b}_j^\dagger\} &= \{\cos\theta_i \hat{i} - \sin\theta_i \tilde{i}^\dagger, \sin\theta_j \hat{j}^\dagger + \cos\theta_j \tilde{j}\} \\ &= \cos\theta_i \sin\theta_j \{\hat{i}, \hat{j}^\dagger\} + \cos\theta_i \cos\theta_j \{i, \tilde{j}\} - \sin\theta_i \sin\theta_j \{\tilde{i}^\dagger, \hat{j}^\dagger\} - \sin\theta_i \cos\theta_j \{\tilde{j}, \tilde{i}^\dagger\} \\ &= (\cos\theta_i \sin\theta_i - \sin\theta_i \cos\theta_i)\delta_{ij} \\ &= 0,\end{aligned} \tag{A.18}$$

$$\begin{aligned}\{\hat{a}_i, \hat{b}_j\} &= \{\cos\theta_i \hat{i} - \sin\theta_i \tilde{i}^\dagger, \sin\theta_j \hat{j} + \cos\theta_j \tilde{j}^\dagger\} \\ &= \cos\theta_i \sin\theta_j \{\hat{i}, \hat{j}\} + \cos\theta_i \cos\theta_j \{i, \tilde{j}^\dagger\} - \sin\theta_i \sin\theta_j \{\hat{j}, \tilde{i}^\dagger\} - \sin\theta_i \cos\theta_j \{\tilde{i}^\dagger, \tilde{j}^\dagger\} \\ &= 0,\end{aligned} \tag{A.19}$$

$$\begin{aligned}\{\hat{a}_i^\dagger, \hat{b}_j^\dagger\} &= \{\cos\theta_i \hat{i}^\dagger - \sin\theta_i \tilde{i}, \sin\theta_j \hat{j}^\dagger + \cos\theta_j \tilde{j}\} \\ &= \cos\theta_i \sin\theta_j \{\hat{i}^\dagger, \hat{j}^\dagger\} + \cos\theta_i \cos\theta_j \{\tilde{j}, \hat{i}^\dagger\} - \sin\theta_i \sin\theta_j \{\tilde{i}, \hat{j}^\dagger\} - \sin\theta_i \cos\theta_j \{\tilde{i}, \tilde{j}\} \\ &= 0,\end{aligned} \tag{A.20}$$

From Eq. (A.12), Eq. (A.13), Eq. (A.14), Eq. (A.15), Eq. (A.16), Eq. (A.17), Eq. (A.18), Eq. (A.19) and Eq. (A.20), we prove that the Bogoliubov transformed Fermionic operators preserves the anti-commutation rule as the original operators.

Appendix B

Proof of vacuum state condition of Bogoliubov transformed operator with the respect to $|\theta(\beta)\rangle$ state

B.1 Proof of the vacuum state condition for Bosonic operators

In this section, we give a rigorous proof that the Bogoliubov transformed Bosonic operators satisfy the vacuum state condition with the respect the $|\theta(\beta)\rangle$ state (described in Eq. (3.74) and Eq. (3.75)). Applying BCH expansion and cannonical commutation rules, we can derive that the Bosonic construction operators ($\hat{i}$, $\hat{i}^\dagger$, $\tilde{i}$, $\tilde{i}^\dagger$) satisfy the following equations:

$$\begin{aligned} e^{-\hat{u}}\hat{i}e^{\hat{u}} &= \hat{i} + \tilde{i}^\dagger, \\ e^{-\hat{u}}\hat{i}^\dagger e^{\hat{u}} &= \hat{i}^\dagger, \\ e^{-\hat{u}}\tilde{i}e^{\hat{u}} &= \tilde{i} + \hat{i}^\dagger, \\ e^{-\hat{u}}\tilde{i}^\dagger e^{\hat{u}} &= \tilde{i}^\dagger, \end{aligned} \tag{B.1}$$

where $\hat{u} \equiv \sum_i \hat{i}^\dagger \tilde{i}^\dagger$.

Similarly, applying BCH, we can prove that

$$\begin{aligned} e^{\beta\hat{h}_0/2}\hat{i}e^{-\beta\hat{h}_0/2} &= e^{-\beta\hbar\omega_i/2}\hat{i} \\ e^{\beta\hat{h}_0/2}\hat{i}^\dagger e^{-\beta\hat{h}_0/2} &= e^{-\beta\hbar\omega_i/2}\hat{i}^\dagger \\ e^{\beta\hat{h}_0/2}\tilde{i}e^{-\beta\hat{h}_0/2} &= \tilde{i} \\ e^{\beta\hat{h}_0/2}\tilde{i}^\dagger e^{-\beta\hat{h}_0/2} &= \tilde{i}^\dagger \end{aligned} \tag{B.2}$$

where $\hat{h}_0 \equiv \sum_i \omega_i \hat{i}^\dagger \hat{i}$.

Applying Eq. (B.1) and Eq. (B.2), we can derive the following expression by inserting

the two identities $e^{\beta\hat{h}_0/2}e^{-\beta\hat{h}_0/2}$ and $e^{\hat{u}}e^{-\hat{u}}$:

$$\begin{aligned}
\hat{i}\left|\theta(\beta)\right\rangle &\equiv \hat{i}e^{-\beta\hat{h}_0/2}e^{\hat{u}}\left|0,\tilde{0}\right\rangle \\
&= e^{-\beta\hat{h}_0/2}e^{\beta\hat{h}_0/2}\hat{i}e^{-\beta\hat{h}_0/2}e^{\hat{u}}\left|0,\tilde{0}\right\rangle \\
&= e^{-\beta\hat{h}_0/2}e^{\hat{u}}e^{-\hat{u}}\hat{i}e^{-\beta\omega_i/2}e^{\hat{u}}\left|0,\tilde{0}\right\rangle \\
&= e^{-\beta\hat{h}_0/2}e^{\hat{u}}e^{-\beta\omega_i/2}(\hat{i}+\tilde{i}^{\dagger})\left|0,\tilde{0}\right\rangle \\
&= e^{-\beta\hat{h}_0/2}e^{\hat{u}}e^{-\beta\omega_i/2}\tilde{i}^{\dagger}\left|0,\tilde{0}\right\rangle \\
&= e^{-\beta\omega_i/2}\tilde{i}^{\dagger}e^{-\beta\hat{h}_0/2}e^{\hat{u}}\left|0,\tilde{0}\right\rangle \\
&= e^{-\beta\omega_i/2}\tilde{i}^{\dagger}\left|\theta(\beta)\right\rangle,
\end{aligned} \tag{B.3}$$

and

$$\begin{aligned}
\tilde{i}\left|\theta(\beta)\right\rangle &\equiv \tilde{i}e^{-\beta\hat{h}_0/2}e^{\hat{u}}\left|0,\tilde{0}\right\rangle \\
&= e^{-\beta\hat{h}_0/2}e^{\beta\hat{h}_0/2}\tilde{i}e^{-\beta\hat{h}_0/2}e^{\hat{u}}\left|0,\tilde{0}\right\rangle \\
&= e^{-\beta\hat{h}_0/2}\tilde{i}e^{\hat{u}}\left|0,\tilde{0}\right\rangle \\
&= e^{-\beta\hat{h}_0/2}e^{\hat{u}}e^{-\hat{u}}\tilde{i}e^{\hat{u}}\left|0,\tilde{0}\right\rangle \\
&= e^{-\beta\hat{h}_0/2}e^{\hat{u}}(\tilde{i}+\hat{i}^{\dagger})\left|0,\tilde{0}\right\rangle \\
&= e^{-\beta\hat{h}_0/2}e^{\hat{u}}\hat{i}^{\dagger}\left|0,\tilde{0}\right\rangle \\
&= e^{-\beta\hat{h}_0/2}\hat{i}^{\dagger}e^{\beta\hat{h}_0/2}e^{-\beta\hat{h}_0/2}e^{\hat{u}}\left|0,\tilde{0}\right\rangle \\
&= e^{-\beta\hbar\omega_i/2}\hat{i}^{\dagger}\left|\theta(\beta)\right\rangle.
\end{aligned} \tag{B.4}$$

Clearly, if we define the Bogoliubov transformed annihilation operators as

$$\hat{a}_i = C(\hat{i} - e^{-\beta\hbar\omega_i/2}\tilde{i}^{\dagger}); \hat{b}_i = C(\tilde{i} - e^{-\beta\hbar\omega_i/2}\hat{i}^{\dagger}), \tag{B.5}$$

where C is an arbitrary constant, the resultant operators satisfy the vacuum state conditions of $\hat{a}_i\left|\theta(\beta)\right\rangle = 0$ and $\hat{b}_i\left|\theta(\beta)\right\rangle = 0$. The corresponding creation operators are the adjoints of the the annihilation operators.

The constants in the expression of the Bogoliubov transformed Bosonic construction operator can be determined by imposing the canonical commutation relation of Bosons:

$$[\hat{a}_i, \hat{a}_i^{\dagger}] = |C|^2\left(1 + e^{-\beta\hbar\omega_i}[\tilde{i}^{\dagger}, \tilde{i}]\right) = 1, \tag{B.6}$$

and

$$[\hat{b}_i, \hat{b}_i^{\dagger}] = |C|^2\left(1 + e^{-\beta\hbar\omega_i}[\hat{i}^{\dagger}, \hat{i}]\right) = 1. \tag{B.7}$$

Taking C to be real and positive,

$$C = (1 - e^{-\beta\hbar\omega_i})^{-\frac{1}{2}}. \tag{B.8}$$

The transformations in Eq. (3.69) and Eq. (3.70) are derived.

B.2 Proof of the vacuum state condition for Fermionic operators

In this section, we give a rigorous proof that the Bogoliubov transformed Fermionic operators satisfy the vacuum state condition with the respect the $|\theta(\beta)\rangle$ state (described in Eq. (3.86) and Eq. (3.87)). Applying BCH expansion and anti-cannonical commutation rules, we can derive that the Fermionic construction operators ($\hat{i}$, $\hat{i}^\dagger$, $\tilde{i}$, $\tilde{i}^\dagger$) satisfy the following equations:

$$\begin{aligned} e^{-\hat{u}}\hat{i}e^{\hat{u}} &= \hat{i} + \tilde{i}^\dagger, \\ e^{-\hat{u}}\hat{i}^\dagger e^{\hat{u}} &= \hat{i}^\dagger, \\ e^{-\hat{u}}\tilde{i}e^{\hat{u}} &= \tilde{i} - \hat{i}^\dagger, \\ e^{-\hat{u}}\tilde{i}^\dagger e^{\hat{u}} &= \tilde{i}^\dagger, \end{aligned} \tag{B.9}$$

where $\hat{u} \equiv \sum_i \hat{i}^\dagger \tilde{i}^\dagger$.

Similarly, applying BCH, we can prove that

$$\begin{aligned} e^{\beta\hat{h}_0/2}\hat{i}e^{-\beta\hat{h}_0/2} &= e^{-\beta\epsilon_i/2}\hat{i} \\ e^{\beta\hat{h}_0/2}\hat{i}^\dagger e^{-\beta\hat{h}_0/2} &= e^{\beta\epsilon_i/2}\hat{i}^\dagger \\ e^{\beta\hat{h}_0/2}\tilde{i}e^{-\beta\hat{h}_0/2} &= \tilde{i} \\ e^{\beta\hat{h}_0/2}\tilde{i}^\dagger e^{-\beta\hat{h}_0/2} &= \tilde{i}^\dagger \end{aligned} \tag{B.10}$$

where $\hat{h}_0 \equiv \sum_i \omega_i \hat{i}^\dagger \hat{i}$.

Applying Eq. (B.9) and Eq. (B.10), we can derive the following expression by inserting the two identities $e^{\beta\hat{h}_0/2}e^{-\beta\hat{h}_0/2}$ and $e^{\hat{u}}e^{-\hat{u}}$:

$$\begin{aligned} \hat{a}_p |\theta(\beta)\rangle &= e^{-\beta\hat{h}_0/2}e^{\beta\hat{h}_0/2}\hat{a}_p e^{-\beta\hat{h}_0/2}e^{\hat{u}} |0,\tilde{0}\rangle \\ &= e^{-\beta\hat{h}_0/2}(\cos\theta_p e^{\beta\hat{h}_0/2}\hat{p}e^{-\beta\hat{h}_0/2} - \sin\theta_p e^{\beta\hat{h}_0/2}\tilde{p}^\dagger e^{-\beta\hat{h}_0/2})e^{\hat{u}} |0,\tilde{0}\rangle \\ &= e^{-\beta\hat{h}_0/2}(\cos\theta_p e^{-\beta\epsilon_p/2}\hat{p} - \sin\theta_p \tilde{p}^\dagger)e^{\hat{u}} |0,\tilde{0}\rangle \\ &= e^{-\beta\hat{h}_0/2}(\cos\theta_p e^{-\beta\epsilon_p/2}e^{\hat{u}}e^{-\hat{u}}\hat{p}e^{\hat{u}} - \sin\theta_p e^{\hat{u}}e^{-\hat{u}}\tilde{p}^\dagger e^{\hat{u}}) |0,\tilde{0}\rangle \\ &= e^{-\beta\hat{h}_0/2}(\cos\theta_p e^{-\beta\epsilon_p/2}e^{\hat{u}}(\hat{p} + \tilde{p}^\dagger) - \sin\theta_p e^{\hat{u}}\tilde{p}^\dagger) |0,\tilde{0}\rangle \\ &= e^{-\beta\hat{h}_0/2}e^{\hat{u}}(\cos\theta_p e^{-\beta\epsilon_p/2} - \sin\theta_p)\tilde{p}^\dagger |0,\tilde{0}\rangle \\ &= 0. \end{aligned} \tag{B.11}$$

We substitute the definition of $\cos\theta_p$ and $\sin\theta_p$ in Eq. (3.83) and Eq. (3.84) to obtain the last equality in Eq. (B.11).

Similarly we have:

$$
\begin{aligned}
\hat{b}_p^\dagger \left|\theta(\beta)\right\rangle &= e^{-\beta\hat{h}_0/2} e^{\beta\hat{h}_0/2} \hat{b}_p^\dagger e^{-\beta\hat{h}_0/2} e^{\hat{u}} \left|0,\tilde{0}\right\rangle \\
&= e^{-\beta\hat{h}_0/2} (\sin\theta_p e^{\beta\hat{h}_0/2} \hat{p}^\dagger e^{-\beta\hat{h}_0/2} + \cos\theta_p e^{\beta\hat{h}_0/2} \tilde{p} e^{-\beta\hat{h}_0/2}) e^{\hat{u}} \left|0,\tilde{0}\right\rangle \\
&= e^{-\beta\hat{h}_0/2} (\sin\theta_p e^{\beta\epsilon_p/2} \hat{p}^\dagger + \cos\theta_p \tilde{p}) e^{\hat{u}} \left|0,\tilde{0}\right\rangle \\
&= e^{-\beta\hat{h}_0/2} (\sin\theta_p e^{\beta\epsilon_p/2} e^{\hat{u}} e^{-\hat{u}} \hat{p}^\dagger e^{\hat{u}} + \cos\theta_p e^{\hat{u}} e^{-\hat{u}} \tilde{p} e^{\hat{u}}) \left|0,\tilde{0}\right\rangle \\
&= e^{-\beta\hat{h}_0/2} (\sin\theta_p e^{\beta\epsilon_p/2} e^{\hat{u}} \hat{p}^\dagger + \cos\theta_p e^{\hat{u}} (\tilde{p} - \hat{p}^\dagger)) \left|0,\tilde{0}\right\rangle \\
&= e^{-\beta\hat{h}_0/2} e^{\hat{u}} (\sin\theta_p e^{\beta\epsilon_p/2} - \cos\theta_p) \hat{p}^\dagger) \left|0,\tilde{0}\right\rangle \\
&= 0.
\end{aligned}
\tag{B.12}
$$

Thus, from Eq. (B.11) and Eq. (B.12), we proved the vacuum state condition for Bogoliubov transformed Fermionic operators.

Appendix C

Proof of the EOMs translate between the TNOE and the TFCC approaches for Bosonic vibrational Hamiltonian

In this appendix, we give a detailed derivation on the EOMs of the Bosonic Hamiltonian given in Eq. (3.112) translate from one to another between the TNOE and the TFCC approaches

We Start from the TNOE approach. Applying Wick's theorem we expand out the EOMs

in Eq. (3.24):

$$-\frac{\mathrm{d}s_0}{\mathrm{d}\beta} = h_0 + \sum_i^M f_i h_i^i + \sum_k^M h_k \bar{f}_k s^k + \sum_k^M h^k f_k s_k + \sum_{kl}^M h_k^l f^l \bar{f}_k s_l^k + \sum_{kl}^M h_k^l \bar{f}_k s^k f_l s_l + \frac{1}{2}\sum_{kl}^M h_{kl} \bar{f}_k \bar{f}_l s^{kl} + \frac{1}{2}\sum_{kl}^M h_{kl} \bar{f}_k s^k \bar{f}_l s^l + \frac{1}{2}\sum_{kl}^M h^{kl} f_k f_l s_{kl} + \frac{1}{2}\sum_{kl}^M h^{kl} f_k s_k f_l s_l, \tag{C.1}$$

$$-\bar{f}_i\frac{\mathrm{d}s^i}{\mathrm{d}\beta} = \bar{f}_i h^i + \sum_k^M h^k \bar{f}_i f_k s_k^i + \sum_k^M h_k \bar{f}_k \bar{f}_i s^{ki} + \sum_k^M \bar{f}_i h^{ik} f_k s_k + \sum_k^M \bar{f}_i h_k^i \bar{f}_k s^k + \sum_{kl}^M h_l^k \bar{f}_i f_k s_k^i \bar{f}_l s^l + \sum_{kl}^M h_l^k f_k s_k \bar{f}_l \bar{f}_i s^{li} + \sum_{kl}^M h^{kl} f_k s_k \bar{f}_i f_l s_l^i + \sum_{kl}^M h_{kl} \bar{f}_k s^k \bar{f}_l \bar{f}_i s^{li}, \tag{C.2}$$

$$-f_i\frac{\mathrm{d}s_i}{\mathrm{d}\beta} = f_i h_i + \sum_k^M h_k \bar{f}_k f_i s_i^k + \sum_k^M f_i h_k^i \bar{f}_k s^k + \sum_k^M h^k f_k f_i s_{ki} + \sum_k^M f_i h_{ki} \bar{f}_k s^k + \sum_{kl}^M h_l^k \bar{f}_l f_i s_i^l f_k s_k + \sum_{kl}^M h_l^k \bar{f}_l s^l f_k f_i s_{ki} + \sum_{kl}^M h^{kl} f_k s_k f_l f_i s_{li} + \sum_{kl}^M h_{kl} \bar{f}_k t^k \bar{f}_k f_i s_i^k, \tag{C.3}$$

$$-\bar{f}_i f_j\frac{\mathrm{d}s_j^i}{\mathrm{d}\beta} = \bar{f}_i f_j h_j^i + \sum_k^M f_j h_j^k f_k \bar{f}_i s_k^i + \sum_k^M \bar{f}_i h_k^i \bar{f}_k f_j s_j^k + \sum_k^M \bar{f}_i h^{ki} f_k f_j s_{kj} + \sum_k^M f_j h_{kj} \bar{f}_k \bar{f}_i s^{ik} + \sum_{kl}^M h_l^k \bar{f}_i f_k s_k^i \bar{f}_l f_j s_j^l + \sum_{kl}^M h_l^k f_k f_j s_{kj} \bar{f}_l \bar{f}_i s^{li} + \sum_{kl}^M h^{kl} f_l f_j s_{lj} \bar{f}_i f_k s_k^i + \sum_{kl}^M h_{kl} \bar{f}_k \bar{f}_i s^{ki} \bar{f}_l f_j s_j^l, \tag{C.4}$$

$$-\bar{f}_i\bar{f}_j\frac{\mathrm{d}s^{ij}}{\mathrm{d}\beta} = \bar{f}_i \bar{f}_j h^{ij} + \sum_k^M \bar{f}_j h_k^j \bar{f}_k \bar{f}_i s^{ki} + \sum_k^M \bar{f}_i h_k^i \bar{f}_k \bar{f}_j s^{kj} + \sum_k^M \bar{f}_i h^{ki} f_k \bar{f}_j s_k^j + \sum_k^M \bar{f}_j h^{kj} f_k \bar{f}_i s_k^i + \sum_{kl}^M h_l^k \bar{f}_l \bar{f}_i s^{li} \bar{f}_j f_k s_k^j + \sum_{kl}^M h_l^k \bar{f}_l \bar{f}_j s^{lj} \bar{f}_i f_k s_k^i + \sum_{kl}^M h^{kl} \bar{f}_i f_k s_k^i \bar{f}_j s_l s_l^j + \sum_{kl}^M h_{kl} \bar{f}_k \bar{f}_i s^{ki} \bar{f}_l \bar{f}_j s^{lj}, \tag{C.5}$$

$$-f_i f_j\frac{\mathrm{d}s_{ij}}{\mathrm{d}\beta} = f_i f_j h_{ij} + \sum_k^M f_i h_i^k f_k f_j s_{kj} + \sum_k^M f_j h_j^k f_k f_i s_{ki} + \sum_k^M f_i h_{ki} \bar{f}_k f_j s_j^k + \sum_k^M f_j h_{kj} \bar{f}_k f_i s_i^k + \sum_{kl}^M h_l^k \bar{f}_l f_i s_i^l f_k f_j s_{kj} + \sum_{kl}^M h_l^k \bar{f}_l f_j s_j^l f_k f_i s_{ki} + \sum_{kl}^M h^{kl} f_l f_i s_{li} f_k f_j s_{kj} + \sum_{kl}^M h_{kl} \bar{f}_k f_i s_i^k \bar{f}_l f_j s_j^l. \tag{C.6}$$

Now we substitute the mappings of cluster amplitude between TNOE and TFCC in Eq. (3.118) and Eq. (3.119), the equations can be re-written as:

$$
\begin{aligned}
-\frac{\mathrm{d}t_0}{\mathrm{d}\beta} &= h_0 + \sum_k \sinh\theta_k sinh\theta_k h_k^k \\
&+ \sum_k^M \left(\cosh\theta_k h_k t^{a_k} + \sinh\theta_k h^k t^{b_k}\right) \\
&+ \frac{1}{2}\sum_{kl}^M \left(\cosh\theta_k \cosh\theta_l h_{kl} t^{a_k a_l} + \sinh\theta_k \sinh\theta_l h^{kl} t^{b_k b_l} + \cosh\theta_l \sinh\theta_k h_k^l t^{a_l b_k} + \sinh\theta_l \cosh\theta_k h_k^l t^{b_l a_k}\right) \\
&+ \frac{1}{2}\sum_{kl}^M \left(\cosh\theta_k \cosh\theta_l h_{kl} t^{a_k} t^{a_l} + \sinh\theta_k \sinh\theta_l h^{kl} t^{b_k} t^{b_l} + \cosh\theta_l \sinh\theta_k h_k^l t^{a_l b_k} + \sinh\theta_l \cosh\theta_k h_k^l t^{b_l a_k}\right),
\end{aligned}
\tag{C.7}
$$

$$
\begin{aligned}
-\frac{\mathrm{d}t^{a_i}}{\mathrm{d}\beta} &= \cosh\theta_i h^i \\
&+ \sum_k^M \left(\cosh\theta_i \cosh\theta_k h_k^i t^{a_k} + \cosh\theta_i \sin\theta_k h^{ik} t^{b_k}\right) + \sum_k \left(\sinh\theta_k h^k t^{b_k a_i} + \cosh\theta_k h_k t^{a_k a_i}\right) \\
&+ \sum_{kl}^M \left(\cosh\theta_k \sinh\theta_l h_l^k t^{a_k} t^{b_l a_i} + \sinh\theta_k \cosh\theta_l h_l^k t^{b_k} t^{a_l a_i}\right) + \\
&+ \sum_{kl}^M \left(\sinh\theta_k \sinh\theta_l h^{kl} t^{b_k} t^{b_l a_i} + \cosh\theta_k \cosh\theta_l h_{kl} t^{a_k} t^{a_l a_i}\right),
\end{aligned}
\tag{C.8}
$$

$$
\begin{aligned}
-\frac{\mathrm{d}t^{b_i}}{\mathrm{d}\beta} &= \sinh\theta_i h_i \\
&+ \sum_k^M \left(\sinh\theta_i \sinh\theta_k h_i^k t^{b_k} + \sinh\theta_i \cos\theta_k h_{ik} t^{a_k}\right) + \sum_k \left(\sinh\theta_k h^k t^{b_i b_k} + \cosh\theta_k h_k t^{a_k b_i}\right) \\
&+ \sum_{kl}^M \left(\cosh\theta_k \sinh\theta_l h_l^k t^{a_k} t^{b_l b_i} + \sinh\theta_k \cosh\theta_l h_l^k t^{b_k} t^{a_l b_i}\right) \\
&+ \sum_{kl}^M \left(\sinh\theta_k \sinh\theta_l h^{kl} t^{b_k} t^{b_l a_i} + \cosh\theta_k \cosh\theta_l h_{kl} t^{a_k} t^{a_l b_i}\right),
\end{aligned}
\tag{C.9}
$$

$$
\begin{aligned}
-\frac{\mathrm{d}t^{a_i b_j}}{\mathrm{d}\beta} &= \cosh\theta_i \sinh\theta_j h^i_j \\
&+ \sum_k^M \left(\sinh\theta_k \sinh\theta_j h^k_j t^{a_i b_k} + \cosh\theta_i \cosh\theta_k h^i_k t^{a_k b_j} + \cosh\theta_i \sinh\theta_k h^{ki} t^{b_k b_j} + \cosh\theta_k \sinh\theta_j h_{kj} t^{a_i a_k}\right) \\
&+ \sum_{kl}^M \left(\sinh\theta_k \cosh\theta_l h^k_l t^{b_k a_i} t^{a_l b_j} + \cosh\theta_k \sinh\theta_l h^k_l t^{a_k a_i} t^{b_l b_j}\right) \\
&+ \sum_{kl}^M \left(\sinh\theta_k \sinh\theta_l h^{kl} t^{b_k a_i} t^{b_l b_j} + \cosh\theta_k \cosh\theta_l h_{kl} t^{a_k a_i} t^{a_l b_j}\right),
\end{aligned}
\tag{C.10}
$$

$$
\begin{aligned}
-\frac{\mathrm{d}t^{a_i a_j}}{\mathrm{d}\beta} &= \cosh\theta_i \cosh\theta_j h^{a_i a_j} \\
&+ \sum_k^M \left(\cosh\theta_j \cosh\theta_k h^j_k t^{a_k a_i} + \cosh\theta_i \sinh\theta_k h^i_k t^{a_k a_j} + \sinh\theta_k \cosh\theta_i h^{ki} t^{b_k a_j} + \sinh\theta_k \cosh\theta_j h^{kj} t^{b_k a_i}\right) \\
&+ \sum_{kl}^M \left(\sinh\theta_k \cosh\theta_l h^k_l t^{a_l a_i} t^{a_j b_k} + \sinh\theta_k \cosh\theta_l h^k_l t^{a_l a_j} t^{a_i b_k}\right) \\
&+ \sum_{kl}^M \left(\sinh\theta_k \sinh\theta_l h^{kl} t^{a_i b_k} t^{a_j b_l} + \cosh\theta_k \cosh\theta_l h_{kl} t^{a_k a_i} t^{a_l a_j}\right),
\end{aligned}
\tag{C.11}
$$

$$
\begin{aligned}
-\frac{\mathrm{d}t^{b_i b_j}}{\mathrm{d}\beta} &= \sinh\theta_i \sinh\theta_j h^{b_i b_j} \\
&+ \sum_k^M \left(\sin\theta_j \sin\theta_k h^j_k t^{b_k b_i} + \sinh\theta_i \sinh\theta_k h^i_k t^{b_k b_j} + \cosh\theta_k \sinh\theta_i h_{ki} t^{a_k b_j} + \cosh\theta_k \sinh\theta_j h^{kj} t^{a_k b_i}\right) \\
&+ \sum_{kl}^M \left(\sinh\theta_k \cosh\theta_l h^k_l t^{a_l b_i} t^{b_j b_k} + \sinh\theta_k \cosh\theta_l h^k_l t^{a_l b_j} t^{b_i b_k}\right) \\
&+ \sum_{kl}^M \left(\sinh\theta_k \sinh\theta_l h^{kl} t^{b_i b_k} t^{b_j b_l} + \cosh\theta_k \cosh\theta_l h_{kl} t^{a_k b_i} t^{a_l b_j}\right).
\end{aligned}
\tag{C.12}
$$

In this derivation a key step is as follow. When there is a contraction between the Hamiltonian and the cluster operator in the TNOE EOM, it will produce a f or $\bar{f}$ factor. Thus, we can re-write the factor into a product of its square root and place one of them in front of the Hamiltonian matrix element and the other in from of the TNOE amplitude. Then, the Hamiltonian matrix element can be converted to a contribution of the renormalized matrix element of the Bogoliubov transformed Hamiltonian and the TNOE amplitude and be mapped to the TFCC amplitude. For example, we can evaluation the them $\sum_k^M \sqrt{\bar{f}_i} h^{ik} f_k \sqrt{f_j} t_{kj}$ in

Eq. (C.10) as follow [1]:

$$\begin{aligned}\sum_{k}^{M}\sqrt{\bar{f}_i}h^{ik}f_k\sqrt{f_j}t_{kj} &= \sum_{k}^{M}\sqrt{\bar{f}_i}h^{ik}\sqrt{f_k}\sqrt{f_k}\sqrt{f_j}t_{kj}\\ &= \sum_{k}^{M}\sqrt{\bar{f}_i}\sqrt{f}_k h^{ik}\sqrt{f_k}\sqrt{f_j}t_{kj}\\ &= \sum_{k}^{M}\cosh\theta_i\sinh\theta_k h^{ik}t^{b_k b_j}.\end{aligned} \tag{C.13}$$

Comparing these equations with the expression of the Bogoliubov transformed Hamiltonian ($\hat{H}\xrightarrow{\text{B.T.}}\tilde{H}$):

$$\begin{aligned}
&\tilde{h}^0 : h_0 + \sum_i \sinh\theta_i\sinh\theta_i h_i^i\\
&\tilde{h}^1 : \sum_i^M(\cosh\theta_i h^i\hat{a}_i^\dagger + \sinh\theta_i h_i\hat{b}_i^\dagger)\\
&\tilde{h}_1 : \sum_i^M(\cosh\theta_i h_i\hat{a}_i + \sinh\theta_i h^i\hat{b}_i)\\
&\tilde{h}^2 : \frac{1}{2}\sum_{ij}^M(\cosh\theta_i\cosh\theta_j h^{ij}\hat{a}_i^\dagger\hat{a}_j^\dagger + \sinh\theta_i\sinh\theta_j h_{ij}\hat{b}_i^\dagger\hat{b}_j^\dagger + \cosh\theta_i\sinh\theta_j h_j^i\hat{a}_i^\dagger\hat{b}_j^\dagger + \sinh\theta_i\cosh\theta_j h_j^i\hat{b}_i^\dagger\hat{a}_j^\dagger)\\
&\tilde{h}_2 : \frac{1}{2}\sum_{ij}^M(\cosh\theta_i\cosh\theta_j h^{ij}\hat{a}_i\hat{a}_j + \sinh\theta_i\sinh\theta_j h_{ij}\hat{b}_i\hat{b}_j + \cosh\theta_i\sinh\theta_j h_j^i\hat{a}_i^\dagger\hat{b}_j^\dagger + \sinh\theta_i\cosh\theta_j h_j^i\hat{b}_i^\dagger\hat{a}_j^\dagger)\\
&\tilde{h}_1^1 : \sum_{ij}^M(\cosh\theta_i\cosh\theta_j h_j^i\hat{a}_i^\dagger\hat{a}_j + \sinh\theta_i\sinh\theta_j h_i^j\hat{b}_i^\dagger\hat{b}_j + \cosh\theta_i\sinh\theta_j h^{ij}\hat{a}_i^\dagger\hat{b}_j + \sinh\theta_i\cosh\theta_j h_{ij}\hat{b}_i^\dagger\hat{a}_j)
\end{aligned} \tag{C.14}$$

Eq. (C.7) can be re-written as:

$$-\frac{dt^0}{d\beta} = \tilde{h}^0 + \sum_q^{2M}\tilde{h}_q t^q + \frac{1}{2}\sum_{pq}^{2M}\tilde{h}_{pq}t^{pq} + \frac{1}{2}\sum_{pq}^{2M}\tilde{h}_{pq}t^{pq}. \tag{C.15}$$

Eq. (C.8) and Eq. (C.9) in combination can be re-written as:

$$-\frac{dt^p}{d\beta} = \tilde{h}^p + \sum_q^{2M}\tilde{h}_q^p t^q + \sum_q^{2M}\tilde{t}_q t^{qp} + \sum_{qr}^{2M}\tilde{h}_{qr}t^q t^{rp}. \tag{C.16}$$

[1] There is a common factor $\sqrt{\bar{f}_i}\sqrt{f_j}$ that cancels out on BHS of the equation.

Eq. (C.10), Eq. (C.11) and Eq. (C.12) in combination can be re-written as:

$$-\frac{dt^{pq}}{d\beta} = \tilde{h}^{pq} + \sum_{r}^{2M} \tilde{h}^{p}_{r} t^{rq} + \sum_{ts}^{2M} \tilde{h}_{rs} t^{rp} t^{sq}. \tag{C.17}$$

In these equations, the summation labels run over the squared Hilbert space in the Bogoliubov representation. For example, for t^{pq} them consists of four blocks and each block has the shape of the double cluster amplitude in TNOE:

$$\boldsymbol{t}^{pq} : \begin{bmatrix} \begin{bmatrix} t^{11} & \dots & t^{M1} \\ & \dots & \\ t^{M1} & \dots. & t^{MM} \end{bmatrix}_{aa} & \begin{bmatrix} t^{M+11} & \dots & t^{2M1} \\ & \dots & \\ t^{M+11} & \dots. & t^{2MM} \end{bmatrix}_{ab} \\ \begin{bmatrix} t^{M+11} & \dots & t^{M+11} \\ & \dots & \\ t^{2M1} & \dots. & t^{2MM} \end{bmatrix}_{ba} & \begin{bmatrix} t^{M+1M_1} & \dots & t^{M+12M} \\ & \dots & \\ t^{2MM+1} & \dots. & t^{2M2M} \end{bmatrix}_{bb} \end{bmatrix}. \tag{C.18}$$

From this derivation, we observe that Eq. (C.15), Eq. (C.16) and Eq. (C.17) are exactly the EOMs in the TFCC approach this problem. Thus, we verify that the EOMs between TNOE and TFCC approach can translate from one to another for Bosonic Hamiltonian given in Eq. (3.112).

Appendix D

Explicit expression of the Bogoliubov transformed two-electron integrals

$$
\begin{aligned}
\tilde{V} = & \sum_{a_p a_q a_r a_s} \tilde{V}^{a_p a_q}_{a_s a_r} \hat{a}^\dagger_p \hat{a}^\dagger_q \hat{a}_r \hat{a}_s + \sum_{b_p a_q a_r a_s} \tilde{V}^{b_p a_q}_{a_s a_r} \hat{b}^\dagger_p \hat{a}^\dagger_q \hat{a}_r \hat{a}_s \\
& + \sum_{a_p b_q a_r a_s} \tilde{V}^{a_p b_q}_{a_s b_r} \hat{a}^\dagger_p \hat{b}^\dagger_q \hat{a}_r \hat{a}_s + \sum_{a_p a_q a_r b_s} \tilde{V}^{a_p a_q}_{b_s a_r} \hat{a}^\dagger_p \hat{a}^\dagger_q \hat{a}_r \hat{b}_s \\
& + \sum_{a_p a_q b_r a_s} \tilde{V}^{a_p a_q}_{a_s b_r} \hat{a}^\dagger_p \hat{a}^\dagger_q \hat{b}_r \hat{a}_s + \sum_{b_p b_q a_r a_s} \tilde{V}^{b_p b_q}_{a_s a_r} \hat{b}^\dagger_p \hat{b}^\dagger_q \hat{a}_r \hat{a}_s \\
& + \sum_{b_p a_q b_r a_s} \tilde{V}^{b_p a_q}_{a_s b_r} \hat{b}^\dagger_p \hat{a}^\dagger_q \hat{b}_r \hat{a}_s + \sum_{b_p a_q a_r b_s} \tilde{V}^{b_p a_q}_{b_s a_r} \hat{b}^\dagger_p \hat{a}^\dagger_q \hat{a}_r \hat{b}_s \\
& + \sum_{a_p b_q b_r a_s} \tilde{V}^{a_p b_q}_{a_s b_r} \hat{a}^\dagger_p \hat{b}^\dagger_q \hat{b}_r \hat{a}_s + \sum_{a_p b_q a_r b_s} \tilde{V}^{a_p b_q}_{b_s a_r} \hat{a}^\dagger_p \hat{b}^\dagger_q \hat{a}_r \hat{b}_s \\
& + \sum_{a_p a_q b_r b_s} \tilde{V}^{a_p a_q}_{b_s b_r} \hat{a}^\dagger_p \hat{a}^\dagger_q \hat{b}_r \hat{b}_s + \sum_{b_p b_q b_r a_s} \tilde{V}^{b_p b_q}_{a_s b_r} \hat{b}^\dagger_p \hat{b}^\dagger_q \hat{b}_r \hat{a}_s \\
& + \sum_{b_p b_q a_r b_s} \tilde{V}^{b_p b_q}_{b_s a_r} \hat{b}^\dagger_p \hat{b}^\dagger_q \hat{a}_r \hat{b}_s + \sum_{b_p a_q b_r b_s} \tilde{V}^{b_p a_q}_{b_s b_r} \hat{b}^\dagger_p \hat{a}^\dagger_q \hat{b}_r \hat{b}_s \\
& + \sum_{a_p b_q b_r b_s} \tilde{V}^{a_p b_q}_{b_s b_r} \hat{a}^\dagger_p \hat{b}^\dagger_q \hat{b}_r \hat{b}_s + \sum_{b_p b_q b_r b_s} \tilde{V}^{b_p b_q}_{b_s b_r} \hat{b}^\dagger_p \hat{b}^\dagger_q \hat{b}_r \hat{b}_s,
\end{aligned}
\tag{D.1}
$$

where

$$\tilde{V}^{a_p a_q}_{a_s a_r} = \cos\theta_p \cos\theta_q \cos\theta_s \cos\theta_r V^{pq}_{sr} \tag{D.2}$$
$$\tilde{V}^{b_p a_q}_{a_s a_r} = \sin\theta_p \cos\theta_q \cos\theta_s \cos\theta_r V^{pq}_{sr} \tag{D.3}$$
$$\tilde{V}^{a_p b_q}_{a_s a_r} = \cos\theta_p \sin\theta_q \cos\theta_s \cos\theta_r V^{pq}_{sr} \tag{D.4}$$
$$\tilde{V}^{a_p a_q}_{b_s a_r} = \cos\theta_p \cos\theta_q \sin\theta_s \cos\theta_r V^{pq}_{sr} \tag{D.5}$$
$$\tilde{V}^{a_p a_q}_{a_s b_r} = \cos\theta_p \cos\theta_q \cos\theta_s \sin\theta_r V^{pq}_{sr} \tag{D.6}$$
$$\tilde{V}^{b_p b_q}_{a_s a_r} = \sin\theta_p \sin\theta_q \cos\theta_s \cos\theta_r V^{pq}_{sr} \tag{D.7}$$
$$\tilde{V}^{b_p a_q}_{b_s a_r} = \sin\theta_p \cos\theta_q \sin\theta_s \cos\theta_r V^{pq}_{sr} \tag{D.8}$$
$$\tilde{V}^{b_p a_q}_{a_s b_r} = \sin\theta_p \cos\theta_q \cos\theta_s \sin\theta_r V^{pq}_{sr} \tag{D.9}$$
$$\tilde{V}^{a_p b_q}_{b_s a_r} = \cos\theta_p \sin\theta_q \sin\theta_s \cos\theta_r V^{pq}_{sr} \tag{D.10}$$
$$\tilde{V}^{a_p b_q}_{a_s b_r} = \cos\theta_p \sin\theta_q \cos\theta_s \sin\theta_r V^{pq}_{sr} \tag{D.11}$$
$$\tilde{V}^{a_p a_q}_{b_s b_r} = \cos\theta_p \cos\theta_q \sin\theta_s \sin\theta_r V^{pq}_{sr} \tag{D.12}$$
$$\tilde{V}^{b_p b_q}_{b_s a_r} = \sin\theta_p \sin\theta_q \sin\theta_s \cos\theta_r V^{pq}_{sr} \tag{D.13}$$
$$\tilde{V}^{b_p b_q}_{a_s b_r} = \sin\theta_p \sin\theta_q \cos\theta_s \sin\theta_r V^{pq}_{sr} \tag{D.14}$$
$$\tilde{V}^{b_p a_q}_{b_s b_r} = \sin\theta_p \cos\theta_q \sin\theta_s \sin\theta_r V^{pq}_{sr} \tag{D.15}$$
$$\tilde{V}^{a_p b_q}_{b_s b_r} = \cos\theta_p \sin\theta_q \sin\theta_s \sin\theta_r V^{pq}_{sr} \tag{D.16}$$
$$\tilde{V}^{b_p b_q}_{b_s b_r} = \sin\theta_p \sin\theta_q \sin\theta_s \sin\theta_r V^{pq}_{sr} \tag{D.17}$$

Appendix E

Subroutines that implement the TFCC residual equations for electronic structrue problem

```
import numpy as np

from pyscf import lib
from pyscf import ao2mo
from pyscf.lib import logger
from pyscf.cc import ccsd
from pyscf.mp import mp2
from pyscf import __config__

BLKMIN = getattr(__config__, 'cc_ccsd_blkmin', 4)
MEMORYMIN = getattr(__config__, 'cc_ccsd_memorymin', 2000)
```

Listing E.1: Import necessary python libraries

```python

### Eqs. (37)-(39) "kappa"
def cc_Foo(t1, t2, F_tilde, V_tilde, flag=False):
    foo = F_tilde['ij']
    Fki = foo.copy()
    if not flag:
        eris_ovov = V_tilde['iajb']
        Fki += 2 * lib.einsum('kcld,ilcd->ki', eris_ovov, t2)
        Fki -= lib.einsum('kdlc,ilcd->ki', eris_ovov, t2)
        Fki += 2 * lib.einsum('kcld,ic,ld->ki', eris_ovov, t1, t1)
        Fki -= lib.einsum('kdlc,ic,ld->ki', eris_ovov, t1, t1)
    return Fki


def cc_Fvv(t1, t2, F_tilde, V_tilde, flag=False):
    fvv = F_tilde['ab']
    Fac = fvv.copy()
    if not flag:
        eris_ovov = V_tilde['iajb']
        Fac -= 2 * lib.einsum('kcld,klad->ac', eris_ovov, t2)
        Fac += lib.einsum('kdlc,klad->ac', eris_ovov, t2)
        Fac -= 2 * lib.einsum('kcld,ka,ld->ac', eris_ovov, t1, t1)
        Fac += lib.einsum('kdlc,ka,ld->ac', eris_ovov, t1, t1)
    return Fac


def cc_Fov(t1, t2, F_tilde, V_tilde, flag=False):
    fov = F_tilde['ia']
    Fkc = fov.copy()
    if not flag:
        eris_ovov = V_tilde['iajb']
        Fkc += 2 * np.einsum('kcld,ld->kc', eris_ovov, t1)
        Fkc -= np.einsum('kdlc,ld->kc', eris_ovov, t1)
    return Fkc

### Eqs. (40)-(41) "lambda"


def cc_Loo(t1, t2, F_tilde, V_tilde, flag=False):
    fov = F_tilde['ia']
    Lki = cc_Foo(t1, t2, F_tilde, V_tilde, flag=flag) + np.einsum('kc,ic->ki',fov, t1)
    if not flag:
        eris_ovoo = V_tilde['iajk']
        Lki += 2*np.einsum('lcki,lc->ki', eris_ovoo, t1)
        Lki -=   np.einsum('kcli,lc->ki', eris_ovoo, t1)
    return Lki


def cc_Lvv(t1, t2, F_tilde, V_tilde, flag=False):
    fov = F_tilde['ia']
    Lac = cc_Fvv(t1, t2, F_tilde, V_tilde, flag=flag) - np.einsum('kc,ka->ac',fov, t1)
    if not flag:
        eris_ovvv = V_tilde['iabc']
        Lac += 2*np.einsum('kdac,kd->ac', eris_ovvv, t1)
        Lac -=   np.einsum('kcad,kd->ac', eris_ovvv, t1)
    return Lac
```

Listing E.2: Subroutines to calculate intermediate quantities for the TFCC singles residual

```
### Eqs. (42)-(45) "chi"
def cc_Woooo(t1, t2, F_tilde, V_tilde):
    eris_ovoo = V_tilde['iajk']
    Wklij  = lib.einsum('lcki,jc->klij', eris_ovoo, t1)
    Wklij += lib.einsum('kclj,ic->klij', eris_ovoo, t1)
    eris_ovov = V_tilde['iajb']
    Wklij += lib.einsum('kcld,ijcd->klij', eris_ovov, t2)
    Wklij += lib.einsum('kcld,ic,jd->klij', eris_ovov, t1, t1)
    Wklij += V_tilde['ijkl'].transpose(0,2,1,3)
    return Wklij


def cc_Wvvvv(t1, t2, F_tilde, V_tilde, flag=False):
    # Incore
    eris_ovvv = V_tilde['iabc']
    Wabcd  = lib.einsum('kdac,kb->abcd', eris_ovvv,-t1)
    Wabcd -= lib.einsum('kcbd,ka->abcd', eris_ovvv, t1)
    Wabcd += V_tilde['abcd'].transpose(0,2,1,3)
    return Wabcd


def cc_Wvovo(t1, t2, F_tilde, V_tilde):
    eris_ovvv = V_tilde['iabc']
    eris_ovoo = V_tilde['iajk']
    Wakci  = lib.einsum('kdac,id->akci', eris_ovvv, t1)
    Wakci -= lib.einsum('lcki,la->akci', eris_ovoo, t1)
    Wakci += V_tilde['ijab'].transpose(2,0,3,1)
    eris_ovov = V_tilde['iajb']
    Wakci -= 0.5*lib.einsum('lckd,ilda->akci', eris_ovov, t2)
    Wakci -= lib.einsum('lckd,id,la->akci', eris_ovov, t1, t1)
    return Wakci


def Wooov(t1, t2, F_tilde, V_tilde):
    eris_ovov = V_tilde['iajb']
    Wklid  = lib.einsum('ic,kcld->klid', t1, eris_ovov)
    Wklid += V_tilde['iajk'].transpose(2,0,3,1)
    return Wklid


def cc_Wvoov(t1, t2, F_tilde, V_tilde):
    eris_ovvv = V_tilde['iabc']
    eris_ovoo = V_tilde['iajk']
    Wakic  = lib.einsum('kcad,id->akic', eris_ovvv, t1)
    Wakic -= lib.einsum('kcli,la->akic', eris_ovoo, t1)
    Wakic += np.asarray(V_tilde['iabj']).transpose(2,0,3,1)
    eris_ovov = V_tilde['iajb']
    Wakic -= 0.5*lib.einsum('ldkc,ilda->akic', eris_ovov, t2)
    Wakic -= 0.5*lib.einsum('lckd,ilad->akic', eris_ovov, t2)
    Wakic -= lib.einsum('ldkc,id,la->akic', eris_ovov, t1, t1)
    Wakic += lib.einsum('ldkc,ilad->akic', eris_ovov, t2)
    return Wakic
```

Listing E.3: Subroutines to calculate intermediate quantities for the TFCC doubles residual

```python
def update_amps(t1, t2, F_tilde, V_tilde):
    """Singles and Doubles residual equation
    """
    fov = F_tilde['ia']
    foo = F_tilde['ij']
    fvv = F_tilde['ab']
    Foo = cc_Foo(t1, t2, F_tilde, V_tilde, flag=flag)
    Fvv = cc_Fvv(t1, t2, F_tilde, V_tilde, flag=flag)
    Fov = cc_Fov(t1, t2, F_tilde, V_tilde, flag=flag)

    # T1 equation
    M = t1.shape[0]
    t1new = np.zeros([M, M])
    t1new += -2*np.einsum('kc,ka,ic->ia', fov, t1, t1)
    t1new +=   np.einsum('ac,ic->ia', Fvv, t1)
    t1new +=  -np.einsum('ki,ka->ia', Foo, t1)
    t1new += 2*np.einsum('kc,kica->ia', Fov, t2)
    t1new +=  -np.einsum('kc,ikca->ia', Fov, t2)
    t1new +=   np.einsum('kc,ic,ka->ia', Fov, t1, t1)
    t1new += fov.conj()
    t1new += 2*np.einsum('kcai,kc->ia', V_tilde['iabj'], t1)
    t1new +=  -np.einsum('kiac,kc->ia', V_tilde['ijab'], t1)
    t1new += 2*lib.einsum('kdac,ikcd->ia', V_tilde['iabc'], t2)
    t1new +=  -lib.einsum('kcad,ikcd->ia', V_tilde['iabc'], t2)
    t1new += 2*lib.einsum('kdac,kd,ic->ia', V_tilde['iabc'], t1, t1)
    t1new +=  -lib.einsum('kcad,kd,ic->ia', V_tilde['iabc'], t1, t1)
    t1new += -2*lib.einsum('lcki,klac->ia', V_tilde['iajk'], t2)
    t1new +=   lib.einsum('kcli,klac->ia', V_tilde['iajk'], t2)
    t1new += -2*lib.einsum('lcki,lc,ka->ia', V_tilde['iajk'], t1, t1)
    t1new +=   lib.einsum('kcli,lc,ka->ia', V_tilde['iajk'], t1, t1)

    # T2 equation
    t2new = np.zeros([M, M, M, M])
    tmp2 = lib.einsum('kibc,ka->abic', V_tilde['ijab'], -t1)
    tmp2 += V_tilde['iabc'].conj().transpose(1,3,0,2)
    tmp = lib.einsum('abic,jc->ijab', tmp2, t1)
    t2new = tmp + tmp.transpose(1,0,3,2)
    tmp2  = lib.einsum('kcai,jc->akij', V_tilde['iajb'], t1)
    tmp2 += V_tilde['iajk'].transpose(1,3,0,2).conj()
    tmp = lib.einsum('akij,kb->ijab', tmp2, t1)
    t2new -= tmp + tmp.transpose(1,0,3,2)
    t2new += V_tilde['iajb'].conj().transpose(0,2,1,3)
    Loo = cc_Loo(t1, t2, F_tilde, V_tilde, flag=flag)
    Lvv = cc_Lvv(t1, t2, F_tilde, V_tilde, flag=flag)
    Woooo = cc_Woooo(t1, t2, F_tilde, V_tilde)
    Wvoov = cc_Wvoov(t1, t2, F_tilde, V_tilde)
    Wvovo = cc_Wvovo(t1, t2, F_tilde, V_tilde)
    Wvvvv = cc_Wvvvv(t1, t2, F_tilde, V_tilde)
    tau = t2 + np.einsum('ia,jb->ijab', t1, t1)
    t2new += lib.einsum('klij,klab->ijab', Woooo, tau)
    t2new += lib.einsum('abcd,ijcd->ijab', Wvvvv, tau)
    tmp = lib.einsum('ac,ijcb->ijab', Lvv, t2)
    t2new += (tmp + tmp.transpose(1,0,3,2))
    tmp = lib.einsum('ki,kjab->ijab', Loo, t2)
    t2new -= (tmp + tmp.transpose(1,0,3,2))
    tmp  = 2*lib.einsum('akic,kjcb->ijab', Wvoov, t2)
    tmp -=   lib.einsum('akci,kjcb->ijab', Wvovo, t2)
    t2new += (tmp + tmp.transpose(1,0,3,2))
    tmp = lib.einsum('akic,kjbc->ijab', Wvoov, t2)
    t2new -= (tmp + tmp.transpose(1,0,3,2))
    tmp = lib.einsum('bkci,kjac->ijab', Wvovo, t2)
    t2new -= (tmp + tmp.transpose(1,0,3,2))

    return t1new, t2new
```

Listing E.4: Subroutines to calculate TFCC singles and doubles residuals

```
def energy(t1, t2, F_tilde, V_tilde):
    '''RCCSD correlation energy'''
    # if t1 is None: t1 = cc.t1
    # if t2 is None: t2 = cc.t2
    # if eris is None: eris = cc.ao2mo()

    e = 2*np.einsum('ia,ia', F_tilde['ia'], t1)
    tau = np.einsum('ia,jb->ijab',t1,t1)
    tau += t2
    eris_ovov = V_tilde['iajb']
    e += 2*np.einsum('ijab,iajb', tau, eris_ovov)
    e +=  -np.einsum('ijab,ibja', tau, eris_ovov)
    if abs(e.imag) > 1e-4:
        logger.warn(cc, 'Non-zero imaginary part found in RCCSD energy %s', e)
    return e.real
```

Listing E.5: Subroutine to calculate the TFCC constant residual

Appendix F

Discussion of spin and spin-adaptation

The Hamiltonian used in the calculations commute with the spin operators:

$$[\hat{H}, \hat{S}_z] = [\hat{H}, \hat{S}_+] = [\hat{H}, \hat{S}_-] = [\hat{H}, \hat{S}^2] = 0. \tag{F.1}$$

As a result, it is convenient to represent the Hamiltonian formally using operator of the unitary group.

$$E_q^p = \hat{p}_\alpha^\dagger \hat{q}_\alpha + \hat{p}_\beta^\dagger \hat{q}_\beta \tag{F.2}$$

$$E_{rs}^{pq} = \hat{p}_\alpha^\dagger \hat{q}_\alpha^\dagger \hat{s}_\alpha \hat{r}_\alpha + \hat{p}_\alpha^\dagger \hat{q}_\beta^\dagger \hat{s}_\beta \hat{r}_\alpha + \hat{p}_\beta^\dagger \hat{q}_\alpha^\dagger \hat{s}_\alpha \hat{r}_\beta + \hat{p}_\beta^\dagger \hat{q}_\beta^\dagger \hat{s}_\beta \hat{r}_\beta \tag{F.3}$$

such that

$$\hat{H} = \sum_{pq} h_q^p E_q^p + \frac{1}{2} \sum_{pqrs} \langle pq|rs\rangle \, E_{rs}^{pq}. \tag{F.4}$$

The integrals are not anti-symmetrized integrals. It is convenient to think of them as $\alpha\beta$-spin integrals:

$$\langle pq|rs\rangle = \langle p_\alpha q_\beta | r_\alpha s_\beta \rangle \equiv V_{Rs}^{pQ} \tag{F.5}$$

In this section we will use upper case to represent β-spin orbitals and lower case to represent α-spin orbitals. We have the relations in terms of spin orbitals.

$$h_q^p = h_Q^P \tag{F.6}$$

$$V_{rs}^{pq} = V_{RS}^{PQ} = V_{rS}^{pQ} - V_{Rs}^{pQ} \tag{F.7}$$

Likewise, the density matrices can be expressed in terms of the E-operators

$$D_{rs}^{pq} = \frac{1}{Z} \operatorname{Tr}\left(E_{rs}^{pq} e^{-\beta \hat{H}}\right) \tag{F.8}$$

$$D_q^p = \frac{1}{Z} \operatorname{Tr}\left(E_q^p e^{-\beta \hat{H}}\right) \tag{F.9}$$

These corresponding density matrices can be expressed in terms of spin-orbitals.

$$d_q^p = d_Q^P \tag{F.10}$$
$$d_{rs}^{pq} = d_{RS}^{PQ} = d_{rS}^{pQ} - d_{sR}^{pQ} \tag{F.11}$$

The same relation hold for the T amplitudes in the Bogoliubov representation.

We can express the cumulants as:

$$C_{rS}^{pQ} = d_{rS}^{pQ} - d_r^p d_S^Q \tag{F.12}$$
$$C_{rs}^{pq} = C_{RS}^{PQ} = C_{rS}^{pQ} - C_{Rs}^{pQ}. \tag{F.13}$$

It follows that in the computer code, in all instances, the variables that are used and manipulated are always the mixed spin $\alpha\beta$ amplitudes: V_{rS}^{pQ}, t_{iJ}^{aB}. and the α-spin one-body analog.

The $\alpha\alpha$ and $\beta\beta$ spin quantities are never constructed explicitly but the necessary formulas are substituted. This is already implemented like this in the spin-adapted CCSD code for closed-shell systems.

It is possible to ignore spin and interpret equations in terms of spatial orbitals. This follows the implementation. Formally, we can derive equation, in particular, the N-representability (P,Q,G cumulant) in terms of spin-orbitals:

$$\left\langle \hat{p}^\dagger \hat{Q}^\dagger \hat{Q} \hat{p} \right\rangle = C_{pQ}^{pQ} + n_p n_Q, \tag{F.14}$$
$$\left\langle \hat{p} \hat{Q} \hat{Q}^\dagger \hat{p}^\dagger \right\rangle = C_{pQ}^{pQ} + \bar{n}_p \bar{n}_Q, \tag{F.15}$$
$$\left\langle \hat{p}^\dagger \hat{Q} \hat{Q}^\dagger \hat{p} \right\rangle = -C_{pQ}^{pQ} + n_p \bar{n}_Q, \tag{F.16}$$
$$\tag{F.17}$$

We have following additional comments on the spin adaptation:

1. To provide a spin-adapted version of the TFCC, it is required that $\hat{h}_0$ is used to define the thermal reference state $|\theta\rangle = e^{-\beta \hat{h}_0/2} |u\rangle$, in a spin-scalar:

$$h_0 = \sum_p \varepsilon_p E_p^p. \tag{F.18}$$

This should be true irrespective of the spin-multiplicity of the ground state (in the case of the O_2 for example). In all cases, one can use exactly the same spin-adapted equations.

2. The Bogoliubov $\tilde{H}$ commute with spin-operators in the Bogoliubov representation.

$$\tilde{S}_z = \sum_p (\hat{p}^\dagger \hat{p} - \hat{P}^\dagger \hat{P}) \tag{F.19}$$

$$\tilde{S}_+ = \sum_p \hat{p}^\dagger \hat{P} \tag{F.20}$$

$$\tilde{S}_- = \sum_p \hat{P}^\dagger \hat{p} \tag{F.21}$$

where p runs over both $\hat{a}_p$ and $\hat{b}_p$ operators. This is analogous to conventional CC. $\tilde{H}$ also commute with $\tilde{N} = \sum_p (\hat{p}^\dagger \hat{p} + \hat{P}^\dagger \hat{P})$

Appendix G

Proof of the connectedness for the CC energy and amplitude equations

In this appendix, we will give a proof of the connectedness of the CC energy and amplitude equations in Eq. (2.47) and Eq. (2.48). In both equations, similarity transformed Hamiltonian $\bar{H} \equiv e^{-\hat{T}} \hat{H} e^{\hat{T}}$ can be expanded applying BCH formula:

$$e^{-\hat{T}} \hat{H} e^{\hat{T}} = \hat{H} + [\hat{H}, \hat{T}] + \frac{1}{2!}[[\hat{H}, \hat{T}], \hat{T}] + ... \tag{G.1}$$

In the BCH expansion in Eq. (G.1), the commutator can be expressed as:

$$[\hat{H}, \hat{T}] = \hat{H}\hat{T} - \hat{T}\hat{H} \tag{G.2}$$

and both products in the commutator can be expanded as their normal product and sum over all contraction with the respect to the reference state according to the Wick's theorem. The normal product of the two terms in Eq. (G.2) cancels out by definition ($\{\hat{H}\hat{T}\} - \{\hat{T}\hat{H}\} = 0$). Thus, the only surviving terms in the commutator in Eq. (G.2) are connected terms with the Hamiltonian operator $\hat{H}$ has at least one contraction with the cluster operator $\hat{T}$. Applying the same argument recursively, the whole BCH expansion in Eq. (G.1) consists of connected terms only:

$$e^{-\hat{T}} \hat{H} e^{\hat{T}} = (\hat{H} e^{\hat{T}})_{conn.} \tag{G.3}$$

Thus, we proved the connectedness of the CC energy and amplitude equations.

Appendix H

Supporting information for chapter 5

H.1 Vibronic model parameters

H.1.1 two by two models

The parameters for both models are listed in Tables H.1 and H.2 below. The operator files for model A, model B, and model C are given in List H.1, List H.2, and List H.3 respectively. model A

Table H.1: two by two model parameters.

Parameter	(eV)
E^a	0.0
E^b	0.2
ω_1	0.2
ω_2	0.3
γ	0.2

Table H.2: in (eV).

Parameter	model A	model B	model C
λ_1	0.5	1.0	0.5
λ_2	-0.25	-0.5	0.25

H.1.2 Water H_2O model

The parameters for the linear vibronic model of water are presented in Table H.3. The operator file is given in List H.4.

Table H.3: H_2O model parameters (eV).

Parameter		Parameter		Parameter	
E^{11}	14.051 208	g_1^{11}	0.650 150	g_3^{13}	−0.213 821
E^{22}	11.785 450	g_2^{11}	0.302 387		
E^{33}	18.280 470	g_1^{22}	0.076 394		
Z.P.E	−0.591 746	g_2^{22}	0.291 455		
ω_1	0.208 018	g_1^{33}	−0.692 915		
ω_2	0.481 209	g_2^{33}	0.857 173		
ω_3	0.494 264				

H.1.3 Ammonia NH_3 model

The parameters for the linear vibronic model of ammonia are presented in Table H.4. The operator file is given in List H.5.

Table H.4: NH_3 model parameters (eV).

Parameter		Parameter		Parameter	
E^{11}	15.526 843	g_1^{11}	0.330 653	g_3^{12}	−0.252 207
E^{22}	9.746 612	g_2^{11}	0.573 074	g_5^{12}	0.108 074
E^{33}	15.526 843	g_3^{11}	0.588 249	g_4^{13}	−0.588 249
Z.P.E	−0.954 114	g_5^{11}	0.332 074	g_6^{13}	−0.332 078
ω_1	0.136 676	g_1^{22}	−0.501 301	g_4^{23}	−0.251 602
ω_2	0.438 180	g_2^{22}	0.154 145	g_6^{23}	0.107 915
ω_3	0.213 508	g_3^{22}	0.000 001		
ω_4	0.213 508	g_5^{22}	−0.000 004		
ω_5	0.453 178	g_1^{33}	0.330 653		
ω_6	0.453 178	g_2^{33}	0.573 074		
		g_3^{33}	−0.588 248		
		g_5^{33}	−0.332 083		

H.1.4 Pyrazine $C_4H_4N_2$ model

The Pyrazine is available at reference: Raab, A., Worth, G. A., Meyer, H. D., & Cederbaum, L. S. (1999). Molecular dynamics of pyrazine after excitation to the S 2 electronic state using a realistic 24-mode model Hamiltonian. The *Journal of chemical physics, 110(2)*, 936-946.

H.1.5 Hexahelicene $C_{26}H_{16}$) model

The Hexahelicene is available at reference: Aranda, D., & Santoro, F. (2021). Vibronic spectra of π-conjugated systems with a multitude of coupled states: A protocol based on

linear vibronic coupling models and quantum dynamics tested on hexahelicene. *Journal of Chemical Theory and Computation* 17(3), 1691-1700.

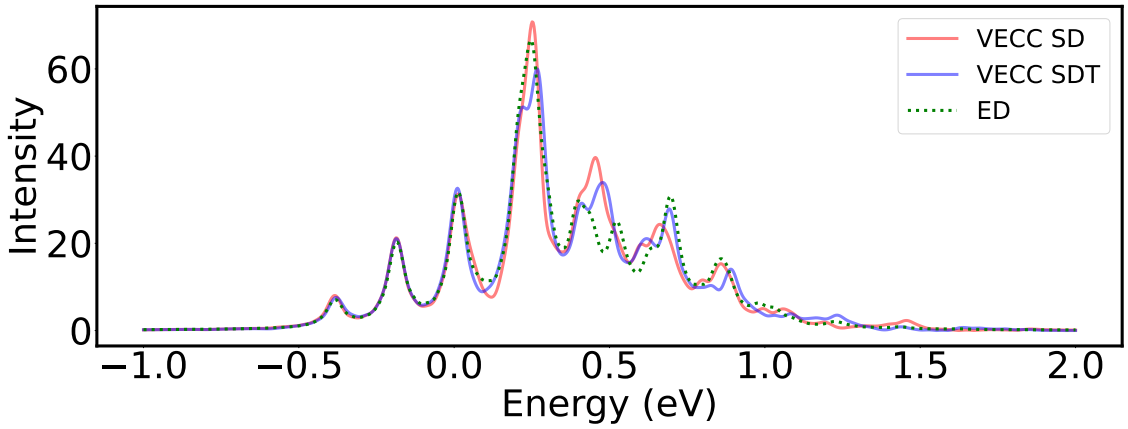
H.2 Spectra simulation for model A and model B

To illustrate the accuracy of the VECC method, we compare to the ED with converged basis for the two by two models on the simulated spectra. We tested on model A and model B which are designed to simulate the strongly vibronic coupling scenarios. Results are shown in Fig. H.1.

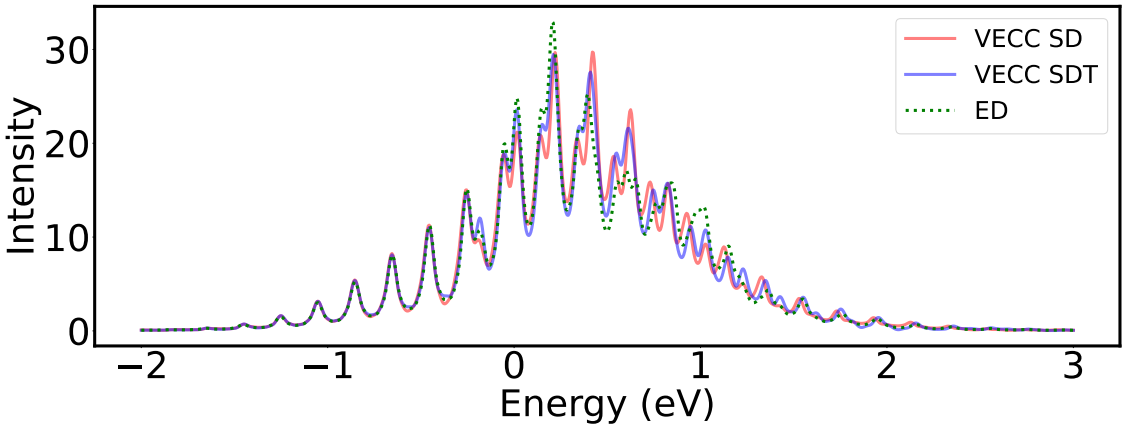
The simulated spectra for model A is given in Fig. H.1a. This is a typical system with a short progression. In general, VECC has good agreement with ED. There are small discrepancies in terms of fine-structure but the band width and shape roughly matches. The spectra for triples (SDT) truncation shows only slight differences with the spectra for doubles (SD) truncation, indicating that VECC is sufficiently converged at SD.

The simulated spectra for model B is given in Fig. H.1b. This is a typical system with long progression. As expected, the simulated spectra shows richer peaks compared to the short progression case. VECC predicts peak positions and intensities consistent with ED. The spectra for SDT and SD show slight differences indicating that VECC is sufficiently converged at SD.

The VECC method shows impressive accuracy. The envelope of the spectra (which is determined by very-short time evolution) is always well reproduced. Somewhat surprisingly, in the ED method, a large basis set (80 basis functions per mode) is required to obtain converged simulated spectra which is computationally expensive and not always feasible for large systems.



(a) Spectra of model A propagated for 100 fs.



(b) Spectra of model B propagated for 100 fs.

Figure H.1: Simulated absorption spectra of two by two models using VECC and ED. Both are generated through a Fourier transform of their time-autocorrelation functions using `autospec84`. Parameters for both models are given in Table H.1 and Table H.2.

H.3 Explicit scheme to test convergence behaviour of Z operator excitation level

Through some mathematical manipulations, we can rewrite the orginal VECC EOM in terms of a linear differential equation of $\hat{C}_x$:

$$i \langle y, n| \frac{d\hat{C}_y}{d\tau} |y, 0\rangle = \sum_x \langle y, n| (\tilde{\hat{\boldsymbol{H}}} - \hat{\rho} + i\frac{d\hat{T}^\dagger}{d\tau})\hat{C}_x |x, 0\rangle . \tag{H.1}$$

By setting

$$\hat{G} \equiv \tilde{\hat{\boldsymbol{H}}} - \hat{\rho} + i\frac{d\hat{T}^\dagger}{d\tau}, \tag{H.2}$$

the original EOM can be simplified as

$$i \langle y, n| \frac{d\hat{C}_y}{d\tau} |y, 0\rangle = \sum_x \langle y, n| \hat{G}\hat{C}_x |x, 0\rangle . \tag{H.3}$$

We solve the EOM for $\hat{C}_x$ in three steps: First, we calculate the double similarity transformed Hamiltonian $\tilde{\tilde{\boldsymbol{H}}}$. Then we apply the Ehrenfest paramaterization to calculate the T residual ($\frac{dT}{d\tau}$), allowing us to determine $\hat{G}$ Finally, we resolve Eq(H.3) in a finite H.O. basis, which can be converted to a matrix equation:

$$i \langle y, n| \frac{d\hat{C}_y}{d\tau} |y, 0\rangle = \sum_{xm} \langle y, n| \hat{G} |x, m\rangle \langle x, m| \hat{C}_x |x, 0\rangle . \tag{H.4}$$

Both matrix elements of $\langle n, y| \hat{G} |m, x\rangle$ and $\langle m, x| \hat{C}_x |0, x\rangle$ can be evaluate using the second quantization rules. Note that the H.O. basis has the same dimension as number of normal mode in the vibronic models. For example, if we have two normal modes in the vibronic model, state $|x, n\rangle$ can be written as:

$$|x, n\rangle \equiv |x, n_1, n_2\rangle \tag{H.5}$$

where n_1, n_2 represent the H.O. basis of the two individual normal mode.

Comparing to the original VECC scheme, another major difference is that we directly propagate $\hat{C}_x$ rather than $\hat{Z}_x$. However, by definition, the excitation level of $\hat{C}_x$ and $\hat{Z}_x$ are the same. Thus the scheme that directly propagate $\hat{Z}_x$ with the same basis truncation level is identical to that of the $\hat{C}_x$.

H.3.1 Scheme to compute diabatic state population

The state population can be calculated using the formula:

$$P_x^{(b)}(\tau) = \frac{\sum_n C_{n,x}^\dagger C_{n,x}}{\sum_{n,y} C_{n,y}^\dagger C_{n,y}}, \tag{H.6}$$

where $C_{n,x} \equiv \langle n, x| \hat{C}_x |0, x\rangle$. In the test scheme we propagate one surface at a time. For a surface b, initially at $\tau = 0$, we set $C_{n,x} = \delta_{x,b}\delta_{n,0}$. The result can be compared with the ED method. In the ED method, $C_{x,n}$ can be expanded into the eigenvalue basis:

$$C_{x,n} = \sum_l e^{-iE_l\tau} V_{x,n,l} V_{b,0,l} \tag{H.7}$$

where $V_{x,n,l}$ are the eigenvector of the vibronic model Hamiltonian.

H.3.2 Scheme to compute ACF and spectra

By definition, $\hat{Z}_x$ can be obtained through the similarity transformation of $\hat{C}_x$:

$$\hat{Z}_x \equiv e^{-\hat{T}^\dagger}\hat{C}_x e^{\hat{T}^\dagger} = (e^{-\hat{T}^\dagger}\hat{C}_x)_{conn.} \tag{H.8}$$

We use the following procedure to obtain $\hat{Z}_x$ from $\hat{C}_x$:

1. resolve $-\hat{T}^\dagger$ and $\hat{T}^\dagger$ in H.O. basis.

$$\langle n| - t_i^* \hat{i} \, |m\rangle = -\sqrt{m} t_m^* \delta_{n,m-1} \tag{H.9}$$
$$\langle n| \, t_i^* \hat{i} \, |m\rangle = \sqrt{m} t_m^* \delta_{n,m-1} \tag{H.10}$$

2. Diagonalize the $\langle m| - \hat{T}^\dagger |n\rangle$ and $\langle m| \hat{T}^\dagger |n\rangle$ matrix:

$$(-\boldsymbol{T}^\dagger)\boldsymbol{U} = \lambda \boldsymbol{U} \tag{H.11}$$
$$(\boldsymbol{T}^\dagger)\boldsymbol{U'} = \gamma \boldsymbol{U'} \tag{H.12}$$

3. Transform the matrix exponential in H.O. basis:

$$\boldsymbol{W} = \boldsymbol{U} e^{\lambda} \boldsymbol{U}^{-1} \tag{H.13}$$
$$\boldsymbol{V} = \boldsymbol{U'} e^{\gamma} \boldsymbol{U'}^{-1} \tag{H.14}$$

4. Evaluate $\hat{Z}_x$ in H.O. basis

$$Z_{x,n} = \sum_{vm} W_{vm} C_{x,m} V_{vn} \tag{H.15}$$

Once we have $\hat{Z}_{x,0}$, we can construct the ACF using the scheme that is the same as the original VECC method and thus obtain the spectra from the ACF.

H.3.3 Make direct comparison to the original operator version of the VECC method

In this section, we proposed a new VECC scheme and we refer it to the matrix version of the VECC method in contrast to the original operator version of the VECC method. There is a slight difference between the two schemes. In the operator version of the VECC method, we restrict maximum net excitation level in $\hat{Z}_x$ operator. For example for double truncation in $\hat{Z}_x$, the maximum allowed excitation is two and for triple truncation in $\hat{Z}_x$, the maximum allowed excitation is three. However, in the matrix version of the VECC method, we apply the finite H.O. basis to resolve $\hat{C}_x$ operator. For N mode systems, with M level truncation of H.O. basis for each mode, the maximum allowed excitation is M^N.

To make the two scheme identical, we can apply an addition projection operator $\hat{P}$ on the $\hat{C}_x$ to restrict maximum level of excitation. For example for a two mode system, if we want to restrict the maximum excitation level to be two. We have:

$$\hat{C}'_x = \hat{P}_{n_1,n_2}\hat{C}_x, \tag{H.16}$$

where

$$\hat{P}_{n_1,n_2} = \begin{cases} \mathbb{1} & if\ n_1 + n_2 \leqslant 2 \\ 0 & if\ n_1 + n_2 > 2 \end{cases}. \tag{H.17}$$

In this way, we can make direct comparison between and matrix-VECC and operator-VECC method.

```
OP_DEFINE-SECTION
title
model A
end-title
end-op_define-section

PARAMETER-SECTION
#                  Frequencies                  #
# ---------------------------------------------- #
w01                       =       0.200000    , ev
w02                       =       0.300000    , ev

#             Electronic Hamitonian             #
# ---------------------------------------------- #
EH_s01_s01                =       0.000000    , ev
EH_s02_s02                =       0.200000    , ev
EH_s03_s03                =       0.000000    , ev

#         Electronic transition moments         #
# ---------------------------------------------- #
Ex_s00_s01                =       0.100000    , ev
Ex_s00_s02                =       0.100000    , ev

#           Linear Coupling Constants           #
# ---------------------------------------------- #
C1_s01_s01_v01            =       0.500000    , ev
C1_s02_s02_v01            =      -0.250000    , ev

C1_s01_s02_v02            =       0.200000    , ev
C1_s02_s01_v02            =       0.200000    , ev
end-parameter-section

HAMILTONIAN-SECTION
 modes    |  el   | v01| v02|

1.00*w01             |2  KE
1.00*w02             |3  KE

0.50*w01             |2  q^2
0.50*w02             |3  q^2

EH_s01_s01                |1 S1&1
EH_s02_s02                |1 S2&2
EH_s03_s03                |1 S3&3

C1_s01_s01_v01            |1 S1&1   |2  q
C1_s02_s02_v01            |1 S2&2   |2  q

C1_s02_s01_v02            |1 S2&1   |3  q
C1_s01_s02_v02            |1 S1&2   |3  q
end-hamiltonian-section

HAMILTONIAN-SECTION_Ex
```

```
 modes    |   el   | v01| v02|

Ex_s00_s01                |1 S3&1
Ex_s00_s02                |1 S3&2
end-hamiltonian-section

end-operator
```

Listing H.1: model A operator file `modelA.op`.

```
OP_DEFINE-SECTION
title
model B
end-title
end-op_define-section

PARAMETER-SECTION
#                  Frequencies                  #
# ---------------------------------------------- #

w01                      =       0.200000    , ev
w02                      =       0.300000    , ev

#             Electronic Hamitonian             #
# ---------------------------------------------- #

EH_s01_s01               =       0.000000    , ev
EH_s02_s02               =       0.200000    , ev
EH_s03_s03               =       0.000000    , ev

#         Electronic transition moments         #
# ---------------------------------------------- #

Ex_s00_s01               =       0.100000    , ev
Ex_s00_s02               =       0.100000    , ev

#          Magnetic transition moments          #
# ---------------------------------------------- #

Mx_s00_s01               =       0.100000    , ev
Mx_s00_s02               =       0.100000    , ev

#           Linear Coupling Constants           #
# ---------------------------------------------- #

C1_s01_s01_v01           =       0.500000    , ev
C1_s02_s02_v01           =      -0.250000    , ev

C1_s02_s01_v02           =       0.200000    , ev
C1_s01_s02_v02           =       0.200000    , ev

end-parameter-section


HAMILTONIAN-SECTION
 modes    |  el  | v01| v02|

1.00*w01            |2  KE
1.00*w02            |3  KE

0.50*w01            |2  q^2
0.50*w02            |3  q^2

```

```
EH_s01_s01                |1 S1&1
EH_s02_s02                |1 S2&2
EH_s03_s03                |1 S3&3

C1_s01_s01_v01            |1 S1&1    |2  q
C1_s02_s02_v01            |1 S2&2    |2  q

C1_s02_s01_v02            |1 S2&1    |3  q
C1_s01_s02_v02            |1 S1&2    |3  q
end-hamiltonian-section

HAMILTONIAN-SECTION_Ex
 modes    |  el   | v01| v02|

Ex_s00_s01                |1 S3&1
Ex_s00_s02                |1 S3&2
end-hamiltonian-section

end-operator
```

Listing H.2: model B operator file `modelB.op`.

```
OP_DEFINE-SECTION
title
model C
end-title
end-op_define-section

PARAMETER-SECTION
#                  Frequencies                  #
# ---------------------------------------------- #

w01                      =       0.200000    , ev
w02                      =       0.300000    , ev

#             Electronic Hamitonian             #
# ---------------------------------------------- #

EH_s01_s01               =       0.000000    , ev
EH_s02_s02               =       0.200000    , ev
EH_s03_s03               =       0.000000    , ev

#         Electronic transition moments         #
# ---------------------------------------------- #

Ex_s00_s01               =       0.100000    , ev
Ex_s00_s02               =       0.100000    , ev

#          Magnetic transition moments          #
# ---------------------------------------------- #

Mx_s00_s01               =       0.100000    , ev
Mx_s00_s02               =       0.100000    , ev

#           Linear Coupling Constants           #
# ---------------------------------------------- #

C1_s01_s01_v01           =       0.500000    , ev
C1_s02_s02_v01           =       0.2500000    , ev

C1_s02_s01_v02           =       0.200000    , ev
C1_s01_s02_v02           =       0.200000    , ev

end-parameter-section

HAMILTONIAN-SECTION
 modes    |  el   | v01| v02|

1.00*w01            |2  KE
1.00*w02            |3  KE

0.50*w01            |2  q^2
0.50*w02            |3  q^2

EH_s01_s01               |1 S1&1
```

```
EH_s02_s02              |1 S2&2
EH_s03_s03              |1 S3&3

C1_s01_s01_v01          |1 S1&1   |2  q
C1_s02_s02_v01          |1 S2&2   |2  q

C1_s02_s01_v02          |1 S2&1   |3  q
C1_s01_s02_v02          |1 S1&2   |3  q
end-hamiltonian-section

HAMILTONIAN-SECTION_Ex
 modes   |  el  | v01| v02|

Ex_s00_s01              |1 S3&1
Ex_s00_s02              |1 S3&2
end-hamiltonian-section

end-operator
```

Listing H.3: model C operator file `modelC.op`.

```
OP_DEFINE-SECTION
title
water
end-title
end-op_define-section

PARAMETER-SECTION
#                  Frequencies                  #
# ---------------------------------------------- #

w01                       =       0.208018    , ev
w02                       =       0.481209    , ev
w03                       =       0.494264    , ev

#             Electronic Hamitonian             #
# ---------------------------------------------- #

EH_s01_s01                =      14.051208    , ev
EH_s02_s02                =      11.785450    , ev
EH_s03_s03                =      18.280470    , ev
EH_s04_s04                =      -0.591746    , ev

#         Electronic transition moments         #
# ---------------------------------------------- #

Ex_s00_s01                =       0.100000    , ev
Ex_s00_s02                =       0.100000    , ev
Ex_s00_s03                =       0.100000    , ev

#           Linear Coupling Constants           #
# ---------------------------------------------- #

C1_s01_s01_v01            =       0.650150    , ev
C1_s01_s01_v02            =       0.302387    , ev
C1_s02_s02_v01            =       0.076394    , ev
C1_s02_s02_v02            =       0.291455    , ev
C1_s03_s03_v01            =      -0.692915    , ev
C1_s03_s03_v02            =       0.857173    , ev

C1_s01_s03_v03            =      -0.213821    , ev
end-parameter-section

HAMILTONIAN-SECTION
 modes    |  el   | v01| v02| v03|

1.00*w01             |2  KE
1.00*w02             |3  KE
1.00*w03             |4  KE

0.50*w01             |2  q^2
0.50*w02             |3  q^2
0.50*w03             |4  q^2

```

```
EH_s01_s01              |1 S1&1
EH_s02_s02              |1 S2&2
EH_s03_s03              |1 S3&3
EH_s04_s04              |1 S4&4

C1_s01_s01_v01          |1 S1&1   |2  q
C1_s01_s01_v02          |1 S1&1   |3  q
C1_s02_s02_v01          |1 S2&2   |2  q
C1_s02_s02_v02          |1 S2&2   |3  q
C1_s03_s03_v01          |1 S3&3   |2  q
C1_s03_s03_v02          |1 S3&3   |3  q

C1_s01_s03_v03          |1 S1&3   |4  q
end-hamiltonian-section

HAMILTONIAN-SECTION_Ex
 modes    |  el  | v01| v02| v03|

Ex_s00_s01              |1 S4&1
Ex_s00_s02              |1 S4&2
Ex_s00_s03              |1 S4&3
end-hamiltonian-section

end-operator
```

Listing H.4: Water (H_2O) operator file `h2o_vibronic_linear.op`.

```
OP_DEFINE-SECTION
title
ammonia
end-title
end-op_define-section

PARAMETER-SECTION
#                   Frequencies                    #
# ---------------------------------------------- #

w01                        =       0.136676    , ev
w02                        =       0.438180    , ev
w03                        =       0.213508    , ev
w04                        =       0.213508    , ev
w05                        =       0.453178    , ev
w06                        =       0.453178    , ev

#              Electronic Hamitonian              #
# ---------------------------------------------- #

EH_s01_s01                 =      15.526843    , ev
EH_s02_s02                 =       9.746612    , ev
EH_s03_s03                 =      15.526843    , ev
EH_s04_s04                 =      -0.954114    , ev

#          Electronic transition moments          #
# ---------------------------------------------- #

Ex_s00_s01                 =       0.100000    , ev
Ex_s00_s02                 =       0.100000    , ev
Ex_s00_s03                 =       0.100000    , ev

#           Linear Coupling Constants             #
# ---------------------------------------------- #

C1_s01_s01_v01             =       0.330653    , ev
C1_s01_s01_v02             =       0.573074    , ev
C1_s01_s01_v03             =       0.588249    , ev
C1_s01_s01_v05             =       0.332074    , ev
C1_s02_s02_v01             =      -0.501301    , ev
C1_s02_s02_v02             =       0.154145    , ev
C1_s02_s02_v03             =       0.000001    , ev
C1_s02_s02_v05             =      -0.000004    , ev
C1_s03_s03_v01             =       0.330653    , ev
C1_s03_s03_v02             =       0.573074    , ev
C1_s03_s03_v03             =      -0.588248    , ev
C1_s03_s03_v05             =      -0.332083    , ev

C1_s01_s02_v03             =      -0.252207    , ev
C1_s01_s02_v05             =       0.108074    , ev
C1_s01_s03_v04             =      -0.588249    , ev
C1_s01_s03_v06             =      -0.332078    , ev
C1_s02_s03_v04             =      -0.251602    , ev
```

```
C1_s02_s03_v06            =       0.107915     , ev
end-parameter-section

HAMILTONIAN-SECTION
 modes    |  el   | v01| v02| v03| v04| v05| v06|

1.00*w01             |2  KE
1.00*w02             |3  KE
1.00*w03             |4  KE
1.00*w04             |5  KE
1.00*w05             |6  KE
1.00*w06             |7  KE

0.50*w01             |2  q^2
0.50*w02             |3  q^2
0.50*w03             |4  q^2
0.50*w04             |5  q^2
0.50*w05             |6  q^2
0.50*w06             |7  q^2

EH_s01_s01               |1 S1&1
EH_s02_s02               |1 S2&2
EH_s03_s03               |1 S3&3
EH_s04_s04               |1 S4&4

C1_s01_s01_v01           |1 S1&1   |2  q
C1_s01_s01_v02           |1 S1&1   |3  q
C1_s01_s01_v03           |1 S1&1   |4  q
C1_s01_s01_v05           |1 S1&1   |6  q
C1_s02_s02_v01           |1 S2&2   |2  q
C1_s02_s02_v02           |1 S2&2   |3  q
C1_s02_s02_v03           |1 S2&2   |4  q
C1_s02_s02_v05           |1 S2&2   |6  q
C1_s03_s03_v01           |1 S3&3   |2  q
C1_s03_s03_v02           |1 S3&3   |3  q
C1_s03_s03_v03           |1 S3&3   |4  q
C1_s03_s03_v05           |1 S3&3   |6  q

C1_s01_s02_v03           |1 S1&2   |4  q
C1_s01_s02_v05           |1 S1&2   |6  q
C1_s01_s03_v04           |1 S1&3   |5  q
C1_s01_s03_v06           |1 S1&3   |7  q
C1_s02_s03_v04           |1 S2&3   |5  q
C1_s02_s03_v06           |1 S2&3   |7  q
end-hamiltonian-section

HAMILTONIAN-SECTION_Ex
 modes    |  el   | v01| v02| v03| v04| v05| v06|

Ex_s00_s01               |1 S4&1
Ex_s00_s02               |1 S4&2
Ex_s00_s03               |1 S4&3

end-hamiltonian-section
```

```
108
109 end-operator
```

Listing H.5: Ammonia (NH_3) operator file `nh3_vibronic_linear.op`.

Appendix I

Supporting information for chapter 6

I.1 Expression of Bogoliubov transformed Hamiltonian (up to quadratic)

In this section, we give detailed expression of the Bogoliubov transformed Hamiltonian defined in Eq. (6.46).

$$
\begin{aligned}
&\tilde{h}^0 : E_0 + \sum_i \sinh\theta_i \sinh\theta_i h_i^i \\
&\tilde{h}^1 : \sum_i (\cosh\theta_i h^i \hat{a}_i^\dagger + \sinh\theta_i h_i \hat{b}_i^\dagger) \\
&\tilde{h}_1 : \sum_i (\cosh\theta_i h_i \hat{a}_i + \sinh\theta_i h^i \hat{b}_i) \\
&\tilde{h}^2 : \frac{1}{2}\sum_{ij} (\cosh\theta_i \cosh\theta_j h^{ij} \hat{a}_i^\dagger \hat{a}_j^\dagger + \sinh\theta_i \sinh\theta_j h_{ij} \hat{b}_i^\dagger \hat{b}_j^\dagger + \cosh\theta_i \sinh\theta_j h_j^i \hat{a}_i^\dagger \hat{b}_j^\dagger + \sinh\theta_i \cosh\theta_j h_j^i \hat{b}_i^\dagger \hat{a}_j^\dagger) \\
&\tilde{h}_2 : \frac{1}{2}\sum_{ij} (\cosh\theta_i \cosh\theta_j h^{ij} \hat{a}_i \hat{a}_j + \sinh\theta_i \sinh\theta_j h_{ij} \hat{b}_i \hat{b}_j + \cosh\theta_i \sinh\theta_j h_j^i \hat{a}_i \hat{b}_j + \sinh\theta_i \cosh\theta_j h_j^i \hat{b}_i \hat{a}_j) \\
&\tilde{h}_1^1 : \sum_{ij} (\cosh\theta_i \cosh\theta_j h_j^i \hat{a}_i^\dagger \hat{a}_j + \sinh\theta_i \sinh\theta_j h_i^j \hat{b}_i^\dagger \hat{b}_j + \cosh\theta_i \sinh\theta_j h^{ij} \hat{a}_i^\dagger \hat{b}_j + \sinh\theta_i \cosh\theta_j h_{ij} \hat{b}_i^\dagger \hat{a}_j)
\end{aligned}
\tag{I.1}
$$

I.2 The initial cluster amplitudes (at high T)

The $\hat{T}$ and $\hat{Z}$ operators in the Bogoliubov representation can be written as:

$$\begin{aligned}\hat{T}^{(w)} = &\sum_i t^{a_i(w)}\hat{a}_i^\dagger + \sum_i t^{b_i(w)}\hat{b}_i^\dagger + \frac{1}{2}\sum_{ij} t^{a_i a_j(w)}\hat{a}_i^\dagger\hat{a}_j^\dagger \\ &+ \frac{1}{2}\sum_{ij} t^{a_i b_j(w)}\hat{a}_i^\dagger\hat{b}_j^\dagger + \frac{1}{2}\sum_{ij} t^{b_i a_j(w)}\hat{b}_i^\dagger\hat{a}_j^\dagger \\ &+ \frac{1}{2}\sum_{ij} t^{b_i b_j(w)}\hat{b}_i^\dagger\hat{b}_j^\dagger,\end{aligned} \tag{I.2}$$

and

$$\begin{aligned}\hat{Z}_x^{(w)} = &z_x^{0(w)} + \sum_i z_x^{a_i(w)}\hat{a}_i^\dagger + \sum_i z_x^{b_i(w)}\hat{b}_i^\dagger \\ &+ \frac{1}{2}\sum_{ij} z_x^{a_i a_j(w)}\hat{a}_i^\dagger\hat{a}_j^\dagger + \frac{1}{2}\sum_{ij} z_x^{a_i b_j(w)}\hat{a}_i^\dagger\hat{b}_j^\dagger \\ &+ \frac{1}{2}\sum_{ij} z_x^{b_i a_j(w)}\hat{b}_i^\dagger\hat{a}_j^\dagger + \frac{1}{2}\sum_{ij} z_x^{b_i b_j(w)}\hat{b}_i^\dagger\hat{b}_j^\dagger\end{aligned} \tag{I.3}$$

We propagate the amplitudes initializing the amplitudes one electronic surface at a time, where this initial surface label is denoted w. At high temperature, ach of the amplitude in Eq. (I.2) and Eq. (I.3) can be mapped to the analytical expression of the thermal density matrix of D.H.O.. The explicit expression for the mapping is as follow:

$$\begin{aligned}t^{a_i(w)} &= -\frac{X_i}{\cosh\theta_i} \\ t^{b_i(w)} &= -\frac{X_i}{\sinh\theta_i} \\ t^{a_i a_j(w)} &= t^{b_i b_j(w)} = 0 \\ t^{a_i b_j(w)} &= t^{b_i a_j(w)} = \delta_{ij}\frac{n_i(\beta) - \cosh^2\theta_i + 1}{\sinh\theta_i\cosh\theta_i}\end{aligned} \tag{I.4}$$

where $X_i \equiv \frac{\lambda_i}{\omega_i}$ and $n_i(\beta) \equiv \frac{1}{1-e^{-\beta\omega_i}}$, and

$$\begin{aligned}z_x^{0(w)} &= \delta_{xw}Q(\beta) \\ z_x^{a_i(w)} &= z_x^{b_i(w)} = z_x^{a_i a_j(w)} \\ &= z_x^{b_i b_j(w)} = z_x^{a_i b_j(w)} = z_x^{b_i a_j(w)} = 0\end{aligned} \tag{I.5}$$

where $Q(\beta) \equiv e^{-\beta(E_0 - \sum_i \frac{(\lambda_{xi}^x)^2}{\omega_i})}\prod_i \frac{1}{1-e^{-\beta\omega_i}}$.

I.3 Motivation of the ansatz for the vibronic problem

In analog to the vibrational problem, the most straightforward ansatz to parameterize the vibronic thermofield state, for surface w is the single exponential ansatz:

$$\begin{aligned} |\phi(\tau)\rangle^{(w)} &\equiv e^{-\tau\hat{\mathbf{H}}}\,|w,U\rangle \\ &= e^{\hat{\mathbf{T}}(\tau)}\,|w,\theta(\beta)\rangle\,, \end{aligned} \tag{I.6}$$

where

$$\hat{\mathbf{T}}(\tau) = \sum_{x,y} |x\rangle\,\hat{T}_{xy}(\tau)\,\langle y| \tag{I.7}$$

and

$$\hat{T}_{xy}(\tau) = t^0_{xy}(\tau) + \sum_p t^p_{xy}\hat{p}^\dagger + \frac{1}{2}\sum_{pq} t^{pq}_{xy}\hat{p}^\dagger\hat{q}^\dagger + ... \tag{I.8}$$

The cluster operator $\hat{T}$ spans both electronic and vibrational DoF. Projecting the vibronic EOM by $\langle z,\theta(\beta)|\,\hat{\Omega}^\dagger_\mu$, in analog to vibrational counterpart in Eq. (6.57), we obtain

$$-\langle z,\theta(\beta)|\,\hat{\Omega}^\dagger_\mu \sum_{xy}\left(e^{-\hat{\mathbf{T}}(\tau)}\right)\frac{d}{d\tau}\left(e^{\hat{\mathbf{T}}}(\tau)\right)|w,\theta(\beta)\rangle = \langle z,\theta(\beta)|\,\hat{\Omega}^\dagger_\mu \sum_{wxy}\left(e^{-\hat{\mathbf{T}}(\tau)}\right)\tilde{\boldsymbol{H}}\left(e^{\hat{\mathbf{T}}(\tau)}\right)|w,\theta(\beta)\rangle\,. \tag{I.9}$$

However, due to the matrix nature of the cluster operator with respect to the electronic DoF, the disconnected contributions in both sides Eq. (I.9) do not cancels out:

$$\sum_x \left(e^{-\hat{\boldsymbol{T}}(\tau)}\right)_{zx}\left(\frac{d}{d\tau}e^{\hat{\boldsymbol{T}}(\tau)}\right)_{xy} \neq \left(\frac{d\hat{\boldsymbol{T}}(\tau)}{d\tau}\right)_{zy} \tag{I.10}$$

and

$$\sum_{w,x}\left(e^{-\hat{T}(\tau)}\right)_{zw}\tilde{\boldsymbol{H}}_{wx}\left(e^{\hat{T}(\tau)}\right)_{xy} \neq \left((\hat{H}e^{\hat{\boldsymbol{T}}(\tau)})_{conn.}\right)_{zy}. \tag{I.11}$$

To avoid this complication, we choose $\hat{T}$ to be pure vibrational and independent of electronic surface. In order to achieve this, we introduce the mixed CC/CI ansatz:

$$|\phi(\tau)\rangle^{(w)} \equiv e^{-\tau\hat{H}}\,|w,U\rangle = e^{\hat{T}^{(w)}(\tau)}\sum_x \hat{Z}^{(w)}_x(\tau)\,|x,\theta(\beta)\rangle\,. \tag{I.12}$$

In this way, $\hat{T}$ has no electronic dependencies and the EOM becomes connected again, i.e.,

$$e^{-\hat{T}^{(w)}(\tau)}\frac{d}{d\tau}e^{\hat{T}^{(w)}(\tau)} = \frac{d\hat{T}^{(w)}(\tau)}{d\tau} \tag{I.13}$$

and

$$e^{-\hat{T}^{(w)}(\tau)}\hat{H}_{xy}e^{\hat{T}^{(w)}(\tau)} = (\hat{H}_{xy}e^{\hat{T}^{(w)}}(\tau))_{conn.}. \tag{I.14}$$

The mixing of electronic states is now all induced by the CI operator $\hat{Z}$. Making use of Eq. (I.13) and Eq. (I.14), the EOM (Eq. (6.92)) for full vibronic coupling problem with mixed CC/CI ansatz can be derived.

I.4 Detailed scheme for calculating the variance of the position (q-variance) using VE-TFCC

In this section, we give the explicit scheme to calculate the q-variance (Δq) from the VE-TFCC approach. By definition $\Delta q_i \equiv \langle \hat{q}_i^2 \rangle - \langle \hat{q}_i \rangle^2$. We can use the general scheme discussed in section 6.4.1 to calculate the individual expectation values $\langle \hat{q} \rangle$ and $\langle \hat{q}^2 \rangle$ and then the variance can be determined. We will elaborate the detailed working equations below.

Firstly we can express the $\hat{q}$ operator in Bosonic construction operators:

$$\hat{q}_i = \frac{1}{\sqrt{2}}(\hat{i}^\dagger + \hat{i}). \tag{I.15}$$

Thus, we can express $\hat{q}^2$ as:

$$\begin{aligned} \hat{q}_i^2 &= \frac{1}{2}(\hat{i}^\dagger + \hat{i})(\hat{i}^\dagger + \hat{i}) \\ &= \frac{1}{2}(\hat{i}^\dagger\hat{i}^\dagger + \hat{i}^\dagger\hat{i} + \hat{i}\hat{i}^\dagger + \hat{i}\hat{i})([\hat{i}, \hat{i}^\dagger] = 1) \\ &= \frac{1}{2}\hat{i}^\dagger\hat{i}^\dagger + \hat{i}^\dagger\hat{i} + \frac{1}{2}\hat{i}\hat{i} + \frac{1}{2}. \end{aligned} \tag{I.16}$$

Making using of Eq. (6.100) and explicit equation of $\hat{q}_i$ and $\hat{q}_i^2$ in Eq. (I.15) and Eq. (I.16), we can express the $\langle \hat{q} \rangle$ and $\langle \hat{q}^2 \rangle$ in terms of the thermal physical reduced density matrices:

$$\langle \hat{q}_i(\tau) \rangle = \frac{1}{\sqrt{2}} \sum_x \left(d_x^{xi}(\tau) + d_{xi}^x(\tau) \right), \tag{I.17}$$

$$\left\langle \hat{q}_i^2(\tau) \right\rangle = \sum_x \left(\frac{1}{2} d_x^{xii}(\tau) + d_{xi}^{xi}(\tau) + \frac{1}{2} d_{xii}^x(\tau) + \frac{1}{2}\delta_{xx} \right), \tag{I.18}$$

where the thermal physical reduced density matrices are defined as:

$$\begin{aligned} d_y^{xi}(\tau) &\equiv \frac{1}{Q(\tau)} \langle x, \theta | \hat{i}^\dagger \left| \phi^{(y)}(\tau) \right\rangle, \\ d_{yi}^x(\tau) &\equiv \frac{1}{Q(\tau)} \langle x, \theta | \hat{i} \left| \phi^{(y)}(\tau) \right\rangle, \\ d_{yj}^{xi}(\tau) &\equiv \frac{1}{Q(\tau)} \langle x, \theta | \hat{i}^\dagger \hat{j} \left| \phi^{(y)}(\tau) \right\rangle, \\ d_y^{xij}(\tau) &\equiv \frac{1}{Q(\tau)} \langle x, \theta | \hat{i}^\dagger \hat{j}^\dagger \left| \phi^{(y)}(\tau) \right\rangle, \\ d_{yij}^x(\tau) &\equiv \frac{1}{Q(\tau)} \langle x, \theta | \hat{i}\hat{j} \left| \phi^{(y)}(\tau) \right\rangle. \end{aligned} \tag{I.19}$$

and the canonical partition function $Q(\tau) \equiv \sum_x z_x^{0(x)}(\tau)$. For simplicity, since all thermal physical reduced density matrices are temperature-dependent, we will drop the temperature

(τ) of them in the rest of this section ($d_y^{x\mu} \equiv d_y^{x\mu}(\tau)$).

Next, we map the thermal physical reduced density matrices from the thermal reduced density matrices in Bogoliubov representation:

$$
\begin{aligned}
d_y^{xi} &= \frac{1}{Q(\tau)} \langle x,\theta| \cosh\theta_i \hat{a}_i^\dagger + \sinh\theta_i \hat{b}_i \left|\phi^{(y)}\right\rangle = \sinh\theta_i \tilde{d}^x_{yb_i}, \\
d_{yi}^{x} &= \frac{1}{Q(\tau)} \langle x,\theta| \cosh\theta_i \hat{a}_i + \sinh\theta_i \hat{b}_i^\dagger \left|\phi^{(y)}\right\rangle = \cosh\theta_i \tilde{d}^x_{ya_i}, \\
d_y^{xij} &= \frac{1}{Q(\tau)} \langle x,\theta| (\cosh\theta_i \hat{a}_i^\dagger + \sinh\theta_i \hat{b}_i)(\cosh\theta_j \hat{a}_j^\dagger + \sinh\theta_j \hat{b}_j \left|\phi^{(y)}\right\rangle = \sinh\theta_i \sinh\theta_j \tilde{d}^x_{yb_ib_j}, \\
d_{yij}^{x} &= \frac{1}{Q(\tau)} \langle x,\theta| (\cosh\theta_i \hat{a}_i + \sinh\theta_i \hat{b}_i^\dagger)(\cosh\theta_j \hat{a}_j + sinh\theta_j \hat{b}_j^\dagger) \left|\phi^{(y)}\right\rangle = \cosh\theta_i \cosh\theta_j \tilde{d}^x_{ya_ia_j}, \\
d_{yj}^{xi} &= \frac{1}{Q(\tau)} \langle x,\theta| (\cosh\theta_i \hat{a}_i^\dagger + \sinh\theta_i \hat{b}_i)(\cosh\theta_j \hat{a}_j + \sinh\theta_j \hat{b}_j^\dagger) \left|\phi^{(y)}\right\rangle \\
&= \sinh\theta_i \cosh\theta_j \tilde{d}^x_{yb_ia_j} + \sinh\theta_i \sinh\theta_j \delta_{ij}\delta_{xy},
\end{aligned}
\tag{I.20}
$$

where $\tilde{d}_y^{x\mu}$ represent thermal reduced density matrices in Bogoliubov representation.

In the last step, we can calculate the thermal reduced density matrices in Bogoliubov representation ($\tilde{d}_y^{x\mu}$) from the cumulant expression of the cluster amplitudes:

$$
\begin{aligned}
d_y^{x0} &= \tilde{d}_y^{x0} = z_x^{0(y)}, \\
\tilde{d}^x_{yp} &= t^{p(y)} z_x^{0(y)} + z_x^{p(y)}, \\
\tilde{d}^x_{ypq} &= t^{pq(y)} z_x^{0(y)} + t^{p(y)} z_x^{q(y)} + t^{q(y)} z_x^{p(y)} + t^{p(y)} t^{q(y)} z_x^{0(y)} + z_x^{pq(y)}.
\end{aligned}
\tag{I.21}
$$

In this way, we complete the explicit scheme to calculate the q-variance. The procedure is in the reverse order as follow:

(1) Calculate reduced thermal density matrices in Bogoliubov representation using the cumulant expression in Eq. (I.21).

(2) Map the reduced thermal density matrices in Bogoliubov representation to physical reduced density matrices using Eq. (I.20).

(3) Calculate expectation value $\langle \hat{q}_i \rangle$ and $\langle \hat{q}_i^2 \rangle$ from physical reduced density matrices using Eq. (I.17) and Eq. (I.18).

(4) Calculate the variance using the formula $\langle \Delta \hat{q}_i^2 \rangle \equiv \langle \hat{q}_i \rangle - \langle \hat{q}_i \rangle^2$.

I.5 Data for standard thermochemistry calculation

I.5.1 Details on calculations of the reaction energy at 0 K

First, we calculated the reaction energy with the noJT approximation. The single point ground state electronic energies for CoF_3 (-1680.9725264215 E_H), F^- (-99.6938067791 E_H) and $CoF_4{}^-$ at its T_d reference structure (-1780.8473934862 E_H) are obtained at the GMC-QDPT/cc-pVTZ level. They are subtracted to give the electronic reaction energy ($E_{\rm el}$) $-$ 475.37 kJ/mol. CoF_3 has a D_{3h} optimized structure with $r_{\rm CF} = 1.71$ Å. To maintain consistency as for $CoF_4{}^-$, the active space with the five 3d-dominated orbitals and six electrons was used for CoF_3. The ground state of CoF_3 adopts a $^5A_1'$ term symbol. The occupation scheme of this state is shown in Fig. 6.6b.

Now, we consider the vibrational and vibronic corrections for the reaction energy. At T = 0 K, there is no rotational and translational correction. Only vibrational ZPE and vibronic ground state energy shall be considered. The ZPE of CoF_3 is 16.37 kJ/mol and there is no ZPE for F^- anion. The vibronic ground state energies of $CoF_4{}^-$ calculated using the block relaxation and VE-TFCC are the essentially identical, 14.48 vs. 14.52 kJ/mol, respectively. We take the VE-TFCC value to calculate the vibrational and vibronic correction of the reaction energy at $T = 0$ K to be $14.52 - 16.37 = -1.85$ kJ/mol. For the noJT approximation, the subtraction of the ZPE in Eq. (6.108) and the ZPE of CoF_3 gives a $20.40 - 16.37 = 4.03$ kJ/mol correction to the reaction energy.

Adding up the electronic and the vibrational and vibronic contributions, the reaction energy at $T = 0$ K is -477.30 kJ/mol in the full JT treatment using VE-TFCC, and -471.34 kJ/mol in the noJT approximation. The $\sim$ 6 kJ/mol difference reflects the JT effect in stabilizing the product and facilitating the reaction. This energy difference is non-negligible compared to the chemical accuracy of 4 kJ/mol. The -477.30 kJ/mol calculated reaction energy is in qualitative agreement with the experimental value of -442.3 ± 25 kJ/mol. [199]

We also examined the difference between static and dynamic JT treatments in calculating the reaction energy. The VE-TFCC result above includes the full dynamic JT effect, since the vibronic Hamiltonian does not impose any restriction of $CoF_4{}^-$ to stay in one of the three minima on the low energy trough of the ground electronic state PES. This restriction corresponds to the static JT treatment. To calculate the reaction energy with only static JT effect, we optimized the $CoF_4{}^-$ structure without imposing any symmetry constraint, and calculated its vibrational frequencies at the optimized structure. All calculations were performed at the same level of theory. The optimized ground state structure is in D_{2d} symmetry and has no imaginary frequency, which meets the anticipation based on the Epikernal Principal. [203] It is distorted from the T_d reference structure along the e_x bending mode shown in Fig. 6.7(a), with the electronic energy -1780.8491766235 E_H, i.e., a 4.68 kJ/mol JT stabilization energy from the T_d reference structure. The stable structure has a ZPE of 20.09 kJ/mol.

I.5.2 Thermal internal energy corrections data

The thermal internal energy data get from the standard thermochemistry calculations is given in Table I.1.

The two columns of data are given for CoF_4^- in the T_d reference structure and D_{2d} ground state global minimum. We emphasize again that the hessian calculation for the T_d structure was performed using averaged PES of the two ^5E component states, which is smooth and gives normal modes that are adapted to the T_d symmetry. The vibrational thermal corrections are identical (undiscernible differences after rounding) for the two structures of CoF_4^-, as the frequencies are only slightly different after the JT distortion, by < 70 cm^{-1} and mostly for splitting degenerate modes to non-degenerate modes due to symmetry lowering, i.e., e mode to $a_1 + b_1$ modes, t_2 modes to $a_1 + e$ or $b_1 + e$ modes. The small differences are blurred in thermal average.

	CoF_3	F^-	$CoF_4^-(T_d)$	$CoF_4^-(D_{2d})$
E_{trans}	3.72	3.72	3.72	3.72
E_{rot}	3.72	0.00	3.72	3.72
E_{vib}	21.69	0.00	29.60	29.60
E_{tot}	29.13	3.72	37.03	37.03

Table I.1: Calculated thermal internal energy corrections (kJ/mol) at 298K for the three species in Eq. 6.105.

I.5.3 Entropies at 298 K

The entropy data get from the standard thermochemistry calculations is given in Table I.2.Again, two columns are given for CoF_4^- for the noJT approximation (T_d) and static JT treatment (D_{2d}).

There is no electronic spin contribution to the reaction entropy. This is because the reactant side (CoF_3 + F^-) and the product side (CoF_4^-) have the same spin multiplicities of 5. Their associated entropies cancel. However, for the noJT approximation, there is an electronic contribution to entropy in the product side of $R\log 2 = 0.006$ kJ/mol/K, due to the doubly spatial degeneracy of the ^5E term symbol of CoF_4^-. It should be added to the S_{tot} of CoF_4^-. Such an electronic spatial degeneracy entropy is inherited by the degeneracies of the vibronic eigenstates that are derived from the JT interaction of the ^5E term symbol. Therefore, in our VE-TFCC calculation, we do not need to explicitly consider the entropy that stems from this degeneracy. For the static JT treatment, there are three D_{2d} distorted CoF_4^- configurations obtained along three directions on the e mode space. Therefore, we need to add the $R\log 3 = 0.009$ kJ/mol/K configuration entropy to the product side.

	CoF_3	F^-	$CoF_4^-(T_d)$	$CoF_4^-(D_{2d})$
S_{trans}	0.168	0.145	0.170	0.170
S_{rot}	0.101	0.000	0.106	0.112
S_{vib}	0.034	0.000	0.054	0.058
S_{tot}	0.303	0.145	0.330	0.340

Table I.2: Calculated entropies (in kJ/mol/K) of the species in Eq. (6.105) at 298K.